Karlsruher Institut für Technologie

Photonic Devices Made from Molecular Materials: A Multi-Scale Modeling Approach

Zur Erlangung des akademischen Grades eines

DOKTORS DER NATURWISSENSCHAFTEN (Dr. rer. nat.)

von der KIT-Fakultät für Physik des
Karlsruher Instituts für Technologie (KIT)
angenommene

DISSERTATION

von

M. Sc. Benedikt Alexander Raphael Zerulla

am Institut für Nanotechnologie

Tag der mündlichen Prüfung:	21. Juni 2024
Referent:	Prof. Dr. Carsten Rockstuhl
Korreferent:	Prof. Dr. Igor Tsukerman

This work (with the exception of reprinted or adapted tables and figures for which the copyright is held by the respective journal) is licensed under a Creative Commons "Attribution-ShareAlike 4.0 International" license. To view a copy of the license, visit https://creativecommons.org/licenses/by-sa/4.0/deed.en.

Abstract

Light-matter interactions of molecules are very important for many technologies influencing the daily life of human beings. Important instances are optical applications of molecular materials such as in organic light-emitting diodes and organic solar cells. Molecular materials with adjustable optical properties are of special interest for functional photonic devices. However, finding suitable molecules for specific optical effects is often demanding as the molecular chemical design space is very large. Simulations, which are potentially considerably less expensive than experiments, mainly incorporate phenomenological descriptions of molecules. The phenomenological description is often not sufficient for a precise quantitative analysis.

To overcome such limitations, we present in this thesis a multi-scale approach to compute the optical response of photonic devices incorporating molecules. In this context, we connect two scientific disciplines to cover several length scales, starting at a single molecule and finishing at an entire photonic device. In contrast to phenomenological descriptions, the computed optical response of finite-size molecular models is based on a quantum-chemical method, namely time-dependent density functional theory. The optical response of the photonic device is calculated using Maxwell scattering simulations. The central object of the multi-scale approach is the transition (T-) matrix, which connects the microscopic description of the optical response of a molecule to the macroscopic description of the photonic device.

We consider the optical properties of various molecules in photonic devices using the multi-scale approach. In this context, we analyze the polarization-dependent response of molecular monolayers on dielectric substrates. This study can potentially be of interest for the *in situ* monitoring of chemical processes. Furthermore, we consider the coupling of optical cavities to molecular films. This analysis could be potentially applied on simulating chemical reactions inside optical cavities. We also design a metasurface of cylinders consisting of a molecular material. The metasurface enhances the circular dichroism signal of the molecular material that is usually very small and difficult to detect. The design of the metasurface is possible due to a homogenization based on the T-matrix of a molecular structure inside a crystalline lattice.

To consider the nonlinear optical response of molecules, we extend the multi-scale approach with an object which we term the Hyper-T-matrix. The Hyper-T-matrix has a similar role for nonlinear optical processes as the T-matrix for linear optical processes. With the extended multi-scale approach, we analyze the second-harmonic generation response of molecular films and enhance it with suitable photonic devices.

We emphasize that the multi-scale approach allows not only to analyze experimental measurements of the optical response of molecules, but also to design photonic devices before they are fabricated. This saves both costs and time, as the design space of the geometry parameters can be efficiently investigated using simulations.

In this thesis, we study various carefully selected optical effects, but the multi-scale approach can be used for multiple further linear and nonlinear optical processes. An example would be higher-order nonlinear optical effects such as third-harmonic generation.

Zusammenfassung

Licht-Materie-Wechselwirkungen von Molekülen sind sehr wichtig für viele Technologien, die den Alltag zahlreicher Menschen beeinflussen. Molekulare Materialien sind beispielsweise essentiell für optische Anwendungen wie organische Leuchtdioden und organische Solarzellen. Von besonderem Interesse für funktionale photonische Systeme sind molekulare Materialien mit veränderbaren optischen Eigenschaften. Allerdings ist es oft anspruchsvoll, geeignete Moleküle für spezifische optische Effekte zu finden, da es sehr viele Möglichkeiten für die Form der Moleküle gibt. Simulationen, die potenziell deutlich kostengünstiger als Experimente sind, beinhalten meist phänomenologische Beschreibungen der Moleküle. Die phänomenologische Beschreibung ist allerdings oftmals nicht ausreichend für eine präzise quantitative Analyse.

Um solche Einschränkungen zu überwinden, präsentieren wir in dieser Dissertation einen Multiskalen-Ansatz, um die optische Antwort photonischer Systeme zu berechnen, die molekulare Struturen beinhalten. In diesem Zusammenhang verbinden wir zwei wissenschaftliche Disziplinen, um verschiedene Längenskalen abzudecken. Wir fangen bei einem einzelnen Molekül an und enden bei einem vollständigen photonischen System. Im Gegensatz zu phänomenologischen Beschreibungen basiert die berechnete optische Antwort endlich großer molekularer Modelle auf einer quantenmechanischen Methode, und zwar der zeitabhängigen Dichtefunktionaltheorie (TD-DFT). Die optische Antwort des photonischen Systems wird mit Maxwell Streusimulationen bestimmt. Das zentrale Objekt des Multiskalen-Ansatzes ist die Transition (T-) matrix, die die mikroskopische Beschreibung der optischen Antwort eines Moleküls mit der makroskopischen Beschreibung des photonischen Systems verbindet.

Wir betrachten mithilfe des Multiskalen-Ansatzes die optischen Eigenschaften verschiedenartiger Moleküle innerhalb photonischer Systeme. In diesem Zusammenhang analysieren wir die polarisationsabhängige Antwort molekularer Monoschichten auf dielektrischen Substraten. Diese Studie kann potenziell von Interesse sein für die *in situ* Betrachtung chemischer Prozesse. Weiterhin betrachten wir die Kopplung optischer Resonatoren mit molekularen Filmen. Diese Analyse kann perspektivisch darauf angewandt werden, chemische Reaktionen innerhalb optischer Resonatoren zu simulieren. Wir gestalten auch eine Metaoberfläche von Zylindern, die aus einem molekularen Material bestehen. Die Metaoberfläche verstärkt das Zirkulardichroismus-Signal des molekularen Materials, welches gewöhnlich sehr klein und schwer zu messen ist. Die Gestaltung der Metaoberfläche wird durch eine Homogenisierung ermöglicht, die auf der T-matrix einer molekularer Struktur innerhalb eines kristallinen Gitters basiert.

Um die nichtlineare optische Antwort von Molekülen zu bestimmen, erweitern wir den Multiskalen-Ansatz mithilfe eines Objektes, das wir die Hyper-T-matrix nennen. Die Hyper-T-matrix hat eine ähnliche Rolle für nichtlineare optische Prozesse inne, wie die T-matrix für lineare optische Prozesse. Mithilfe des erweiterten Multiskalen-Ansatzes analysieren wir die frequenzverdoppelte Antwort molekularer Filme und verstärken diese mit geeigneten photonischen Systemen.

Wir betonen, dass der Multiskalen-Ansatz nicht nur die Analyse experimenteller Messungen der optischen Antwort von Molekülen erlaubt, sondern auch die Gestaltung photonischer

Systeme bevor diese hergestellt werden. Dies spart sowohl Kosten als auch Zeit, da die Parameter der Geometrie effizient mit Simulationen erforscht werden können.

Wir studieren in dieser Dissertation verschiedenartige, sorgfältig ausgewählte optische Effekte, aber der Multiskalen-Ansatz kann für viel mehr lineare und nichtlineare optische Prozesse verwendet werden. Ein Beispiel sind nichtlineare optische Effekte höherer Ordnung wie Frequenzverdreifachung.

Publications

I contributed to the following publications, incorporating peer-reviewed articles, articles submitted for review, and conference contributions. Bold letters indicate publications, which are central to this thesis.

Peer-Reviewed Articles

[P1] R. Venkitakrishnan, Y. Augenstein, B. Zerulla, F. Z. Goffi, M. Plum, and C. Rockstuhl, "On the physical significance of non-local material parameters in optical metamaterials," *New Journal of Physics* **25**, 123014 (2023).

[P2] L. Rebholz, M. Krstić, B. Zerulla, M. Pawlak, W. Lewandowski, I. Fernandez-Corbaton, and C. Rockstuhl, "Separating the material and geometry contribution to the circular dichroism of chiral objects made from chiral media," *ACS Photonics* **11**, 1771–1779 (2024).

[P3] **B. Zerulla, C. Li, D. Beutel, S. Oßwald, C. Holzer, J. Bürck, S. Bräse, C. Wöll, I. Fernandez-Corbaton, L. Heinke, C. Rockstuhl, and M. Krstić, "Exploring functional photonic devices made from a chiral metal–organic framework material by a multiscale computational method," *Advanced Functional Materials* 34, 2301093 (2024).**

[P4] **B. Zerulla, M. Krstić, D. Beutel, C. Holzer, C. Wöll, C. Rockstuhl, and I. Fernandez-Corbaton, "A multi-scale approach for modeling the optical response of molecular materials inside cavities," *Advanced Materials* 34, 2200350 (2022).**

[P5] **B. Zerulla, R. Venkitakrishnan, D. Beutel, M. Krstić, C. Holzer, C. Rockstuhl, and I. Fernandez-Corbaton, "A T-matrix based approach to homogenize artificial materials," *Advanced Optical Materials* 11, 2201564 (2023).**

[P6] **B. Zerulla, D. Beutel, C. Holzer, I. Fernandez-Corbaton, C. Rockstuhl, and M. Krstić, "A multi-scale approach to simulate the nonlinear optical response of molecular nanomaterials," *Advanced Materials* 36, 2311405 (2024).**

[P7] **B. Zerulla, A. L. Díaz, C. Holzer, C. Rockstuhl, I. Fernandez-Corbaton, and M. Krstić, "Surface second-harmonic generation in centrosymmetric molecular crystalline materials: How thick is the surface?" *Advanced Optical Materials* 36, 2311405 (2024).**

[P8] **B. Zerulla, M. Krstić, S. Chen, Z. Yu, D. Beutel, C. Holzer, M. Nyman, A. Nefedov, Y. Wang, T. Mayerhöfer, C. Wöll, and C. Rockstuhl, "Polarization-dependent effects in vibrational absorption spectra of 2D finite-size adsorbate islands on dielectric substrates," *Physiscal Chemistry Chemical Physics* 26, 13683–13693 (2024).**

[P9] Y. J. Franzke, C. Holzer, J. H. Andersen, T. Begušić, F. Bruder, S. Coriani, F. Della Sala, E. Fabiano, D. A. Fedotov, S. Fürst, S. Gillhuber, R. Grotjahn, M. Kaupp, M. Kehry, M. Krstić, F. Mack, S. Majumdar, B. D. Nguyen, S. M. Parker, F. Pauly, A. Pausch, E. Perlt, G. S. Phun, A. Rajabi, D. Rappoport, B. Samal, T. Schrader, M. Sharma, E. Tapavicza, R. S. Treß, V. Voora, A. Wodyński, J. M. Yu, B. Zerulla, F. Furche, C. Hättig, M. Sierka, D. P. Tew, and F. Weigend, "TURBOMOLE: Today and Tomorrow," *Journal of Chemical Theory and Computation* **19**, 6859–6890 (2023).

Articles Submitted for Review

[S1] L. Freter, B. Zerulla, M. Krstić, C. Holzer, C. Rockstuhl, and I. Fernandez-Corbaton, "A tensor product space for studying the interaction of bipartite states of light with nanostructures," *(Preprint) arXiv:2404.18498* (2024).

Conference Contributions

[C1] B. Zerulla, M. Krstić, D. Beutel, C. Holzer, C. Wöll, C. Rockstuhl, and I. Fernandez-Corbaton, "A virtual design platform for molecular materials in photonic cavities," in *Virtual Materials Design, CECAM Flagship Workshop*, (poster) (2022).

[C2] B. Zerulla, R. Venkitakrishnan, D. Beutel, M. Krstić, C. Holzer, C. Rockstuhl, and I. Fernandez-Corbaton, "A T-matrix based approach to homogenize materials and metamaterials," in *Metamaterials 2022, 16th International Congress on Artificial Materials for novel wave phenomena*, (oral presentation) (2022).

[C3] B. Zerulla, M. Krstić, D. Beutel, C. Holzer, C. Wöll, C. Rockstuhl, and I. Fernandez-Corbaton, "A multi-scale approach to simulate molecules in complex photonic devices," in *CLEO 2023, FW4H.3*, (oral presentation) (2023).

Conference Contributions Presented by Others

[CO1] C. Rockstuhl, A. Rahimzadegan, T. D. Karamanos, R. Alaee, A. G. Lamprianidis, D. Beutel, R. W. Boyd, C. Holzer, M. Krstić, B. Zerulla, and I. Fernandez-Corbaton, "A comprehensive multipolar theory for metasurfaces and metamaterials," in *Metamaterials XIII*, (oral presentation), Vol. PC12130, PC1213001, edited by K. F. MacDonald, I. Staude, and A. V. Zayats (2022).

[CO2] B. Zerulla, M. Krstic, D. Beutel, C. Holzer, C. Rockstuhl, and I. Fernandez-Corbaton, "Molecules in (fancy) cavities," in *Nanophotonics IX*, (oral presentation), Vol. PC12131, PC1213111, edited by D. L. Andrews, A. J. Bain, and J.-M. Nunzi (2022).

[CO3] R. Venkitakrishnan, B. Zerulla, F. Z. Goffi, M. Plum, and C. Rockstuhl, "On the physical significance of non-local material parameters," in *Metamaterials 2022, 16th International Congress on Artificial Materials for novel wave phenomena*, (poster) (2022).

[CO4] B. Zerulla, M. Krstić, D. Beutel, C. Holzer, C. Wöll, C. Rockstuhl, and I. Fernandez-Corbaton, "Computing the optical response of molecular materials: from nano to device scales," in *Metamaterials 2022, 16th International Congress on Artificial Materials for novel wave phenomena*, (oral presentation) (2022).

[CO5] C. Rockstuhl, A. Rahimzadegan, T. Karamanos, R. Alaee, A. Lamprianidis, D. Beutel, N. Perdana, R. Boyd, C. Holzer, M. Krstić, B. Zerulla, and I. Fernandez-Corbaton, "A unifying T-matrix approach to describe natural and artificial photonic materials," in *Metamaterials 2022, 16th International Congress on Artificial Materials for novel wave phenomena*, (oral presentation) (2022).

[CO6] C. Rockstuhl, D. Beutel, N. Perdana, B. Zerulla, N. Asadova, P. Garg, A. Lamprianidis, R. Venkitakrishnan, L. Rebholz, M. Nyman, C. Holzer, M. Krstić, and I. Fernandez-Corbaton, "Current developments in describing photonic materials using a T-matrix approach: from a general data format and public repository to the solution of inverse problems," in *Metamaterials 2023, 17th International Congress on Artificial Materials for novel wave phenomena*, (oral presentation) (2023).

[CO7] L. Rebholz, M. Krstić, B. Zerulla, M. Pawlak, W. Lewandowski, I. Fernandez-Corbaton, and C. Rockstuhl, "Separating the material and geometry contribution to the circular dichroism of chiral objects made from chiral media," in *Metamaterials 2023, 17th International Congress on Artificial Materials for novel wave phenomena*, (oral presentation) (2023).

[CO8] M. Krstić, C. Holzer, B. Zerulla, D. Beutel, C. Li, L. Heinke, C. Wöll, I. Fernandez-Corbaton, and C. Rockstuhl, "How can (TD-)DFT improve multi-scale optical simulations of novel nano-materials and devices?" In *CLEO 2023, FM1E.3*, (oral presentation) (2023).

[CO9] C. Rockstuhl, D. Beutel, B. Zerulla, N. Perdana, M. Nyman, C. Holzer, M. Krstić, and I. Fernandez-Corbaton, "Multiscale modeling of molecular nanophotonic materials," in *Future of Nanophotonic Scattering*, (oral presentation) (2023).

[CO10] C. Rockstuhl, D. Beutel, B. Zerulla, N. Perdana, M. Nyman, C. Holzer, M. Krstić, and I. Fernandez-Corbaton, "Multiscale modeling of molecular nanophotonic materials," in *NOMA*, (oral presentation) (2023).

[CO11] M. Krstić, B. Zerulla, C. Holzer, D. Beutel, A. Fingolo, L. Heinke, I. Fernandez-Corbaton, C. Wöll, and C. Rockstuhl, "Optical properties of metal-organic frameworks and devices thereof," in *FUTURE3DAM*, (poster) (2023).

[CO12] C. Rockstuhl, D. Beutel, B. Zerulla, M. Nyman, C. Holzer, M. Krstić, and I. Fernandez-Corbaton, "A multi-scale approach to simulate the nonlinear optical response of molecular nanomaterials," in *16th Annual Meeting Photonic Devices*, (oral presentation) (2024).

[CO13] M. Krstić, B. Zerulla, A. L. Díaz, C. Holzer, D. Beutel, I. Fernandez-Corbaton, and C. Rockstuhl, "A multi-scale approach to simulate the nonlinear optical response of molecular nanomaterials in the bulk and from the surface," in *SPIE Optical Systems Design*, (oral presentation) (2024).

Peer-Reviewed Articles and Conference Contributions Based on Bachelor Thesis

[B1] X. Jin, R. Schneider, R. Popescu, J. Seeger, J. Grutke, B. Zerulla, M. Hetterich, D. Hariskos, W. Witte, M. Powalla, and D. Gerthsen, "Chemical phases in the solution-grown Zn(O,S) buffer of post-annealed Cu(In,Ga)Se_2 solar cells investigated by transmission electron microscopy and electroreflectance," *Journal of Applied Physics* **133**, 165303 (2023).

[B2] J. Seeger, B. Zerulla, J. Grutke, W. Witte, D. Hariskos, O. Kiowski, H. Kalt, and M. Hetterich, "Electroreflectance studies of Zn(O,S) buffer layers in Cu(In,Ga)Se_2 solar cells: Bandgap energies and secondary phases," in *2019 IEEE 46th Photovoltaic Specialists Conference (PVSC)* (2019), pp. 0949–0952.

Contents

Abstract i

Zusammenfassung iii

Publications v
Peer-Reviewed Articles . . . v
Articles Submitted for Review . . . vi
Conference Contributions . . . vi
Conference Contributions Presented by Others . . . vi
Peer-Reviewed Articles and Conference Contributions Based on Bachelor Thesis . viii

Contents ix

List of Figures xi

List of Tables xiii

1. Introduction 1

2. Classical Electromagnetics 5
2.1. Macroscopic Electromagnetics . . . 6
2.1.1. Maxwell's Macroscopic Equations . . . 6
2.1.2. Constitutive Relations for Linear and Nonlinear Optics . . . 7
2.1.3. Description of Electromagnetic Waves in Chiral Media . . . 9
2.2. Microscopic Electromagnetics . . . 11
2.2.1. Maxwell's Microscopic Equations . . . 11
2.2.2. Transition from the Microscopic to the Macroscopic Description of Electromagnetics . . . 12

3. T-matrix Formalism for Linear Optics 17
3.1. Definition and Properties of the T-matrix . . . 17
3.2. Simulation Principle for the Optical Response of Macroscopic Structures with the T-matrix . . . 23

4. Density Functional Theory to Simulate the Optical Response of Molecules 27
4.1. Basic Principles of Density Functional Theory . . . 27
4.2. Computation of Linear Polarizabilities and First Hyperpolarizabilities . . . 30

5. Homogenization Approach Based on the Effective T-matrix 33
5.1. Definition of the Effective T-matrix and Derivation of Effective Material Parameters . . . 34
5.1.1. Definition of the Effective T-matrix . . . 34
5.1.2. Derivation of Effective Material Parameters . . . 36

5.2. Workflow for the Homogenization Approach 38
5.3. Homogenization of a Chiral Zn-L-Camphoric Acid-Dabco SURMOF 41
5.4. Homogenization of Metamaterials 41
5.4.1. Gold Spheres in Cubic Lattice 42
5.4.2. Cut-Plate Pairs in Cubic Lattice 45

6. Linear Optical Response of Molecules in Photonic Devices 49
6.1. Multi-Scale Approach to Compute the Linear Optical Response of Molecules 50
6.2. Polarization-Dependent Optical Response of Molecular Islands on Dielectric Substrates 51
6.3. Coupling of Molecular Films to Photonic Cavities 58
6.3.1. Zn-SiPc-SURMOF-2 59
6.3.2. Chiral UiO-67-BINOL MOF 65
6.3.3. TDBC J-Aggregates Embedded in a Polyvinyl Alcohol Polymer 70
6.4. Metasurface of a Structured Molecular Film 75
6.4.1. Design of the Metasurface 76
6.4.2. Circular Dichroism Signal of the Metasurface for Varying Wavelengths 77

7. Nonlinear Optical Response of Molecules in Photonic Devices 81
7.1. Multi-Scale Approach to Compute the Nonlinear Optical Response of Molecules 82
7.1.1. The Hyper-T-Matrix and its Role for the Multi-Scale Approach 83
7.1.2. SHG Signal of a Crystalline Urea Thin Film in a Vacuum 85
7.1.3. Coupling of a Urea Thin Film to a Photonic Cavity 90
7.2. Surface SHG Signal of Centrosymmetric Molecular Crystalline Materials . . . 92
7.2.1. (TD)-DFT Simulations 93
7.2.2. Surface SHG Signal of a Finite Film of the Molecular Crystal in a Vacuum and on a Substrate 96

8. Conclusions and Outlook 101

Bibliography 105

A. Results for Three-Linker Model of Zn-SiPc-SURMOF-2 123

B. Results for Different Molecular Models of TDBC-J-Aggregates in a PVA Polymer 125

C. Study of Different Finite-Size Molecular Models of the Urea Crystal 127

Acknowledgements 129

Selbstständigkeitserklärung 131

List of Figures

2.1. Scheme and Energy Level Diagram of SHG 9

3.1. Visualization of the Scattering Process Described with the T-matrix 21
3.2. Sketch of Setup of Periodic Lattice Surrounded by Homogeneous Layers . . . 24

5.1. Workflow of Homogenization Approach 39
5.2. Band Structure of a Chiral Zn-L-Camphoric Acid-Dabco SURMOF 40
5.3. Effective Material Parameters and Optical Response of Zn-L-Camphoric Acid-Dabco SURMOF 42
5.4. Band Structure and Effective T-matrix of a Cubic Lattice of Gold Spheres . . 43
5.5. Effective Material Parameters and Optical Response of Cubic Lattice of Gold Spheres 44
5.6. Homogenization of Cubic Lattice of Cut-Plate Pairs 47
5.7. Comparison Between Both Methods to Obtain Effective T-matrix 48

6.1. Workflow of the Multi-Scale Approach 50
6.2. CO and CO_2 Molecule 52
6.3. Absorption Cross Sections of CO and CO_2 Molecules 53
6.4. Schematic IRRAS Setup 54
6.5. Optical Response of CO Molecules on a Ceria Substrate 55
6.6. Optical Response of CO_2 Molecules on Ceria and Al_2O_3 Substrates 56
6.7. Experimentally Measured Absorption Spectra of Zn-SiPc-SURMOF-2 58
6.8. Scheme of Simulated Setup of Zn-SiPc-SURMOF-2 Inside Cavity 59
6.9. Orientationally Averaged Absorption Cross Sections of Finite-Size Model of Zn-SiPc-SURMOF-2 60
6.10. Absorption Spectra of Thin Film of Zn-SiPc-SURMOF-2 in Vacuum 61
6.11. Absorption Spectra of Thin Film of Zn-SiPc-SURMOF-2 in Cavity 62
6.12. Mode Analysis of Cavity Filled with Zn-SiPc-SURMOF-2 63
6.13. Unit Cell, XRD, Finite-Size Model, and SEM Images of UiO-67-*R*-BINOL MOF 64
6.14. TD-DFT Spectra of Finite-Size Model of UiO-67-*R*-BINOL MOF 66
6.15. Schematic Setups for Simulations of UiO-67-BINOL MOF Thin Film on Substrate and Inside Cavity 67
6.16. Absorption and Circular Dichroism Spectra for UiO-67-*R*-BINOL MOF and UiO-67-*S*-BINOL MOF 68
6.17. Absorption and Circular Dichroism Spectra for UiO-67-*R*-BINOL MOF and UiO-67-*S*-BINOL MOF Films with Fixed Thickness 70
6.18. Mode Analysis of Cavity Filled with UiO-67-*R*-BINOL-MOF 71
6.19. Models of Cluster of TDBC J-Aggregates 72
6.20. Orientationally Averaged Absorption Cross Sections of Different Models of TDBC J-Aggregates 73
6.21. Mode Analysis of a Cavity Filled with TDBC J-Aggregates in a PVA Polymer 74

6.22. Absorption Spectra of a Cavity Filled with TDBC J-Aggregates in a PVA Polymer . . . 74
6.23. Mode Analysis of Cavity Filled with TDBC J-Aggregates in a PVA Polymer with Higher Concentration . . . 75
6.24. Single Cylinder Consisting of UiO-67-*R*-BINOL MOF and Metasurface of Cylinders . . . 76
6.25. Effective Permittivity and Chirality of UiO-67-*R*-BINOL-MOF . . . 77
6.26. Optical Response of Metasurface of UiO-67-*R*-BINOL MOF Cylinders . . . 78
6.27. Dipolar Entries of (Renormalized) T-matrix of Single UiO-67-*R*-BINOL MOF Cylinder and of Metasurface of Cylinders . . . 79

7.1. Different Views and One-Photon Absorption Cross Section of the Finite-Size Molecular Model of Urea . . . 86
7.2. Dominating Components of First Hyperpolarizability Tensor and Scheme of the Hyperpolarizability and Hyper-T-matrix of Urea . . . 87
7.3. Diagonal Entries of Permittivity Tensor and Second-Order Susceptibility Tensor of Urea . . . 88
7.4. Thin Film of Urea Molecular Crystal in a Vacuum and in a Cavity . . . 89
7.5. Field Amplitudes of SHG Plane Waves of Urea Thin Film . . . 91
7.6. Linear and Nonlinear Optical Response of Urea Thin Film Inside a Cavity . . . 92
7.7. Four Unit Cells and Stack of the 7,9-Dibromobenzo[*h*]quinolin-10-ol crystal . . . 94
7.8. Electrostatic Potential and Total Electron Density Difference of Finite-Size Molecular Models of the 7,9-Dibromobenzo[*h*]quinolin-10-ol Crystal . . . 95
7.9. SHG Field Amplitudes of Crystalline Molecular Film of 7,9-Dibromobenzo[*h*]quinolin-10-ol . . . 98
7.10. Linear Optical Response of Crystalline Molecular Film of 7,9-Dibromobenzo[*h*]quinolin-10-ol on a Substrate . . . 99
7.11. Nonlinear Optical Response of Crystalline Molecular Film of 7,9-Dibromobenzo[*h*]quinolin-10-ol on a Substrate . . . 100

A.1. Orientationally Averaged Absorption Cross Sections of Second Finite-Size Model of Zn-SiPc-SURMOF-2 . . . 123
A.2. Absorption Spectra of the Zn-SiPc-SURMOF-2 for Second Finite-Size Model 124

B.1. Mode Analysis of a Cavity Filled with TDBC J-Aggregates (Model “2 × 4”) in a PVA Polymer . . . 125
B.2. Mode Analysis of a Cavity Filled with TDBC J-Aggregates (Model “2 × 6”) in a PVA Polymer . . . 126

C.1. Model Size Study of the Urea Crystal . . . 127

List of Tables

7.1. Dominating component of the first hyperpolarizability tensors of the finite-size molecular models of the different layers of 7,9-Dibromobenzo[*h*]quinolin-10-ol 97

1 | Introduction

Molecules are essential for multiple areas of application. The areas of application range from processes in the human body and medical treatments [1–8], food chemistry [9–11], rubbers and plastics that are bio-degradable, for instance [12–17], quantum-information technology [18–20], to storage of data or other molecules [21, 22]. Optical applications are of special interest, as molecular materials can be used for photonic devices such as organic solar cells [23–28] and organic light-emitting diodes [29–33].

The fabrication of molecular materials advances very fast, and there is large interest in new developments. A few instances are the fabrication of biomaterials through self-assembling molecules [34], high-quality perovskite films for solar cells [35], color-tuned highly fluorescent organic nanowires and nanofabrics [36], molecular junctions [37, 38], layer-by-layer assembled metal-organic framework thin films [39], stimuli-responsive smart materials for sensors [40], and one-dimensional aramid nanofibers [41].

Very often, however, fabrication progresses are time demanding and expensive. Due to the very large chemical design space of molecules, an unexplored potential exists for improving optical effects. It is also very challenging to experimentally investigate this chemical design space. Theoretical investigations of molecules are, therefore, intrinsically important, as they are potentially less expensive than experimental investigations.

Phenomenological descriptions of optical properties of molecules are common in several studies. In [42, 43], for instance, the phenomenological model of a dielectric permittivity of a molecular film leads to a very good agreement of simulated and measured spectra. A drawback of many phenomenological descriptions is, however, that assumptions are very often necessary for some simulation parameters. Furthermore, the experimental spectra sometimes have to be measured beforehand to determine the molecular properties in simulations.

Optical simulations of molecules based on *ab initio* quantum-chemical methods, such as (time-dependent) density functional theory ((TD)-DFT), are potentially more precise and can be performed before the experiment. It is, therefore, possible to decide based on a simulation, which molecule is suitable for a specific optical effect, for instance. Furthermore, one can design experimental setups via *ab initio* based simulations of molecules to enhance specific optical effects.

This thesis is centered around a multi-scale approach to compute the optical response of photonic devices made from molecular materials. In this context, we refer to a procedure as a multi-scale approach that starts with a description of the properties of a finite-size molecular model and ending at the response of a macroscopic film or device. Besides their characteristic of connecting several length scales, multi-scale approaches also often combine several scientific disciplines. There are multiple different multi-scale approaches in literature. We want to emphasize that the principle of a multi-scale approach starting at a finite-size model is used for many different sciences. An instance is the spread of viruses, which covers different size levels from individual cells, organisms, and populations [44]. Here, the hosts are the objects which are scaled. The investigation of the British Columbia wildfires in 2017 is another example for a multi-scale approach, in the context of which the spread of fires and the injection of aerosol particles into the stratosphere are considered [45]. Also, the evaluation

of the vitality of the Gombe dialect of the African language Fulfulde is studied on different scales of usage [46]. Multi-scale graph neural networks working on different geographic levels can be used to predict COVID-19 positivity and hospitalization [47].

Focusing on molecules as objects of interest, there is also a variety of multi-scale approaches. An instance is a molecular dynamics model discussed for strongly coupled molecules incorporating different confined light modes to gain knowledge about how cavities modify chemical reactions in Refs. [48, 49].

In this thesis, we present a multi-scale approach to discuss the optical properties of photonic devices that incorporate molecules. We connect *ab initio* quantum-chemical methods, namely TD-DFT, to Maxwell scattering simulations. The element, which enables the combination of these two scientific disciplines in the context of linear optical phenomena, is Waterman's **t**ransition (T-)matrix [50]. The T-matrix represents the scattering response of an object, and is used in several propgramm suites such as *mpGMM* [51], *treams* [52, 53], *CELES* [54, 55], *SMUTHI* [56, 57], and *MULTEM 2* [58]. It can be computed with quantum-chemical methods such as TD-DFT [59], and is used in this thesis to obtain the optical response of planar structures, and to calculate effective parameters of molecular materials. The material parameters can be used to design objects of arbitrary shape. The T-matrix is, therefore, the bridge between the microscopic and macroscopic description of the linear optical effects discussed in this thesis.

We analyze both linear and nonlinear optical phenomena of molecules within photonic devices. To prepare these discussions, we introduce the fundamentals of electromagnetic phenomena in Chapter 2. This introduction includes Maxwell's macroscopic equations and constitutive relations used for describing linear and nonlinear optics on the device level. Furthermore, we consider the propagation of electromagnetic waves in chiral media, introduce Maxwell's microscopic equations, and discuss the transition from the microscopic to the macroscopic description of electromagnetics.

Chapter 3 explains the T-matrix formalism. In this context, we introduce the T-matrix with the simple instance of a homogeneous sphere and explain how the optical response of stacked two-dimensional lattices of scatterers combined with homogeneous slabs is computed. The computation of the optical response of such a system is a major principle of the two simulation packages *mpGMM* [51] and *treams* [52, 53] used in this thesis.

In Chapter 4, we present the fundamentals of (TD)-DFT, starting at the quantum-mechanic description of a molecular system, the Hohenberg-Kohn theorems, and the Kohn-Sham equations. Then, we explain the principles used to compute the optical properties of finite-size molecular models.

Chapters 5, 6, and 7 discuss topics, which originate from the work the author was involved in.

Chapter 5 introduces a homogenization approach for molecular materials and metamaterials. The approach is based on an object termed "effective T-matrix", which incorporates lattice interactions of the building blocks of the materials. From the effective T-matrix, material parameters are derived that do not depend on the propagation direction of an illumination.

In Chapter 6, we introduce the T-matrix based multi-scale approach for linear optics. In the context of linear optical phenomena, we study on the one hand the polarization dependent response of molecular monolayers deposited on dielectric substrates. The results of these studies can potentially play a role for the experimental consideration of chemical reactions. On the other hand, we analyze the coupling of optical cavities to different molecular films. In this context, we consider crystalline materials and an effective medium of randomly oriented

molecules. Due to the different nature of the films, we gain knowledge about different coupling regimes. Furthermore, we design a metasurface of cylinders which consist of chiral molecules. Chiral molecules are not superimposable on their mirror image [60] and are very important for the production of medicines such as L-Thyroxin. They show a difference of the absorption signals related to the two different kinds of polarization handedness of light. Based on the homogenization approach from Chapter 5, we design a metasurface to enhance this difference of the signals. In the context of the discussion of optical phenomena, we make use of the fact that the multi-scale approach enables the consideration of single molecules, a monolayer, and of entire photonic devices.

Chapter 7 extends the multi-scale approach from Chapter 6 to nonlinear optical phenomena. To describe nonlinear optical phenomena, we introduce an object termed "Hyper-T-matrix", which can also be obtained based on TD-DFT simulations. We use the Hyper-T-matrix to extend the multi-scale approach for the computation of the second-harmonic generation (SHG) signal of photonic devices incorporating molecules. In this context, we enhance the SHG signal of a specific molecular film with an optical cavity and study the SHG response of films consisting of a centrosymmetric molecular material. The SHG response of such films originates from the symmetry breaking at their surface. The study of the surface SHG response enables fascinating insights into the question, how thick the surface of the film is that contributes to the SHG signal. We also enhance this signal with a Kretschmann-like setup. The multi-scale approach enables, therefore, the consideration of both linear and nonlinear optical effects of photonic devices incorporating molecules.

In Chapter 8, we conclude the thesis and give an outlook on possible future research directions.

2 | Classical Electromagnetics

In this chapter, we discuss the fundamentals of the linear and nonlinear optical effects, which are analyzed in this thesis. Traditionally, all these effects, and indeed the entire interaction between light and matter, can be characterized by the relationship between the electromagnetic fields and the polarizations they induce in the material. This relationship is called the constitutive relations, and having a proper understanding of these constitutive relations is key to explore the relevant effects [61]. Linear optics describes phenomena that are based on a linear dependence of the polarization on the fields in the constitutive relations. Nonlinear optical phenomena are based on a nonlinear relationship between them.

In this chapter, we start with the macroscopic constitutive relations for linear optics and extend them to nonlinear optics. Understanding the nonlinear constitutive relations enables the description of nonlinear optical effects analyzed in this thesis. While linear optics has been discussed for many decades or even centuries, nonlinear optical effects such as second harmonic generation [62] have gained a lot of interest only with the development of the first laser in 1960 [63]. The invention of the laser was decisive since it provides the high intensity necessary for observing nonlinear effects [63, 64]. The basis of both linear and nonlinear optics are Maxwell's equations. Together with the constitutive relations, they are used to analyze all linear and nonlinear optical effects. In this thesis, a specific type of molecular material is very important. It consists of molecules whose mirror image cannot be superimposed by any means with the original molecules. Such molecules are called chiral [60]. In comparison to materials that do not show such a property (achiral materials), electric fields and magnetic fields are coupled in chiral media. We analyze such media with specific constitutive relations, which we consider below.

As the constitutive relations of chiral and achiral media differ, the propagation of electromagnetic waves in them must be described differently. Therefore, we discuss below how the propagation of electromagnetic waves through chiral media can be represented. Due to the coupling between electric and magnetic fields, phenomena such as circular dichroism and optical rotation occur, which are related to the absorption and the change of the polarization state of light interacting with chiral media. Circular dichroism is a phenomenon that we discuss in this thesis in more detail.

While the interaction between light and macroscopic objects is described with the macroscopic Maxwell equations and constitutive relations, the interaction between light and microscopic objects, such as molecules, is described with the microscopic Maxwell equations and induced multipole moments. Therefore, we finally introduce the microscopic Maxwell equations and explain the transition between the microscopic and the macroscopic description of electromagnetism.

In Section 2.1, we discuss the macroscopic description of electromagnetism. In Subsection 2.1.1, Maxwell's macroscopic equations are introduced both in the time and frequency domain. Subsection 2.1.2 discusses the constitutive relations used in this thesis to describe light-matter interaction. Here, we consider both linear and nonlinear constitutive relations. In Subsection 2.1.3, we describe the propagation of electromagnetic waves in chiral media. Section 2.2 introduces the microscopic description of electromagnetism. In this regard, we

discuss Maxwell's microscopic equations in Subsection 2.2.1 and the transition from the microscopic to the macroscopic description by introducing multipolar moments in Subsection 2.2.2.

2.1. Macroscopic Electromagnetics

In this thesis, both the macroscopic and microscopic description of electromagnetics is important, as we consider both the interaction of light with entire photonic devices and single molecules In this section, we introduce the macroscopic description of electromagnetism. This description is used to analyze the interaction between electromagnetic waves and macroscopic media. For macroscopic media, the number of nuclei and electrons is sufficiently large within a volume that is small compared to any other relevant length scales, so that the oscillations of the electromagnetic fields, produced by the nuclei and electrons, are flatted by spatial averaging [61]. So instead of discussing individual molecules or atoms, the properties of matter are considered at a continuous level.

2.1.1. Maxwell's Macroscopic Equations

Maxwell's equations are used to describe electromagnetic effects. In the time domain, the macroscopic equations read [61, Eq. (I.1a)]

$$\begin{aligned}
\nabla \cdot \tilde{\boldsymbol{D}}(\boldsymbol{r},t) &= \tilde{\rho}_{\text{ext}}(\boldsymbol{r},t)\,, \\
\nabla \cdot \tilde{\boldsymbol{B}}(\boldsymbol{r},t) &= 0\,, \\
\nabla \times \tilde{\boldsymbol{E}}(\boldsymbol{r},t) &= -\frac{\partial}{\partial t}\tilde{\boldsymbol{B}}(\boldsymbol{r},t)\,, \\
\nabla \times \tilde{\boldsymbol{H}}(\boldsymbol{r},t) &= \tilde{\boldsymbol{J}}_{\text{ext}}(\boldsymbol{r},t) + \frac{\partial}{\partial t}\tilde{\boldsymbol{D}}(\boldsymbol{r},t)\,.
\end{aligned} \tag{2.1}$$

$\tilde{\boldsymbol{D}}(\boldsymbol{r},t)$ is the electric displacement at position $\boldsymbol{r}$ and time t, $\tilde{\boldsymbol{B}}(\boldsymbol{r},t)$ is the magnetic flux density, $\tilde{\boldsymbol{E}}(\boldsymbol{r},t)$ is the electric field, and $\tilde{\boldsymbol{H}}(\boldsymbol{r},t)$ is the magnetic field. In the thesis, we assume the absence of external charges $\tilde{\rho}_{\text{ext}}(\boldsymbol{r},t)$ and external currents $\tilde{\boldsymbol{J}}_{\text{ext}}(\boldsymbol{r},t)$.

Linear optics is commonly described in frequency domain. To transfer Maxwell's equations from time into frequency domain, we introduce the Fourier transformation as

$$\underline{\boldsymbol{E}}(\boldsymbol{r},\omega) = \int \mathrm{d}t \tilde{\boldsymbol{E}}(\boldsymbol{r},t)\mathrm{e}^{\mathrm{i}\omega t}\,, \qquad \tilde{\boldsymbol{E}}(\boldsymbol{r},t) = \frac{1}{2\pi}\int \mathrm{d}\omega \underline{\boldsymbol{E}}(\boldsymbol{r},\omega)\mathrm{e}^{-\mathrm{i}\omega t}\,, \tag{2.2}$$

where $\underline{\boldsymbol{E}}(\boldsymbol{r},\omega)$ is the Fourier transform of the electric field $\tilde{\boldsymbol{E}}(\boldsymbol{r},t)$. In frequency domain, Maxwell's equations are [61, Eq. (6.130)]

$$\begin{aligned}
\nabla \cdot \underline{\boldsymbol{D}}(\boldsymbol{r},\omega) &= 0\,, \\
\nabla \cdot \underline{\boldsymbol{B}}(\boldsymbol{r},\omega) &= 0\,, \\
\nabla \times \underline{\boldsymbol{E}}(\boldsymbol{r},\omega) &= \mathrm{i}\omega \underline{\boldsymbol{B}}(\boldsymbol{r},\omega)\,, \\
\nabla \times \underline{\boldsymbol{H}}(\boldsymbol{r},\omega) &= -\mathrm{i}\omega \underline{\boldsymbol{D}}(\boldsymbol{r},\omega)\,.
\end{aligned} \tag{2.3}$$

2.1.2. Constitutive Relations for Linear and Nonlinear Optics

To describe light-matter interactions, constitutive relations are required in addition to Maxwell's equations. The constitutive relations link the fields in the material to each other. In the following, we consider constitutive relations both for linear and nonlinear optics.

Linear Optics

We first consider linear, anisotropic, nonlocal, dispersive, time-invariant and achiral media. With the general electric and magnetic response functions, $\mathbf{R}^{\mathrm{e}}(\boldsymbol{r},t)$ and $\mathbf{R}^{\mathrm{m}}(\boldsymbol{r},t)$, we have [61],

$$\tilde{\boldsymbol{D}}(\boldsymbol{r},t) = \sum_i \hat{\boldsymbol{e}}_i \sum_j \int_{\mathbb{R}^3} \mathrm{d}\boldsymbol{r}' \int_{-\infty}^{\infty} \mathrm{d}t' R^{\mathrm{e}}_{ij}(\boldsymbol{r}-\boldsymbol{r}',t-t')\tilde{E}_j(\boldsymbol{r}',t')\,, \tag{2.4}$$

$$\tilde{\boldsymbol{B}}(\boldsymbol{r},t) = \sum_i \hat{\boldsymbol{e}}_i \sum_j \int_{\mathbb{R}^3} \mathrm{d}\boldsymbol{r}' \int_{-\infty}^{\infty} \mathrm{d}t' R^{\mathrm{m}}_{ij}(\boldsymbol{r}-\boldsymbol{r}',t-t')\tilde{H}_j(\boldsymbol{r}',t')\,. \tag{2.5}$$

As we assume temporal causality, the response functions are zero for $t' > t$. This means that at time t, only fields prior to t enter [61]. For the Fourier transformed equations, we have [61, Eq. (I.11)]

$$\begin{aligned} \underline{\boldsymbol{D}}(\boldsymbol{r},\omega) &= \sum_i \hat{\boldsymbol{e}}_i \sum_j \int_{\mathbb{R}^3} \mathrm{d}\boldsymbol{r}' \varepsilon_{ij}(\boldsymbol{r}-\boldsymbol{r}',\omega)\underline{E}_j(\boldsymbol{r}',\omega)\,, \\ \underline{\boldsymbol{B}}(\boldsymbol{r},\omega) &= \sum_i \hat{\boldsymbol{e}}_i \sum_j \int_{\mathbb{R}^3} \mathrm{d}\boldsymbol{r}' \mu_{ij}(\boldsymbol{r}-\boldsymbol{r}',\omega)\underline{H}_j(\boldsymbol{r}',\omega)\,, \end{aligned} \tag{2.6}$$

with the electric permittivity tensor $\boldsymbol{\varepsilon}(\boldsymbol{r},\omega)$ and the magnetic permeability tensor $\boldsymbol{\mu}(\boldsymbol{r},\omega)$, which correspond to the electric and magnetic response functions in the frequency domain.

In this thesis, we only consider local media so that the convolution kernels in Eq. (2.6) reduce to delta distributions. We can, therefore, replace the integrals in Eq. (2.6) by tensor products,

$$\underline{\boldsymbol{D}}(\boldsymbol{r},\omega) = \boldsymbol{\varepsilon}(\boldsymbol{r},\omega)\underline{\boldsymbol{E}}(\boldsymbol{r},\omega)\,, \qquad \underline{\boldsymbol{B}}(\boldsymbol{r},\omega) = \boldsymbol{\mu}(\boldsymbol{r},\omega)\underline{\boldsymbol{H}}(\boldsymbol{r},\omega)\,. \tag{2.7}$$

We can also extend these constitutive relations to chiral and reciprocal media. For these media, an electromagnetic coupling occurs, which can be seen in the dependence of the electric displacement on the magnetic field, and of the magnetic flux density on the electric field, [65, Eqs. (1.51), (1.71)]:

$$\begin{pmatrix} \underline{\boldsymbol{D}}(\boldsymbol{r},\omega) \\ \underline{\boldsymbol{B}}(\boldsymbol{r},\omega) \end{pmatrix} = \begin{pmatrix} \boldsymbol{\varepsilon}(\boldsymbol{r},\omega) & \mathrm{i}\boldsymbol{\kappa}(\boldsymbol{r},\omega)\sqrt{\varepsilon_0\mu_0} \\ -\mathrm{i}\boldsymbol{\kappa}^{\mathrm{T}}(\boldsymbol{r},\omega)\sqrt{\varepsilon_0\mu_0} & \boldsymbol{\mu}(\boldsymbol{r},\omega) \end{pmatrix} \begin{pmatrix} \underline{\boldsymbol{E}}(\boldsymbol{r},\omega) \\ \underline{\boldsymbol{H}}(\boldsymbol{r},\omega) \end{pmatrix}\,. \tag{2.8}$$

$\boldsymbol{\kappa}(\boldsymbol{r},\omega)$ is the chirality tensor. For isotropic media, all material parameters are scalars. We additionally introduce the relative permittivity $\boldsymbol{\varepsilon}_{\mathrm{r}}(\boldsymbol{r},\omega) = \boldsymbol{\varepsilon}(\boldsymbol{r},\omega)/\varepsilon_0$ and the relative permeability $\boldsymbol{\mu}_{\mathrm{r}}(\boldsymbol{r},\omega) = \boldsymbol{\mu}(\boldsymbol{r},\omega)/\mu_0$. ε_0 is the vacuum permittivity and μ_0 is the vacuum permeability. For homogeneous media, the material tensors do not depend on $\boldsymbol{r}$.

Equation (2.8) describes linear, anisotropic, local, dispersive, time-invariant, reciprocal, and chiral media. According to Lord Kelvin, an object is called chiral if its mirror image cannot be superposed with the original object [60]. Producing an entire material made out of

many chiral objects, such as molecules in our case, gives rise to a chiral medium that requires $\boldsymbol{\kappa}(\boldsymbol{r},\omega)$ to describe its properties. Due to chirality, the electric displacement is coupled to the magnetic field and the magnetic flux density is coupled to the electric field. Due to reciprocity, the coupling is described by the same chirality tensor $\boldsymbol{\kappa}(\boldsymbol{r},\omega)$ [65]. It shall be noted that there are several notations of the constitutive relations used to describe chirality in literature. These can be found in [66], for instance.

The linear light-matter interactions discussed in this thesis can be entirely described with Maxwell's equations in (2.3) and the constitutive relations in Eq. (2.8). For describing nonlocal effects, we refer to the constitutive relations discussed in [67], for instance.

Second-Order Nonlinear Optics

Nonlinear optical effects are based on nonlinear light-matter interactions. In the following, we concentrate on second-order nonlinear effects in homogeneous media. In this regard, the polarization induced in the material depends on products of two components of the electric field and not just on a single one. In our discussion of nonlinear optical effects, we neglect electromagnetic coupling terms. This is based on the fact that current density-functional theory software packages, which we use to compute optical properties of molecules, do not provide electromagnetic coupling terms for nonlinear optics. We further assume in the following that the considered media are homogeneous and non-magnetic.

In the context of linear optics, the electric displacement in an achiral medium can also be expressed as [61, Eq. (I.9)]

$$\underline{\boldsymbol{D}}(\boldsymbol{r},\omega) = \varepsilon_0 \underline{\boldsymbol{E}}(\boldsymbol{r},\omega) + \underline{\boldsymbol{P}}_{\mathrm{e}}(\boldsymbol{r},\omega)\,, \tag{2.9}$$

where $\underline{\boldsymbol{P}}_{\mathrm{e}}(\boldsymbol{r},\omega)$ is the electric polarization in the material induced by an electromagnetic wave. We have [64, Eq. (5.3-17), (5.3-20)]

$$\underline{\boldsymbol{P}}_{\mathrm{e}}(\boldsymbol{r},\omega) = \varepsilon_0 \boldsymbol{\chi}(\omega) \underline{\boldsymbol{E}}(\boldsymbol{r},\omega) \quad \text{and} \quad \boldsymbol{\varepsilon}(\omega) = \varepsilon_0 \left(\mathbb{1}_3 + \boldsymbol{\chi}(\omega)\right)\,, \tag{2.10}$$

with the electric susceptibility tensor $\boldsymbol{\chi}(\omega)$ and the 3×3-identity matrix $\mathbb{1}_3$. Equation (2.10) corresponds to a linear relationship between the polarization and the electric field.

In nonlinear optics, we add a term $\boldsymbol{P}_{\mathrm{NL,e}}$ for which the relation between the polarization and electric field is nonlinear. An instance for second-order effects is second-harmonic generation (SHG), for which a component of the polarization is proportional to the product of two components of the electric field, i.e., $P_{\mathrm{NL,e},i} \propto E_j E_k$. In an SHG-process, an electromagnetic wave at frequency ω does not only cause an electromagnetic wave at the same frequency, due to the linear response of the medium, but also an electromagnetic wave at the frequency 2ω, see Figure 2.1**(a)**. The process occurs due to the nonlinear susceptibility $\boldsymbol{\chi}^{(2)}$. Figure 2.1**(b)** shows the energy level diagram for this process. In this regard, one is considering two photons of the fundamental electromagnetic wave at frequency ω in the nonlinear optical material, which cause transitions to and between virtual states (dashed lines) to produce a single photon at frequency 2ω. Virtual states can be considered as a combination of an energy eigenstate of an atom and an energy eigenstate of a photon of the radiation field [63]. The process starts at an atomic ground state (straight line).

To analyze the process of SHG in the more formal framework presented in Section 1.3. of [63], for instance, we concentrate on monochromatic fields. A monochromatic field in time domain is given by [63, Eq. (1.3.2)]

$$\tilde{\boldsymbol{E}}(\boldsymbol{r},t) = \frac{1}{2}\left(\boldsymbol{E}(\boldsymbol{r};\omega)\mathrm{e}^{-\mathrm{i}\omega t} + \text{c.c.}\right)\,, \tag{2.11}$$

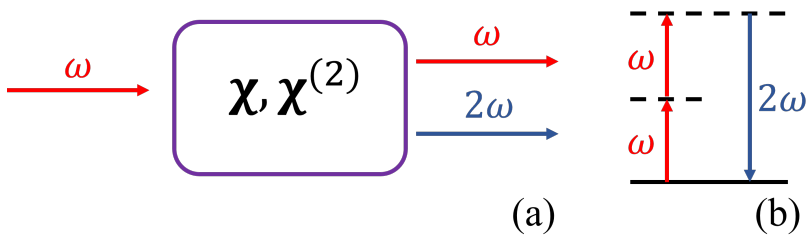

Figure 2.1.: Scheme **(a)** and energy level diagram **(b)** of second-harmonic generation. In this process, an electromagnetic wave at frequency ω produces an electromagnetic wave at frequency 2ω due to the nonlinear susceptibility $\boldsymbol{\chi}^{(2)}$ of the material.

where c.c. denotes complex conjugation of the previous term. $\boldsymbol{E}(\boldsymbol{r};\omega)$ is a complex monochromatic field amplitude, which does not explicitly depend on the frequency ω. In this context, ω is a parameter. One can see that products of the electric fields with the resulting mixing of frequencies represent different nonlinear effects such as second-harmonic generation ($\omega+\omega=2\omega$) or optical rectification ($\omega-\omega=0$), see [63]. In the case of SHG, the nonlinear polarization is defined as [63, Eq. (1.3.11)]

$$\tilde{\boldsymbol{P}}_{\mathrm{NL,e}}(\boldsymbol{r},t)=\frac{1}{2}\left(\boldsymbol{P}_{\mathrm{NL,e}}(\boldsymbol{r};\Omega)\mathrm{e}^{-\mathrm{i}\Omega t}+\mathrm{c.c.}\right)\,, \tag{2.12}$$

with [63, Eq. (1.3.17)]

$$\boldsymbol{P}_{\mathrm{NL,e}}(\boldsymbol{r};\Omega)=\frac{1}{2}\epsilon_0\sum_{i,j,k}\hat{\boldsymbol{e}}_i\chi^{(2)}_{ijk}(-\Omega,\omega,\omega)E_j(\boldsymbol{r};\omega)E_k(\boldsymbol{r};\omega)\,, \tag{2.13}$$

$\Omega=2\omega$, and the second-order susceptibility $\boldsymbol{\chi}^{(2)}(-\Omega,\omega,\omega)$, which is a third-rank tensor. For a centrosymmetric material, we have $\boldsymbol{\chi}^{(2)}(-\Omega,\omega,\omega)=0$ due to symmetry reasons [63]. SHG, therefore, vanishes in the bulk of a centrosymmetric system. We discuss in Chapter 7, however, that an SHG signal can be produced from a spatial domain close to the surface of the material. Via Maxwell's equations, one can show that the polarization from Eq. (2.13), oscillating at $\Omega=2\omega$ generates an electromagnetic wave at the SHG frequency. Note that a factor of 1/2 is added in Eq. (2.13) in comparison to [63], as we use the real part of the fields while [63] uses twice the real part.

To describe the interaction of light with matter in the framework of linear optics, Maxwell's equations and the constitutive relations are the same for complex monochromatic field amplitudes $\boldsymbol{E}(\boldsymbol{r};\omega)$ and Fourier transforms $\underline{\boldsymbol{E}}(\boldsymbol{r},\omega)$. We use complex monochromatic field amplitudes in nonlinear optics to avoid complicated convolutions in frequency domain, which do not appear in linear optics for Fourier transforms. The Fourier transform of the second-order susceptibility is given in [63, Eq. (1.6.9)], for instance.

2.1.3. Description of Electromagnetic Waves in Chiral Media

In this subsection, we consider linear, isotropic, and homogeneous media with the relative permittivity $\varepsilon_{\mathrm{r}}(\omega)$ and the relative permeability $\mu_{\mathrm{r}}(\omega)$. If they are additionally achiral, the propagation of a monochromatic electromagnetic wave through such media is described with the Helmholtz wave equation,

$$\left(\Delta+\frac{\omega^2}{c_0^2}\varepsilon_{\mathrm{r}}(\omega)\mu_{\mathrm{r}}(\omega)\right)\boldsymbol{E}(\boldsymbol{r};\omega)=0\,, \tag{2.14}$$

which can be derived from Maxwell's equations and the constitutive relations [68]. $c_0 = 1/\sqrt{\varepsilon_0\mu_0}$ is the speed of light in vacuum. Solutions to the Helmholtz wave equation are elliptically polarized plane waves with the electric field

$$\boldsymbol{E}(\boldsymbol{r};\omega) = \boldsymbol{E}_0 \mathrm{e}^{\mathrm{i}\boldsymbol{k}(\omega)\cdot\boldsymbol{r}} \,. \tag{2.15}$$

Linearly and circularly polarized plane waves are special cases. $\boldsymbol{k}(\omega)$ is the wave vector with the norm $|\boldsymbol{k}(\omega)| = k(\omega) = \frac{\omega}{c_0}\sqrt{\varepsilon_\mathrm{r}(\omega)\mu_\mathrm{r}(\omega)}$, which is commonly referred to as the wavenumber. $\boldsymbol{E}_0$ is the complex amplitude of the field, for which $\boldsymbol{k}(\omega)\cdot\boldsymbol{E}_0 = 0$ holds.

For chiral media with the chirality parameter $\kappa(\omega)$, we have more complicated constitutive relations. Hence, the curl equations for the electric and magnetic fields are, in general, not diagonal but read as [65, Eq. (3.26)]

$$\begin{pmatrix} \nabla\times\boldsymbol{E}(\boldsymbol{r};\omega) \\ \nabla\times\boldsymbol{H}(\boldsymbol{r};\omega) \end{pmatrix} = \omega \begin{pmatrix} \kappa(\omega)\sqrt{\varepsilon_0\mu_0} & \mathrm{i}\mu(\omega) \\ -\mathrm{i}\varepsilon(\omega) & \kappa(\omega)\sqrt{\varepsilon_0\mu_0} \end{pmatrix} \begin{pmatrix} \boldsymbol{E}(\boldsymbol{r};\omega) \\ \boldsymbol{H}(\boldsymbol{r};\omega) \end{pmatrix} . \tag{2.16}$$

By diagonalizing this matrix equation, one derives fields whose polarization does not change upon propagation through the chiral media in contrast to the electric and magnetic fields [65, Eq. (3.28)], [69, Eq. (8.9)]. These fields are the Riemann-Silberstein vectors [70, 71]

$$\boldsymbol{G}_\pm(\boldsymbol{r};\omega) = \frac{1}{\sqrt{2}}\left(\boldsymbol{E}(\boldsymbol{r};\omega) \pm \mathrm{i}\sqrt{\frac{\mu_\mathrm{r}(\omega)}{\varepsilon_\mathrm{r}(\omega)}} Z_0 \boldsymbol{H}(\boldsymbol{r};\omega)\right) . \tag{2.17}$$

Here, we use the notation of [72, Eq. (2.36)]. $Z_0 = \sqrt{\frac{\mu_0}{\varepsilon_0}}$ is the vacuum impedance. The matrix equation for the Riemann-Silberstein vectors reads [65, Eq. (3.29)],

$$\begin{pmatrix} \nabla\times\boldsymbol{G}_+(\boldsymbol{r};\omega) \\ \nabla\times\boldsymbol{G}_-(\boldsymbol{r};\omega) \end{pmatrix} = \begin{pmatrix} k_+(\omega) & 0 \\ 0 & -k_-(\omega) \end{pmatrix} \begin{pmatrix} \boldsymbol{G}_+(\boldsymbol{r};\omega) \\ \boldsymbol{G}_-(\boldsymbol{r};\omega) \end{pmatrix} . \tag{2.18}$$

The corresponding wavenumbers are

$$k_\pm(\omega) = \frac{\omega}{c_0}\left(\sqrt{\varepsilon_\mathrm{r}(\omega)\mu_\mathrm{r}(\omega)} \pm \kappa(\omega)\right) . \tag{2.19}$$

One can show that the helicity operator for monochromatic fields is $\boldsymbol{\Lambda} = \frac{\nabla\times}{k(\omega)}$ [73, Eq. (2)]. We conclude, therefore, that [74, Eq. (2)],

$$\boldsymbol{\Lambda}\boldsymbol{G}_\pm(\boldsymbol{r};\omega) = \pm\boldsymbol{G}_\pm(\boldsymbol{r};\omega) \,. \tag{2.20}$$

$\boldsymbol{G}_\pm(\boldsymbol{r};\omega)$ are the eigenvectors of the helicity operator with eigenvalues ± 1. A field, which is a superposition of left-handed circularly polarized plane waves, corresponds to $\boldsymbol{G}_+(\boldsymbol{r};\omega)$. Likewise, a field, which is a superposition of right-handed circularly polarized plane waves, corresponds to $\boldsymbol{G}_-(\boldsymbol{r};\omega)$ [74]. $\boldsymbol{G}_\pm(\boldsymbol{r};\omega)$ are fields of pure helicity, used for describing the propagation of electromagnetic waves through chiral media.

In the following, we consider a chiral film in a host medium. The film is illuminated subsequently by two plane waves with helicity ± 1. We observe that $\boldsymbol{G}_\pm(\boldsymbol{r};\omega)$ have different wavenumbers $k_\pm(\omega) = \frac{\omega}{c_0}\left(\sqrt{\varepsilon_\mathrm{r}(\omega)\mu_\mathrm{r}(\omega)} \pm \kappa(\omega)\right)$. Therefore, the two plane waves of opposite helicity ± 1 are absorbed differently [60]. We call this phenomenon absorption circular dichroism [60], which is quantified in this thesis as

$$\mathrm{ACD} = \frac{A_+ - A_-}{2} \,, \tag{2.21}$$

with the absorption

$$A_{\pm} = 1 - T_{\pm} - R_{\pm} \tag{2.22}$$

of the respective plane waves. $T_{\pm}$ and $R_{\pm}$ are the power transmittance and power reflectance, respectively.

In chemistry and biology, a common spectroscopic quantity is the transmission circular dichroism in the units mdeg [75, P3],

$$\mathrm{CD(mdeg)} = \arctan\left(\frac{\sqrt{T_-} - \sqrt{T_+}}{\sqrt{T_-} + \sqrt{T_+}}\right) \cdot \frac{180 \cdot 1000}{\pi} \,. \tag{2.23}$$

We use these two measures to quantify the circular dichroism of light interacting with chiral molecular media and devices built thereof. Note that it is also common to abbreviate the absorption circular dichroism with "CD" and the transmission circular dichroism with "TCD". As we compare our results to spectroscopic measurements, however, we use the notation from Eqs. (2.21) and (2.23), which is more common in chemistry and biology.

Optical rotation is another important phenomenon occurring for light which interacts with chiral media [60]. It describes the change of the polarization state of a linearly polarized plane wave, due to the different real parts of $k_+(\omega)$ and $k_-(\omega)$.

2.2. Microscopic Electromagnetics

In Section 2.1, we considered the propagation of light in macroscopic media. In the following, we introduce the microscopic description of electromagnetism to consider the interaction of light with single molecules, for instance. Then, we perform the transition from the microscopic to the macroscopic description. In this regard, we observe that the spatially averaged response of microscopic objects can be expressed via multipole moments.

2.2.1. Maxwell's Microscopic Equations

We follow the discussion of Section (6.6) from [61]. We discuss a system consisting of nuclei and electrons considered as point charges. In the time domain, we describe electromagnetic effects in such a system with Maxwell's microscopic equations [61, Eq. (6.64)]:

$$\begin{aligned}
\nabla \cdot \tilde{\boldsymbol{e}}(\boldsymbol{r}, t) &= \frac{\tilde{\eta}(\boldsymbol{r}, t)}{\varepsilon_0} \,, \\
\nabla \cdot \tilde{\boldsymbol{b}}(\boldsymbol{r}, t) &= 0 \,, \\
\nabla \times \tilde{\boldsymbol{e}}(\boldsymbol{r}, t) &= -\frac{\partial}{\partial t} \tilde{\boldsymbol{b}}(\boldsymbol{r}, t) \,, \\
\nabla \times \tilde{\boldsymbol{b}}(\boldsymbol{r}, t) &= \mu_0 \tilde{\boldsymbol{j}}(\boldsymbol{r}, t) + \frac{1}{c_0^2} \frac{\partial}{\partial t} \tilde{\boldsymbol{e}}(\boldsymbol{r}, t) \,.
\end{aligned} \tag{2.24}$$

$\tilde{\boldsymbol{e}}(\boldsymbol{r}, t)$ is the microscopic electric field and $\tilde{\boldsymbol{b}}(\boldsymbol{r}, t)$ is the microscopic magnetic flux density. The microscopic charge density is defined as [61, Eq. (6.71)]

$$\tilde{\eta}(\boldsymbol{r}, t) = \sum_j q_j \delta(\boldsymbol{r} - \boldsymbol{r}_j(t)) \,, \tag{2.25}$$

with the position vector $\boldsymbol{r}_j(t)$ of point charge q_j. $\tilde{\boldsymbol{j}}(\boldsymbol{r}, t)$ is the microscopic current density.

2.2.2. Transition from the Microscopic to the Macroscopic Description of Electromagnetics

To perform the transition from the microscopic to the macroscopic description of electromagnetism, we spatially average over the microscopic quantities. Macroscopic media consist, roughly, of 10^{23} nuclei and electrons per cm^3 [61]. Oscillations of the microscopic quantities in space and time are usually averaged out by measuring devices, because the corresponding large oscillation frequencies cannot be detected. In general, time averaging is not necessary after spatial averaging, as usually only the microscopic oscillations are present, which oscillate with the frequency of the applied fields [61].

We define the spatial average of a field $\tilde{\boldsymbol{e}}(\boldsymbol{r},t)$ with respect to a test function $f(\boldsymbol{r})$ as [61, Eq. (6.65)]

$$\langle \tilde{\boldsymbol{e}}(\boldsymbol{r},t)\rangle = \int_{\mathbb{R}^3} \mathrm{d}\boldsymbol{r}' f(\boldsymbol{r}')\tilde{\boldsymbol{e}}(\boldsymbol{r}-\boldsymbol{r}',t)\,. \tag{2.26}$$

The test function $f(\boldsymbol{r})$ is non-zero around $\boldsymbol{r}=0$. One can use Gaussian functions for $f(\boldsymbol{r})$, but, in general, it does not have to be explicitly defined, as long as it is continuous and sufficiently smooth [61].

Maxwell's equations include both space and time derivatives of the fields. The derivative of a spatially averaged quantity with respect to space is [61, Eq. (6.67)]

$$\frac{\partial}{\partial r_i}\langle \tilde{\boldsymbol{e}}(\boldsymbol{r},t)\rangle = \left\langle \frac{\partial}{\partial r_i}\tilde{\boldsymbol{e}}(\boldsymbol{r},t)\right\rangle\,, \tag{2.27}$$

and the derivative with respect to time is [61, Eq. (6.67)]

$$\frac{\partial}{\partial t}\langle \tilde{\boldsymbol{e}}(\boldsymbol{r},t)\rangle = \left\langle \frac{\partial}{\partial t}\tilde{\boldsymbol{e}}(\boldsymbol{r},t)\right\rangle\,. \tag{2.28}$$

The macroscopic electric field and the macroscopic magnetic flux density are spatial averages of the respective microscopic quantities. We, therefore, define them as [61, Eq. (6.68)]

$$\tilde{\boldsymbol{E}}(\boldsymbol{r},t) = \langle \tilde{\boldsymbol{e}}(\boldsymbol{r},t)\rangle\,, \qquad \tilde{\boldsymbol{B}}(\boldsymbol{r},t) = \langle \tilde{\boldsymbol{b}}(\boldsymbol{r},t)\rangle\,, \tag{2.29}$$

so that two macroscopic Maxwell equations follow [61, Eq. (6.69)]:

$$\nabla\cdot\tilde{\boldsymbol{B}}(\boldsymbol{r},t) = 0\,, \qquad \nabla\times\tilde{\boldsymbol{E}}(\boldsymbol{r},t) = -\frac{\partial}{\partial t}\tilde{\boldsymbol{B}}(\boldsymbol{r},t) \tag{2.30}$$

follow. Furthermore, we have [61, Eq. (6.70)]

$$\nabla\cdot\tilde{\boldsymbol{E}}(\boldsymbol{r},t) = \frac{\langle\tilde{\eta}(\boldsymbol{r},t)\rangle}{\varepsilon_0}\,, \qquad \frac{1}{\mu_0}\nabla\times\tilde{\boldsymbol{B}}(\boldsymbol{r},t) = \langle\tilde{\boldsymbol{j}}(\boldsymbol{r},t)\rangle + \varepsilon_0\frac{\partial}{\partial t}\tilde{\boldsymbol{E}}(\boldsymbol{r},t)\,. \tag{2.31}$$

In the following, we show that the spatially averaged charge density can be expressed as a sum of electric multipole moments. For equation (2.31), we have to derive expressions for the spatial average of the microcopic charge density and of the microscopic current density. We start with the microscopic charge density. It is a sum of the free and bound charges [61, Eq. (6.72)]

$$\tilde{\eta}(\boldsymbol{r},t) = \tilde{\eta}_{\mathrm{free}}(\boldsymbol{r},t) + \tilde{\eta}_{\mathrm{bound}}(\boldsymbol{r},t)\,, \tag{2.32}$$

where

$$\tilde{\eta}_{\text{bound}}(\boldsymbol{r},t) = \sum_n \tilde{\eta}_n(\boldsymbol{r},t)\,, \qquad \tilde{\eta}_n(\boldsymbol{r},t) = \sum_{j(n)} q_j \delta(\boldsymbol{r}-\boldsymbol{r}_j(t))\,. \tag{2.33}$$

$\tilde{\eta}_n(\boldsymbol{r},t)$ is the charge density of an object n. In the following, we assume that the object n is a molecule. We define the position vectors $\boldsymbol{r}_{jn}(t)$ of the charges q_j of molecule n with respect to a fixed position vector $\boldsymbol{r}_n(t)$. Then, we have [61, Eq. (6.74)]

$$\langle \tilde{\eta}_n(\boldsymbol{r},t)\rangle = \sum_{j(n)} q_j f(\boldsymbol{r}-\boldsymbol{r}_n(t)-\boldsymbol{r}_{jn}(t))\,. \tag{2.34}$$

This expression can be approximated by a Taylor series with respect to the small distance $\boldsymbol{r}-\boldsymbol{r}_n(t)$ [61]:

$$\langle \tilde{\eta}_n(\boldsymbol{r},t)\rangle = \sum_{j(n)} q_j \left[f(\boldsymbol{r}-\boldsymbol{r}_n(t)) - \boldsymbol{r}_{jn}(t)\cdot\nabla f(\boldsymbol{r}-\boldsymbol{r}_n(t))\right] + \dots\,. \tag{2.35}$$

Here, we derived a very import finding, as the terms in the sum correspond to molecular multipole moments [61, Eqs. (6.75), (6.76)]:

$$q_n = \sum_{j(n)} q_j \tag{2.36}$$

is the molecular charge, and

$$\tilde{\boldsymbol{p}}_{\text{e},n}(\boldsymbol{r},t) = \sum_{j(n)} q_j \boldsymbol{r}_{jn}(t) \tag{2.37}$$

is the molecular electric dipole moment. Here, we write down only dipoles explicitly. As molecules are usually considerably smaller than the wavelength of the fields, this is, in general, sufficient. For larger objects, quadrupoles, octupoles, etc. might have to be considered as well. One can express, furthermore, the spatial average of the molecular charge density as [61, Eq. (6.79)]

$$\langle \tilde{\eta}_n(\boldsymbol{r},t)\rangle = \langle q_n \delta(\boldsymbol{r}-\boldsymbol{r}_n(t))\rangle - \nabla\cdot\langle \tilde{\boldsymbol{p}}_{\text{e},n}(\boldsymbol{r},t)\delta(\boldsymbol{r}-\boldsymbol{r}_n(t))\rangle + \dots\,, \tag{2.38}$$

so that the spatially averaged response of a molecule can be considered as a sum of point electric multipoles.

Below, we show that the spatially averaged current density of a molecule can be expressed as a sum of point magnetic multipoles. This is a key finding for the description of the interaction of molecules with electromagnetic waves, as by computing the dipole moments of a molecule, its optical response can be obtained. We continue with the transition to the macroscopic Maxwell equations. The spatial average of the microscopic charge density is computed by adding the contributions from all molecules and from the free charges [61, Eq. (6.87)]

$$\langle \tilde{\eta}(\boldsymbol{r},t)\rangle = \tilde{\rho}_{\text{ext}}(\boldsymbol{r},t) - \nabla\cdot\tilde{\boldsymbol{P}}_{\text{e}}(\boldsymbol{r},t)\,, \tag{2.39}$$

with the macroscopic charge density [61, Eq. (6.88)]

$$\tilde{\rho}_{\text{ext}}(\boldsymbol{r},t) = \langle \tilde{\eta}_{\text{free}}(\boldsymbol{r},t)\rangle + \left\langle \sum q_n \delta(\boldsymbol{r}-\boldsymbol{r}_n(t))\right\rangle\,, \tag{2.40}$$

and the macroscopic electric polarization [61, Eq. (6.89)]

$$\tilde{\boldsymbol{P}}_{\mathrm{e}}(\boldsymbol{r},t) = \left\langle \sum_n \tilde{\boldsymbol{p}}_{\mathrm{e},n}(\boldsymbol{r},t)\delta(\boldsymbol{r}-\boldsymbol{r}_n(t)) \right\rangle . \tag{2.41}$$

Therefore [61, Eq. (6.91)],

$$\nabla \cdot \left[\varepsilon_0 \tilde{\boldsymbol{E}}(\boldsymbol{r},t) + \tilde{\boldsymbol{P}}_{\mathrm{e}}(\boldsymbol{r},t)\right] = \tilde{\rho}_{\mathrm{ext}}(\boldsymbol{r},t) \tag{2.42}$$

follows from $\varepsilon_0 \nabla \cdot \tilde{\boldsymbol{E}}(\boldsymbol{r},t) = \langle \tilde{\eta}(\boldsymbol{r},t)\rangle$. Comparing to the macroscopic Maxwell equations (2.1), we have

$$\nabla \cdot \tilde{\boldsymbol{D}}(\boldsymbol{r},t) = \tilde{\rho}_{\mathrm{ext}}(\boldsymbol{r},t)\,, \tag{2.43}$$

with the electric displacement [61, Eq. (6.92)]

$$\tilde{\boldsymbol{D}}(\boldsymbol{r},t) = \varepsilon_0 \tilde{\boldsymbol{E}}(\boldsymbol{r},t) + \tilde{\boldsymbol{P}}_{\mathrm{e}}(\boldsymbol{r},t)\,. \tag{2.44}$$

The same principles can be used for the spatial average of $\tilde{\boldsymbol{j}}(\boldsymbol{r},t)$, which is also expressed as a sum of a term due to the free charges and a term due to the bound charges of the molecules. One can derive [61, Eq. (6.96)]

$$\langle \tilde{j}_i(\boldsymbol{r},t)\rangle = \tilde{J}_{\mathrm{ext},i}(\boldsymbol{r},t) + \frac{\partial}{\partial t}\left[\tilde{D}_i(\boldsymbol{r},t) - \varepsilon_0 \tilde{E}_i(\boldsymbol{r},t)\right] + \sum_{ls} \epsilon_{ils} \frac{\partial}{\partial r_l} \frac{\tilde{P}_{\mathrm{m},s}(\boldsymbol{r},t)}{\mu_0}\,, \tag{2.45}$$

neglecting higher order terms due to the small velocities of the molecules. ϵ_{ils} is the Levi-Civita symbol. The macroscopic magnetic polarization is defined as [61, Eq. (6.98)]

$$\tilde{\boldsymbol{P}}_{\mathrm{m}}(\boldsymbol{r},t) = \left\langle \mu_0 \sum_n \tilde{\boldsymbol{p}}_{\mathrm{m},n}(\boldsymbol{r},t)\delta(\boldsymbol{r}-\boldsymbol{r}_n(t)) \right\rangle , \tag{2.46}$$

with the molecular magnetic dipole moment [61, Eq. (6.95)]

$$\tilde{\boldsymbol{p}}_{\mathrm{m},n}(\boldsymbol{r},t) = \sum_{j(n)} \frac{q_j}{2} \left(\boldsymbol{r}_{jn}(t) \times \boldsymbol{v}_{jn}(t)\right) . \tag{2.47}$$

$\boldsymbol{v}_{jn}(t)$ is the velocity of charge q_j in molecule n. Comparing to the macroscopic Maxwell equations (2.1), we have

$$\nabla \times \tilde{\boldsymbol{H}}(\boldsymbol{r},t) = \tilde{\boldsymbol{J}}_{\mathrm{ext}}(\boldsymbol{r},t) + \frac{\partial}{\partial t}\tilde{\boldsymbol{D}}(\boldsymbol{r},t) \tag{2.48}$$

with the magnetic field [61, Eq. (6.99)]

$$\tilde{\boldsymbol{H}}(\boldsymbol{r},t) = \frac{1}{\mu_0}\left[\tilde{\boldsymbol{B}}(\boldsymbol{r},t) - \tilde{\boldsymbol{P}}_{\mathrm{m}}(\boldsymbol{r},t)\right] . \tag{2.49}$$

We observe that the description of macroscopic media consisting of microscopic objects, such as molecules, can be performed by considering the multipole moments of the microscopic objects. For the description of molecules, usually electric and magnetic dipoles are sufficient. For larger objects, the consideration has to be extended to incorporate quadrupoles, octupoles

etc. This is an essential finding, since the computation of the electric and magnetic dipolar response of molecules allows to calculate macroscopic quantities. We introduce in Chapter 3 the T-matrix, which describes the multipolar response of an object. In Chapter 4, we show that the T-matrix of a molecule can be computed with density-functional theory.

In this chapter, we presented the fundamentals of linear and nonlinear optics. We introduced the macroscopic Maxwell equations both in time and frequency domain. Together with the linear constitutive relations and the addition of a nonlinear term, Maxwell's equations will be used to describe all linear and nonlinear optical effects in this thesis. We concluded the chapter by considering the microscopic Maxwell equations and performing the transition from to the microscopic to the macroscopic description. In this context, we observed that the spatial average of the microscopic charge and current densities leads to a sum over multipole moments.

In the next chapter, we introduce the T-matrix formalism used to obtain the optical response of the molecular systems that we consider in this thesis. The T-matrix represents the response of finite-size objects expanded with multipolar coefficients. It can be used, therefore, as a bridge between the microcopic description of single molecules and the macroscopic description of photonic devices incorporating the molecules.

3 | T-matrix Formalism for Linear Optics

The transition (T-)matrix of an object was introduced by Waterman to describe its electromagnetic scattering response [50]. The T-matrix relates the multipolar field coefficients of an incident electromagnetic wave to the corresponding multipolar field coefficients of a scattered electromagnetic wave. It constitutes a very comprehensive representation of the linear optical properties of an object. Once the T-matrix of a single object is known, it can be used to describe the optical response of macroscopic photonic materials made from many of these objects. Two instances are the computation of the macroscopic optical response of stacked two-dimensional periodic lattices of scatterers in combination with isotropic slabs [51, 76, 77] and the analysis of multipolar couplings in periodic systems [78]. The T-matrix is an essential object in this thesis by many means. For instance, the T-matrix can be used as the bridge between the quantum-chemical and the optical scattering analysis of molecules: We see in Subsection 2.2.2 that the transition from the microscopic to the macroscopic description of electromagnetism is based on the multipolar moments of the microscopic objects, which make up the macroscopic media. The T-matrix can be used to represent the scattering response of such objects with respect to an incident field. Both the incident and the scattered fields are expanded in vector spherical waves with corresponding multipolar coefficients. If the microscopic object is a finite-size molecular model, the T-matrix can be computed from its polarizability tensor. The latter can be calculated with quantum-chemical methods such as time-dependent density functional theory. With the T-matrix of a molecule at hand, the optical response of a photonic device containing this molecule can be computed with Maxwell's scattering simulations. The T-matrix can be considered, therefore, as the bridge between the microscopic and macroscopic description of the electromagnetic phenomena discussed in this thesis.

In Section 3.1, we define and analyze different properties of the T-matrix. Here, we show the computation principle of the T-matrix of a homogeneous, isotropic, and achiral sphere, the transformation of the T-matrix between different basis sets, and its computation from the polarizability tensor. In Section 3.2, it is explained how the optical response of macroscopic photonic structures made from different objects is simulated based on the T-matrix. In this regard, we introduce some principles of the two program suites *mpGMM* [51] and *treams* [52, 53], which are used for optical simulations in this thesis.

3.1. Definition and Properties of the T-matrix

In this thesis, we use Waterman's T-matrix [50] to characterize the electromagnetic scattering off an object and to describe the optical properties of macroscopic systems. In the following, we consider an object surrounded by a homogeneous, isotropic, and achiral environment. The environment, frequently called the host material, is described by a permittivity ε_h and a permeability μ_h. In the remaining chapter, we do not write the frequency ω as an explicit argument for better readability. In [69], the procedure to solve the scattering off a homogeneous, isotropic, and achiral sphere in a homogeneous achiral environment has been described, which we summarize in the following to demonstrate the computation of

a T-matrix for a simple case. The framework of this procedure is called Mie theory after Gustav Mie.

In the framework of Mie theory, first, a homogeneous space is considered, in which eigenmodes to Maxwell's equations are seeked in spherical coordinates. Spherical coordinates are chosen, as they are most suitable due to the spherical geometry of the considered scatterer. Knowing the field expansions in the homogeneous space, incident, internal, and scattered fields can be expanded correspondingly. The amplitudes of those fields are found by exploiting interface conditions. This is in complete analogy to compute the transmission and reflection coefficients of a plane wave at planar interfaces. Due to the spherical symmetry of the scatterer, the different modes in the expansion of the scattered and internal fields do not couple so that explicit expressions can be found for the amplitudes. In the following, we elaborate on this procedure in more detail.

First, we have to find elementary solutions to the vectorial Helmholtz wave equation [69, Eq. (3.6)]

$$\left(\Delta + k^2\right) \boldsymbol{E}(\boldsymbol{r}) = 0\,, \tag{3.1}$$

where k is the wavenumber in the respective material.

Instead of solving the vectorial Helmholtz equation directly, we introduce a scalar function $\psi(\boldsymbol{r})$, solving the scalar Helmholtz equation

$$\left(\Delta + k^2\right) \psi(\boldsymbol{r}) = 0\,. \tag{3.2}$$

If $\psi(\boldsymbol{r})$ solves the scalar Helmholtz equation, the vector functions [69, Eq. (4.1)]

$$\boldsymbol{M}(k\boldsymbol{r}) = \nabla \times (\boldsymbol{r}\psi(\boldsymbol{r})) \quad \text{and} \quad \boldsymbol{N}(k\boldsymbol{r}) = \frac{\nabla \times \boldsymbol{M}(\boldsymbol{r})}{k} \tag{3.3}$$

solve the vectorial Helmholtz equation. Both $\boldsymbol{M}(k\boldsymbol{r})$ and $\boldsymbol{N}(k\boldsymbol{r})$ are free of divergence. For the generating function we choose the ansatz $\psi(r,\theta,\varphi) = R(r)\Theta(\theta)\Phi(\varphi)$. Then, the solution to the scalar Helmholtz equation is [69, Eqs. (4.15), (4.16)]

$$\psi_{l,m}(r,\theta,\varphi) = z_l(kr) Y_{l,m}(\theta,\varphi)\,, \tag{3.4}$$

$l \in \mathbb{N}$, $m \in \{-l, -l+1, \ldots, l\}$. $Y_{l,m}(\theta,\varphi)$ are the spherical harmonics [61, Eq. (3.53)]

$$Y_{l,m}(\theta,\varphi) = \sqrt{\frac{2l+1}{4\pi}\frac{(l-m)!}{(l+m)!}}\mathrm{e}^{\mathrm{i}m\varphi} P_l^m\left(\cos(\theta)\right)\,, \tag{3.5}$$

with the associated Legendre polynomials $P_l^m\left(\cos(\theta)\right)$ [61, Eq. (3.50)]. $z_l(kr)$ are the spherical Bessel functions. $\boldsymbol{M}(k\boldsymbol{r})$ and $\boldsymbol{N}(k\boldsymbol{r})$ are computed from $\psi(\boldsymbol{r})$ with Eq. (3.3), and they are called vector spherical waves.

The choice of the spherical Bessel function depends on the domain of the scattering problem in which the field is expanded. Inside the sphere, the field has to be finite at the origin. We choose here, therefore, the Bessel function of the first kind $j_l(kr)$ to later expand the internal field [69, Eq. (4.40)]. Outside the sphere, the field is a sum of the illumination, which also has to be finite at the origin, and of the scattered wave. For the illumination, $j_l(kr)$ is chosen again. For the scattered wave, we choose the Hankel function of first kind $h_l^{(1)}(kr)$, which corresponds to an outgoing spherical wave in the limit of large distances with respect to the sphere [69, Eqs.(4.42), (4.45)].

Once we know the fundamental expansion to the involved field, we proceed by writing the electric field outside the illuminated scatterer as a sum of the incident and scattered fields. Both fields are given by a multipolar expansion into vector spherical waves in the frequency domain and the field outside the scatterer reads as [79, Eqs. (4), (14)][P4, Eq. (1)]

$$\begin{aligned}\boldsymbol{E}^{\mathrm{out}}(\boldsymbol{r}) = \sum_{l=1}^{\infty}\sum_{m=-l}^{l}\Big(&a_{l,m,\mathrm{N}}\boldsymbol{N}_{l,m}^{(1)}(k\boldsymbol{r}) + a_{l,m,\mathrm{M}}\boldsymbol{M}_{l,m}^{(1)}(k\boldsymbol{r}) \\ &+c_{l,m,\mathrm{N}}\boldsymbol{N}_{l,m}^{(3)}(k\boldsymbol{r}) + c_{l,m,\mathrm{M}}\boldsymbol{M}_{l,m}^{(3)}(k\boldsymbol{r})\Big)\,.\end{aligned} \tag{3.6}$$

Here, $\boldsymbol{r}$ is defined with respect to the origin of the object. $\boldsymbol{N}_{l,m}^{(1)}(k\boldsymbol{r})$ and $\boldsymbol{M}_{l,m}^{(1)}(k\boldsymbol{r})$ correspond to vector spherical waves, for which Bessel functions of the first kind describe the radial dependence. $\boldsymbol{N}_{l,m}^{(3)}(k\boldsymbol{r})$ and $\boldsymbol{M}_{l,m}^{(3)}(k\boldsymbol{r})$ correspond to vector spherical waves, for which Hankel functions of the first kind describe the radial dependence. $\boldsymbol{N}_{l,m}^{(1,3)}(k\boldsymbol{r})$ and $\boldsymbol{M}_{l,m}^{(1,3)}(k\boldsymbol{r})$ are vector spherical waves of well-defined parity. For regular waves, $\boldsymbol{N}_{l,m}^{(1,3)}(k\boldsymbol{r})$ corresponds to transverse magnetic (TM) modes and $\boldsymbol{M}_{l,m}^{(1,3)}(k\boldsymbol{r})$ corresponds to transverse electric (TE) modes [59].

Inside the sphere, the field is

$$\boldsymbol{E}^{\mathrm{ins}}(\boldsymbol{r}) = \sum_{l=1}^{\infty}\sum_{m=-l}^{l}\Big(f_{l,m,\mathrm{N}}\boldsymbol{N}_{l,m}^{(1)}(k\boldsymbol{r}) + f_{l,m,\mathrm{M}}\boldsymbol{M}_{l,m}^{(1)}(k\boldsymbol{r})\Big)\,. \tag{3.7}$$

The corresponding magnetic fields can be computed from the electric fields with Maxwell's equations. The multipolar expansion coefficients $a_{l,m,\mathrm{N}}$ and $a_{l,m,\mathrm{M}}$ of the illuminating plane wave are known. Equation (19) of [51], for instance, can be used to compute the multipolar expansion coefficients of a plane wave of well-defined helicity. These can be used to compute the expansion coefficients of a plane wave of well-defined parity, as we show below. To compute the coefficients $c_{l,m,\mathrm{N}}$ and $c_{l,m,\mathrm{M}}$ of the scattered wave, the interface conditions at the boundary of the sphere are enforced. They read

$$\big(\boldsymbol{E}^{\mathrm{out}}(\boldsymbol{r}) - \boldsymbol{E}^{\mathrm{ins}}(\boldsymbol{r})\big)\times\hat{\boldsymbol{n}} = 0 \quad \text{and} \quad \big(\boldsymbol{H}^{\mathrm{out}}(\boldsymbol{r}) - \boldsymbol{H}^{\mathrm{ins}}(\boldsymbol{r})\big)\times\hat{\boldsymbol{n}} = 0\,, \tag{3.8}$$

where $\hat{\boldsymbol{n}}$ is the normal vector on the boundary of the sphere pointing to the outside. We note that modes with different multipolar order are orthogonal and do not couple. Therefore, we have sets of two coupled equations from these two interface conditions, which are independent from each other. For each multipolar order, there is one set of two coupled equations. From these equations, analytical terms result for the amplitude coefficients of the scattered and the internal field. Mostly, we concentrate on the scattered field.

The T-matrix now relates the multipolar expansion coefficients $a_{l,m,\mathrm{N}}$ and $a_{l,m,\mathrm{M}}$ of the incident field to the coefficients $c_{l,m,\mathrm{N}}$ and $c_{l,m,\mathrm{M}}$ of the scattered field, schematically depicted

in Figure 3.1. For that purpose, we arrange the coefficients in column vectors [59, Eq. (3)]

$$\boldsymbol{a} = \begin{pmatrix} a_{1,-1,\mathrm{N}} \\ a_{1,0,\mathrm{N}} \\ a_{1,1,\mathrm{N}} \\ a_{2,-2,\mathrm{N}} \\ \vdots \\ a_{1,-1,\mathrm{M}} \\ a_{1,0,\mathrm{M}} \\ a_{1,1,\mathrm{M}} \\ a_{2,-2,\mathrm{M}} \\ \vdots \end{pmatrix} \quad \text{and} \quad \boldsymbol{c} = \begin{pmatrix} c_{1,-1,\mathrm{N}} \\ c_{1,0,\mathrm{N}} \\ c_{1,1,\mathrm{N}} \\ c_{2,-2,\mathrm{N}} \\ \vdots \\ c_{1,-1,\mathrm{M}} \\ c_{1,0,\mathrm{M}} \\ c_{1,1,\mathrm{M}} \\ c_{2,-2,\mathrm{M}} \\ \vdots \end{pmatrix}, \tag{3.9}$$

so that

$$\boldsymbol{c} = \mathbf{T}\boldsymbol{a}\,. \tag{3.10}$$

Because of the way the column vectors $\boldsymbol{a}$ and $\boldsymbol{c}$ are defined above, the T-matrix has the shape [59, Eq. (5)]

$$\mathbf{T} = \begin{pmatrix} \mathbf{T}_{\mathrm{NN}} & \mathbf{T}_{\mathrm{NM}} \\ \mathbf{T}_{\mathrm{MN}} & \mathbf{T}_{\mathrm{MM}} \end{pmatrix}, \tag{3.11}$$

where $\mathbf{T}_{\mathrm{NN}}$, $\mathbf{T}_{\mathrm{NM}}$, $\mathbf{T}_{\mathrm{MN}}$, and $\mathbf{T}_{\mathrm{MM}}$ are block matrices consisting of sorted purely dipolar ($l = 1$), quadrupolar ($l = 2$), octupolar ($l = 3$), etc. terms and multipolar coupling ($l = 1 \leftrightarrow l = 2$, $l = 1 \leftrightarrow l = 3$, etc.) terms. For spheres, the block matrices are diagonal [80] as the vector spherical harmonics are orthogonal and do not couple.

For an arbitrary object, we also establish Eq. (3.10). In this case, however, the T-matrix will be dense. The T-matrix $\mathbf{T}$ of an object depends generally on its geometry and its material parameters but not on the incident field [65]. From the known T-matrices of single isolated objects, one can consider a finite cluster of these objects and compute T-matrices of the scatterers which incorporate the multi-scattering between the objects. A procedure to compute such T-matrices for arbitrarily shaped objects is described in [52, 80].

For numerical simulations, l is a finite number so that $\mathbf{T}$ has finite dimensions. The maximum value for l is chosen so that $\mathbf{T}$ sufficiently describes the scattering off an object. The T-matrices of the considered molecules are purely dipolar ($l = 1$) as they are very small in comparison to the wavelength of the incident light [59, P3–P8]. For larger objects, describing their response with Maxwell's equations, higher multipolar orders have to be considered.

In this thesis, we also consider chiral molecules. For chiral objects, an expansion using vector spherical waves with well-defined helicity is more convenient, see [51, Eq. (14)], for instance. These vector spherical waves of well-defined helicity read as

$$\boldsymbol{A}^{(1,3)}_{l,m,\pm}(k_\pm \boldsymbol{r}) = \frac{\boldsymbol{N}^{(1,3)}_{l,m}(k_\pm \boldsymbol{r}) \pm \boldsymbol{M}^{(1,3)}_{l,m}(k_\pm \boldsymbol{r})}{\sqrt{2}}\,, \tag{3.12}$$

with the wavenumber $k_\pm$ for the respective helicity in the respective domain, see Eq. (2.19). This is because $\boldsymbol{A}^{(1,3)}_{l,m,\pm}(k_\pm \boldsymbol{r})$ are in contrast to $\boldsymbol{N}^{(1,3)}_{l,m}(k_\pm \boldsymbol{r})$ and $\boldsymbol{M}^{(1,3)}_{l,m}(k_\pm \boldsymbol{r})$ solutions to

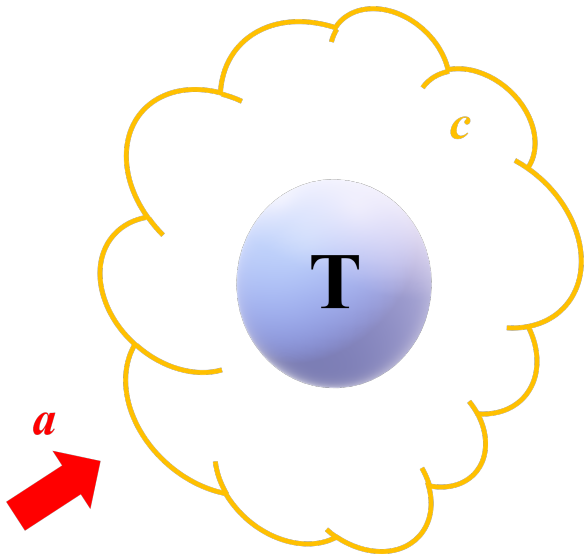

Figure 3.1.: Visualization of the scattering process described with the T-matrix. A plane wave is incident, which is expanded in vector spherical waves with the multipolar expansion coefficients arranged in $\boldsymbol{a}$. The plane wave scatters off an object described with the T-matrix $\mathbf{T}$. The scattered light is also expanded in vector spherical waves. Its multipolar expansion coefficients are arranged in $\boldsymbol{c}$.

Maxwell's equations in chiral media [51]. Outside the scatterer, we express the electric field, therefore, as [51, Eq. (13)]

$$\begin{aligned}\boldsymbol{E}^{\text{out}}(\boldsymbol{r}) = \sum_{l=1}^{\infty}\sum_{m=-l}^{l}\Big(&b_{l,m,+}\boldsymbol{A}^{(1)}_{l,m,+}(k_+\boldsymbol{r}) + b_{l,m,-}\boldsymbol{A}^{(1)}_{l,m,-}(k_-\boldsymbol{r}) \\ &+d_{l,m,+}\boldsymbol{A}^{(3)}_{l,m,+}(k_+\boldsymbol{r}) + d_{l,m,-}\boldsymbol{A}^{(3)}_{l,m,-}(k_-\boldsymbol{r})\Big)\ .\end{aligned} \tag{3.13}$$

Equation (3.12) describes the transition of vector spherical waves from the basis of well-defined parity to the basis of well-defined helicity. From this follows [59, Eq. (S47)]

$$\begin{pmatrix}\mathbf{T}_{++} & \mathbf{T}_{+-}\\ \mathbf{T}_{-+} & \mathbf{T}_{--}\end{pmatrix} = \frac{1}{2}\begin{pmatrix}\mathbb{1} & \mathbb{1}\\ \mathbb{1} & -\mathbb{1}\end{pmatrix}\begin{pmatrix}\mathbf{T}_{\text{NN}} & \mathbf{T}_{\text{NM}}\\ \mathbf{T}_{\text{MN}} & \mathbf{T}_{\text{MM}}\end{pmatrix}\begin{pmatrix}\mathbb{1} & \mathbb{1}\\ \mathbb{1} & -\mathbb{1}\end{pmatrix} \tag{3.14}$$

for the T-matrix. $\mathbf{T}_{++}$, $\mathbf{T}_{+-}$, $\mathbf{T}_{-+}$, and $\mathbf{T}_{--}$ are the block matrices of the T-matrix $\mathbf{T}_{\text{Hel}}$ in the basis of well-defined helicity. Arranging the multipolar expansion coefficients of the incident field $b_{l,m,+}$ and $b_{l,m,-}$ and the scattered field $d_{l,m,+}$ and $d_{l,m,-}$ in the column vectors

[59, Eq. (8)]

$$\boldsymbol{b} = \begin{pmatrix} b_{1,-1,+} \\ b_{1,0,+} \\ b_{1,1,+} \\ b_{2,-2,+} \\ \vdots \\ b_{1,-1,-} \\ b_{1,0,-} \\ b_{1,1,-} \\ b_{2,-2,-} \\ \vdots \end{pmatrix} \quad \text{and} \quad \boldsymbol{d} = \begin{pmatrix} d_{1,-1,+} \\ d_{1,0,+} \\ d_{1,1,+} \\ d_{2,-2,+} \\ \vdots \\ d_{1,-1,-} \\ d_{1,0,-} \\ d_{1,1,-} \\ d_{2,-2,-} \\ \vdots \end{pmatrix}, \tag{3.15}$$

we have

$$\boldsymbol{d} = \mathbf{T}_{\mathrm{Hel}} \boldsymbol{b}\,. \tag{3.16}$$

The T-matrices of a homogeneous achiral [69] and of a layered chiral sphere [81] can be computed analytically. For more complicated objects, finite-element (FEM) based methods can be used [82–84]. We aim on describing the scattering of molecules with the T-matrix. The T-matrix of the molecules discussed in this thesis are computed with time-dependent functional theory (TD-DFT) [59], which is an *ab initio* quantum-chemical method. Another instance for an *ab initio* quantum-chemical method is Hartree-Fock theory. We show in Chapter 4 that with quantum-chemical methods, the 3×3 dipolar polarizability tensors $\boldsymbol{\alpha}_{\mathrm{ee}}$, $\boldsymbol{\alpha}_{\mathrm{em}}$, $\boldsymbol{\alpha}_{\mathrm{me}}$, and $\boldsymbol{\alpha}_{\mathrm{mm}}$ can be computed. In [59], it is shown that these matrices are equivalent to the dipolar blocks of the T-matrix in the basis of well-defined parity. This equivalence originates from the fact that the optical response of a microscopic object can be described via its multipolar moments. On the one hand, the multipolar moments can be computed with the T-matrix as it describes the scattering response of the object in a multipolar expansion. On the other hand, we show in Chapter 4 that the dipolar moments can be also directly computed from the dipolar polarizability tensors. The relationship between the dipolar polarizability tensors and the dipolar blocks of the T-matrix is [59, Eq. (6)]

$$\begin{pmatrix} \mathbf{T}_{\mathrm{NN}} & \mathbf{T}_{\mathrm{NM}} \\ \mathbf{T}_{\mathrm{MN}} & \mathbf{T}_{\mathrm{MM}} \end{pmatrix} = \frac{\mathrm{i} c_{\mathrm{h}} Z_{\mathrm{h}} k_{\mathrm{h}}^3}{6\pi} \begin{pmatrix} \mathbf{C}\left(\boldsymbol{\alpha}_{\mathrm{ee}}\right)\mathbf{C}^{-1} & \mathbf{C}\left(-\mathrm{i}\boldsymbol{\alpha}_{\mathrm{em}}/Z_{\mathrm{h}}\right)\mathbf{C}^{-1} \\ \mathbf{C}\left(\mathrm{i}\boldsymbol{\alpha}_{\mathrm{me}}/c_{\mathrm{h}}\right)\mathbf{C}^{-1} & \mathbf{C}\left(\boldsymbol{\alpha}_{\mathrm{mm}}/(c_{\mathrm{h}} Z_{\mathrm{h}})\right)\mathbf{C}^{-1} \end{pmatrix}. \tag{3.17}$$

In Eq. (3.17), $c_{\mathrm{h}} = 1/\sqrt{\varepsilon_{\mathrm{h}}\mu_{\mathrm{h}}}$ is the speed of light in the host medium, $Z_h = \sqrt{\mu_{\mathrm{h}}/\varepsilon_{\mathrm{h}}}$ is the impedance of the host medium, and $\mathbf{C}$ is a 3×3 matrix describing the transition from Cartesian to spherical coordinates. This is necessary as the polarizability tensors are usually given in the Cartesian basis [59]. With [59, Eq. (S8)], we have

$$\mathbf{C} = \frac{1}{\sqrt{2}} \begin{pmatrix} 1 & \mathrm{i} & 0 \\ 0 & 0 & 1 \\ -1 & \mathrm{i} & 0 \end{pmatrix}. \tag{3.18}$$

In the next chapter, we describe in detail how the dipolar polarizabilities are computed with quantum-chemical methods.

3.2. Simulation Principle for the Optical Response of Macroscopic Structures with the T-matrix

To simulate the optical response of stacked two-dimensional periodic lattices of molecules in combination with homogeneous isotropic slabs, the codes multi-layered periodic General Mie-Method (*mpGMM*) [51] and *treams* [52, 53] by Dominik Beutel are used. *mpGMM* is a software code which is written in the commercial software MATLAB [85]. For an extended software package written in Python, we refer to *treams* [52, 53]. Note that in [58, 86, 87] it is presented how to solve a system of layered lattices of spheres, while in *mpGMM* and *treams* the scatterer can be in principle of arbitrary shape as long as its T-matrix is known. This is of special importance for the work presented here as molecules of non-spherical shape are discussed.

Both, *mpGMM* and *treams*, are based on the theory presented in [51, 52]. The basic principle of both software suites utilized in this thesis is that the response of two-dimensional lattices, slabs, and the influence of displacements between the lattices in all three dimensions are computed first separately and then combined in a second step. This is achieved by computing matrices relating in- and outgoing plane waves for each layer and by combining these matrices to a single matrix. This final matrix describes the entire stack and can be used to compute the transmittance and reflectance of plane waves with different angles of incidence and polarizations.

We consider a structure, which is infinitely extended in two dimensions and finite in the third dimension. The third dimension is considered as the z-axis. The structure consists of stacked two-dimensional lattices and homogeneous layers, and is illuminated by a plane wave propagating in positive z-direction. It has a wave vector $\boldsymbol{k}_{0,s,\uparrow}$ and helicity s. A sketch of the setup is displayed in Figure 3.2.

In general, the electric field leaving a specific layer of the structure can be expressed as a sum of up- and downward propagating plane waves [51, Eqs. (5)]

$$\boldsymbol{E}(\boldsymbol{r}) = \sum_{s=\pm} \sum_{d=\uparrow\downarrow} \sum_{\boldsymbol{g}} \zeta_{\boldsymbol{g},s,d} \hat{\boldsymbol{e}}_s(\boldsymbol{k}_{\boldsymbol{g},s,d}) \mathrm{e}^{\mathrm{i}\boldsymbol{k}_{\boldsymbol{g},s,d}\cdot\boldsymbol{r}} \,, \tag{3.19}$$

with expansion coefficients $\zeta_{\boldsymbol{g},s,d}$ and polarization directions $\hat{\boldsymbol{e}}_s(\boldsymbol{k}_{\boldsymbol{g},s,d})$. $\boldsymbol{g}$ is a reciprocal lattice vector. $d = \uparrow\downarrow$ indicates, whether a plane wave is propagating in positive ($\uparrow$) or negative ($\downarrow$) z-direction. Considering a finite number of diffraction orders of the two-dimensional lattices, we arrange the expansion coefficients in vectors and relate them via Q-matrices [51, Eqs. (6)]:

$$\begin{pmatrix} \boldsymbol{\zeta}_{2,\uparrow} \\ \boldsymbol{\zeta}_{1,\downarrow} \end{pmatrix} = \begin{pmatrix} \boldsymbol{Q}_{\uparrow\uparrow} & \boldsymbol{Q}_{\uparrow\downarrow} \\ \boldsymbol{Q}_{\downarrow\uparrow} & \boldsymbol{Q}_{\downarrow\downarrow} \end{pmatrix} \begin{pmatrix} \boldsymbol{\zeta}_{1,\uparrow} \\ \boldsymbol{\zeta}_{2,\downarrow} \end{pmatrix} \,. \tag{3.20}$$

A layer can be a two-dimensional lattice, an interface, or a slab. In the following, we explain how the Q-matrix of a two-dimensional lattice is computed.

In Eq. 3.10, we define the T-matrix $\mathbf{T}$ of a single scatterer. If that object is placed periodically into a two-dimensional lattice, not only the primary illuminating plane wave with multipolar coefficients $\boldsymbol{b}_0$ has to be incorporated but also the interaction between all scatterers of the lattice. The expansion coefficients of the totally scattered field of the object at the origin of the lattice are given by [51, Eq. (16)]

$$\boldsymbol{d}_{0,\mathrm{tot}} = \mathbf{T}_{\mathrm{Hel}} \left(\mathbf{b}_0 + \sum_{\boldsymbol{R}\neq 0} \mathbf{C}^{(3)}(-\boldsymbol{R}) \mathrm{e}^{\mathrm{i}\boldsymbol{k}_\parallel\cdot\boldsymbol{R}} \boldsymbol{d}_{0,\mathrm{tot}} \right) \,. \tag{3.21}$$

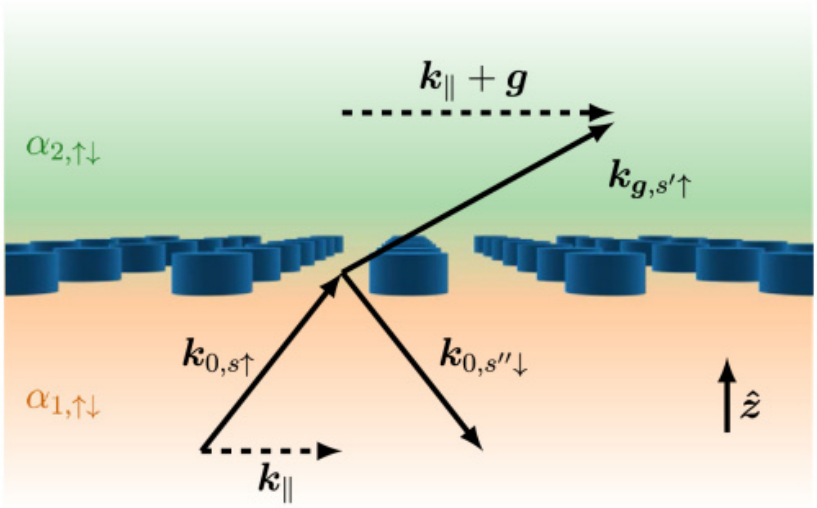

Figure 3.2.: Sketch of general setup of periodic lattice surrounded by homogeneous layers, which is simulated with *mpGMM* and *treams*. The setup is illuminated from below by a plane wave with wave vector $\boldsymbol{k}_{0,s,\uparrow}$ and helicity s. It has a component $\boldsymbol{k}_{\parallel}$, which is parallel to the lattice. The diffraction orders of the lattice have a parallel component of $\boldsymbol{k}_{\parallel} + \boldsymbol{g}$. $\boldsymbol{g}$ is a reciprocal lattice vector. In this thesis, not cylinders but molecules arranged in a lattice are considered. Reprinted with permission from [51]. Copyright © 2021 Optical Society of America.

Here, the first term describes the primary illumination and the second term represents the interaction between the scatterers placed at lattice sites $\boldsymbol{R}$. $\mathbf{C}^{(3)}(-\boldsymbol{R})$ is a matrix consisting of translation addition coefficients transforming the scattered field coefficients $\mathrm{e}^{\mathrm{i}\boldsymbol{k}_{\parallel}\boldsymbol{R}}\boldsymbol{d}_{0,\mathrm{tot}}$ of the other scatterers into field coefficients being incident on the scatterer at the origin. The translation addition coefficients for vector spherical waves derived by [88, 89] can be found in [90]. The component $\boldsymbol{k}_{\parallel}$ of the wave vector is parallel to the lattice. The sum in Eq. 3.21 includes all lattice points except from the central particle whose scattering response is computed. From Eq. (3.21) follows [51, Eq. (17)]

$$\boldsymbol{d}_{0,\mathrm{tot}} = \left(\mathbb{1} - \mathbf{T}_{\mathrm{Hel}} \sum_{\boldsymbol{R}\neq 0} \mathbf{C}^{(3)}(-\boldsymbol{R}) \mathrm{e}^{\mathrm{i}\boldsymbol{k}_{\parallel}\cdot\boldsymbol{R}} \right)^{-1} \mathbf{T}_{\mathrm{Hel}} \boldsymbol{b}_0 \,, \tag{3.22}$$

where the sum over the lattice points is evaluated with Ewald's summation method [91, 92]. The advantage of this summation method is that it converges reliably much faster in comparison to a direct summation procedure [93]. This is achieved by splitting the sum into two parts. For small distances, the sum is evaluated in the real space. For large distances, the sum is evaluated in the reciprocal space. For a detailed analysis of Ewald's summation method used to compute multi-scattering problems, we refer to [93].

By transforming the scattered vector spherical wave expansion coefficients into plane wave coefficients [94], the totally scattered electric field can be expressed as a sum over diffracted plane waves. The exact expression for the expansion of the fields scattered in $\downarrow$-direction and

↑-direction is [51, Eq. (21)]

$$\boldsymbol{E}_{s,d=\downarrow\uparrow}(\boldsymbol{r}) = \sum_{\boldsymbol{g}} \sum_{s=\pm} E_s^{\boldsymbol{k}_\parallel+\boldsymbol{g},s} \hat{\boldsymbol{e}}_s(\boldsymbol{k}_{\boldsymbol{k}_\parallel+\boldsymbol{g},s,d}) \mathrm{e}^{\mathrm{i}\boldsymbol{k}_{\boldsymbol{k}_\parallel+\boldsymbol{g},s,d}\cdot\boldsymbol{r}} , \tag{3.23}$$

with the diffracted plane wave expansion coefficients [51, Eq. (22)]

$$E_s^{\boldsymbol{k}_\parallel+\boldsymbol{g},s} = \sum_{l=1}^{\infty} \sum_{m=-l}^{l} d_{0,\mathrm{tot},l,m;s} \frac{2\pi\gamma_{l,m}}{Ak_s\Gamma_{\boldsymbol{k}_\parallel+\boldsymbol{g},s}\mathrm{i}^{l+1}} \left(\frac{m}{\sin(\theta)} P_l^m(\cos(\theta)) + s\frac{\partial}{\partial\theta} P_l^m(\cos(\theta)) \right) . \tag{3.24}$$

In Eq. (3.23), $\boldsymbol{k}_{\boldsymbol{k}_\parallel+\boldsymbol{g},s,d}$ is the wave vector of the respective diffracted plane wave with helicity s, and $\hat{\boldsymbol{e}}_\pm(\boldsymbol{k}_{\boldsymbol{k}_\parallel+\boldsymbol{g},s,d})$ is the polarization direction of the respective diffracted wave. In Eq. (3.24), $\Gamma_{\boldsymbol{k}_\parallel+\boldsymbol{g},s}$ is the z-component of the diffracted wave vector. $\boldsymbol{g}$ is a reciprocal lattice vector. A is the area of the considered unit cell. $\gamma_{l,m}$ is a normalization factor of the vector spherical wave, and θ is the complex angle of the diffracted wave vector with respect to the z-axis.

After adding the incident field, the coefficients $E_\mathrm{s}^{\boldsymbol{k}_\parallel+\boldsymbol{g},s}$ are arranged in the Q-matrices $\boldsymbol{Q}_{d,d'}$, which relate the in- and outgoing diffracted plane waves of the two-dimensional lattice.

By assembling the reflection $r_{ss'}(\boldsymbol{k}_\parallel+\boldsymbol{g})$ and transmission coefficients $t_{ss'}(\boldsymbol{k}_\parallel+\boldsymbol{g})$ at interfaces in Q-matrices [51, Eqs. (11)-(12b)]

$$\boldsymbol{Q}_{d,d;\boldsymbol{g},s;\boldsymbol{g}',s'} = \delta_{\boldsymbol{g},\boldsymbol{g}'} t_{ss'}(\boldsymbol{k}_\parallel+\boldsymbol{g}), \tag{3.25}$$

$$\boldsymbol{Q}_{d,d';\boldsymbol{g},s;\boldsymbol{g}',s'} = \delta_{\boldsymbol{g},\boldsymbol{g}'} r_{ss'}(\boldsymbol{k}_\parallel+\boldsymbol{g}), \qquad d \neq d' , \tag{3.26}$$

and the propagation through homogeneous isotropic media introducing a displacement vector $\boldsymbol{d}$ also in Q-matrices [51, Eqs. (9)]

$$\boldsymbol{Q}_{d,d';\boldsymbol{g},s;\boldsymbol{g}',s'} = \delta_{d,d'}\delta_{\boldsymbol{g},\boldsymbol{g}'}\delta_{s,s'}\mathrm{e}^{\mathrm{i}\boldsymbol{k}_{\boldsymbol{g},s,d}\cdot\boldsymbol{d}} , \tag{3.27}$$

one can combine all Q-matrices into a single Q-matrix [51, Eqs. (7), (8)]. This is especially efficient if a structure is repeated, since the combination of Q-matrices consists of matrix multiplications. Out of this Q-matrix describing the entire macroscopic system, the reflectance and transmittance of an incident plane wave can be computed. The procedure is used to compute the response of various different systems such as photonic devices consisting of filled cavities, see for instance [76, 77, P4]. Furthermore, the combined Q-matrix of a two-dimensional lattice and the spacing between neighboring lattices, which are repeated in z-direction, can be used to compute the band structure of the corresponding three-dimensional material [51, 86].

In this chapter, we introduced the T-matrix and some of its basic properties. Based on this, we presented how the optical response of a macroscopic system of stacked two-dimensional lattices and slabs can be computed. This is essential for this thesis, as the procedure enables us to obtain the optical response of stacked molecular lattices in combination with homogeneous slabs, for instance. In the next chapter, we show how the T-matrix is computed for molecules with quantum-chemical *ab initio* methods.

4 | Density Functional Theory to Simulate the Optical Response of Molecules

In this chapter, we discuss how the dipolar T-matrix of molecules is computed using time-dependent density functional theory (TD-DFT). TD-DFT is an *ab initio* quantum-chemical method. The optical properties of the molecules are, therefore, computed based on their quantum-chemical properties from the Schrödinger equation.

The relationship between the quantum-chemical properties and the optical properties is an essential part of the multi-scale approach we will discuss in Chapters 6 and 7. We showed already in Eq. (3.17) that the dipolar T-matrix is equivalent to the dipolar polarizability tensor of an object. The equivalence can be seen in the dipolar response of an object, which can be computed with the T-matrix, presented in Chapter 3, but also with the polarizability tensor. The latter is shown in this chapter. In contrast to phenomenological approaches, in which the polarizability of a molecule or the permittivity of a molecular film is estimated, the polarizability tensor and subsequently the T-matrix of finite molecular structures are computed with quantum-chemical methods in our approach. Afterward, we perform the transition from the microscopic description of a finite molecular structure to the macroscopic description of a monolayer of molecules, a finite film of molecules, and of photonic devices. In this regard, we use the T-matrix as described in Section 3.2. In Chapter 7, we extend the concept and will introduce later the Hyper-T-matrix to express the nonlinear optical response of molecular structures inside photonic devices. In analogy to the relation between the T-matrix and the polarizability tensor, the Hyper-T-matrix can be computed from the first hyperpolarizability tensor of a molecule. This is a quantity which can also be computed with TD-DFT.

Generally, DFT is a powerful tool to compute quantum-chemical properties of many different structures. To introduce the reader to the framework of DFT as far as it is relevant to this thesis, this chapter aims at providing a short overview about the way (TD-)DFT can be used to obtain the optical response of molecules. For a broader overview about DFT, we refer to [95], and for a broader overview about quantum-chemical methods in general, we refer to [96].

In Section 4.1, we present the basic principles of DFT. This includes its general foundation, the Hohenberg-Kohn Theorem, the Kohn-Sham equations, and a short introduction to basis sets and functionals. In Section 4.2, we discuss how the dipolar polarizability tensor and the first hyperpolarizability tensor of molecules are computed.

4.1. Basic Principles of Density Functional Theory

One major goal of DFT is to determine the quantum-chemical properties of structures such as energy states. In quantum-chemistry, a structure is usually described with its Hamilton operator and the Schrödinger equation. Here, we consider a molecular system consisting of nuclei with mass M_k, charg Z_k, and position $\boldsymbol{R}_k$, and electrons with mass m, charge e, and

position $\boldsymbol{r}_i$. The Hamilton operator of such a system in atomic units is [97, Eqs. (3.2)-(3.11)]

$$\begin{aligned}\hat{H} &= \hat{T}_\mathrm{e} + \hat{T}_\mathrm{C} + \hat{V}_\mathrm{e-e} + \hat{V}_\mathrm{C-C} + \hat{V}_\mathrm{e-C} \\ &= -\sum_i \frac{1}{2}\frac{\partial^2}{\partial \boldsymbol{r}_i^2} - \sum_k \frac{m}{2M_k}\frac{\partial^2}{\partial \boldsymbol{R}_k^2} \\ &+ \sum_{i<j} \frac{1}{|\boldsymbol{r}_i - \boldsymbol{r}_j|} + \sum_{k<l} \frac{Z_k Z_l}{|\boldsymbol{R}_k - \boldsymbol{R}_l|} - \sum_{i,k} \frac{Z_k}{|\boldsymbol{r}_i - \boldsymbol{R}_k|}\,.\end{aligned} \tag{4.1}$$

Note that in atomic units, all position vectors are given in units of the Bohr radius a_0 [97]. The energies are given in units of $E_0 = me^4/\hbar^2 = 27.2\,\mathrm{eV}$ [97]. The transition from SI to atomic units can be performed by setting $e = -1$ and $m = a_0 = \hbar = 1$. In Eq. (4.1), $\hat{T}_\mathrm{e}$ is the kinetic energy of the electrons, $\hat{T}_\mathrm{C}$ is the kinetic energy of the nuclei, $\hat{V}_\mathrm{e-e}$ is the interaction potential between the electrons, $\hat{V}_\mathrm{C-C}$ is the interaction potential between the nuclei, and $\hat{V}_\mathrm{e-C}$ is the potential between the nuclei and the electrons. To simplify the procedure of finding the energy states of the system, for instance, the Born-Oppenheimer Approximation is used. The Born-Oppenheimer Approximation suggests to neglect the kinetic energy of the nuclei, as they are much heavier than the electrons. We write $\hat{H} = \hat{H}_0 + \hat{T}_\mathrm{C}$ with [97, Eqs. (3.12)]

$$\hat{H}_0 = \hat{T}_\mathrm{e} + \hat{V}_\mathrm{e-e}(\{\boldsymbol{r}\}) + \hat{V}_\mathrm{C-C}(\{\boldsymbol{R}\}) + \hat{V}_\mathrm{e-C}(\{\boldsymbol{r}\};\{\boldsymbol{R}\})\,. \tag{4.2}$$

Here, $\{\boldsymbol{r}\}$ is the set of the positions of the electrons, and $\{\boldsymbol{R}\}$ is the set of the positions of the nuclei. Schrödinger's stationary equation for the electrons is [97, Eqs. (3.13)]

$$\hat{H}_0\phi(\{\boldsymbol{r}\};\{\boldsymbol{R}\}) = \epsilon(\{\boldsymbol{R}\})\phi(\{\boldsymbol{r}\};\{\boldsymbol{R}\})\,, \tag{4.3}$$

where the fixed positions of the nuclei ($\{\boldsymbol{R}\}$) enter as parameters in the wave functions $\phi(\{\boldsymbol{r}\};\{\boldsymbol{R}\})$ and their energy eigenvalues $\epsilon(\{\boldsymbol{R}\})$.

Often, one is interested in the ground-state energy E_0 of the system, which is, according to the variational principle, the infimum [95, Eqs. (1.4)]

$$E_0 = \inf_{\phi \in W^{N_\mathrm{e}}} \langle \phi | \hat{H}_0 | \phi \rangle\,. \tag{4.4}$$

Here, W^{N_e} is the set of N_e antisymmetric electronic wave functions ϕ, which have a finite kinetic energy. The idea of DFT is to express this variational principle using only the electron density. The Hohenberg-Kohn theorems justify this idea [95]: It is possible to express the energy solely by the electron density without evaluating the wave function. The first theorem states that the energy potential is uniquely determined by the density up to a constant. The second theorem says that the electron density can be computed by the variational principle, as the energy of a guessed density is always larger than the exact energy of the electronic ground state. This is a minimization problem. Kinetic and exchange energy terms including correlation terms are, however, not known. Approximations are required for these terms that are part of the total energy of the system [96]. This problem is simplified by the ansatz of Kohn and Sham who re-introduced molecular orbitals [98]. The idea of Kohn and Sham is to express the kinetic energy term via two terms from which one is exact and one corresponds to a correction. The kinetic energy is computed from the molecular orbitals assuming that the electrons are non-interacting. Then, one introduces the correction to the kinetic energy via an exchange-correlation term, including interaction between the electrons. The advantage

of the Kohn-Sham formulation is that only approximations are necessary for the exchange-correlation energy [96].

Based on these, the Kohn-Sham equations have been derived [98, Eq. (2.8)], [95, Eq. (1.21)]

$$\left(-\frac{1}{2}\boldsymbol{\nabla}^2 + \hat{v}_{\mathrm{eff}}(\boldsymbol{r})\right)\psi_i(\boldsymbol{r}) = \epsilon_i\psi_i(\boldsymbol{r})\,. \tag{4.5}$$

In Eq. (4.5), ϵ_i are the corresponding Lagrange multipliers which are the Kohn-Sham orbital energies, $\hat{v}_{\mathrm{eff}}(\boldsymbol{r})$ is a sum of the nucleus-electron Coulomb interaction $\hat{v}_{\mathrm{e-C}}(\boldsymbol{r})$, the external potential $\hat{v}_{\mathrm{ext}}(\boldsymbol{r})$, and the Hartree-exchange-correlation potential $\hat{v}_{\mathrm{H_{xc}}}(\boldsymbol{r})$ from the electron-electron interaction,

$$\hat{v}_{\mathrm{eff}}(\boldsymbol{r}) = \hat{v}_{\mathrm{e-C}}(\boldsymbol{r}) + \hat{v}_{\mathrm{ext}}(\boldsymbol{r}) + \hat{v}_{\mathrm{H_{xc}}}(\boldsymbol{r})\,. \tag{4.6}$$

The Hartree-exchange-correlation potential is defined as $\hat{v}_{\mathrm{H_{xc}}}(\boldsymbol{r}) = \frac{\partial \hat{E}_{\mathrm{H_{xc}}}(\rho(\boldsymbol{r}))}{\partial \rho(\boldsymbol{r})}$ with $\hat{E}_{\mathrm{H_{xc}}}$ being the unknown Hartree-exchange-correlation energy [95, Eq. (1.22)]. $\psi_i(\boldsymbol{r})$ are the spatial molecular orbitals. The sum of their squared absolute values coincides with the electron density [96, Eq. (6.14)]

$$\rho(\boldsymbol{r}) = \sum_{i=1}^{N_{\mathrm{e}}} \left|\psi_i(\boldsymbol{r})\right|^2\,. \tag{4.7}$$

Note that the energy terms $\hat{v}_{\mathrm{e-C}}(\boldsymbol{r})$ and $\hat{v}_{\mathrm{H_{xc}}}(\boldsymbol{r})$ are expressed in terms of this electron density.

The molecular orbitals are expanded in basis functions $\xi_{\zeta,n,l,m}(r,\theta,\varphi)$, which are called atomic orbitals [96]. Commonly, Slater-Type Orbitals (STOs) and Gaussian-Type Orbitals (GTOs) are used. STOs are expressed in spherical coordinates as [96, Eq. (5.1)]

$$\xi_{\zeta,n,l,m}(r,\theta,\varphi) = NY_{l,m}(\theta,\varphi)r^{n-1}\mathrm{e}^{-\zeta r}\,, \tag{4.8}$$

where N is a normalization constant. They provide a fast convergence with growing number of basis functions. STOs are usually used for atomic and diatomic systems and for semi-empirical methods, where three- and four-center two-electron integrals can be neglected [96]. GTOs have the functional form of [96, Eq. (5.1)]

$$\xi_{\zeta,n,l,m}(r,\theta,\varphi) = NY_{l,m}(\theta,\varphi)r^{2n-2-l}\mathrm{e}^{-\zeta r^2}\,. \tag{4.9}$$

Note that they are also commonly expressed in Cartesian coordinates. Due to their zero slope at the nucleus and the fast decrease of their radial part far away from the nucleus in comparison to STOs, more GTOs are required to achieve the same accuracy as with STOs. The required integrals for their use, however, are much easier to be computed, so that GTOs are preferred for the sake of computational efficiency [96]. Usually GTOs are centered at the nuclei, but it is also possible to place them at the center of a bond, for instance [96].

A basis set is referred to as Single Zeta (SZ) basis set if it only consists of the necessary functions to minimally describe the occupied orbitals of the neutral atoms. A Double Zeta (DZ) basis set has twice as many basis functions, while a Triple Zeta (TZ) basis set consists of three times the number of basis functions inside the SZ basis [96]. Polarization functions enable a more flexible description of the density beyond occupied orbitals. They lead to the polarized split valence (SVP) and triple zeta valence (TZVP) type basis sets [96, 99].

Above, we state that the Hatree-exchange-correlation potential is unknown, entering the Kohn-Sham equations for the description of the considered system. There are different approximations for the exchange-correlation potential. One of the most important ones are the generalized-gradient approximations (GGA), where the exchange-correlation potential is determined by the particle density and its gradient, see [95, Eq. (1.115)]. Important instances of GGA functionals are Becke88 (B88), Perdew-Burke-Ernzerhof (PBE), and Becke97 GGA (B97-GGA) functionals.

Meta-GGAs describe the functional additionally in dependence of the second derivative of the density of states [95]. Hybrid functionals include the Hartree-Fock exchange in the exchange-correlation term. In this regard, the inclusion is optimized [95]. The Hartree-Fock exchange is sometimes also referred to as exact exchange. In the Hartree-Fock ansatz, every electron is exposed to the field of the nuclei and a mean field of the other electrons. Important instances for hybrid functionals are B3LYP and PBE0.

4.2. Computation of Linear Polarizabilities and First Hyperpolarizabilities

TD-DFT is essential for computing linear polarizabilities and first order hyperpolarizabilities in the framework of this thesis. Both represent the response of a molecule to a monochromatic electromagnetic wave on the microscopic level. The molecule is placed in the origin of the coordinate system, so we do not write $\boldsymbol{r}$ explicitly as an argument. Following up the discussion in Subsection 2.2.2, the linear optical response of the molecule is represented by the electric dipole moment

$$\boldsymbol{p}_{\mathrm{e}}(\omega) = \boldsymbol{\alpha}_{\mathrm{ee}}(\omega)\boldsymbol{E}(\omega) + \boldsymbol{\alpha}_{\mathrm{em}}(\omega)\boldsymbol{H}(\omega)\,, \tag{4.10}$$

and the magnetic dipole moment

$$\boldsymbol{p}_{\mathrm{m}}(\omega) = \boldsymbol{\alpha}_{\mathrm{me}}(\omega)\boldsymbol{E}(\omega) + \boldsymbol{\alpha}_{\mathrm{mm}}(\omega)\boldsymbol{H}(\omega)\,, \tag{4.11}$$

see [59, Eq. (1)]. Here, we use the 3×3 polarizability tensors $\boldsymbol{\alpha}_{\mathrm{ee}}$, $\boldsymbol{\alpha}_{\mathrm{em}}$, $\boldsymbol{\alpha}_{\mathrm{me}}$, and $\boldsymbol{\alpha}_{\mathrm{mm}}$. These are computed with TD-DFT as sketched below. $\boldsymbol{E}(\omega)$ and $\boldsymbol{H}(\omega)$ are the fields of the electromagnetic wave.

Neglecting nonlinear electromagnetic coupling and magnetic terms, the nonlinear optical response is represented by the electric dipole moment [100, Eq.(1)]

$$\boldsymbol{p}_{\mathrm{NL,e}}(\omega_\gamma) = \frac{1}{2}\sum_{i,j,k} \hat{\boldsymbol{e}}_i \beta_{ijk}(\omega_\gamma, \omega_\alpha, \omega_\delta) E_j(\omega_\alpha) E_k(\omega_\delta)\,, \tag{4.12}$$

$\boldsymbol{\beta}(\omega_\gamma, \omega_\alpha, \omega_\delta)$ is the first hyperpolarizability, with $\omega_\gamma = \omega_\alpha + \omega_\delta$. For SHG, we have $\omega_\alpha = \omega_\delta$. $\hat{\boldsymbol{e}}_i$ is a unit vector.

In the following, we sketch the calculation of the polarizability tensors. The idea is to introduce a perturbation term to the Hamilton operator and compute transition dipole moments. In combination with the (unperturbed) Kohn-Sham equations, the coupled-perturbed Kohn-Sham equations follow. From these, the polarizability tensors are obtained. We start by considering the linear optical response of the system to a time-dependent electric field $\tilde{\boldsymbol{E}}(t)$ of an electromagnetic wave. The Hamilton operator of the perturbed system is

$$\hat{H}(t) = \hat{H}_0 + \hat{V}_{\mathrm{e}}(t)\,, \tag{4.13}$$

where $\hat{H}_0$ is the Hamilton operator of the unperturbed system and $\hat{V}_\mathrm{e}(t) = -\hat{\boldsymbol{\mu}}_\mathrm{e} \cdot \tilde{\boldsymbol{E}}(t)$ is the perturbation with the electric dipole moment operator $\hat{\boldsymbol{\mu}}_\mathrm{e}$ [63, Eq. (3.2.3)]. With the magnetic dipole moment operator $\hat{\boldsymbol{\mu}}_\mathrm{m}$, one can write, correspondingly, $\hat{V}_\mathrm{m}(t) = -\hat{\boldsymbol{\mu}}_\mathrm{m} \cdot \tilde{\boldsymbol{H}}(t)$ for the perturbation due to a time-dependent magnetic field $\tilde{\boldsymbol{H}}(t)$. With the definition of the electric $\hat{\boldsymbol{\mu}}_\mathrm{e}$ and magnetic dipole $\hat{\boldsymbol{\mu}}_\mathrm{m}$ operators, based on Eqs. (2.37) and (2.47), one can derive their corresponding transition dipole moments, [P4, Eq. (9), Eq. (10)]

$$p^\mathrm{e}_{pq} = q^{\mathrm{e}*}_{pq} = \langle \psi_p | \boldsymbol{r} | \psi^*_q \rangle \,, \tag{4.14}$$

$$p^\mathrm{m}_{pq} = q^{\mathrm{m}*}_{pq} = \frac{\mathrm{i}}{2c_0} \langle \psi_p | (\boldsymbol{r} - \boldsymbol{R}) \times \boldsymbol{\nabla} | \psi^*_q \rangle \,, \tag{4.15}$$

which are collected in the vectors $\boldsymbol{p}^\nu$ and $\boldsymbol{q}^\nu$, representing the external electric or magnetic dipolar fields, with $\nu \in \{\mathrm{e}, \mathrm{m}\}$. ψ_p and ψ_q are the Kohn-Sham eigenstates of the ground state.

With the Hamilton operator of the perturbed system at hand, the coupled-perturbed Kohn-Sham (CPKS) equations can be derived from the Kohn-Sham equations of the unperturbed system in Eq. (4.5), see [101]. The linear optical response to a time-dependent perturbation of the system by the electromagnetic wave is described with the CPKS equations that read as [102, Eq. (13)], [101, Eq. (25)], [103, Eq. (1)], [P4, Eq. (7)],

$$|\boldsymbol{x}^\nu(\omega), \boldsymbol{y}^\nu(\omega)\rangle = -(\boldsymbol{\Lambda}(\omega) - \omega\boldsymbol{\Delta})^{-1} |\boldsymbol{p}^\nu, \boldsymbol{q}^\nu\rangle \,, \tag{4.16}$$

with the frequency ω of the perturbation. $\boldsymbol{\Lambda}(\omega)$ and $\boldsymbol{\Delta}$ are 2×2 supermatrices,

$$\boldsymbol{\Delta} = \begin{pmatrix} \mathbb{1} & 0 \\ 0 & -\mathbb{1} \end{pmatrix} , \qquad \boldsymbol{\Lambda}(\omega) = \begin{pmatrix} \mathbf{A}(\omega) & \mathbf{B}(\omega) \\ \mathbf{B}^*(\omega) & \mathbf{A}^*(\omega) \end{pmatrix} . \tag{4.17}$$

Here, $\mathbf{A}(\omega)$ and $\mathbf{B}(\omega)$ are coupling matrices, forming the Hessian of the Kohn-Sham matrix [102, 104]. The terms for $\mathbf{A}(\omega)$ and $\mathbf{B}(\omega)$ for an electromagnetic wave as perturbation can be found in [101, Eq.(27)], [103, Eqs.(2), (3)], [105, Eqs.(17a), (17b)], and [P4, Eqs. (11), (12)]. $\boldsymbol{x}^\nu(\omega)$ and $\boldsymbol{y}^\nu(\omega)$ are perturbation coefficients that represent the response of the ground-state density of the molecular orbitals ψ_i to the perturbation denoted by ν [P4, 101].

Having solved the CPKS equations, one can use $\boldsymbol{x}^\nu(\omega)$ and $\boldsymbol{y}^\nu(\omega)$ to compute the polarizability tensor [101, Eq.(31)], [P4, Eq. (17)]

$$\boldsymbol{\alpha}_{\nu\nu'}(\omega) = \langle \boldsymbol{p}^\nu, \boldsymbol{q}^\nu | (\boldsymbol{\Lambda}(\omega) - \omega\boldsymbol{\Delta})^{-1} | \boldsymbol{p}^{\nu'}, \boldsymbol{q}^{\nu'} \rangle = \langle \boldsymbol{x}^\nu(\omega), \boldsymbol{y}^\nu(\omega) | \boldsymbol{p}^{\nu'}, \boldsymbol{q}^{\nu'} \rangle \,. \tag{4.18}$$

For a single frequency, three equations have to be solved for each $\boldsymbol{\alpha}_{\nu\nu'}(\omega)$, due to the three Cartesian axes. The frequency ω is in general complex, representing the finite lifetime of the excited states [P4]. With Eq. (3.17), one can derive the dipolar T-matrix from the polarizability tensor.

We move on to the nonlinear optical response. In comparison to the calculation of the polarizability tensors, we extend the analysis to a second-order response equation. From this equation, the hyperpolarizability tensor is obtained. For better readability, the superscripts α, δ, and γ refer in the following to the frequencies ω_α, ω_β, and ω_γ as arguments. To obtain the electric hyperpolarizability tensor, which relates the product of two electric field components to the electric dipole moment, see Eq. (4.12), we consider the second-order response equation [101, Eq. (43)], [105, Eq. (27)]

$$|\boldsymbol{x}^{(\alpha\delta)}, \boldsymbol{y}^{(\alpha\delta)}\rangle = (\boldsymbol{\Lambda}^\gamma - (\omega_\alpha + \omega_\delta)\boldsymbol{\Delta})^{-1} \, |\boldsymbol{p}^{(\alpha\delta)}, \boldsymbol{q}^{(\alpha\delta)}\rangle \,. \tag{4.19}$$

The expressions for the external fields $\boldsymbol{p}^{(\alpha\delta)}$ and $\boldsymbol{q}^{(\alpha\delta)}$ can be found in [101, Eq. (39)] and [105, Eqs. (28a), (28b)]. Having solved Eq. (4.19), we obtain the electric hyperpolarizability [101, Eq. (43)], [105, Eq. (22)]

$$\beta^{\gamma\alpha\delta} = \mathrm{Tr}\left(\hat{v}^{(\gamma)} K^{(\alpha\delta)}\right) + \langle \boldsymbol{p}^{\gamma}, \boldsymbol{q}^{\gamma} | \boldsymbol{x}^{(\alpha\delta)}, \boldsymbol{y}^{(\alpha\delta)} \rangle \,, \tag{4.20}$$

with the unrelaxed density matrices [101, Eq. (38)], [105, Eq. (24a), (24b)]

$$K_{ij}^{(\alpha\delta)} = -\sum_{a} \left(x_{ja}^{(\alpha)} y_{ia}^{(\delta)} + y_{ia}^{(\alpha)} x_{ja}^{(\delta)} \right) \tag{4.21}$$

and

$$K_{ab}^{(\alpha\delta)} = \sum_{i} \left(y_{ib}^{(\alpha)} x_{ia}^{(\delta)} + x_{ia}^{(\alpha)} y_{ib}^{(\delta)} \right) \,. \tag{4.22}$$

Here, the first order quantities $\boldsymbol{x}^{\alpha}$, $\boldsymbol{y}^{\alpha}$, $\boldsymbol{p}^{\gamma}$, and $\boldsymbol{q}^{\gamma}$, and the solution vectors $\boldsymbol{x}^{(\alpha\delta)}$, $\boldsymbol{y}^{(\alpha\delta)}$ of Eq. (4.19) occur. The indices i and a refer to occupied and virtual orbitals. $\hat{v}^{(\gamma)}$ is the time-independent coefficient of the time-dependent external potential $\hat{v}(t) = \sum_{\gamma} \hat{v}^{(\gamma)} \mathrm{e}^{-\mathrm{i}\omega_{\gamma} t} + \hat{v}^{(-\gamma)} \mathrm{e}^{\mathrm{i}\omega_{\gamma} t}$ [105, Eq. (4)].

In Chapter 7, we will introduce an object termed "Hyper-T-matrix". The Hyper-T-matrix can be directly calculated from the first hyperpolarizability tensor, similar to the T-matrix which can be computed from the polarizability tensor.

In this chapter, the basic principles of (TD-)DFT were summarized. The principle of the computation of polarizability tensors and first hyperpolarizability tensors with TD-DFT was introduced. These are used to compute T-matrices and Hyper-T-matrices of molecules which are considered in this thesis to design and analyze photonic devices. The latter are used to discuss linear and nonlinear optical effects of molecules. Note that starting at Eq. (4.13), only electronic transitions are discussed. To include vibrational transitions to the dipolar polarizabilities, see [106].

In the next chapter, we discuss a homogenization approach for materials consisting of a three-dimensional periodic arrangement of scatterers based on their T-matrix. We use this homogenization procedure mainly to obtain effective material parameters of molecular materials. The T-matrix of the underlying finite-size molecular models is computed with the methods presented in Chapter 4.

5 | Homogenization Approach Based on the Effective T-matrix

The homogenization of an arrangement of discrete scatterers has been of interest for many decades to obtain effective material parameters [107–135]. This is because with the effective material parameters of a material at hand, the computation of the optical response of a system consisting of this material is considerably simplified. A typical homogenization theory is that of Clausius-Mosotti [61], Bruggeman [136], or Maxwell-Garnett [113].

By homogenizing a lattice of discrete scatterers, one aims at replacing the discrete granular material by a homogeneous medium characterized by effective material parameters that appear in a constitutive relation supposedly representing the material. Combining the effective material parameters via the constitutive relations with specific interface conditions, one can compute the optical response of an arbitrarily shaped object consisting of the homogenized material. Homogenization is an essential tool to analyze and design photonic devices consisting of molecular materials. For macroscopic objects, which consist of molecular materials and are more complicated than films, the effective parameters of the molecular materials can be used to compute their optical response. An instance are cylinders consisting of a chiral molecular material, which we consider in Chapter 6.

There is a very important requirement for the computation of the optical response of an arbitrarily shaped object consisting of a homogenized material: The effective material parameters are not allowed to depend on the direction of the wave vector of the incident wave, but only on its absolute value [P5]. If the effective material parameters depend on the propagation of the incident wave, it would not be clear which material parameters determined the scattering of light off an object which is more complicated than a planar slab [P5].

Other restrictions to various homogenization approaches, such as the Clausius-Mosotti theory [114], are the assumptions of small inclusion volumes and small lattice constants in comparison to the wavelength of light. In this context, higher multipoles of the scattering objects are neglected, and the lattice interaction of the scatterers is only computed in the long wavelength limit.

We discuss in this chapter a homogenization approach which is based on the effective T-matrix of the considered three-dimensional lattice of scatterers. The effective T-matrix and the homogenization approach are discussed in [P5].

The effective T-matrix describes the scattering off an object inside the lattice. In the context of the discussed transition from the microscopic to the macroscopic description of electromagnetics in Subsection 2.2.2, the effective T-matrix enables the computation of an effective polarization of the lattice of scatterers. It takes into account the exact multi-scattering between the scatterers inside the lattice without long wavelength approximations. Additionally, the effective T-matrix is independent of the Bloch phase so that the effective material parameters, obtained from the effective T-matrix, can be used to describe the optical response of objects illuminated by plane waves with different propagation directions.

In Chapters 6 and 7, we use the effective T-matrix based homogenization approach presented in [P5] to compute the effective material parameters of molecular materials. With

these effective material parameters at hand, one can design more complicated structures than planar films. Such structures are metasurfaces of molecular materials, for instance. The concept of the effective T-matrix and the homogenization approach have been developed in cooperation with Ramakrishna Venkitakrishnan, Dominik Beutel, and Ivan Fernandez-Corbaton. The DFT computations, used to homogenize molecular materials, have been prepared and performed by Marjan Krstić and Christof Holzer. The optical simulations have been performed by the author.

The chapter is structured as follows. Section 5.1 discusses the effective T-matrix and its properties and presents the derivation of the material parameters in terms of the effective T-matrix. Section 5.2 explains the workflow of the homogenization approach. Sections 5.3 and 5.4 demonstrate the homogenization approach with the instances of a molecular material and two metamaterials, respectively.

5.1. Definition of the Effective T-matrix and Derivation of Effective Material Parameters

The effective T-matrix of a three-dimensional lattice of scatterers is the central object of the presented homogenization approach. We see below that it incorporates the complete multipolar lattice interaction of the scatterers and enables the computation of effective polarizations, representing the effective optical response of the material. From these macroscopic polarizations, we derive effective material parameters. We emphasize that in contrast to other approaches used to homogenize metamaterials, we do not use any fitting techniques in the homogenization procedure. We express the effective material properties explicitly once the T-matrix of the unit cell is obtained and the lattice is defined for its arrangement.

In the following, we start by deriving the effective T-matrix which does not depend on the Bloch phase. This guarantees that we can use the effective material parameters, obtained from the effective T-matrix, for computing the optical response of objects illuminated by different plane waves.

5.1.1. Definition of the Effective T-matrix

In Eq. (3.22), we define the expansion coefficients of the totally scattered field of an object at the origin of a two-dimensional lattice. The matrix relating the incident field coefficients to the totally scattered field coefficients can be considered as a renormalized T-matrix [78]. Equivalently to the two-dimensional lattice discussed in [78], we define a renormalized T-matrix of the three-dimensional lattice as [P5, Eq. (1)]

$$\tilde{\mathbf{T}}_{\mathrm{ren,Hel}}(\boldsymbol{k}) = \left(\mathbb{1} - \mathbf{T}_{\mathrm{Hel}} \sum_{\boldsymbol{R}\neq 0} \mathbf{C}^{(3)}(-\boldsymbol{R}) \mathrm{e}^{\mathrm{i}\boldsymbol{k}\cdot\boldsymbol{R}} \right)^{-1} \mathbf{T}_{\mathrm{Hel}} \,. \tag{5.1}$$

Here, we consider a three-dimensional lattice of identical scatterers represented by their T-matrix $\mathbf{T}_{\mathrm{Hel}}$, which are placed at lattice sites $\boldsymbol{R}$. The lattice sum in Eq. (5.1) can be computed with *treams* [52, 53]. The scalar product of the Bloch wave vector $\boldsymbol{k}$ and the lattice sites $\boldsymbol{R}$ defines the Bloch phase. As in Eq. 3.21, $\mathbf{C}^{(3)}(-\boldsymbol{R})$ is a matrix consisting of translation addition coefficients to transform scattered field coefficients from one particle into incident field coefficients on another particle. While $\tilde{\mathbf{T}}_{\mathrm{ren,Hel}}(\boldsymbol{k})$ can be used to compute the response of the three-dimensional lattice with respect to a specific plane wave with wave vector $\boldsymbol{k}$, it

is not suitable to compute effective material parameters. This is because the matrix depends on the Bloch wave vector. In [P5], two methods are presented to obtain an effective T-matrix, which does not depend on the Bloch wave vector.

The first method is based on the computation of the T-matrix with the finite-element method from [82]. The idea behind the method is that first, the scattering solutions are found for a sufficiently large set of incident plane waves considering their own renormalized T-matrices $\tilde{\mathbf{T}}_{\mathrm{ren,Hel}}(\boldsymbol{k})$, and then these solutions are inversely used to obtain an effective T-matrix, which does not depend on the Bloch wave vector. Note that we operate in the following in the basis of well-defined helicity. We compute the scattering coefficients [P5, Eq. (2)]

$$\tilde{\boldsymbol{d}}_{\lambda}^{\boldsymbol{k}} = \tilde{\mathbf{T}}_{\mathrm{ren,Hel}}(\boldsymbol{k})\boldsymbol{b}_{\lambda}^{\boldsymbol{k}} \tag{5.2}$$

for a finite number $2K$ of incident plane waves with wave vector $\boldsymbol{k}$, helicity $\lambda = \pm 1$, and multipolar expansion coefficients $\boldsymbol{b}_{\lambda}^{\boldsymbol{k}}$. Note that we select K different wave vectors and use every wave vector twice due to the two different helicities. Then, we define the Bloch wave vector independent effective T-matrix $\mathbf{T}_{\mathrm{eff,Hel}}$ as [P5, Eq. (3)]

$$(\tilde{\boldsymbol{d}}_{\lambda=1}^{\boldsymbol{k}_1}, \tilde{\boldsymbol{d}}_{\lambda=-1}^{\boldsymbol{k}_1}, \ldots, \tilde{\boldsymbol{d}}_{\lambda=1}^{\boldsymbol{k}_K}, \tilde{\boldsymbol{d}}_{\lambda=-1}^{\boldsymbol{k}_K}) = \mathbf{T}_{\mathrm{eff,Hel}}(\boldsymbol{b}_{\lambda=1}^{\boldsymbol{k}_1}, \boldsymbol{b}_{\lambda=-1}^{\boldsymbol{k}_1}, \ldots, \boldsymbol{b}_{\lambda=1}^{\boldsymbol{k}_K}, \boldsymbol{b}_{\lambda=-1}^{\boldsymbol{k}_K}), \tag{5.3}$$

so that $\mathbf{T}_{\mathrm{eff,Hel}}$ responds to an incident plane wave with wave vector $\boldsymbol{k}$ in the same way as $\tilde{\mathbf{T}}_{\mathrm{ren,Hel}}(\boldsymbol{k})$. In contrast to $\tilde{\mathbf{T}}_{\mathrm{ren,Hel}}(\boldsymbol{k})$, the matrix $\mathbf{T}_{\mathrm{eff,Hel}}$ satisfies this effect for all incident plane waves simultaneously. By solving Eq. (5.3), the effective T-matrix is obtained. Note that the total number of incident plane waves $2K$ has to be sufficiently larger than the rank of the effective T-matrix [82].

The second method represents a rigorous derivation of the effective T-matrix. We define an operator $\hat{\tilde{\mathbf{T}}}_{\mathrm{ren,Hel}}(\hat{\boldsymbol{k}})$ for the renormalized T-matrix [P5, Eq. (7)],

$$\hat{\tilde{\mathbf{T}}}_{\mathrm{ren,Hel}}(\hat{\boldsymbol{k}})|\hat{\boldsymbol{k}}, \lambda\rangle = \sum_{\tilde{l},\tilde{m},\tilde{\lambda}} \tilde{d}_{\tilde{l},\tilde{m},\tilde{\lambda}}(\hat{\boldsymbol{k}}, \lambda)|\tilde{l}, \tilde{m}, \tilde{\lambda}\rangle\,. \tag{5.4}$$

Here $\hat{\boldsymbol{k}}$ is the direction of the Bloch wave vector, and k its absolute value, $\boldsymbol{k} = k\hat{\boldsymbol{k}}$. The incident plane wave with propagation direction $\hat{\boldsymbol{k}}$ and helicity $\lambda = \pm 1$ is here represented by $|\hat{\boldsymbol{k}}, \lambda\rangle$. $|\tilde{l}, \tilde{m}, \tilde{\lambda}\rangle$ are specific vector spherical waves of the wave scattered into the far-field. $\tilde{d}_{\tilde{l},\tilde{m},\tilde{\lambda}}(\hat{\boldsymbol{k}}, \lambda)$ are the corresponding expansion coefficients.

We expand the incident vector spherical waves in plane waves according to [P5, Eq. (8)]

$$|l, m, \lambda\rangle = \int \mathrm{d}\hat{\boldsymbol{k}}\xi_{l,m,\lambda}(\hat{\boldsymbol{k}})|\hat{\boldsymbol{k}}, \lambda\rangle = \int_0^{\pi} \mathrm{d}\theta_{\hat{\boldsymbol{k}}} \sin\theta_{\hat{\boldsymbol{k}}} \int_{-\pi}^{\pi} \mathrm{d}\varphi_{\hat{\boldsymbol{k}}}\xi_{l,m,\lambda}(\hat{\boldsymbol{k}})|\hat{\boldsymbol{k}}, \lambda\rangle\,, \tag{5.5}$$

with $\theta_{\hat{\boldsymbol{k}}} = \arccos k_{\mathrm{z}}/k$ and $\varphi_{\hat{\boldsymbol{k}}} = \arctan k_{\mathrm{y}}/k_{\mathrm{x}}$. Based on [94, Eqs. (37a) and (37b)] and [51, Eq. (S3c)], the plane wave expansion coefficients for Bessel functions are [P5, Eq. (9)]

$$\xi_{l,m,\lambda}(\hat{\boldsymbol{k}}) = \frac{\gamma_{l,m}}{4\pi \mathrm{i}^{l+1}} \left(\frac{m}{\sin\theta_{\hat{\boldsymbol{k}}}} P_m^l(\cos\theta_{\hat{\boldsymbol{k}}}) + \lambda \frac{\partial}{\partial\theta_{\hat{\boldsymbol{k}}}} P_m^l(\cos\theta_{\hat{\boldsymbol{k}}}) \right) \mathrm{e}^{\mathrm{i}m\varphi_{\hat{\boldsymbol{k}}}}\,. \tag{5.6}$$

In Eq. (5.6), we have [51, Eq. (S3d)]

$$\gamma_{l,m} = \mathrm{i}\sqrt{\frac{2l+1}{4\pi} \frac{(l-m)!}{l(l+1)(l+m)!}} \tag{5.7}$$

and the associated Legendre polynomials $P_m^l(\cos\theta_{\hat{\boldsymbol{k}}})$.

We define an element of the direction independent effective T-matrix as $\langle\bar{\lambda},\bar{m},\bar{l}|\hat{\mathbf{T}}_{\mathrm{eff,Hel}}|l,m,\lambda\rangle$. With Eq. (5.5) and the requirement that $\hat{\mathbf{T}}_{\mathrm{eff,Hel}}$ responds in the same way as $\hat{\tilde{\mathbf{T}}}_{\mathrm{ren,Hel}}(\boldsymbol{k})$ to a plane wave with wave vector $\boldsymbol{k}$, the identity

$$\langle\bar{\lambda},\bar{m},\bar{l}|\hat{\mathbf{T}}_{\mathrm{eff,Hel}}|l,m,\lambda\rangle = \int \mathrm{d}\hat{\boldsymbol{k}}\xi_{l,m,\lambda}(\hat{\boldsymbol{k}})\langle\bar{\lambda},\bar{m},\bar{l}|\hat{\tilde{\mathbf{T}}}_{\mathrm{ren,Hel}}(\hat{\boldsymbol{k}})|\hat{\boldsymbol{k}},\lambda\rangle \tag{5.8}$$

follows. With Eq. (5.4), we have [P5, Eq. (11)]

$$\begin{aligned}\langle\bar{\lambda},\bar{m},\bar{l}|\hat{\mathbf{T}}_{\mathrm{eff,Hel}}|l,m,\lambda\rangle &= \sum_{\tilde{l},\tilde{m},\tilde{\lambda}}\int_0^{\pi}\mathrm{d}\theta_{\hat{\boldsymbol{k}}}\sin\theta_{\hat{\boldsymbol{k}}}\int_{-\pi}^{\pi}\mathrm{d}\varphi_{\hat{\boldsymbol{k}}}\xi_{l,m,\lambda}(\hat{\boldsymbol{k}})\tilde{d}_{\tilde{l},\tilde{m},\tilde{\lambda}}(\hat{\boldsymbol{k}},\lambda)\langle\bar{\lambda},\bar{m},\bar{l}|\tilde{l},\tilde{m},\tilde{\lambda}\rangle \\ &= \int_0^{\pi}\mathrm{d}\theta_{\hat{\boldsymbol{k}}}\sin\theta_{\hat{\boldsymbol{k}}}\int_{-\pi}^{\pi}\mathrm{d}\varphi_{\hat{\boldsymbol{k}}}\xi_{l,m,\lambda}(\hat{\boldsymbol{k}})\tilde{d}_{\bar{l},\bar{m},\bar{\lambda}}(\hat{\boldsymbol{k}},\lambda)\,,\end{aligned} \tag{5.9}$$

which follows from $\langle\bar{\lambda},\bar{m},\bar{l}|\tilde{l},\tilde{m},\tilde{\lambda}\rangle = \delta_{\bar{l},\tilde{l}}\delta_{\bar{m},\tilde{m}}\delta_{\bar{\lambda},\tilde{\lambda}}$. To compute the Bloch wave vector independent effective T-matrix with Eq. (5.9), $\tilde{d}_{\bar{l},\bar{m},\bar{\lambda}}(\hat{\boldsymbol{k}},\lambda)$ is obtained for a finite but yet sufficiently large number of propagation directions with Eq. (5.4). The wave vectors for the specific directions in both procedures are computed with a method from [137]. They correspond to evenly spaced points on the surface of a sphere. Due to this fact, the last integral in Eq. (5.9) can be evaluated as a Riemann sum of equally weighted terms.

We use the first method to obtain the direction independent effective T-matrix for all instances in this thesis. In Section 5.4, we show for a specific structure that both methods lead to effective T-matrices whose difference is negligible.

The effective T-matrix incorporates all multipolar lattice interactions between the scatterers and is, therefore, most suitable for a homogenization approach. We note that the effective T-matrix is, in principle, valid for all multipolar orders which are also used for the T-matrix of the single scatterer. The effective material parameters that we consider here are, however, only computed from the dipolar part of the effective T-matrix. They incorporate the coupling of dipoles to all higher order multipoles, but not the quadrupole-quadrupole coupling, for instance.

5.1.2. Derivation of Effective Material Parameters

In the following, we derive effective material parameters in terms of the effective T-matrix of a three-dimensional lattice of scatterers. The effective material parameters, which are computed from the dipolar part of the effective T-matrix, are the tensorial effective electric permittivity $\boldsymbol{\varepsilon}_{\mathrm{eff}}(\boldsymbol{r},\omega) = \varepsilon_0\boldsymbol{\varepsilon}_{\mathrm{r,eff}}(\boldsymbol{r},\omega)$, the effective magnetic permeability $\boldsymbol{\mu}_{\mathrm{eff}}(\boldsymbol{r},\omega) = \mu_0\boldsymbol{\mu}_{\mathrm{r,eff}}(\boldsymbol{r},\omega)$, and the effective chirality $\boldsymbol{\kappa}_{\mathrm{eff}}(\boldsymbol{r},\omega)$. $\boldsymbol{\varepsilon}_{\mathrm{r,eff}}(\boldsymbol{r},\omega)$ and $\boldsymbol{\mu}_{\mathrm{r,eff}}(\boldsymbol{r},\omega)$ are the relative permittivity and permeability, respectively. These material parameters are commonly also called local material parameters as they relate fields at a point $\boldsymbol{r}$ to fields at the same point $\boldsymbol{r}$. For non-local material parameters, which relate fields at different points to each other, we refer to [67, 125], for instance. As the effective material parameters represent homogeneous media, we omit $\boldsymbol{r}$ as argument in the following.

The derivation is based on the macroscopic effective polarization of the three-dimensional lattice, which can be directly obtained from the effective T-matrix. Similar to Subsection 2.2.2, we find, therefore, a transition from the optical response of a microscopic scatterer to the optical response of the macroscopic material. The scatterers are placed in an

achiral host medium with permittivity ε_h, magnetic permeability μ_0, and wave impedance $Z_\mathrm{h} = \sqrt{\mu_0/\varepsilon_\mathrm{h}}$. The speed of light is $c_\mathrm{h} = 1/\sqrt{\varepsilon_\mathrm{h}\mu_0}$, and the wave number is $k_\mathrm{h} = \omega\sqrt{\varepsilon_\mathrm{h}\mu_0}$. We start at the anisotropic and chiral constitutive relations from Eq. (2.8), relating the monochromatic fields

$$\begin{pmatrix} \boldsymbol{D}(\omega) \\ \boldsymbol{B}(\omega) \end{pmatrix} = \begin{pmatrix} \boldsymbol{\varepsilon}_\mathrm{eff}(\omega) & \mathrm{i}\boldsymbol{\kappa}_\mathrm{eff}(\omega)\sqrt{\varepsilon_0\mu_0} \\ -\mathrm{i}\boldsymbol{\kappa}_\mathrm{eff}^\mathrm{T}(\omega)\sqrt{\varepsilon_0\mu_0} & \boldsymbol{\mu}_\mathrm{eff}(\omega) \end{pmatrix} \begin{pmatrix} \boldsymbol{E}_\mathrm{int}(\omega) \\ \boldsymbol{H}_\mathrm{int}(\omega) \end{pmatrix} . \tag{5.10}$$

We introduced the relation between the displacement field and the magnetic flux density on the one hand and the polarizations of a macroscopic medium on the other hand in Eqs. (2.44) and (2.49). Now, we relate $\boldsymbol{D}(\omega)$ and $\boldsymbol{B}(\omega)$ to the effective electric polarization $\boldsymbol{P}_\mathrm{eff,e}(\omega)$ and the effective magnetic polarization $\boldsymbol{P}_\mathrm{eff,m}(\omega)$ of the lattice via [P5, Eq. (16)]

$$\begin{pmatrix} \boldsymbol{D}(\omega) \\ \boldsymbol{B}(\omega) \end{pmatrix} = \begin{pmatrix} \varepsilon_\mathrm{h}\mathbb{1}_3 & 0 \\ 0 & \mu_0\mathbb{1}_3 \end{pmatrix} \begin{pmatrix} \boldsymbol{E}_\mathrm{int}(\omega) \\ \boldsymbol{H}_\mathrm{int}(\omega) \end{pmatrix} + \begin{pmatrix} \boldsymbol{P}_\mathrm{eff,e}(\omega) \\ \boldsymbol{P}_\mathrm{eff,m}(\omega) \end{pmatrix} . \tag{5.11}$$

The effective polarizations of the lattice can be directly expressed through the dipolar part of the effective T-matrix $\mathbf{T}_\mathrm{eff,Cart}^{l,l'=1,1}$ of a scatterer in the parity basis and in Cartesian coordinates. Equivalently to Eq. (3.17), the effective T-matrix is transferred from the spherical to the Cartesian basis with the matrix $\mathbf{C}$ from Eq. (3.18). The effective T-matrix describes that the effective polarizations are induced by the externally applied electric $\boldsymbol{E}_\mathrm{ext}(\omega)$ and magnetic fields $\boldsymbol{H}_\mathrm{ext}(\omega)$ [P5, Eq. (12)]:

$$\begin{pmatrix} \boldsymbol{P}_\mathrm{eff,e}(\omega) \\ \boldsymbol{P}_\mathrm{eff,m}(\omega) \end{pmatrix} = nq \begin{pmatrix} \mathbf{T}_\mathrm{eff,NN,Cart}^{l,l'=1,1} & \mathrm{i}Z_\mathrm{h}\mathbf{T}_\mathrm{eff,NM,Cart}^{l,l'=1,1} \\ -\mathrm{i}Z_\mathrm{h}\mathbf{T}_\mathrm{eff,MN,Cart}^{l,l'=1,1} & Z_\mathrm{h}^2\mathbf{T}_\mathrm{eff,MM,Cart}^{l,l'=1,1} \end{pmatrix} \begin{pmatrix} \boldsymbol{E}_\mathrm{ext}(\omega) \\ \boldsymbol{H}_\mathrm{ext}(\omega) \end{pmatrix} . \tag{5.12}$$

In Eq. (5.12), n is the concentration of the scatterers per unit cell and $q = \frac{-\mathrm{i}6\pi}{c_\mathrm{h}Z_\mathrm{h}k_\mathrm{h}^3}$, see [59, Eq. (S15)].

Inside a unit volume of the homogenized material, the fields are not equal to the externally applied fields, as the material responds to them with depolarization fields given by the depolarization matrix $\mathbf{L}$ and the effective polarizations. The internal fields are [P5, Eq. (14)]

$$\begin{pmatrix} \boldsymbol{E}_\mathrm{int}(\omega) \\ \boldsymbol{H}_\mathrm{int}(\omega) \end{pmatrix} = \begin{pmatrix} \boldsymbol{E}_\mathrm{ext}(\omega) \\ \boldsymbol{H}_\mathrm{ext}(\omega) \end{pmatrix} - \begin{pmatrix} \frac{1}{\varepsilon_\mathrm{h}}\mathbf{L} & 0 \\ 0 & \frac{1}{\mu_0}\mathbf{L} \end{pmatrix} \begin{pmatrix} \boldsymbol{P}_\mathrm{eff,e}(\omega) \\ \boldsymbol{P}_\mathrm{eff,m}(\omega) \end{pmatrix} . \tag{5.13}$$

For a cubic unit volume, we have $\mathbf{L} = 1/3\mathbb{1}_3$, for cuboids one can find a formula for $\mathbf{L}$ in [138, 139]. We rewrite Eq. (5.13) to obtain

$$\begin{pmatrix} \boldsymbol{E}_\mathrm{ext}(\omega) \\ \boldsymbol{H}_\mathrm{ext}(\omega) \end{pmatrix} = \begin{pmatrix} \boldsymbol{E}_\mathrm{int}(\omega) \\ \boldsymbol{H}_\mathrm{int}(\omega) \end{pmatrix} + \begin{pmatrix} \frac{1}{\varepsilon_\mathrm{h}}\mathbf{L} & 0 \\ 0 & \frac{1}{\mu_0}\mathbf{L} \end{pmatrix} \begin{pmatrix} \boldsymbol{P}_\mathrm{eff,e}(\omega) \\ \boldsymbol{P}_\mathrm{eff,m}(\omega) \end{pmatrix} , \tag{5.14}$$

so that one can replace the external fields in Eq. (5.12) to derive a relationship between the polarizations and the internal fields,

$$\begin{aligned} \begin{pmatrix} \boldsymbol{P}_\mathrm{eff,e}(\omega) \\ \boldsymbol{P}_\mathrm{eff,m}(\omega) \end{pmatrix} = nq & \begin{pmatrix} \mathbf{T}_\mathrm{eff,NN,Cart}^{l,l'=1,1} & \mathrm{i}Z_\mathrm{h}\mathbf{T}_\mathrm{eff,NM,Cart}^{l,l'=1,1} \\ -\mathrm{i}Z_\mathrm{h}\mathbf{T}_\mathrm{eff,MN,Cart}^{l,l'=1,1} & Z_\mathrm{h}^2\mathbf{T}_\mathrm{eff,MM,Cart}^{l,l'=1,1} \end{pmatrix} \\ & \times \left[\begin{pmatrix} \boldsymbol{E}_\mathrm{int}(\omega) \\ \boldsymbol{H}_\mathrm{int}(\omega) \end{pmatrix} + \begin{pmatrix} \frac{1}{\varepsilon_\mathrm{h}}\mathbf{L} & 0 \\ 0 & \frac{1}{\mu_0}\mathbf{L} \end{pmatrix} \begin{pmatrix} \boldsymbol{P}_\mathrm{eff,e}(\omega) \\ \boldsymbol{P}_\mathrm{eff,m}(\omega) \end{pmatrix} \right] . \end{aligned} \tag{5.15}$$

Equation (5.15) can be rewritten to express the polarizations in terms of the internal fields. Then, the polarizations are inserted into Eq. (5.11). From the comparison with the constitutive relations in Eq. (5.10), we derive the effective material parameters [P5, Eq. (17)]

$$\begin{aligned}
&\begin{pmatrix} \boldsymbol{\varepsilon}_{\text{eff}}(\omega) & \mathrm{i}\boldsymbol{\kappa}_{\text{eff}}(\omega)\sqrt{\varepsilon_0\mu_0} \\ -\mathrm{i}\boldsymbol{\kappa}_{\text{eff}}^{\mathrm{T}}(\omega)\sqrt{\varepsilon_0\mu_0} & \boldsymbol{\mu}_{\text{eff}}(\omega) \end{pmatrix} \\
&= \begin{pmatrix} \varepsilon_{\mathrm{h}}\mathbb{1}_3 & 0 \\ 0 & \mu_0\mathbb{1}_3 \end{pmatrix} + n\left(\mathbb{1}_6 - nq\begin{pmatrix} \frac{1}{\varepsilon_{\mathrm{h}}}\mathbf{T}^{l,l'=1,1}_{\text{eff,NN,Cart}}\mathbf{L} & \mathrm{i}c_{\mathrm{h}}\mathbf{T}^{l,l'=1,1}_{\text{eff,NM,Cart}}\mathbf{L} \\ -\mathrm{i}\frac{Z_{\mathrm{h}}}{\varepsilon_{\mathrm{h}}}\mathbf{T}^{l,l'=1,1}_{\text{eff,MN,Cart}}\mathbf{L} & c_{\mathrm{h}}Z_{\mathrm{h}}\mathbf{T}^{l,l'=1,1}_{\text{eff,MM,Cart}}\mathbf{L} \end{pmatrix}\right)^{-1} \times \\
&\times q\begin{pmatrix} \mathbf{T}^{l,l'=1,1}_{\text{eff,EE,Cart}} & \mathrm{i}Z_{\mathrm{h}}\mathbf{T}^{l,l'=1,1}_{\text{eff,EM,Cart}} \\ -\mathrm{i}Z_{\mathrm{h}}\mathbf{T}^{l,l'=1,1}_{\text{eff,ME,Cart}} & Z_{\mathrm{h}}^2\mathbf{T}^{l,l'=1,1}_{\text{eff,MM,Cart}} \end{pmatrix}.
\end{aligned} \tag{5.16}$$

In comparison to classical theories such as Clausius-Mosotti [61] or Lorentz-Lorenz theory [113], which also have the concept of an effective polarization, the interaction between the scatterers is not introduced via the depolarization tensor, but by the effective T-matrix. The effective T-matrix and effective material parameters derived in this section are at the heart of the homogenization approach that we present in the following.

5.2. Workflow for the Homogenization Approach

In this section, we outline the workflow of the effective T-matrix based homogenization approach depicted in Figure 5.1. We start by computing the T-matrix of the single object, and defining the lattice vectors $\boldsymbol{a}_x$, $\boldsymbol{a}_y$, and $\boldsymbol{a}_z$. For spheres, the T-matrix can be computed with Mie theory. For more complicated structures, one can use the finite-element method (FEM) [82, 83]. For the molecular structures analyzed in this thesis, TD-DFT is used, see Chapter 4.

The next step discusses the essential question, whether the lattice of scatterers is homogenizable. We note that the effective material parameters describing a homogeneous effective medium cannot depend on the Bloch wave vector. The material properties of the medium exist and are independent of the characteristics of a specific field probing for the material properties. If a material shows, for instance, Bragg reflections, the effective material parameters cannot be independent of the propagation direction of the propagating wave. This implies that the material is not homogenizable [140]. Bragg reflections occur as the light explicitly probes the periodicity of the underlying medium that, therefore, cannot be considered as homogeneous. In a homogeneous medium, Bragg reflections do not occur. By considering the band structures $\lambda(k_z)$ or $f(k_z)$ of the lattice of scatterers, one can deduce whether the material is homogenizable in the considered spectral domain [P5, 140]. λ is the wavelength and f is the frequency of the considered light in vacuum. k_z is the effective wave number in the material. In the discussion of band structures, we restrict ourselves to this z-component for the sake of simplicity. In the case of weak anisotropy, this is sufficient. In general, one would have to consider all spatial dimensions.

Bragg reflections occur close to the edge of the Brillouin zone, where the effective propagation constant equals $k_z = \pi/a$ for a cubic lattice. a is the lattice constant of the material. Due to the constructive interference between the waves reflected off consecutive layers of scatterers, broad reflection bands occur when probed with an external field. These are related to regions in the energy band structures in which propagation is not allowed inside the material. For an instance below, we will see that the influence of the Bragg gap is already visible in

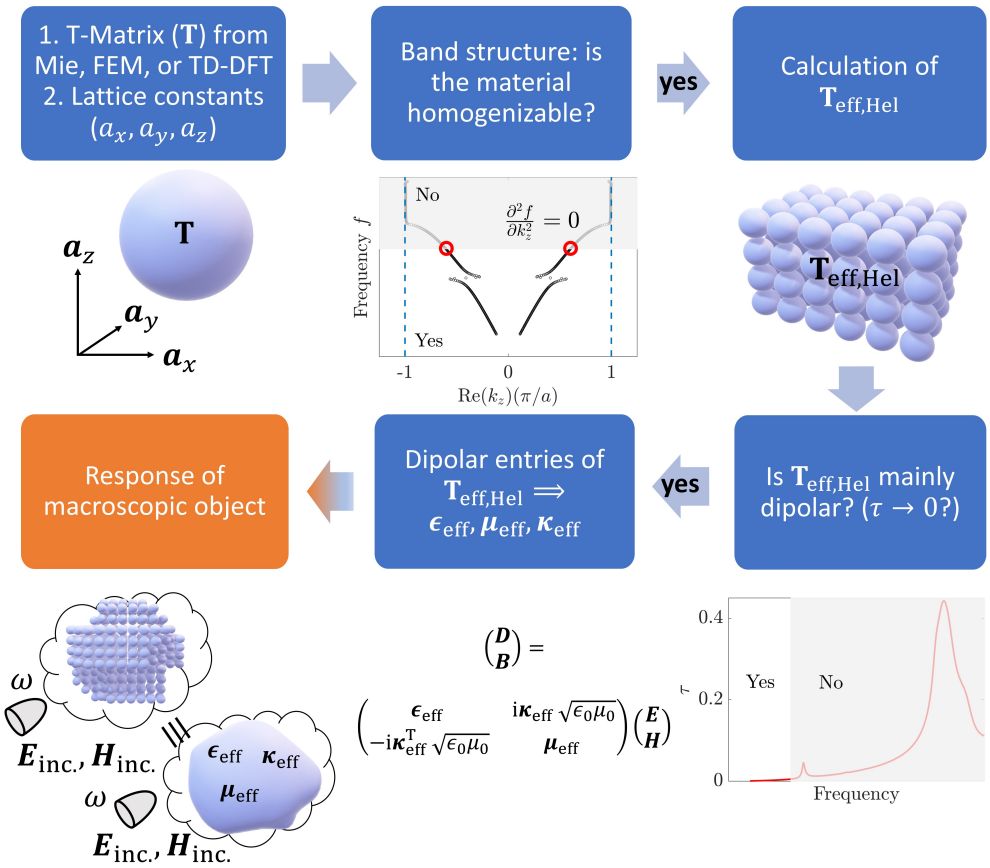

Figure 5.1.: Workflow of the presented homogenization approach starting at computing the T-matrix of the single unit cell and defining the lattice constants of the three-dimensional lattice. The band structure is inspected to decide whether the material is homogenizable. If it is homogenizable, the direction independent effective T-matrix $\mathbf{T}_{\mathrm{eff,Hel}}$ is obtained. If $\mathbf{T}_{\mathrm{eff,Hel}}$ is mainly dipolar, the effective permittivity $\boldsymbol{\varepsilon}_{\mathrm{eff}}$, permeability $\boldsymbol{\mu}_{\mathrm{eff}}$, and chirality $\boldsymbol{\kappa}_{\mathrm{eff}}$ are computed from its dipolar part in the parity basis and Cartesian coordinates. These quantities can be used in a finite-element method based solver, for instance, to calculate the optical response of an arbitrarily shaped object consisting of the material. Adapted with permission from [P5]. Copyright © 2022 John Wiley and Sons.

the band structure for propagation constants smaller than π/a. This influence manifests in a bending of the dispersion curves.

For the instances and spectral domains which we consider, we analyze whether the band structure becomes $\frac{\mathrm{d}^2 f}{\mathrm{d}k_z^2} = 0$ close to the edge of the Brillouin zone, assuming that there is one material resonance at lower frequencies [P5]. If the band structure does not show such a point close to the edge of the Brillouin zone, we deduce that the material is homogenizable in the considered frequency range. In the frequency range, in which the Bragg effect influences the light propagation, the material is not homogenizable.

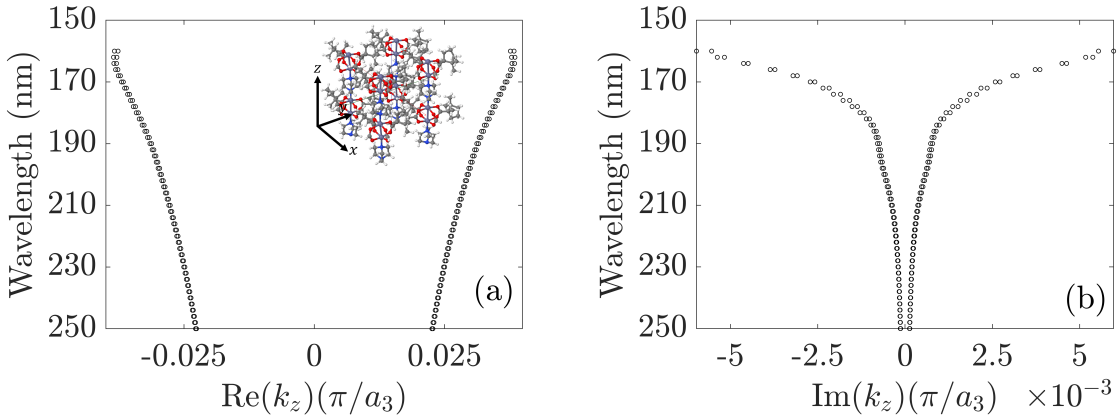

Figure 5.2.: Band structure of a chiral Zn-L-camphoric acid-dabco SURMOF for real **(a)** and imaginary part of the effective propagation constant k_z **(b)**. The band structure is not close to the Brillouin edge. Therefore, the material is homogenizable. The finite-size molecular model of the SURMOF, created by Marjan Krstić, is shown in the inset of **(a)**. Adapted with permission from [P5]. Copyright © 2022 John Wiley and Sons.

We emphasize that to ultimately deduce whether a material is homogenizable, one would have to analyze it in a more complicated way. For our instances, however, the criterion discussed above is sufficient to clarify whether the material is homogenizable.

At smaller frequencies where the material is homogenizable, we continue in the next step by computing the frequency dependent but direction independent effective T-matrix, as described in the previous section. The lattice sum in Eq. (5.1) is computed with *treams* [52, 53]. It was mentioned above that only effective material parameters are considered which are computed from the dipolar part of $\mathbf{T}_{\text{eff,Hel}}$. They only describe the optical response of the material sufficiently, if $\mathbf{T}_{\text{eff,Hel}}$ is mainly dipolar, i.e. higher multipolar orders are negligible. To check this for a given material, we construct an object $\mathbf{T}^{\text{dip}}_{\text{eff,Hel}}$ that consists of the effective dipole-dipole part of $\mathbf{T}_{\text{eff,Hel}}$ and has the same dimensions. Except from the dipole-dipole part, all other entries of $\mathbf{T}^{\text{dip}}_{\text{eff,Hel}}$ are zero. For determining the contribution of higher multipolar orders, we define the quantity [P5, Eq. (6)]

$$\tau\left(\mathbf{T}_{\text{eff,Hel}}\right) = \sqrt{\frac{\operatorname{Tr}\left\{\left(\mathbf{T}^{\text{dip}}_{\text{eff,Hel}} - \mathbf{T}_{\text{eff,Hel}}\right)^{\dagger}\left(\mathbf{T}^{\text{dip}}_{\text{eff,Hel}} - \mathbf{T}_{\text{eff,Hel}}\right)\right\}}{2\left(\operatorname{Tr}\left\{\mathbf{T}^{\text{dip}}_{\text{eff,Hel}}{}^{\dagger}\mathbf{T}^{\text{dip}}_{\text{eff,Hel}}\right\} + \operatorname{Tr}\left\{\mathbf{T}^{\dagger}_{\text{eff,Hel}}\mathbf{T}_{\text{eff,Hel}}\right\}\right)}}\,, \tag{5.17}$$

where $\tau\left(\mathbf{T}_{\text{eff,Hel}}\right) \in [0,1]$. The quantity measures essentially how dipolar the effective T-matrix is. If $\tau\left(\mathbf{T}_{\text{eff,Hel}}\right) = 0$, $\mathbf{T}_{\text{eff,Hel}}$ is purely dipolar. The larger the value is, the stronger the impact of higher-order multipolar components in the effective T-matrix. In case $\tau\left(\mathbf{T}_{\text{eff,Hel}}\right)$ is sufficiently close to zero, $\boldsymbol{\varepsilon}_{\text{eff}}(\omega)$, $\boldsymbol{\mu}_{\text{eff}}(\omega)$, and $\boldsymbol{\kappa}_{\text{eff}}(\omega)$ are computed. The latter quantity is only non-zero, if the material is chiral. These effective material parameters can be used in FEM based program suites such as COMSOL Multiphysics [141] or JCMsuite [142] to compute the optical response of an arbitrarily shaped object. We stress that a strict criterion of what exactly means close to zero cannot be given.

5.3. Homogenization of a Chiral Zn-L-Camphoric Acid-Dabco SURMOF

We demonstrate the presented workflow at the example of the chiral Zn-L-camphoric acid-dabco SURMOF [P5]. A MOF is a crystalline **m**etal-**o**rganic **f**ramework consisting of metal atoms connected to each other by organic linkers. A SURMOF is a **sur**face-mounted (or anchored) MOF. For a more detailed description of MOFs and SURMOFs, their preparation, and their applications, see [143–147], for instance. The SURMOF material is chosen here as an instance for which the homogenization approach is safely applicable and because of its chiral properties. A finite-size molecular model of the Zn-L-camphoric acid-dabco SURMOF is depicted in the inset of Figure 5.2**(a)**. It consists of zinc paddle wheels, which are connected by chiral L-camphoric acid linker molecules in the xy-plane. In the z-direction, the layers are connected by dabco pillar linkers. The T-matrix of the finite-size molecular model is computed with TD-DFT with the development version of the TURBOMOLE code [148, P9]. In these calculations, the CAM-B3LYP functional [149] and the def2-SVP basis set [99] are used. The lattice constants in the xy-plane are $a_x = a_y = 2.079\,\mathrm{nm}$, and $a_z = 1.922\,\mathrm{nm}$ in the z-direction. For such a small molecular unit, it is sufficient to restrict the consideration to dipoles. The steps to obtain the dipole polarizability tensor of a finite molecular model with TD-DFT are discussed in Chapter 6 in more detail.

In the next step, the band structure is computed with *mpGMM* [51] from the combined Q-matrix of the two-dimensional lattice and the vacuum spacing between the lattices. Their individual Q-matrices are characterized by Eqs. (3.24) and (3.27). The band structure is depicted in Figure 5.2**(a)** and **(b)** for the real and imaginary part of the propagation constant k_z. We observe that the dispersion bands are far away from the edge of the Brillouin zone so that Bragg reflections do not occur. The material is perfectly homogenizable. Here, only $\boldsymbol{\varepsilon}_{\mathrm{r,eff}}(\omega)$ and $\boldsymbol{\kappa}_{\mathrm{eff}}(\omega)$ are of interest, as the material does not show a magnetic response. The diagonal entries of the relative permittivity and of the chirality are depicted in Figure 5.3**(a)** and **(b)**. We observe especially in the chirality that the object is anisotropic.

In the following, we verify the reliability of our homogenization by studying the optical response of a slab once at the level of the effective properties and once at the level of the individual molecules forming the material. If the agreement is sufficiently good, the correctness of the approach is indicated. Therefore, the effective material parameters are used to compute the absorption of a normal incident left-circularly polarized plane wave and the absorption circular dichroism of a 77 nm thick slab in COMSOL [141]. The slab is schematically shown in the inset of Figure 5.3**(c)**. For the reference spectra, *mpGMM* [51] is used to solve the multi-scattering problem as described in Chapter 3 in a direct manner based on the T-matrix of the finite-size molecular model. In Figure 5.3**(c)**, the reference spectra are depicted as solid lines and the spectra obtained with COMSOL are depicted as dashed lines. We observe a perfect agreement. These results support the use of the homogenization approach for multi-scale approach analyses of molecular structures in the Chapters 6 and 7. It is, however, also insightful to apply the homogenization procedure to materials that are more demanding to homogenize.

5.4. Homogenization of Metamaterials

In this section, we consider two different metamaterials to demonstrate the applicability of the homogenization approach. First, we analyze gold spheres arranged in a cubic lattice.

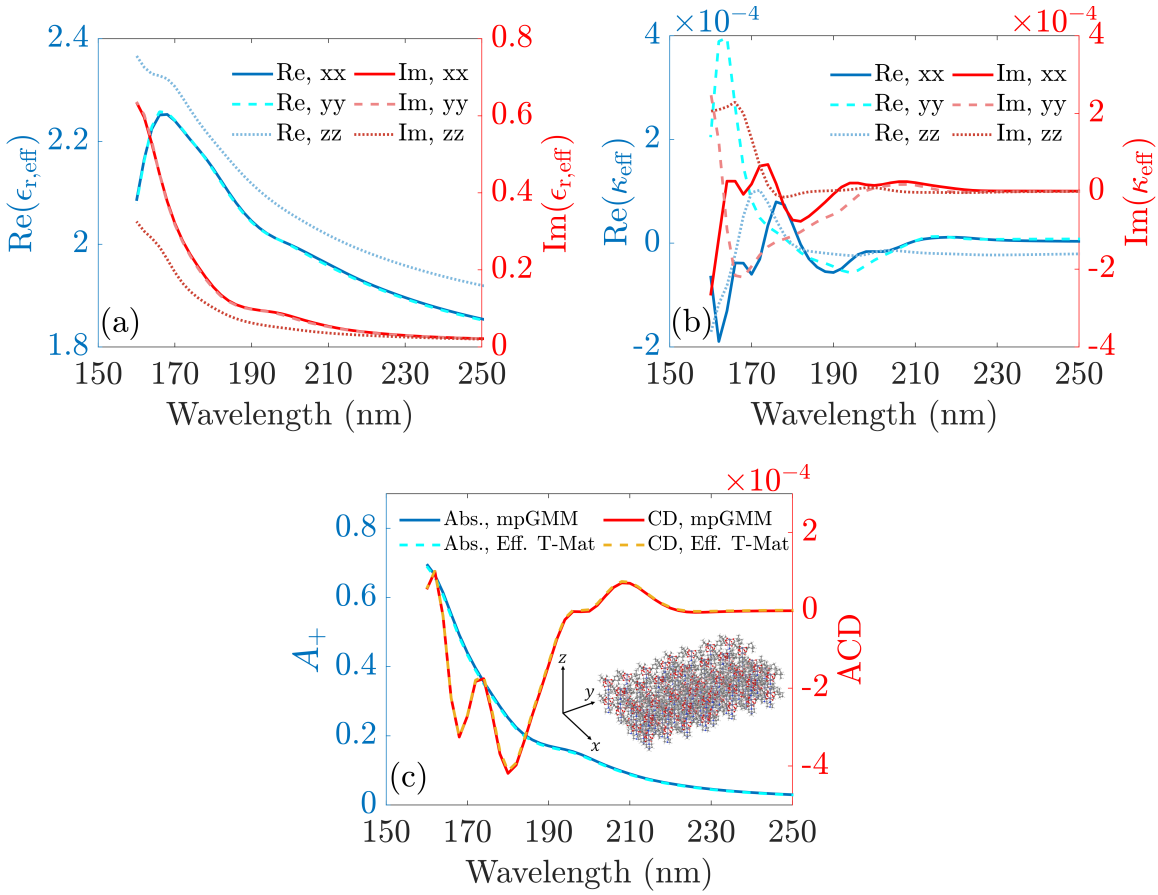

Figure 5.3.: Diagonal entries of effective permittivity **(a)** and effective chirality **(b)**. Both quantities are anisotropic. **(c)** Absorption of normal incident left-circulary polarized plane wave and absorption circular dichroism of a slab of a 77 nm thick slab. The results obtained directly with the full-wave solver *mpGMM* and the results obtained with COMSOL based on the effective T-matrix agree perfectly. **(b)** and **(c)** are adapted with permission from [P5]. Copyright © 2022 John Wiley and Sons.

This is still a material which can be considered as rather safe to homogenize. Afterward, we study a system of cut-plate pairs that are more macroscopic in size.

5.4.1. Gold Spheres in Cubic Lattice

With the first instance, we demonstrate how important it is for specific materials to take the multipolar lattice interaction into account to homogenize the material accurately. The considered material consists of gold spheres with a radius of $R = 1\,\mathrm{nm}$, separated by each other with a lattice constant of $a = 2.05\,\mathrm{nm}$. The spheres are surrounded by a host medium with a permittivity of $\varepsilon_{\mathrm{r,h}} = 2.25$. The host material is isotropic [P5, 150]. For gold, the material parameters from [151] are used. We emphasize that this example is of illustrative character to show the influence of lattice interactions. In fact, the spheres tend to be at the limit to be describable with bulk material parameters and are so close to each other that

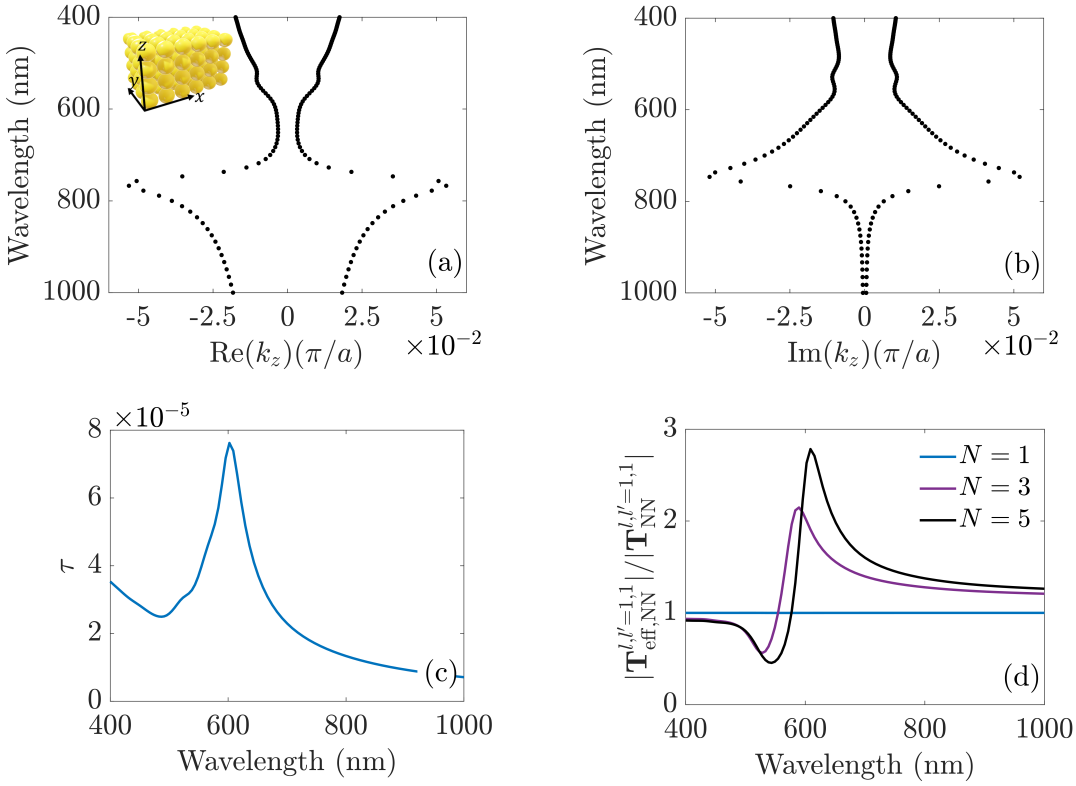

Figure 5.4.: Band structure of a cubic lattice of gold spheres for real **(a)** and imaginary part **(b)** of the propagation constant k_z. The lattice is depicted in the inset of **(a)**. As the band structure does not show a resonance close to the Brillouin edge, the material is homogenizable. **(c)** The quantity τ is used as a measure for the non-dipolar part of the effective T-matrix. As τ is close to zero, the dipolar part of the effective T-matrix is sufficient to describe the material. Panel **(d)** shows the ratio between the effective electric dipolar part $|\mathbf{T}^{l,l'=1,1}_{\mathrm{eff,NN}}|$ and the electric dipolar part $|\mathbf{T}^{l,l'=1,1}_{\mathrm{NN}}|$ of the single sphere. For the effective electric dipolar part, up to $N = 1$, up to $N = 3$, and up to $N = 5$ multipoles are incorporated. For $N = 3$ and $N = 5$, a resonance is observable, which shifts and is more intense for $N = 5$. It is, therefore, important to incorporate enough multipolar orders in order to accurately describe the optical response of the material. **(a)**-**(c)** are adapted with permission from [P5]. Copyright © 2022 John Wiley and Sons.

electron tunneling and electron spill-out could occur. These effects are not taken into account here. This has, however, no impact on the liability of the homogenization procedure.

The T-matrix of a single sphere is computed with Mie theory. For the computation, up to $N = 5$ multipolar orders are incorporated. We emphasize upfront that these higher order multipoles have to be included to correctly describe the interaction of the particle in the lattice. In Figures 5.4**(a)** and **(b)**, the band structure of the material is depicted. As Bragg gaps do not occur in this frequency range, the material is perfectly homogenizable. Additionally, we observe in Figure 5.4**(c)** that higher multipolar orders in the effective T-matrix are negligibly small. In Figure 5.4**(d)**, the ratios are shown between the absolute

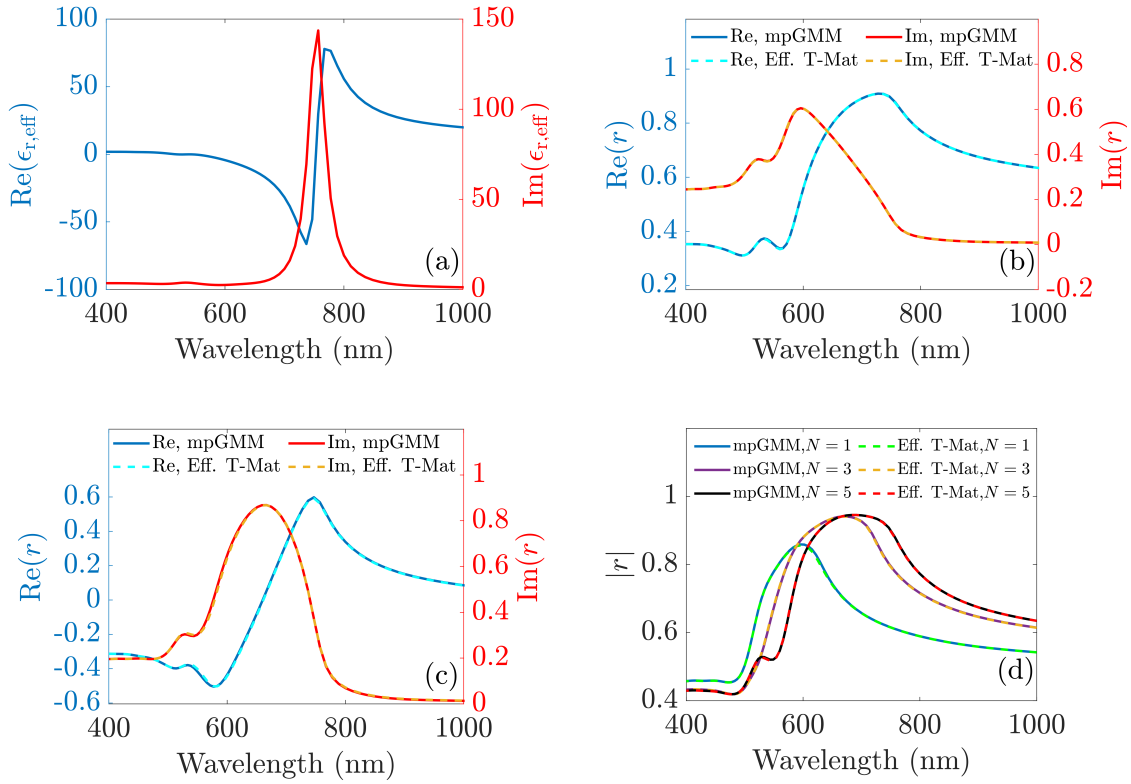

Figure 5.5.: Effective material parameters and optical response of a cubic lattice of gold spheres. Panel **(a)** depicts the relative permittivity of the material. The permittivity shows a sharp resonance. Panels **(b)** and **(c)** show the reflection coefficient of a 2.15 mm thick slab of the material for a plane wave under normal incidence and under oblique incidence with an angle of incidence of 75°, respectively. The agreement between the spectra obtained directly with the full-wave solver *mpGMM* and the spectra obtained with the material parameters from the effective T-matrix is perfect. Panel **(d)** depicts the reflection coefficient for incorporating up to $N = 1$, $N = 3$, and $N = 5$ multipoles in the calculation of the T-matrix for the full-wave solver and for the effective T-matrix. The agreement between the different methods is perfect in each case. It is, however, not sufficient to incorporate only dipoles ($N = 1$), as the spectrum shifts by incorporating higher multipoles. Adapted with permission from [P5]. Copyright © 2022 John Wiley and Sons.

value of the effective electric dipolar entry $|\mathbf{T}^{l,l'=1,1}_{\text{eff,NN}}|$ and the electric dipolar entry of a single sphere $|\mathbf{T}^{l,l'=1,1}_{\text{NN}}|$, taking into account up to $N = 1$, up to $N = 3$, and up to $N = 5$ multipolar orders in the effective T-matrix, respectively. We observe that the ratios differ considerably from each other, demonstrating the strong lattice interaction due to higher multipoles renormalizing the dipoles [P5].

In the next step, we consider the effective permittivity computed from the direction independent effective T-matrix. The other material parameters are not of interest since the material does not show a magnetic optical response and is achiral. The isotropic effective

permittivity is shown in Figure 5.5**(a)**. We observe both a strong resonant and dispersive character. The observed resonance originates from the plasmonic resonance of the individual gold nanoparticles shifted to longer wavelengths due to lattice interaction.

Now, we consider a macroscopic sample. It is a film of the stacked lattices in a vacuum, which is illuminated by a TM-polarized plane wave. TM-polarization of a normal incident plane wave propagating in positive z-direction corresponds in this thesis to a linear polarization along the x-axis. TE-polarization of a normal incident plane wave corresponds to a linear polarization along the y-axis. For oblique incidence of the plane wave, both polarizations are rotated correspondingly.

In Figure 5.5**(b)** and **(c)**, the absolute values of the reflection coefficients of a 2.15 mm thick slab are shown for normal and for oblique incidence of a TM-polarized plane wave. The propagation direction for the oblique incidence is $\hat{\boldsymbol{k}}_{\mathrm{inc}} = [\sin(\theta), 0, \cos(\theta)]^{\mathrm{T}}$ with $\theta = 75°$. The transmission coefficient is not shown, as it is negligibly small due to the large thickness of the film.

For both normal and oblique incidence, we observe a perfect agreement between the reference solutions computed with *mpGMM* and the spectra based on the effective material parameters. In Figure 5.5**(d)**, we additionally display the reflection coefficients for normal incidence, taking into account $N = 1$, $N = 3$, and up to $N = 5$ multipolar orders, respectively. We observe that the reference solution and the solution based on the effective material parameters agree always perfectly. Taking into account higher multipoles is, however, necessary as the spectrum shifts and a second peak appears for $N = 5$. The multipolar lattice interaction is for this instance very pronounced. This is due to the small distance between the spheres. Their small distance causes their evanescent fields to overlap close to plasmonic resonances leading to mode hybridization [P5, 152].

We conclude that this instance clearly demonstrates that homogenization approaches exclusively based on the consideration of dipole-dipole interactions cannot describe the optical response of such a material sufficiently, as they do not take into account the renormalization of the dipoles due to higher-order multipoles. The material is, however, perfectly homogenizable and is a prototypical instance for a metamaterial.

5.4.2. Cut-Plate Pairs in Cubic Lattice

With the last instance, we show the limits of the presented homogenization approach and of homogenization in general [P5]. The considered material consists of cut-plate pairs arranged in a cubic lattice with a lattice constant of $a = 200\,\mathrm{nm}$. The structure is surrounded by air. The cut-plate pairs have a radius of $R = 90\,\mathrm{nm}$ and consist of two gold plates with the thickness of 30 nm, separated by a 5 nm thick dielectric layer with $\varepsilon_{\mathrm{r,Diel}} = 2.25$ [153]. For the gold plates, the material parameters from [154] are taken. The lattice of the cut-plate pairs is schematically shown in the inset of Figure 5.6**(a)**. The T-matrix of the single object is computed with JCMsuite [142], taking into account up to $N = 7$ multipoles. For this instance, we use frequencies $f = \omega/2\pi$ for the spectra instead of wavelengths. This is because for this material a Bragg gap appears and the dispersive details are better observable when displayed as a function of the frequency. When plotted as a function of the wavelength, the response appears to be compressed and stretched at shorter and longer wavelengths, respectively.

The band structure of the material is depicted in Figures 5.6**(a)** and **(b)**. The dispersion band starts to bend at 240 THz, due to the Bragg gap which occurs between 300 THz and 550 THz. We conclude, therefore, that the material is not homogenizable for frequencies larger than 240 THz for which $\frac{\mathrm{d}^2 f}{\mathrm{d}k_z^2} = 0$ is approximately satisfied, illustrated with a

gray shade. To demonstrate the impact of the Bragg gap on the accuracy of the results of the homogenization approach, we nevertheless continue to compute the effective material parameters.

In Figure 5.6**(c)** and **(d)**, the xx-components of the effective permeability and effective permittivity are shown, which are the only relevant components for a propagation along the z-direction, as the xx- and yy-components are the same. We observe a magnetic and an electric resonance at different frequencies. The resonance of the relative permittivity occurs, however, in the non-homogenizable range. The material shows both a magnetic and electronic resonance due to the symmetric/anti-symmetric behavior of the modes of the cut-plate pairs [153, 155].

As an instance for a macroscopic sample, we are now considering a slab of nine layers corresponding to a thickness of 1800 nm in a vacuum. The transmission and reflection coefficients are displayed in Figure 5.6**(e)** and **(f)**, respectively. As illumination, a TM-polarized plane wave under normal incidence is chosen. We observe that the spectra, obtained directly with *mpGMM* and based on the effective material parameters, agree well in the homogenizable range but strongly disagree in the non-homogenizable range. This is also observable for the dispersion bands in Figure 5.6**(a)** and **(b)** computed with the effective propagation constant $k_z = \frac{\omega}{c}\sqrt{\varepsilon_{\mathrm{r},xx}\mu_{\mathrm{r},xx}}$. As expected, the reflection of the material shows a Bragg band in the non-homogenizable range. The discrepancies in the homogenizable range are mainly related to the fact that $\tau\left(\mathbf{T}_{\mathrm{eff,Hel}}\right)$ depicted in Figure 5.6**(f)** is not sufficiently small, so that higher multipoles are not negligible in this frequency range. We emphasize that no homogenization approach would lead to reliable effective material parameters in the frequency range of the Bragg resonance, as the material is not homogenizable in this regime. The disagreement we see is, therefore, not a problem of our approach but of homogenization in general. One might improve the situation by using non-local constitutive relations in the homogenized material but this will not solve the problem that the material is simply not homogenizable.

Above, two methods were described to compute the effective T-matrix. For this example of cut-plate pairs, the difference of the effective T-matrices obtained with both methods is studied in the following. We evaluate the difference between between the effective T-matrix $\mathbf{T}_{\mathrm{eff,Hel,Eq}}$, computed with the first method, and the effective T-matrix $\mathbf{T}_{\mathrm{eff,Hel,An}}$, computed with the second method, by

$$\Delta\left(\mathbf{T}_{\mathrm{eff,Hel,Eq}}, \mathbf{T}_{\mathrm{eff,Hel,An}}\right) = \sqrt{\frac{\mathrm{Tr}\left\{\left(\mathbf{T}_{\mathrm{eff,Hel,Eq}} - \mathbf{T}_{\mathrm{eff,Hel,An}}\right)^{\dagger}\left(\mathbf{T}_{\mathrm{eff,Hel,Eq}} - \mathbf{T}_{\mathrm{eff,Hel,An}}\right)\right\}}{2\left(\mathrm{Tr}\left\{\mathbf{T}^{\dagger}_{\mathrm{eff,Hel,Eq}}\mathbf{T}_{\mathrm{eff,Hel,Eq}}\right\} + \mathrm{Tr}\left\{\mathbf{T}^{\dagger}_{\mathrm{eff,Hel,An}}\mathbf{T}_{\mathrm{eff,Hel,An}}\right\}\right)}}\,, \tag{5.18}$$

where $\Delta\left(\mathbf{T}_{\mathrm{eff,Hel,Eq}}, \mathbf{T}_{\mathrm{eff,Hel,An}}\right) \in [0, 1]$. For $\Delta\left(\mathbf{T}_{\mathrm{eff,Hel,Eq}}, \mathbf{T}_{\mathrm{eff,Hel,An}}\right) = 0$, the matrices are perfectly identical. In Figure 5.7, the difference of the effective T-matrices is depicted. It is negligibly small so that we conclude that both methods lead to reliable results.

We discussed in this chapter a homogenization approach based on the propagation direction independent effective T-matrix for a molecular material and for two more convential metamaterials. The effective T-matrix completely describes the optical response of a given material incorporating its multipolar lattice interaction. The dipolar part of the effective T-matrix is renormalized by higher-order multipolar contributions, and it is used to compute

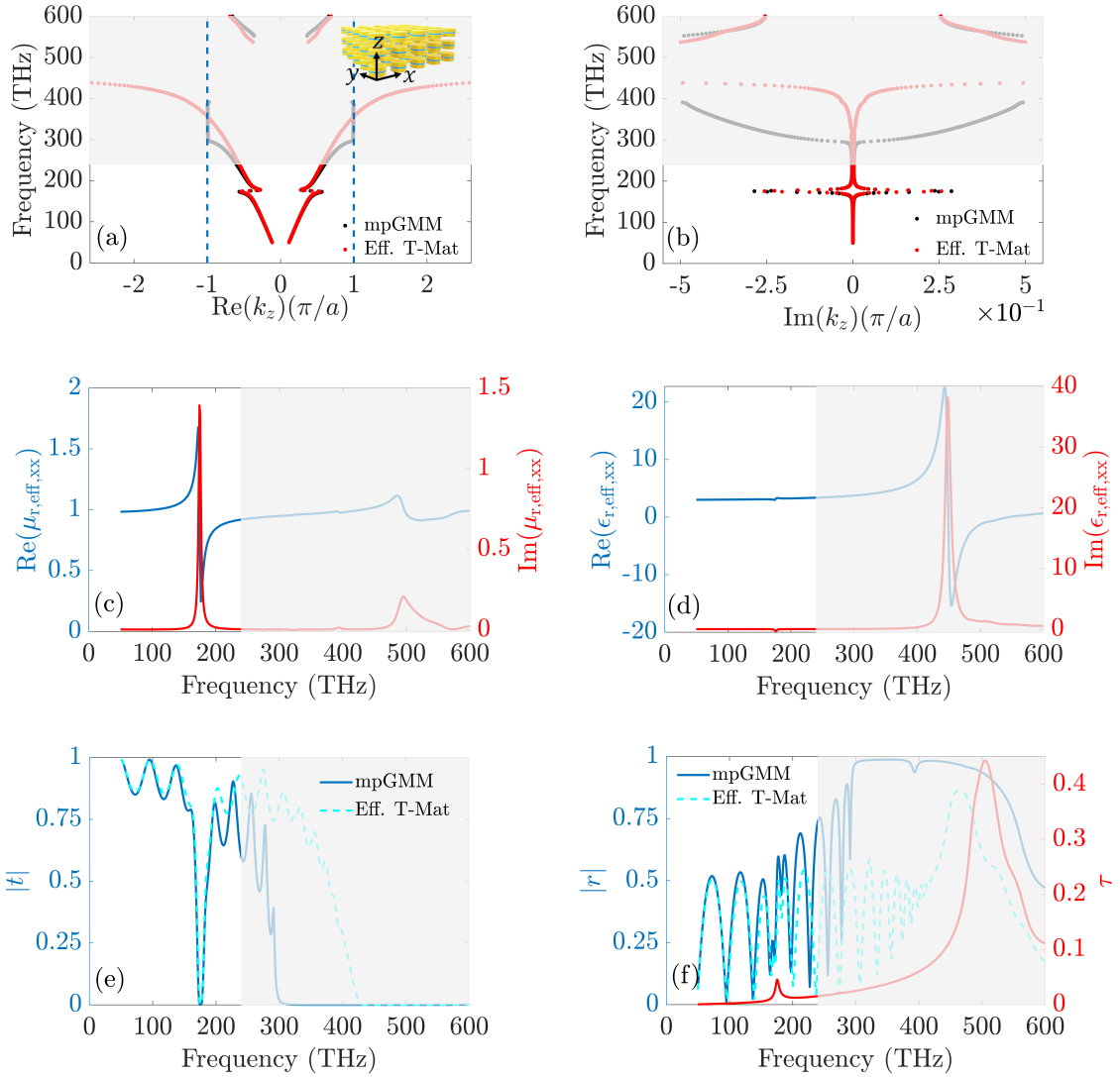

Figure 5.6.: Homogenization of a cubic lattice of cut-plate pairs. Panels **(a)** and **(b)** show the band structure of the lattice of cut-plate pairs for the real and imaginary part of the propagation constant, respectively. The material is schematically shown in the inset of **(a)**. The cut-plate pairs consist of two gold plates separated by a thin insulator. The band structure shows a Bragg gap beginning at 300 THz. From 240 THz on, the band starts to bend, due to the influence of the Bragg gap. In this frequency range, the material is not homogenizable which is indicated by the gray shade. Beginning at 240 THz, the band structure computed with the full-wave solver *mpGMM* differs from the band structure obtained with the material parameters from the effective T-matrix. Panels **(c)** and **(d)** depict the effective permeability and permittivity of the material, respectively. Both show resonances in different frequency ranges. There are two main observations for the transmission **(e)** and reflection coefficients **(f)** of a thin film, obtained with *mpGMM* and with the material parameters from the effective T-matrix. First, the spectra agree well in the homogenizable range. In this range, discrepancies can be related to non-negligible higher-order multipoles shown in red in **(f)**. Second, one observes in both spectra the Bragg band starting at 300 THz. Adapted with permission from [P5]. Copyright © 2022 John Wiley and Sons.

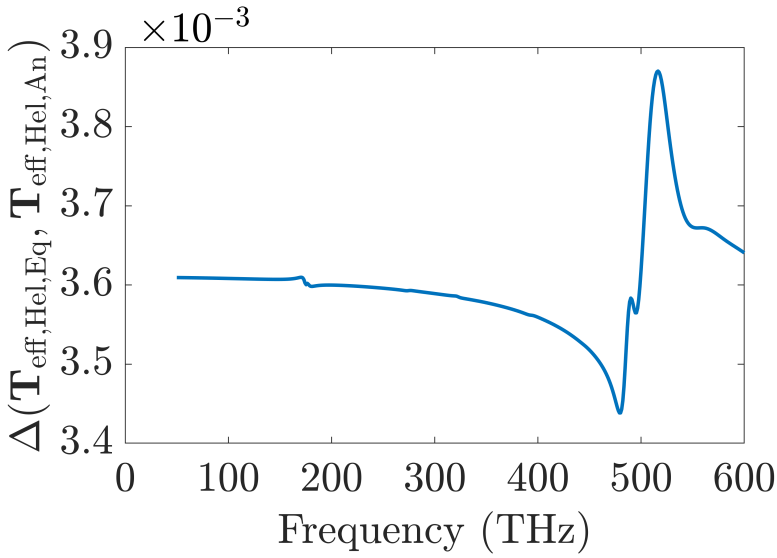

Figure 5.7.: Difference between the effective T-matrices of the three-dimensional lattice of cut-plate pairs, computed with the two methods presented in this chapter. Adapted with permission from [P5]. Copyright © 2022 John Wiley and Sons.

effective material parameters. We showed that in the case of large lattice interactions, it is very important to take the multipolar interactions into account. In the frequency range, in which a material exhibits Bragg resonances, the homogenization approach cannot be reliably used, as the effective material parameters are not independent of the propagation direction of the illuminating plane wave.

In the following chapter, we use the homogenization method to compute the effective material parameters of molecular nanomaterials in order to analyze and design more complex photonic devices, such as a metasurface of cylinders consisting of molecular structures. Here we use that the effective material parameters are independent of the illumination direction.

6 | Linear Optical Response of Molecules in Photonic Devices

In this chapter, we apply the presented techniques to analyze and enhance linear optical phenomena of molecules in different photonic devices. In this regard, we follow a specific multi-scale approach presented in [P4].

To analyze and enhance specific optical phenomena of molecules in a photonic device, such as the circular dichroism, the optical properties of the molecular material have to be obtained first. These properties can then be used to compute the optical response of simple structures, such as molecular thin films. In a further step, photonic devices can be designed to enhance specific optical effects. This analysis has to cope with two main challenges. First, multiple different length scales are involved. Considering single molecules and finite molecular clusters, one is analyzing structures of the order of some Ångströms up to a few nanometers [P4]. Macroscopic photonic devices can have spatial dimensions in the order of millimeters. A suitable multi-scale approach should, therefore, bridge several length scales, so that photonic devices can be designed on the basis of the optical response of a single molecule or finite molecular cluster.

The second challenge concerns the fact that different scientific disciplines are connected in a multi-scale simulation approach for the analysis of molecules [P4]. Properties of the finite-size molecular models, such as their polarizability, are computed with TD-DFT on the basis of electronic transitions, see Chapter 4, or on the basis of vibrational transitions, see [106], for instance. Maxwell scattering theory is used to calculate the optical response of finite-size molecular models and of the entire photonic device.

A multi-scale approach solving the two challenges concerning different length scales and disciplines is not only suitable to explain experimental measurements. Before a measurement, it is also helpful to predict results and design photonic devices accurately to avoid demanding and expensive experiments.

In Section 6.1, such a multi-scale approach is discussed. In the following sections, we demonstrate the transition from single molecules, over monolayers and thin films, to entire photonic devices. The T-matrix from Chapter 3 serves as bridge between the microscopic and macroscopic description of the optical response of the molecules. In Section 6.2, we consider the polarization-dependent optical response of finite molecular islands and monolayers on dielectric substrates. In Section 6.3, different molecules inside photonic cavities are analyzed, namely two crystalline molecular films and a mixture of randomly oriented molecules. Here, we consider the coupling between optical modes of the cavities and resonances of the molecular film, which is very important for several applications as we discuss below. In Section 6.4, we analyze a metasurface of cylinders consisting of a chiral molecular material. The metasurface is designed to enhance the circular dichroism of the molecular material.

6.1. Multi-Scale Approach to Compute the Linear Optical Response of Molecules

In this section, we outline the multi-scale workflow presented in [P4]. It has been developed in close cooperation with Marjan Krstić, Dominik Beutel, Christof Holzer, Carsten Rockstuhl, and Ivan Fernandez-Corbaton, and is based on a former cooperation between Ivan Fernandez-Corbaton and Wim Klopper [59]. The multi-scale workflow is shown in Figure 6.1. It combines (TD)-DFT computations (green boxes) and Maxwell scattering simulations (blue boxes). The first step of the approach is the characterization of structural properties of the molecular material. For periodic crystalline materials such as metal-organic frameworks (MOFs), for instance, the structure of a unit cell of the material is optimized with a periodic DFT code such as CP2K [156]. In this step, also the lattice vectors of the unit cell are defined. Here, the results can be compared to experimental spectra such as X-ray diffraction (XRD) results, if available.

In the next step, one selects a molecular model of finite size, which is analyzed with TD-DFT to obtain dynamic polarizabilities, see Chapter 4. This is because software packages such as TURBOMOLE [P9] can only be used to compute the polarizabilities of finite-size

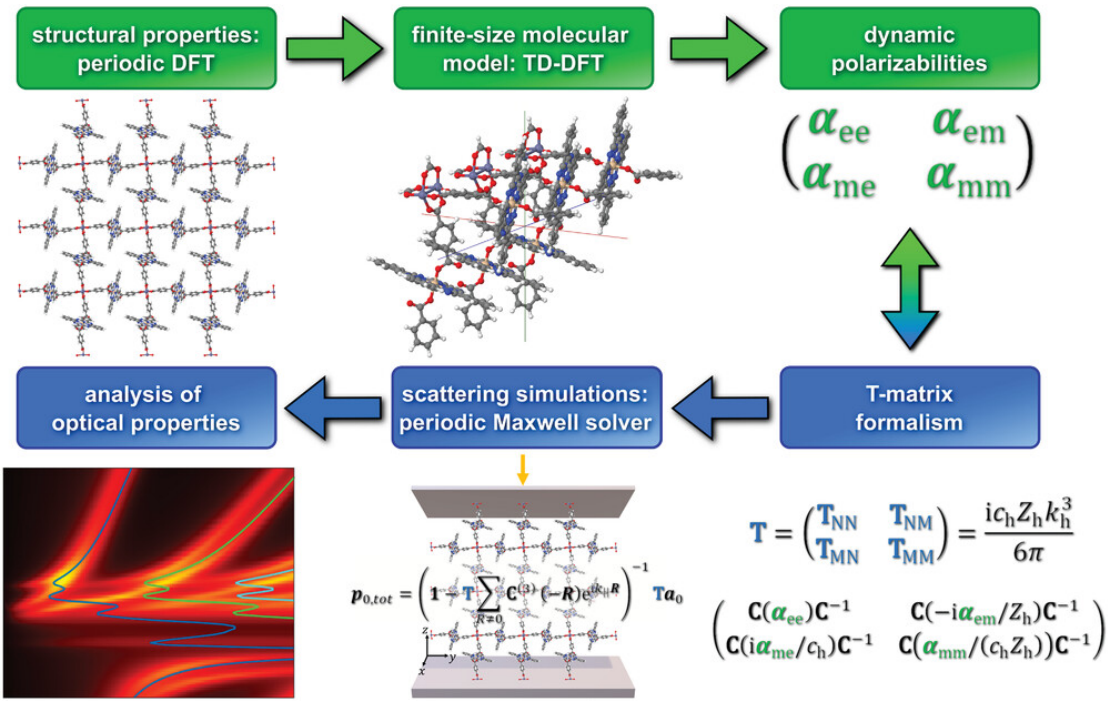

Figure 6.1.: Workflow of the presented multi-scale approach. The top row concerns the DFT simulations. First, the geometry of the molecular material is optimized. Then, a finite-size model is chosen to perform TD-DFT simulations to compute the polarizability tensor. The bottom row concerns the multi-scattering simulations. From the polarizability tensor, the T-matrix is computed, which can be used for the multi-scattering simulations to compute the optical response of molecules within photonic devices. Created in cooperation with Marjan Krstić and Ivan Fernandez-Corbaton. Reprinted with permission from [P4]. Copyright © 2022 John Wiley and Sons.

models but not of periodic systems. In the choice of the finite-size model, some restrictions apply. First, the size of the model has to be large enough to sufficiently incorporate the electronic or vibrational interactions between the molecules. The size, however, cannot be chosen arbitrarily large, due to the computational costs of TD-DFT. These increase with the size of the model. Second, the unit cell of the molecular film should be cubic, if possible. This is a requirement to avoid a large overlap of the smallest circumscribing spheres of neighboring unit cells. The smallest circumscribing spheres are called Rayleigh spheres. For a detailed discussion of the Rayleigh hypothesis, see [157], for instance. The applied computational methods, see Chapter 3, assume that the Rayleigh spheres of neighboring unit cells do not overlap [80, 158]. If the overlap is sufficiently small, the optical response of the global structure can still be computed accurately [159]. The possible overlap of the Rayleigh spheres of neighboring molecular unit cells, however, can be considered as a drawback of the presented approach.

With TD-DFT, the dynamic polarizability tensors of the finite-size molecular model are calculated. From the polarizability tensors, the T-matrix is obtained with Eq. (3.17). The T-matrix is used to compute the optical response of a film inside a cavity, for instance, with *mpGMM* [51] or *treams* [52, 53]. Here, the methods presented in Chapter 3 are used. The T-matrix is also used to calculate effective material parameters with the methods described in Chapter 5. These can be used to design a metasurface of the molecular material, for instance. The T-matrix is, therefore, the connection between the microscopic description of a finite-size molecular model via its dipole moments and the macroscopic description of entire photonic devices. In the following sections, we apply the multi-scale approach on different instances. Here, we make use of the fact that the multi-scale approach enables the transfer from single molecules, over monolayers, to macroscopic films and devices.

6.2. Polarization-Dependent Optical Response of Molecular Islands on Dielectric Substrates

In this section, we consider the optical response of molecular islands and monolayers which are deposited on a dielectric substrate. This analysis is published in [P8]. The DFT computations for this study have been prepared and performed by Marjan Krstić and Christof Holzer. The three-/four layer model studies have been performed by Thomas G. Mayerhöfer. Shuang Chen, Zairan Yu, Alexei Nefedov, Yuemin Wang, and Christof Wöll have been responsible for the experimental measurements. The concept of including both electric and vibrational contributions to the T-matrix has been developed in cooperation with Markus Nyman, Marjan Krstić, Christof Holzer, and Carsten Rockstuhl. The optical simulations have been performed by the author with *treams* [52, 53].

In this section, we analyze the transition from the response of one molecule, over islands of finite size, to the response of infinite adsorbate layers. In this regard, we demonstrate that the presented multi-scale approach can be used to describe the systems across different length scales and the transition between them. The major interest of the study concerns the variation of the dip and peak positions in reflectance spectra of TE- and TM-polarized light.

Experimentally, these spectra are measured with infrared reflection-absorption spectroscopy (IRRAS) [160–163]. For Si-H on Si(100) substrates, Chabal and colleagues measured such shifts [164]. Yang *et al.* measured shifts for CO [42] and for N_2O on ceria [43], which amount to $20\,\mathrm{cm}^{-1}$ in the latter case.

The experimentally measured curves in [42, 43] have been accompanied by simulations based on a three-layer model of the setup. The purpose of this model is to explain the experimentally obtained difference in the dip and peak positions measured in TE- and TM-polarization. In the three-layer study, the molecular layer has been modeled using a dielectric permittivity of the molecular layer. Details about three-layer model studies can be found in [42, P8], for instance. For oblique illumination of the film on a substrate with TM-polarized plane waves, the TM-polarized electric field has a vertical and a parallel component with respect to the substrate. Both, the parallel component of the TM-polarized electric field and the TE-polarized electric field, have to be continuous at the interfaces of vacuum/film and film/substrate. The experimentally measured spectra show for TM- and TE-polarization extrema, which can be related to the coupling of the electric fields to the molecular resonances [42, 43]. In the study [42], it has been shown, that the different behavior of the vertical component of the TM-polarized and the TE-polarized electric field leads to a shift between the extrema of the spectra. The film was in this previous study represented by a dielectric permittivity. Yang *et al.* explain in [42] that the wavenumber of maximum reflectance of the vertical component of the TM-polarized electric field with respect to the substrate is connected to the maximum of the imaginary part of the inverse of the dielectric permittivity associated to the molecular axis. The maximum reflectance of the TE-polarized light is connected to the maximum of the imaginary part of the permittivity. Since these maxima appear at two different wavenumbers, the experimentally observed shift in the spectra could be explained.

Such a phenomenological description via a dielectric permittivity model of the monolayer is not suitable for finite-sized molecular islands, since they cannot be represented by a dielectric

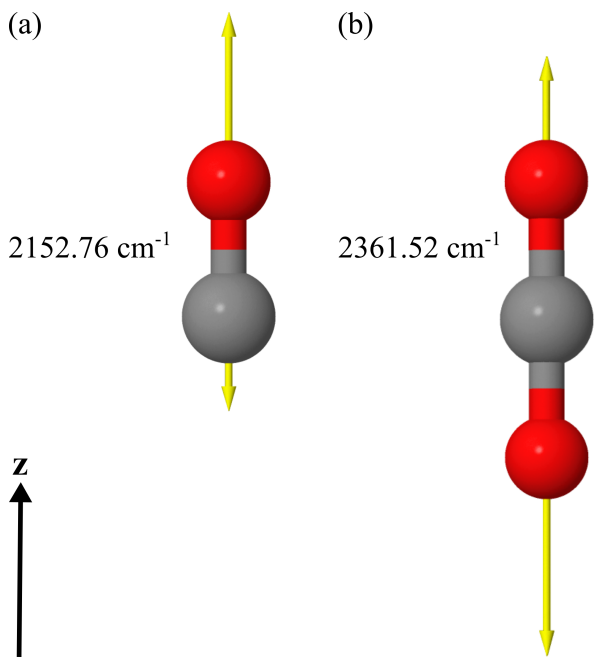

Figure 6.2.: CO **(a)** and CO_2 **(b)** molecule, aligned along the z-axis. The geometries are optimized with DFT. The respective resonance frequencies of their vibrational modes (yellow arrows) are indicated. Created by Marjan Krstić. Reprinted with permission from [P8]. Copyright © 2024 The PCCP Owner Societies.

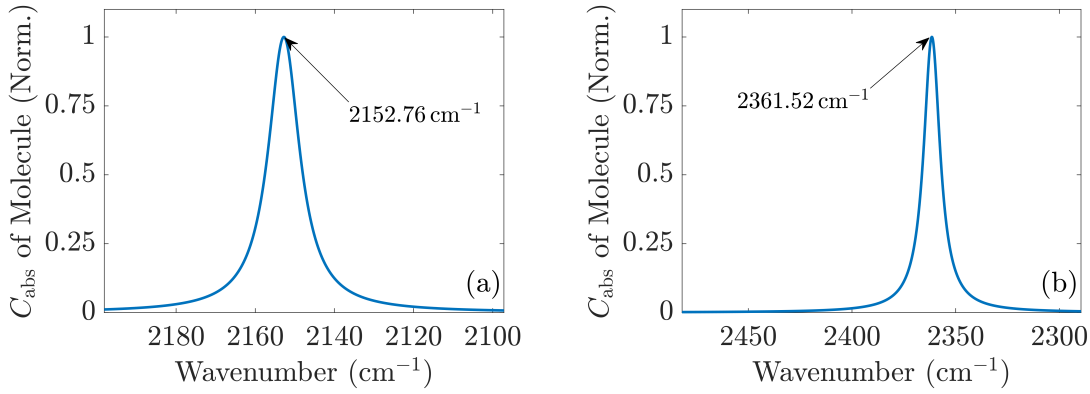

Figure 6.3.: Absorption cross sections of a CO **(a)** and a CO_2 molecule **(b)** in the gas phase. The absorption cross sections show a resonance with respect to a plane wave with an electric field polarized along the z-axis. Adapted with permission from [P8]. Copyright © 2024 The PCCP Owner Societies.

permittivity. This is because the finite islands are considerably smaller than the wavelength of the illumination. Strictly speaking, only the response of media infinitely extended into space can be represented by a dielectric permittivity, see Eq. (1) of [P1]. To discuss the optical response of finite-size islands, one can apply the presented *ab initio* multi-scale approach. We consider molecular islands of CO and CO_2 which are deposited on dielectric substrates of ceria and Al_2O_3.

(TD)-DFT Simulations

With TD-DFT, the polarizabilities of single CO and CO_2 molecules are computed, see Chapter 4, and used to obtain their T-matrices, corresponding to the first row of the multi-scale approach in Figure 6.1. The T-matrix is further used to perform multi-scale simulations. These steps correspond to the second row in Figure 6.1. First, the geometries of the molecules are optimized to reach the minimum on the potential energy surface of the ground electronic state. Both are shown in Figure 6.2, together with their vibrational resonance frequencies. With TD-DFT, the vibrational and electronic polarizabilities are computed with the development version of TURBOMOLE [P9, 165]. The functional used for the TD-DFT computations is the hybrid PBE0 exchange-correlation functional [166, 167]. The basis set is def2-TZVP [99], see Chapter 4.

Optical Response of Islands of CO and CO_2 on Dielectric Substrates

We continue by considering the optical response of the molecules on dielectric substrates. We are analyzing the optical response of the molecules at infrared wavelengths. Therefore, a vibrational contribution $\mathbf{T}_{\text{vib}}$ and an electric contribution $\mathbf{T}_{\text{el}}$ to the T-matrix have to be included [P8, Eq. (1)]:

$$\mathbf{T} = \mathbf{T}_{\text{vib}} + \mathbf{T}_{\text{el}} \,. \tag{6.1}$$

$\mathbf{T}_{\text{el}}$ includes the less-dispersive contribution of electronic transitions in the visible and the UV wavelength range. It is incorporated to correctly obtain the intensity of the simulated

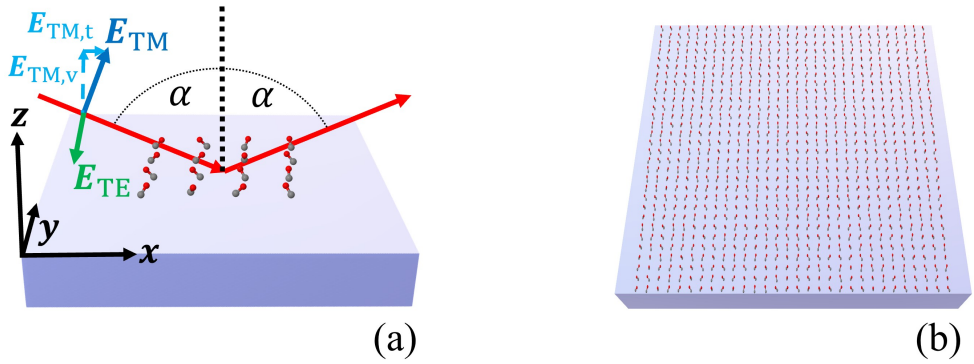

Figure 6.4.: Schematic IRRAS setup. Panel **(a)** shows the setup considered in the simulations and in the measurements. The reflectance is evaluated for plane waves with fields being TE- and TM-polarized. The TM-polarized electric field can be split in a part, which is vertical to the surface, and a part, which is tangential to the surface. The plane waves are oblique incident with an angle α on the 2D adsorbate layers and the molecular islands. Panel **(b)** depicts an infinite 2D adsorbate layer deposited on a dielectric substrate. The molecular model was created by Marjan Krstić. Adapted with permission from [P8]. Copyright © 2024 The PCCP Owner Societies.

curves. In Figures 6.3**(a)** and **(b)**, the absorption cross sections of CO and CO_2 in the gas phase are shown with respect to a plane wave with a z-polarized electric field. The absorption cross sections are computed by

$$C_{\mathrm{abs}} = C_{\mathrm{ext}} - C_{\mathrm{sca}} \,, \tag{6.2}$$

with the extinction cross section [168, Eq. (5.18b)]

$$C_{\mathrm{ext}} = -\frac{1}{k^2} \sum_{m=-1}^{1} \mathrm{Re}\left(a_{1,m,\mathrm{N}} c^*_{1,m,\mathrm{N}} + a_{1,m,\mathrm{M}} c^*_{1,m,\mathrm{M}}\right) \,, \tag{6.3}$$

and the scattering cross section [168, Eq. (5.18a)]

$$C_{\mathrm{sca}} = \frac{1}{k^2} \sum_{m=-1}^{1} \left(|c_{1,m,\mathrm{N}}|^2 + |c_{1,m,\mathrm{M}}|^2\right) \,, \tag{6.4}$$

where $a_{1,m,\mathrm{N}}$, $a_{1,m,\mathrm{M}}$ and $c_{1,m,\mathrm{N}}$, $c_{1,m,\mathrm{M}}$ are the multipolar expansion coefficients of the incident and the scattered fields, respectively, see Chapter 3. They are related by the T-matrix $\mathbf{T}$ via Eq. (3.10). As the molecules are aligned along the z-axis, the response to a plane wave with a z-polarized electric field shows a resonance.

We consider in the following the optical response of the molecules deposited on dielectric substrates. For the multi-scale simulations, *treams* [52, 53] is used. In Figure 6.4**(a)**, the setup for the simulations is shown. In Figure 6.4**(b)**, an infinite 2D adsorbate layer is schematically displayed. This resembles the situation from the experimental measurements

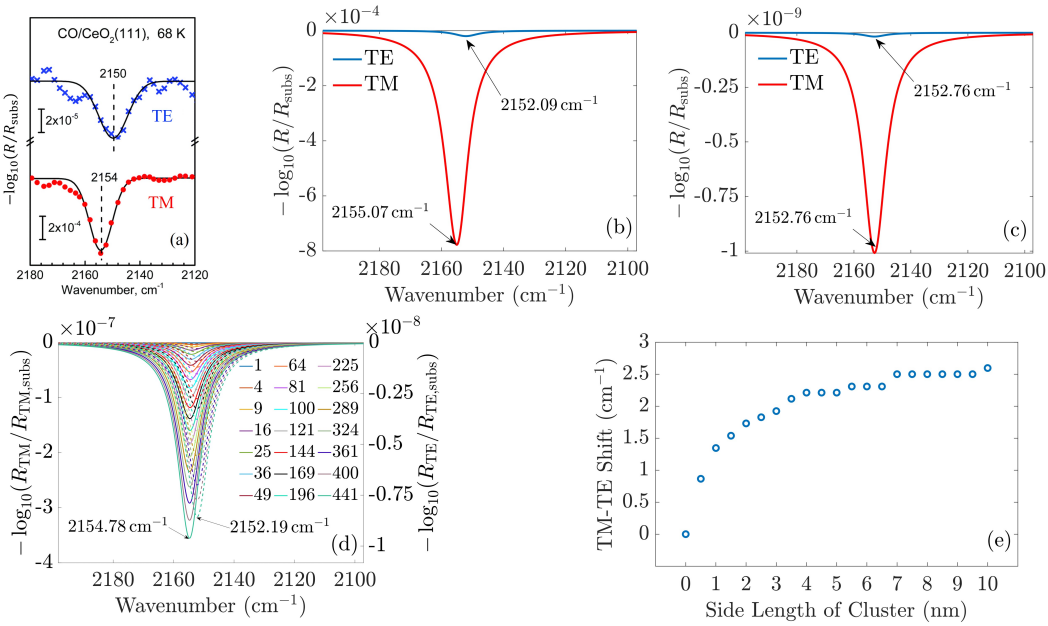

Figure 6.5.: Optical response of CO molecules on a ceria substrate. Panel **(a)** depicts the measured IRRAS spectra (dots and crosses) of an adsorbate layer of CO molecules deposited on a ceria substrate. Panels **(b)**, **(c)**, and **(d)** show the simulated spectra of a 2D adsorbate layer, of a single molecule, and of islands with increasing size deposited on a ceria substrate, respectively. Panel **(e)** depicts the shift between the dips of the TE- and the TM-spectra. The shift increases with the size of the island. **(a)** is adapted with permission from [42] under a CC BY-NC 3.0 Deed license. Copyright © 2020 The PCCP Owner Societies. **(b)**-**(e)** are adpated with permission from [P8]. Copyright © 2024 The PCCP Owner Societies.

of CO and CO_2 monolayers adsorbed on dielectric substrates. Analogous to the experimental studies [42, 43], we consider as illumination a plane wave that is either TE- or TM-polarized. The angle of incidence is $\alpha = 80°$. The TM-polarized electric field of the oblique illumination can be separated into a component $\boldsymbol{E}_{\mathrm{TM,v}}$ vertical to the film and a component $\boldsymbol{E}_{\mathrm{TM,t}}$ tangential to the film. As we stated above, these components satisfy different continuity conditions concerning an electric field at the interface of two different media. Here, the vertical component $\boldsymbol{E}_{\mathrm{TM,v}}$ is of special interest, since it leads to a different reflectance behavior in comparison to the TE-polarized plane wave [42]. Both $\boldsymbol{E}_{\mathrm{TM,t}}$ and $\boldsymbol{E}_{\mathrm{TE}}$ are tangential to the substrate and have to be continuous. As $\boldsymbol{E}_{\mathrm{TE}}$ and $\boldsymbol{E}_{\mathrm{TM,t}}$ have to be continuous and $\boldsymbol{E}_{\mathrm{TM,v}}$ not, their reflectance spectra are, on a macroscopic level, determined by the inverse of the molecular film permittivity and the permittivity itself, respectively [42]. As the permittivity and its inverse are in general shifted to each other, the peaks/dips of the reflectance spectra related to $\boldsymbol{E}_{\mathrm{TM,v}}$ and related to $\boldsymbol{E}_{\mathrm{TE}}$ and $\boldsymbol{E}_{\mathrm{TM,t}}$ are shifted to each other.

Besides the infinite 2D adsorbate layers, which can be also described by a phenomenological permittivity, we also consider square superlattices of finite molecular islands and infinite 2D adsorbate layers. The lattice constant of the superlattice is set to 500 nm to guarantee that the molecules of neighboring islands are not interacting with each other and that diffraction does not occur. A superlattice deposited on an infinite substrate has to be considered as we cannot simulate a single finite cluster deposited on a subtrate with *treams* [52, 53]. We

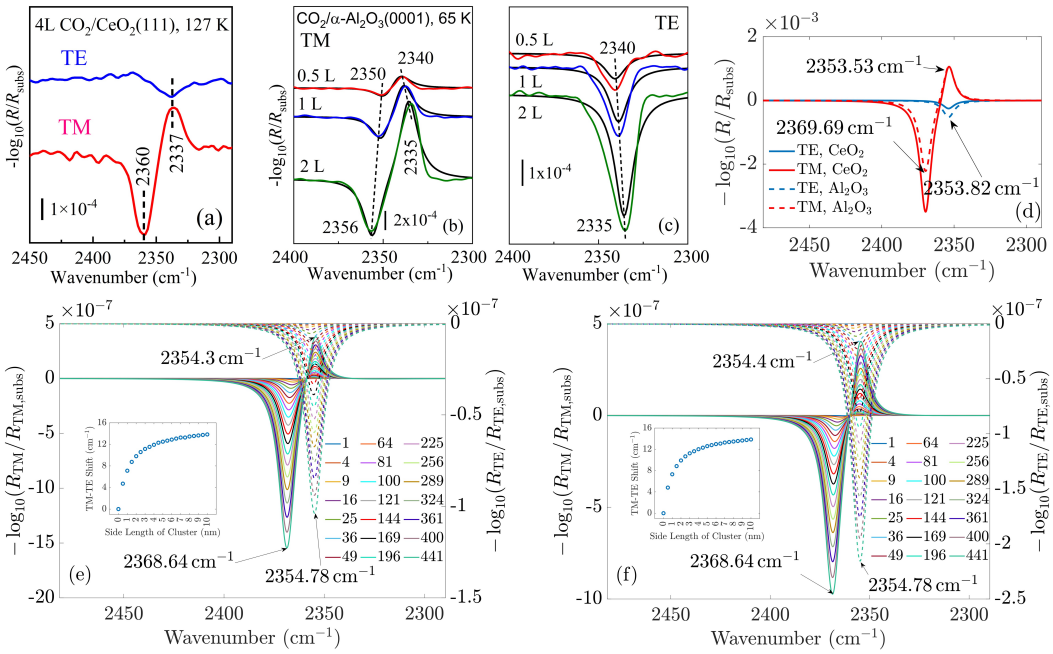

Figure 6.6.: Optical response of CO_2 molecules on ceria and Al_2O_3 substrates. Panel **(a)** shows the measured IRRAS spectra of CO_2 deposited on a ceria substrate, and panels **(b)** and **(c)** show the corresponding spectra for an Al_2O_3 substrate, respectively. The measured IRRAS spectra in **(b)** and **(c)** (red, blue, and green lines) are accompanied by phenomenological four-layer model studies (black lines). In **(b)** and **(c)**, the spectra are displayed for different coverage rates of the substrate. Panel **(d)** depicts the spectra for both substrates simulated with the multi-scale approach. The agreement of the position of the dips and peaks between experiment and multi-scale simulations is good. The spectra of finite islands with their respective shifts are shown in **(e)** for ceria and in **(f)** for Al_2O_3, respectively. The shift increases with the size of the island and gets close to the result of the monolayer. **(a)**-**(c)** have been originally created by Yuemin Wang. Adapted with permission from [P8]. Copyright © 2024 The PCCP Owner Societies.

emphasize, however, that the optical response originates from the individual islands, as they do not interact with each other due to the large lattice constant of the superlattices. The finite-size molecular islands are of specific interest as they show the strength of the multi-scale approach covering different length scales.

First, we concentrate on CO molecules on a ceria substrate. Considering the properties of the CO molecules, as in [42], a tilt angle of the molecular axis of 46° is assumed with respect to the z-axis, which can be partly a consequence of thermally occupied frustrated rotations. The T-matrix is averaged across the azimuthal angles, as the azimuthal orientation is assumed to be random [42]. The dielectric permittivity of ceria is set to 5.31 [42]. The distance between the molecules inside an island and inside the infinite 2D adsorbate layers is set to 0.5 nm. A square arrangement is also assumed for the molecules inside the islands. For the distance between the center of mass of the CO molecules and the surface of the substrate,

a value of 0.3446 nm is estimated. This is based on the distance between the center-of-mass of the molecule and the atom connected to the surface, and on the distance between the surface and this atom.

First, we analyze the optical response of the infinite 2D adsorbate layer of CO molecules, which we directly compare to the experimental and theoretical three-layer studies from [42]. In Figure 6.5**(a)**, the measured spectra from [42] are displayed. For the spectra, we consider the negative logarithm of the reflectance R of the molecules on the substrate divided by the reflectance R_{subs} of the uncovered substrate, $-\log_{10}\left(\frac{R}{R_{\text{subs}}}\right)$. This quantity corresponds to the experimentally measured absorbance, see [P8]. In Figure 6.5**(b)**, the simulated spectra are shown for TE- and TM-polarized incident light. The position of the dips and their shift agrees very well between the experiment and our simulations. This demonstrates that the multi-scale approach is very useful to accompany experimental results with theoretical simulations, and motivates us to predict results, which are more demanding to measure but yet important to estimate the influence of finite-size effects.

In the next step, we make use of the fact that within our multi-scale approach, finite islands of molecules can be considered with *treams* [52, 53]. We analyze the spectra for islands of one molecule and up to 441 CO molecules on a ceria substrate in Figures 6.5**(c)** and **(d)**. The corresponding shifts of the TE and TM-spectra are displayed in Figure 6.5**(e)**. For a single molecule, one does not observe a shift. For an island of four molecules (0.5 nm x 0.5 nm), the shift is $0.9\,\text{cm}^{-1}$. For an island of 441 molecules (10 nm x 10 nm), the shift is $2.6\,\text{cm}^{-1}$ which is close to the shift of $3\,\text{cm}^{-1}$ for an infinite 2D adsorbate layer. As we observe a shift for all islands except of the single molecule, we conclude that the shift between the TE- and TM-spectra occurs on a macroscopic level due to the interaction between the molecules on the microscopic level. This interaction is not present for a single molecule. With increasing island size, the interaction of the dipole moments of the molecules can be captured by means of a dielectric permittivity. This represents the transition from finite islands to monolayers.

Next, we concentrate on CO_2 molecules deposited on ceria and Al_2O_3. For Al_2O_3, the dielectric permittivity is set to 3.075 [169]. The tilt angle of the CO_2 molecules is set to 60°. For the distance between the center of mass of the CO_2 molecule and the substrate, we estimate a value of 0.3581 nm. All the other parameters are the same as for CO.

The experimental spectra for ceria and Al_2O_3 are displayed in Figure 6.6**(a)**, **(b)**, and **(c)**, respectively. We observe for Al_2O_3 in Figure 6.6**(b)** and **(c)** that the dips and peaks of the absorbance spectra shift for different values of the coverage of the substrate by the molecules. The simulated spectra of the infinite 2D lattice are shown in Figure 6.6**(d)** for both substrates. The agreement of the positions of the dips and peaks measured in the experiment and computed in the simulations is good. In the simulations, the shift between the TE- and TM-spectra is $15.87\,\text{cm}^{-1}$. This is a larger value in comparison to the value observed for CO molecules. Slight disagreements between the dips and peaks observed in the experiments and the simulations can be related to the influence of the coverage of the substrate by the molecules, which shift the dips and peaks of the absorbance in the experiments, see Figure 6.6**(b)** and **(c)**.

A prominent feature of the spectra is that we observe one dip and one peak for the TM-spectra in comparison to CO molecules. The dip is related to the component vertical to the substrate, and the peak is related to the parallel component [P8, 170, 171]. Their occurrence can be also explained with the continuity relation for an electric field at the interface of two media. Similar to the TE-polarized field, the reflectance of the parallel component is determined by the permittivity and not its inverse. Since the signs of the

imaginary parts of the permittivity and its inverse are different, those two extrema have different signs. For CO, the shift between the extrema of the vertical and parallel component is so small that the extremum of the parallel component is overlayed by the extremum of the vertical component. While the discussion of this effect relies for monolayers on the model of a dielectric permittivity, the same explanation applies for the islands, considering the interaction of their dipole moments, which emerges as a dielectric permittivity in the case of a monolayer.

In Figure 6.6**(e)** and **(f)**, the finite size study for ceria and Al_2O_3 is displayed. Here, we again observe that the shift of the TM and TE dips is zero for a single molecule and increases with the size of the 2D island. For islands consisting of considerably more than 441 molecules, we can, therefore, exclude the influence of finite size effects. This study shows that the presented *ab initio* multi-scale approach exhibits considerable predictive power, and can be used to examine scenarios difficult to study in an experiment. These experimental studies can be supported beforehand by such prior theoretical simulations.

6.3. Coupling of Molecular Films to Photonic Cavities

In this section, we consider the optical response of molecular films inside photonic cavities. For this analysis, the discussion of multi-layered systems is important. We perform, therefore, a transition from the response of a finite-size molecular model, computed with TD-DFT, to the response of a photonic device containing a macroscopic film. The photonic cavities consist of two metallic mirrors. The coupling of both the filling medium and the cavity is of large interest for many applications, since the optical response of the filled cavity is often considerably different from the response of the filling medium, see [172–181], for instance.

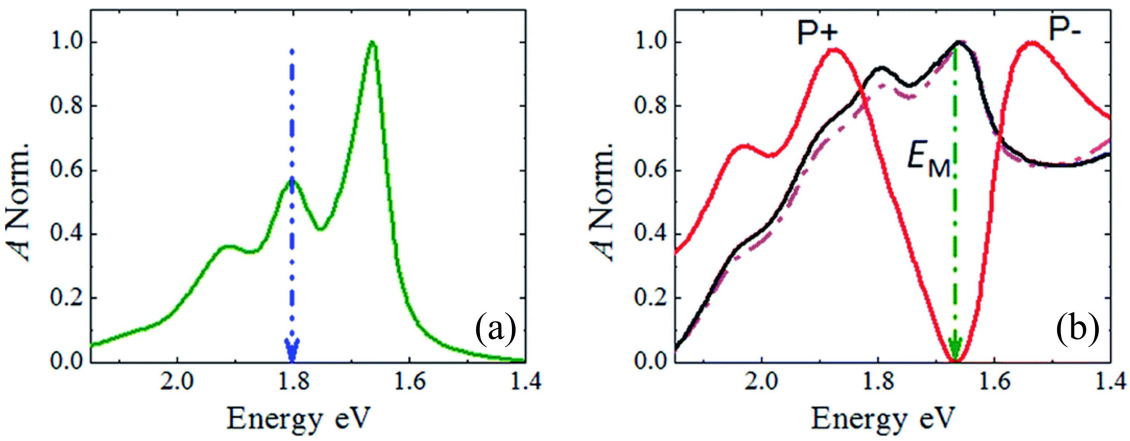

Figure 6.7.: Experimentally measured absorption spectra of Zn-SiPc-SURMOF-2 on a silver substrate **(a)**, and inside a cavity of silver mirrors **(b)**. For the SURMOF on the substrate, three absorption peaks are visible at 1.67 eV, at 1.8 eV, and close to 1.9 eV. For the SURMOF with a thickness of 400 nm inside the cavity, the absorption spectrum (red) shows two peaks at 1.52 eV and 1.87 eV, centered around 1.67 eV. Adapted with permission from [172] under a CC BY-NC 3.0 Deed license. Copyright © 2020 The PCCP Owner Societies.

The different applications range from modifying chemical reactions [176–178], over quantum-electrodynamical phenomena [172], to exciton polaritons [181].

6.3.1. Zn-SiPc-SURMOF-2

The first instance, which we consider, is a Zn-SiPc-SURMOF-2. We recall that SURMOFs are surface-mounted metal-organic frameworks. A SURMOF-2 consists of two-dimensional planar layers with isoreticular structure. These are connected to each other by weak van der Waals interactions in the third dimension [182]. SURMOFs are of large interest for us, since they can be represented by stacked two-dimensional lattices of molecules. This is a major application of our multi-scale approach. In [172], the optical response of the SURMOF on a substrate and inside a cavity has been experimentally considered. Three absorption peaks are measured of a thin film of the SURMOF deposited on a silver substrate. These are located at 1.67 eV, at 1.8 eV, and close to 1.9 eV, see the green line in Figure 6.7**(a)**. The peak at 1.67 eV is the most dominant one. In the next step, Haldar *et al.* consider the film with a thickness of 400 nm inside a cavity [172]. The cavity consists of a silver mirror of a thickness of 10 nm at the illumination side and a silver mirror of a thickness of 30 nm on the other side of the film. The absorption spectrum of this cavity shows two separated peaks at 1.52 eV and 1.87 eV, which are centered around 1.67 eV, see Figure 6.7**(b)**. In contrast to the situation before, a minimum of the intensity is observed at this energy. In [172], it is concluded that the most dominant absorption peak of the film on the substrate is split for the filled cavity, due to the coupling between the optical modes of the cavity and the

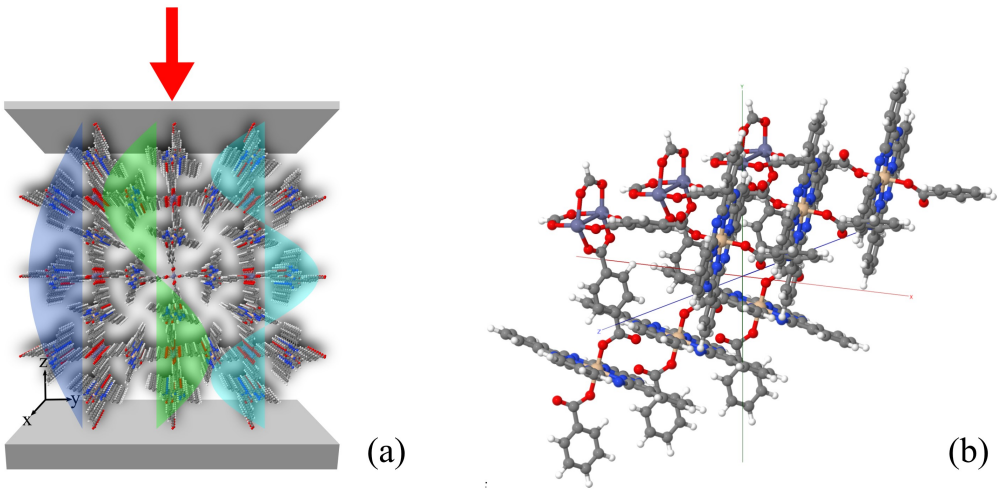

Figure 6.8.: Scheme of the simulated setup of the Zn-SiPc-SURMOF-2 inside a cavity **(a)**. Both mirrors consist of silver thin films. The top mirror has a thickness of 10 nm. The bottom mirror has a thickness of 30 nm. The cavity is illuminated from above with a normal incident plane wave propagating in −z-direction. Panel **(b)** shows the finite-size model used for the TD-DFT simulations of the polarizability tensor of the Zn-SiPc-SURMOF-2. Originally created by Marjan Krstić. Adapted with permission from [P4]. Copyright © 2022 John Wiley and Sons.

absorption resonance of the SURMOF. This is commonly referred to as Rabi splitting and strong coupling [172, 183].

Motivated by these experimental findings, the optical response of the SURMOF inside the cavity is theoretically analyzed in [P4]. This serves as a demonstrating instance for an application of our approach and to gain knowledge about the coupling nature between the cavity and the SURMOF. The filled cavity is schematically shown in Figure 6.8**(a)**. It is analyzed with the presented workflow in Figure 6.1. The DFT computations for this analysis have been prepared and performed by Marjan Krstić and Christof Holzer. The mode analysis of the filled cavity has been developed by Ivan Fernandez-Corbaton. The optical simulations have been performed by the author with *mpGMM* [51].

(TD)-DFT Simulations

The first step of the analysis is the optimization of the geometry parameters with CP2K [156] of a unit cell within the periodic material. Here, the lattice constants are defined by experiments with 1.1 nm in the x-direction and 2.1 nm in the y- and z-directions [172].

To perform TD-DFT calculations, a cluster-like finite-size molecular model is chosen. It consists of three Zn-paddle wheels and three SiPc linkers in the horizontal and vertical direction, see Figure 6.8**(b)**. As the finite-size model corresponds to three unit cells along the x-direction, the lattice constants for the optical simulations are $a_x = 3.3\,\text{nm}$, $a_y = 2.1\,\text{nm}$, and $a_z = 2.1\,\text{nm}$. The polarizability tensors are computed as described in Chapter 4 by means of the ωB97x-d DFT functional [184] and the def2-TZVP basis set [99]. The computation is performed with a development version of the TURBOMOLE package [148, P9].

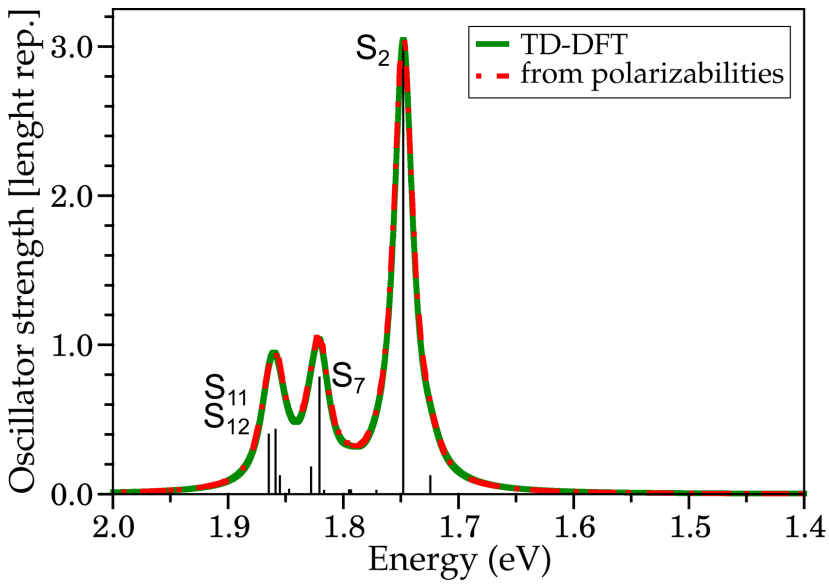

Figure 6.9.: Orientationally averaged absorption cross sections computed directly with TD-DFT and obtained from the polarizability tensor of the finite-size model in Figure 6.8**(b)**. Both absorption spectra agree perfectly with each other and show peaks between 1.7 eV and 1.9 eV. The positions agree well with the peaks from the experimentally measured spectrum in Figure 6.7**(a)**. Created by Marjan Krstić. Adapted with permission from [P4]. Copyright © 2022 John Wiley and Sons.

We can already compare the response of the finite-size molecular model to the experiment by means of TD-DFT: The orientationally averaged absorption cross sections computed from the polarizabilities and directly with TD-DFT are shown in Figure 6.9. We observe that the positions and the shape of the absorption peaks agree well with the experimental spectrum. In Appendix A, we consider a second finite-size molecular model, which leads to similar results concerning the spectra of the film in a vacuum and inside a cavity, which we discuss in the following. This supports the assumption that the model analyzed here is suitable to sufficiently describe the optical response of the film with the multi-scale approach.

Optical Response of the SURMOF Film in a Vacuum and Inside a Cavity

To obtain the macroscopic optical response of the film in a vacuum and the filled cavity, we compute the interaction in one layer, and the stacked layers are coupled as described in Chapter 3. Figure 6.10**(a)** shows the absorption spectrum of the SURMOF film in a vacuum

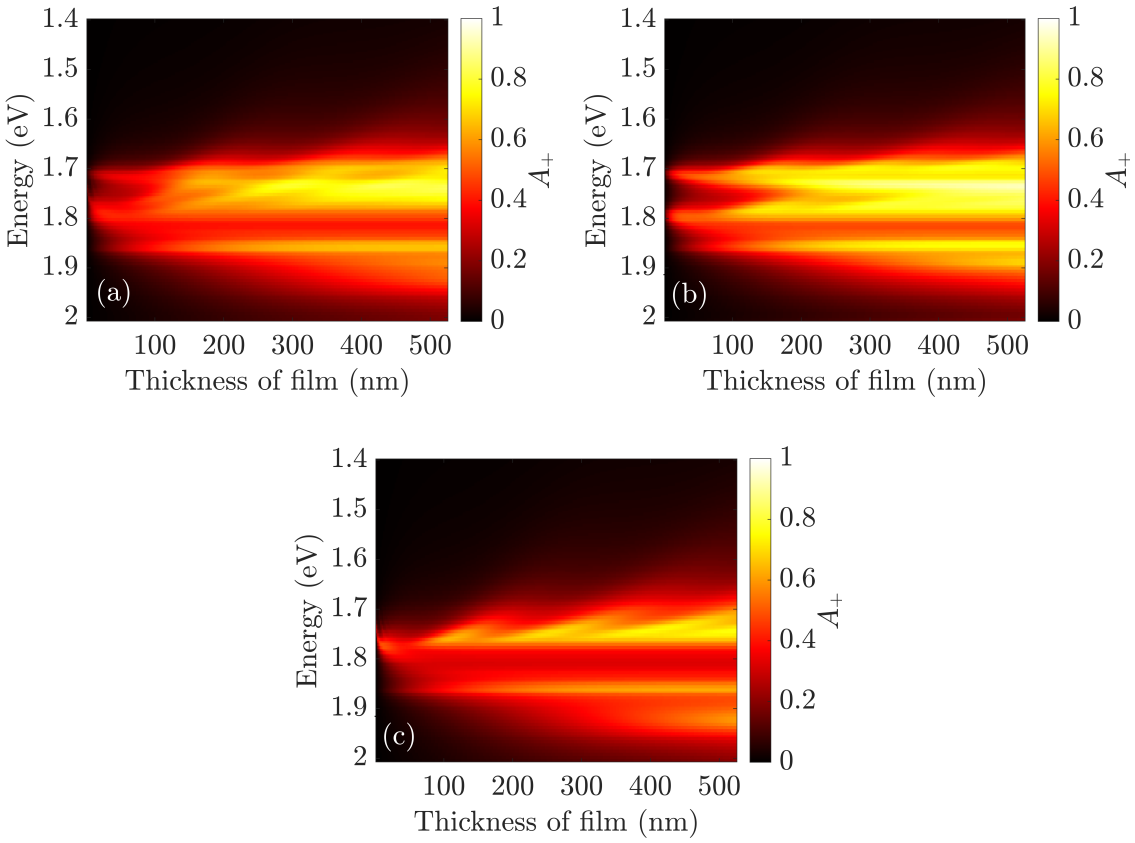

Figure 6.10.: Simulated absorption spectra of the thin film of the Zn-SiPc-SURMOF-2 in a vacuum. The illumination is a normal incident plane wave, which is left-handed circularly polarized **(a)**, TE-polarized **(b)**, and TM-polarized **(c)**, respectively. All spectra show broad absorption between 1.7 eV and 1.9 eV. The spectra in **(b)** and **(c)** differ from each other since the molecular material does not exhibit a C_4-symmetry with respect to the z-axis. Adapted with permission from [P4]. Copyright © 2022 John Wiley and Sons.

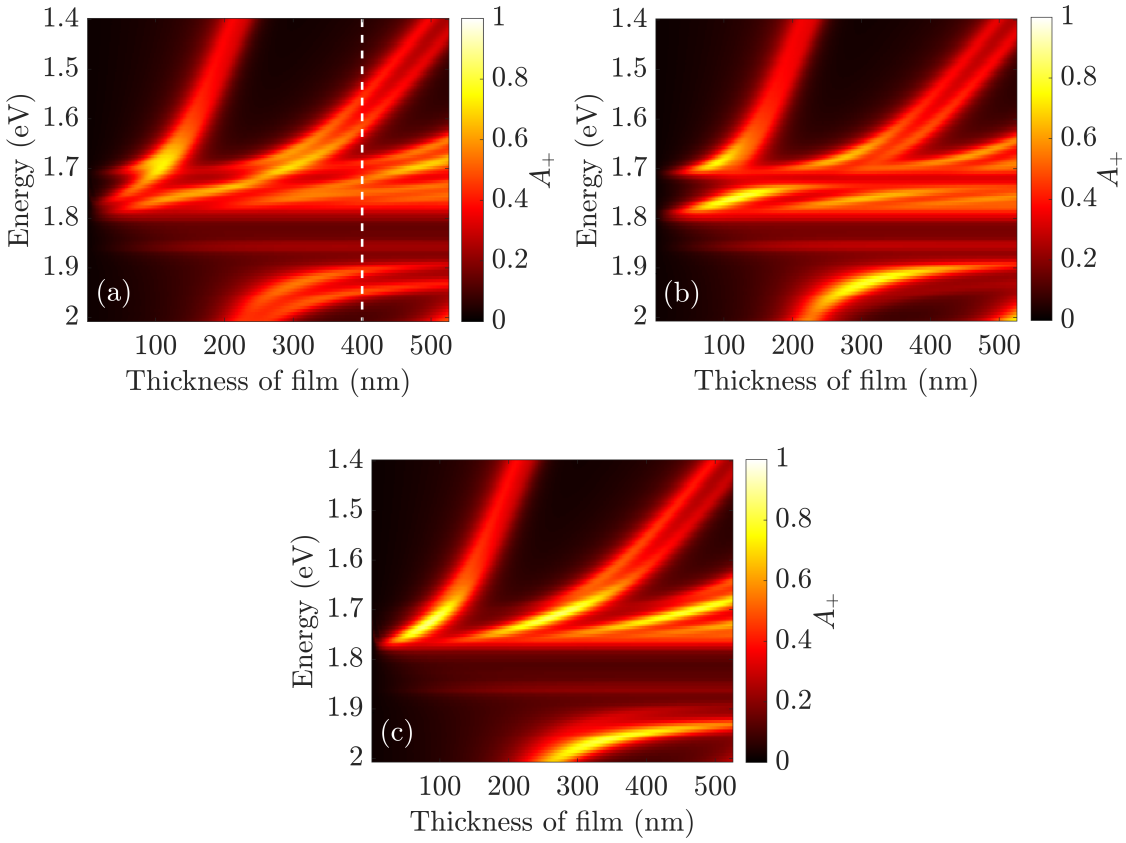

Figure 6.11.: Simulated absorption spectra of the thin film of the Zn-SiPc-SURMOF-2 in the cavity. The illumination is a left-handed circularly polarized **(a)**, a TE-polarized **(b)**, and a TM-polarized plane wave **(c)**. For all spectra, the straight absorption lines of the cavity are bent close to the energy range between 1.7 eV and 1.9 eV, in which the SURMOF material shows absorption resonances. Due to the anisotropy of the material, all absorption lines appear twofold. For the TE- and TM-polarized plane wave, one of the absorption lines is always less intensive. Adapted with permission from [P4]. Copyright © 2022 John Wiley and Sons.

for different wavelengths of a plane wave and different values of the thickness of the film. The thickness is increased by adding a corresponding number of molecular layers in the simulation. The plane wave is normal incident and left-handed circularly polarized. We observe a broad range of large absorption between 1.7 eV and 1.9 eV. This agrees with the absorption spectrum in Figure 6.9 computed with DFT and the experimentally measured spectra in Figure 6.7, which show three absorption peaks in this energy range. Here, circularly polarized light is used to simulate the situation of unpolarized light considered in [172]. In Figures 6.10**(b)** and **(c)**, the absorption spectra of TE- and TM-polarized plane waves are depicted. As the molecular crystal does not have a C_4-symmetry with respect to the z-axis, both spectra differ from each other. We recall that for normal incidence, TE-polarization corresponds to a polarization along the y-axis and TM-polarization corresponds to a polarization along the x-axis.

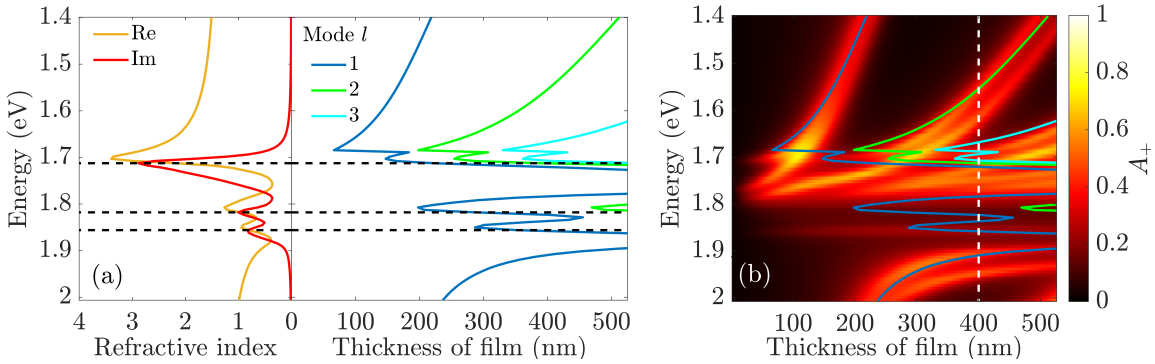

Figure 6.12.: Effective refractive index and mode analysis **(a)** and absorption spectrum of the cavity filled with the Zn-SiPc-SURMOF-2 **(b)**, plotted with a modified version of [185]. The computed cavity modes agree well with the lines of large absorption. Differences can be related to neglecting the anisotropy for the computation of the refractive index. At the thickness of 400 nm (dashed white line), which is also considered in the experiment in [172], two different cavity modes are observed. This is due to the considerable dispersion of the refractive index.

In the next step, we analyze the response of the filled cavity. Figures 6.11**(a)**, **(b)**, and **(c)** display the absorption spectra for a left-circularly, TE-, and TM-polarized incident plane wave, respectively. There are three main observations for the spectrum in Figure 6.11**(a)**. First, there are straight absorption lines which are bent in the region between 1.7 eV and 1.9 eV, where the SURMOF shows broad absorption. The straight absorption lines are the cavity modes, as we show below. The cavity modes are bent, due to the coupling to the SURMOF. This implies that the presence of the SURMOF strongly influences the nature of the propagation of the light inside the cavity. Second, at the thickness of the cavity of 400 nm used in the experimental measurements from [172] and indicated with a white dashed line in Figure 6.11**(a)**, two dominant absorption peaks can be observed at approximately 1.6 eV and 1.9 eV. The positions of these peaks agree well with the positions of the absorption peaks measured in the experiment. These two peaks are analyzed in detail below. Third, every absorption line consists of two closely neighboring lines. Since the spectra for linearly polarized plane waves in Figures 6.11**(b)** and **(c)** always show one of both lines more pronounced, we deduce that the twofold occurrence is caused by the anisotropy of the SURMOF material. We also observe both lines for the two linear polarizations, as the x- and y-axis of the SURMOF material are not its principal axes.

Mode Analysis of the Filled Cavity

To further characterize the optical response of the filled cavity and, more specifically, the peaks at approximately 1.6 eV and 1.9 eV, the refractive index $n_{\mathrm{S}}(\omega) = \sqrt{\varepsilon_{\mathrm{r,eff}}\mu_{\mathrm{r,eff}}}$ of the film is computed with the homogenization method described in Chapter 5. As the mode analyis is restricted to scalar values of the refractive index, the four blocks of the T-matrix of the finite-size molecular model are rotationally averaged. The lattice constants are also averaged. As we are mainly interested in a qualitative interpretation of the absorption spectrum, this simplified method is sufficient for the further analysis. With the refractive index of the

material at hand, we perform a mode analysis of the absorption spectrum. The cavity modes are obtained by solving the phase-matching condition for coherently forming a mode, which reflects off the interfaces between the molecular film and the mirrors. It is given by [P4, Eq. (5)]

$$2\left|\mathrm{Real}\{k_z(\omega)\}\right|L(\omega) + \phi_1(\omega) + \phi_2(\omega) = 2\pi l\,. \tag{6.5}$$

As we consider normal incidence in z-direction, the real part of the z-component of the wave vector is $|\mathrm{Real}\{k_z(\omega)\}| = \frac{\omega \mathrm{Real}\{n_\mathrm{S}(\omega)\}}{c_0}$. $L(\omega)$ is the thickness of the film, $l \in \mathbb{Z}$ denotes the mode index, and $\phi_1(\omega)$ and $\phi_2(\omega)$ correspond to the phases of the reflection coefficients at the two mirrors. As the phases of the reflection coefficients can be computed with *mpGMM* [51], one can determine the necessary thickness $L(\omega)$ of the cavity for a specific mode at a frequency ω. It is given by [P4, Eq. (6)]

$$L(\omega) = \frac{c_0}{\omega \mathrm{Real}\{n_\mathrm{S}(\omega)\}}\left(\pi l - \frac{\phi_1(\omega) + \phi_2(\omega)}{2}\right)\,. \tag{6.6}$$

Both the refractive index and the cavity modes are shown together with the absorption spectrum of the cavity filled with the SURMOF in Figures 6.12**(a)** and **(b)**. First, we

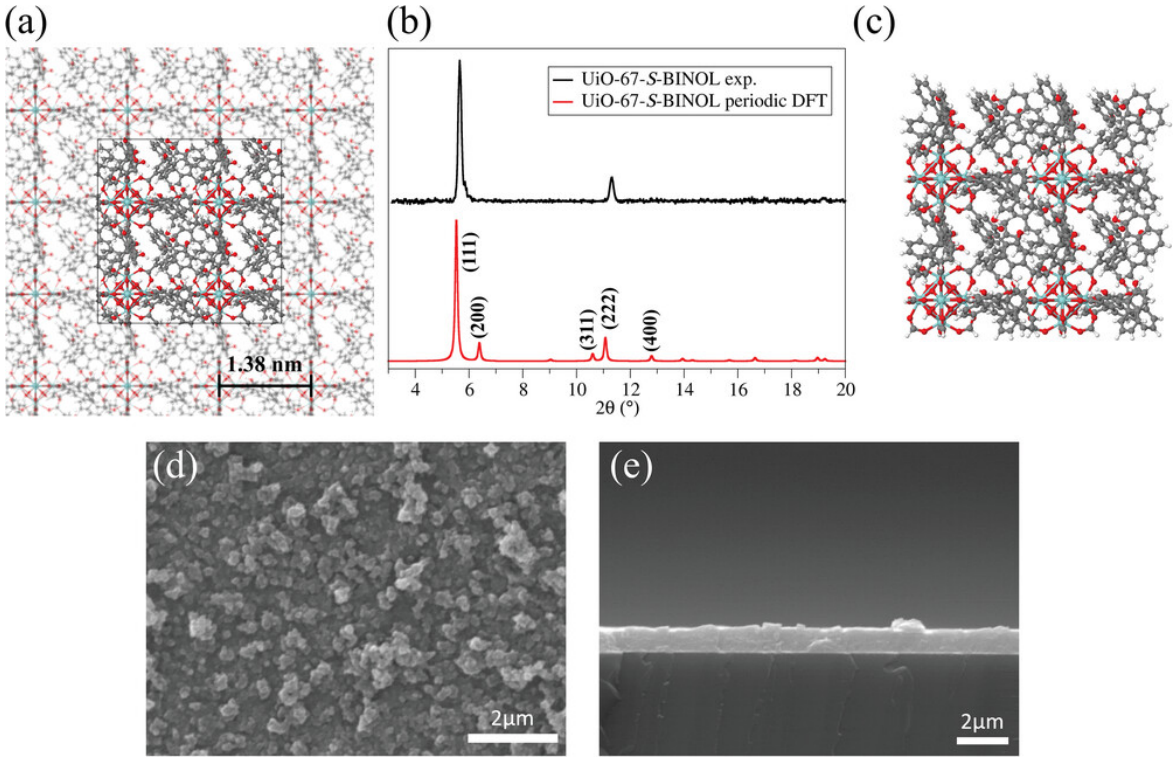

Figure 6.13.: Optimized unit cell of the UiO-67-*R*-BINOL MOF **(a)**. In panel **(b)**, the simulated and measured XRD out-of-plane diffractograms are depicted. Panel **(c)** shows the finite-size molecular model used for the TD-DFT and multi-scale simulation. Panels **(d)** and **(e)** depict the top- and side-view SEM images of the MOF film deposited on a glass substrate, respectively. Created by Marjan Krstić. Reprinted with permission from [P3]. Copyright © 2023 John Wiley and Sons.

observe a good agreement between the cavity modes and the absorption lines of the cavity. Discrepancies are due to the negligence of the anisotropy of the material in the computation of the modes. Second, we consider the film thickness of 400 nm more closely. Here, we observe that the two absorption peaks at 1.6 eV and 1.9 eV correspond to two different cavity modes. This is a surprising result as usually one observes a single split cavity mode, see [183]. We relate this observation to the large dispersion of the refractive index of the SURMOF material, which varies between 0.4 and 3.4 for the two energy regions. The strong dispersion has the following effect: For energies around 1.9 eV, the refractive index is very low, so that here the first cavity mode is present at a thickness of 400 nm. For energies around 1.6 eV, the refractive index is considerably larger. Here, the second cavity mode occurs at a thickness of 400 nm. With the next two instances of molecular materials, we take a close look on the occurrence of split cavity modes and compare the results to each other.

6.3.2. Chiral UiO-67-BINOL MOF

In the next example, we consider a chiral UiO-67-BINOL metal-organic framework. We recall that chiral molecules cannot be superimposed on their mirror image. This leads to interesting optical phenomena. One instance is circular dichroism which is equal to the difference of the absorption of left- and right-handed circularly polarized plane waves. Note that the circular dichroism signal is in the considered wavelength range related to electronic transitions [P3]. It is also commonly referred to as electronic circular dichroism. In the infrared wavelength range, chiral molecules show a circular dichroism signal related to vibrational transitions. This is commonly referred to as vibrational circular dichroism, see [106]. The optical properties of the UiO-67-BINOL MOF have been analyzed both theoretically and experimentally in [P3]. The DFT computations for this analysis have been prepared and performed by Marjan Krstić and Christof Holzer. Chun Li, Simon Oßwald, Jochen Bürck, and Lars Heinke have been the main responsible persons for the experimental studies. The optical simulations have been performed by the author with *mpGMM* [51].

The MOF is a Zirconium-based UiO-67 type MOF. The organic linkers are chiral [1,1'-Binaphtalene]-2,2'-diol (BINOL) molecules. For the experimental measurements, a film of this MOF is grown via vapor-assisted conversion [186] on a quartz substrate. This enables a precise control of the thickness of the final film.

(TD)-DFT Simulations

The dipolar polarizability tensor and the T-matrix are computed with the same workflow as for the previous example of the Zn-SiPc-SURMOF-2. First, the periodic DFT code CP2K is used to optimize the material [156]. As the BINOL likers are chiral, an *R*-version and a *S*-version of the MOF exist. All size dimensions are the same for both enantiomers. The dimensions of the unit cell, depicted in Figure 6.13**(a)**, are computed to be the same in all directions with $a = 2.7647106$ nm. With DFT, the X-ray diffraction pattern is calculated. It is depicted in Figure 6.13**(b)** together with the experimentally measured out-of-plane diffractogram of the UiO-67-*S*-BINOL MOF thin film. Due to the good agreement, we deduce that the geometry parameters of the simulated model represent the structure of the grown film. In the next step, the finite-size molecular model of the optimized material is selected. In comparison to the unit cell considered in CP2K, the difference is that the finite-size molecular model used for the computation of the T-matrix does not exhibit cut molecules or broken bonds. The latter is achieved by saturating the bonds with hydrogen atoms. The

finite-size molecular model of the UiO-67-*R*-BINOL version is depicted in Figure 6.13**(c)**. It consists of 1074 atoms. In Figures 6.13**(d)** and **(e)**, we show scanning electron microscopy images of the experimentally grown thin MOF film. It covers the substrate and shows several crystallites.

The dipolar polarizability and the T-matrix of the finite-size molecular model are computed with TURBOMOLE [148, P9] as described in Chapter 4. Here, the PBE functional [187, 188] and the def2-SVP basis set [99] are used. The T-matrix of the *S*-version, which corresponds to the mirror image of the MOF, is obtained by mirroring the T-matrix of the *R*-version. The trace of the imaginary part of the electric-electric tensor $\boldsymbol{\alpha}_{\mathrm{ee}}$ and the trace of the real part of the electric-magnetic tensor $\boldsymbol{\alpha}_{\mathrm{em}}$ can be used to compute the absorption and electronic circular dichroism (ECD) spectra of the orientationally averaged molecular models, respectively. Both quantities are in arbitrary units. They are shown together with the respective experimentally measured values in Figures 6.14**(a)** and **(b)**. The ECD spectra computed from the polarizability tensors are scaled so that the intensities of the simulated and measured peaks agree at 334 nm. The agreement of the position of the peaks is good for all spectra. In this study, we plot the spectra over varying wavelengths and not energies, since this is more common in the context of discussing circular dichroism of chiral molecules.

Optical Response of the Chiral MOF Film on a Substrate and Inside a Cavity

The T-matrices obtained with TD-DFT are used to compute the optical response of a macroscopic thin film on a glass substrate and inside an optical cavity consisting of two aluminum mirrors. Both setups are depicted in Figure 6.15. In the case of the film on the glass substrate, the substrate is assumed to extend into the entire upper half-space to avoid an influence of a finite thickness. The scanning electron microscope images of the thin film in Figure 6.13 show various crystalline domains of the film, which are differently oriented with respect to each other. Therefore, the four block matrices of the T-matrix of the finite-size molecular model

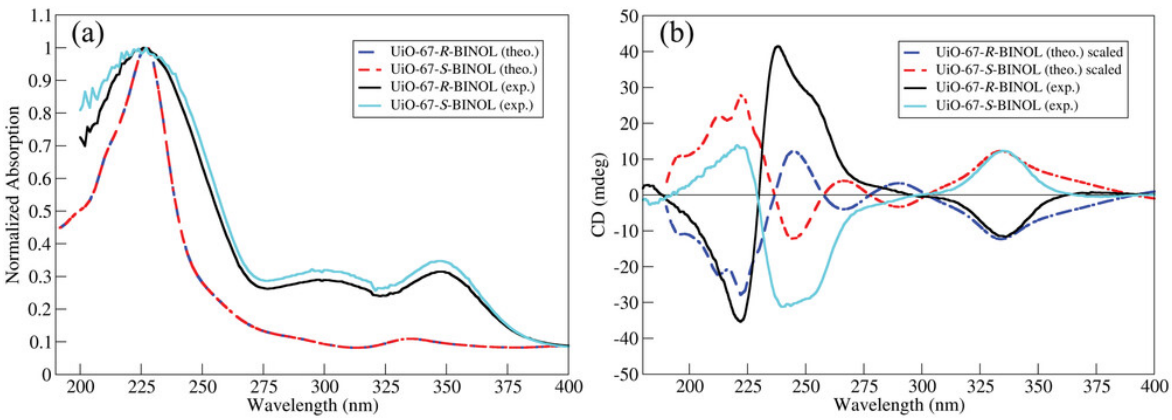

Figure 6.14.: Orientationally averaged absorption **(a)** and circular dichroism spectra **(b)** of the finite-size molecular model of the UiO-67-*R*-BINOL MOF obtained with TD-DFT. The spectra are compared to experimental measurements of a thin film. The circular dichroism spectra computed with TD-DFT are normalized to match the intensity of the peaks at 334 nm. The shape and position of the peaks agree well. Created by Marjan Krstić. Reprinted with permission from [P3]. Copyright © 2023 John Wiley and Sons.

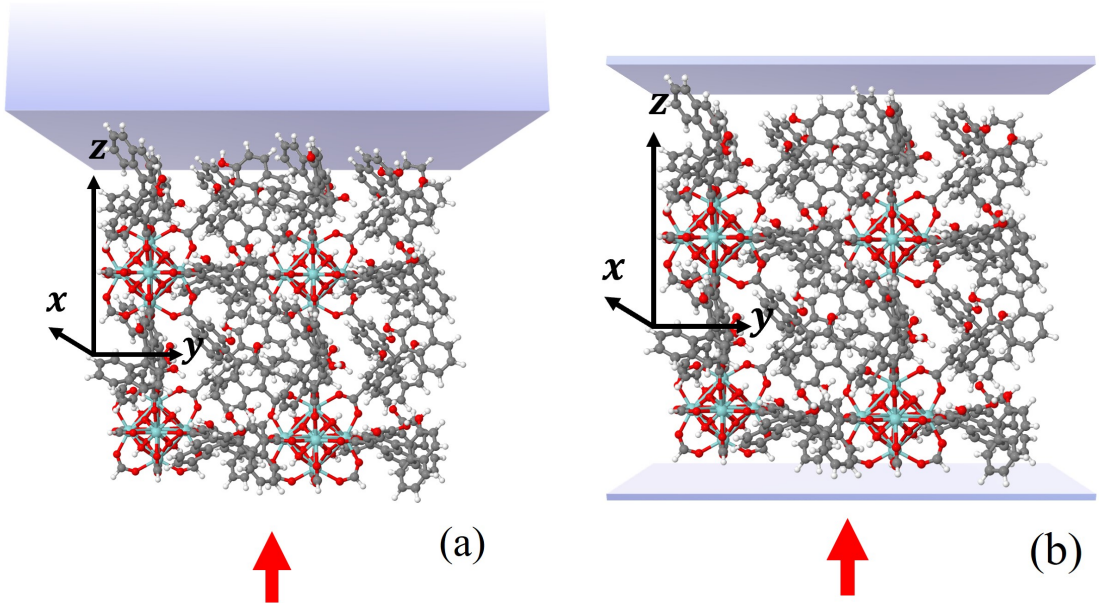

Figure 6.15.: Schematic setups for the simulations of the UiO-67-BINOL MOF thin film. In panel **(a)**, the UiO-67-BINOL MOF is deposited on a glass substrate. Panel **(b)** shows the thin film inside a cavity made of aluminum mirrors. The bottom mirror has a thickness of 10 nm, the top mirror has a thickness of 30 nm. Both setups are illuminated with a normal incident plane wave from below, which propagates in z-direction. The molecular model was created by Marjan Krstić. Adapted with permission from [P3]. Copyright © 2023 John Wiley and Sons.

are rotationally averaged. This is also motivated by the fairly good qualitative agreement between the DFT computed spectra and the experimentally measured spectra.

We consider three different quantities to characterize the optical response of the macroscopic photonic devices, which are illuminated from below with a normal incident circularly polarized plane wave. First, we analyze the absorption $A_{\pm}$ of left-handed (+) and right-handed (−) circularly polarized plane waves, defined in Eq. (2.22). Second, we consider the absorption circular dichroism ACD, defined in Eq. (2.21). Third, the transmission circular dichroism CD in "mdeg" is analyzed. We use its definition from Eq. (2.23). All quantities are computed with *mpGMM* [51].

We first concentrate on the repsonse of the MOF thin films on a glass substrate with a dielectric permittivity of $\varepsilon_{\mathrm{r}} = 2.25$. The thickness of the film is modified by varying the number of layers in z-direction. In Figure 6.16, the absorption of a left-handed circularly polarized plane wave (**(a)** and **(b)**), the ACD (**(c)** and **(d)**), and the CD spectra (**(e)** and **(f)**) are depicted for different wavelengths of the illumination and different values of the thickness of both the UiO-67-*R*-BINOL and UiO-67-*S*-BINOL films, respectively. The circular dichroism spectra of the two enantiomers are perfect mirror images with respect

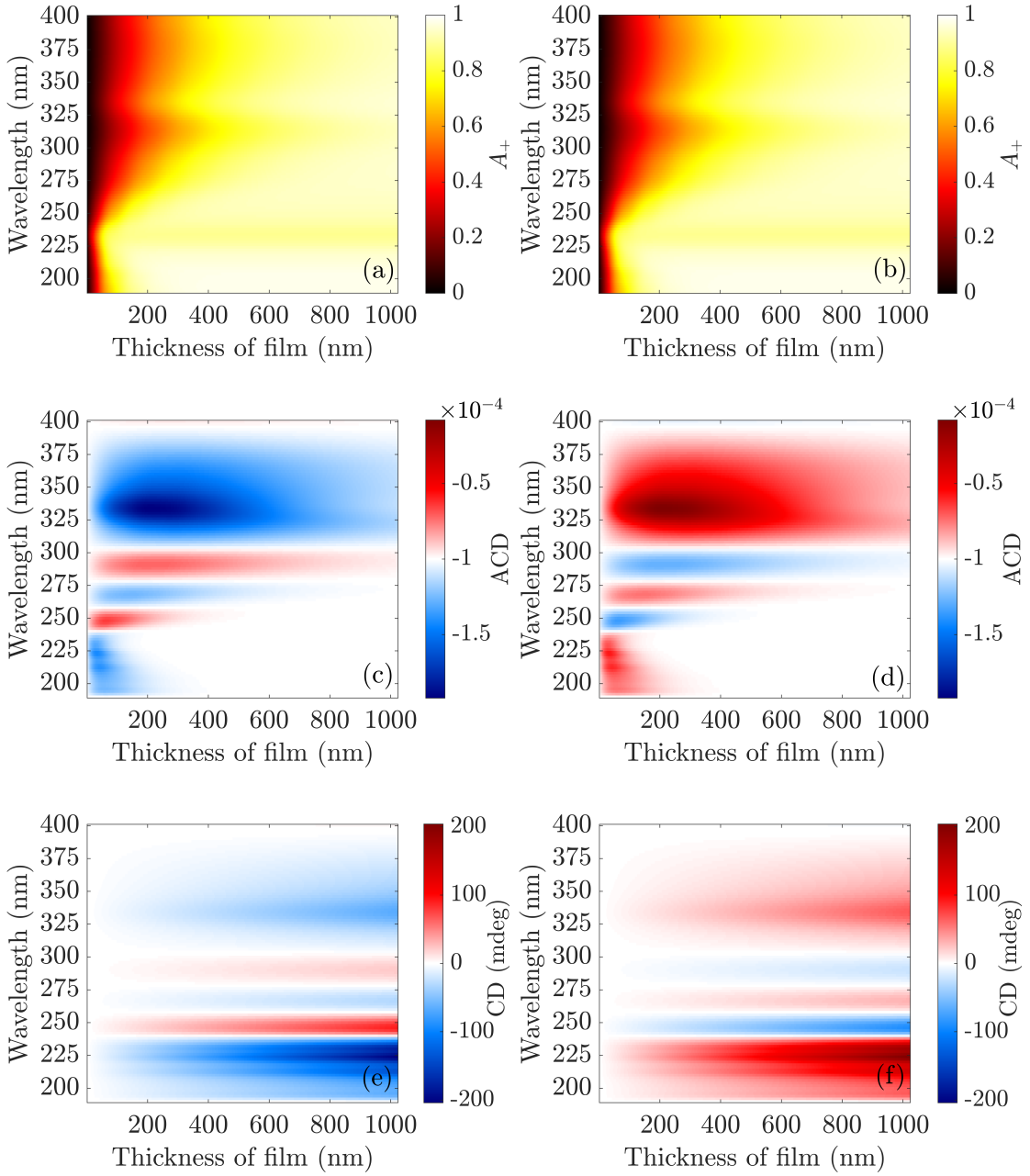

Figure 6.16.: Absorption **(a)**,**(b)**, ACD **(c)**,**(d)**, and CD spectra **(e)**,**(f)** of a thin film of a UiO-67-*R*-BINOL MOF and a UiO-67-*S*-BINOL MOF in vacuum, respectively. The circular dichroism spectra of the two mirrored versions of the MOF are perfect mirror images of each other. The circular dichroism changes its sign for different wavelengths. Adapted with permission from [P3]. Copyright © 2023 John Wiley and Sons.

to each other. Similar to the circular dichroism spectra obtained with DFT, the circular dichroism spectra in Figure 6.16 show different signs for varying wavelengths, showing the dispersive nature of the chiral optical response of the molecules.

For a more conclusive analysis of the dependence of the optical properties on the thickness of the film and a better comparison to the experimentally measured CD spectra, we select three different values of the thickness, namely 250 nm, 500 nm, and 1000 nm. The respective absorption, ACD, and CD spectra are shown in Figure 6.17. Each row corresponds to a specific thickness. The experimentally measured CD spectra are additionally shown in Figure 6.17**(f)**, since the thickness of the film in the experiment is in the range between 500 nm and 1000 nm. We observe that the absorption increases with growing film thickness in the entire wavelength range, because the interaction between light and material is increased. The ACD declines since the transmission signal decreases for larger values of the thickness. In contrast to the ACD, the CD increases with the thickness since the denominator in Eq. (2.23) decreases. The simulated and experimentally measured CD spectra for a thickness of 500 nm in Figure 6.17**(f)** agree well, considering both the position and the intensity of the peaks. This demonstrates the performance of the presented multi-scale approach and the good quality of the prepared film. Discrepancies concerning the intensities of the spectra can be related to possible differences between the thickness chosen in the simulations and the thickness of the actually experimentally characterized thin film. This is also supported by the observation that the agreement between the experimentally measured and the theoretically simulated spectra is better for a thin film of a thickness of 250 nm.

In the next step, we continue with our discussion about the optical coupling of molecular materials to a metallic optical cavity. For this purpose, we consider the optical cavity depicted in Figure 6.15**(b)**, which is filled with the UiO-67-*R*-BINOL MOF. The cavity consists of two aluminum mirrors with a thickness of 10 nm (bottom) and 30 nm (top). The material parameters of aluminum are taken from [189]. We repeat the mode analysis, which we described above, to gain more knowledge about the propagation of the light inside the cavity. In Figure 6.18**(a)**, the effective refractive index is shown together with the modes of the filled cavity. The refractive index is computed with the homogenization approach from Chapter 5. The absorption of the filled cavity for a normal incident left-handed circularly polarized plane wave is depicted in Figure 6.18**(b)** for different wavelengths and different values of the thickness of the film. We observe that the bright regions of high absorption agree very well with the modes of the optical cavity. Especially for low thicknesses, we also see a splitting of the cavity modes, due to the coupling of the cavity and the MOF material. For this MOF, two cavity modes do not occur for the same thickness in the considered wavelength range, provided that the thickness is sufficiently small. This can be related to the small dispersion of the refractive index in comparison to the Zn-SiPc-SURMOF-2. In the discussion of the third instance of a molecular material, we analyze this different coupling behavior more in detail.

Now, we pick a specific thickness to demonstrate the splitting of the absorption peak of the MOF into two peaks due to the coupling to the cavity. In Figure 6.18**(c)**, we show the absorption for a thickness of the film of 47 nm, both in a vacuum and inside the cavity. We observe that the absorption peak of the film in a vacuum is split due to the coupling to the cavity. This is commonly referred to as Rabi splitting and strong coupling [172, 183]. Ref. [172] also suggests to use such a coupling for quantum-electro-dynamical phenomena.

Furthermore, we consider the influence of the cavity on the ACD. The ACD of the filled cavity is depicted in Figure 6.18**(d)** together with the cavity modes. Overall, the ACD exhibits considerably smaller values than the thin film on the substrate. This can be related to two aspects. First, with each reflection off the planar mirrors, the helicity of the plane wave is flipped [190]. The ACD signal cancels, therefore, with each reflection to some extent. Second, a larger absorption, connected to the cavity modes, leads also to a smaller ACD

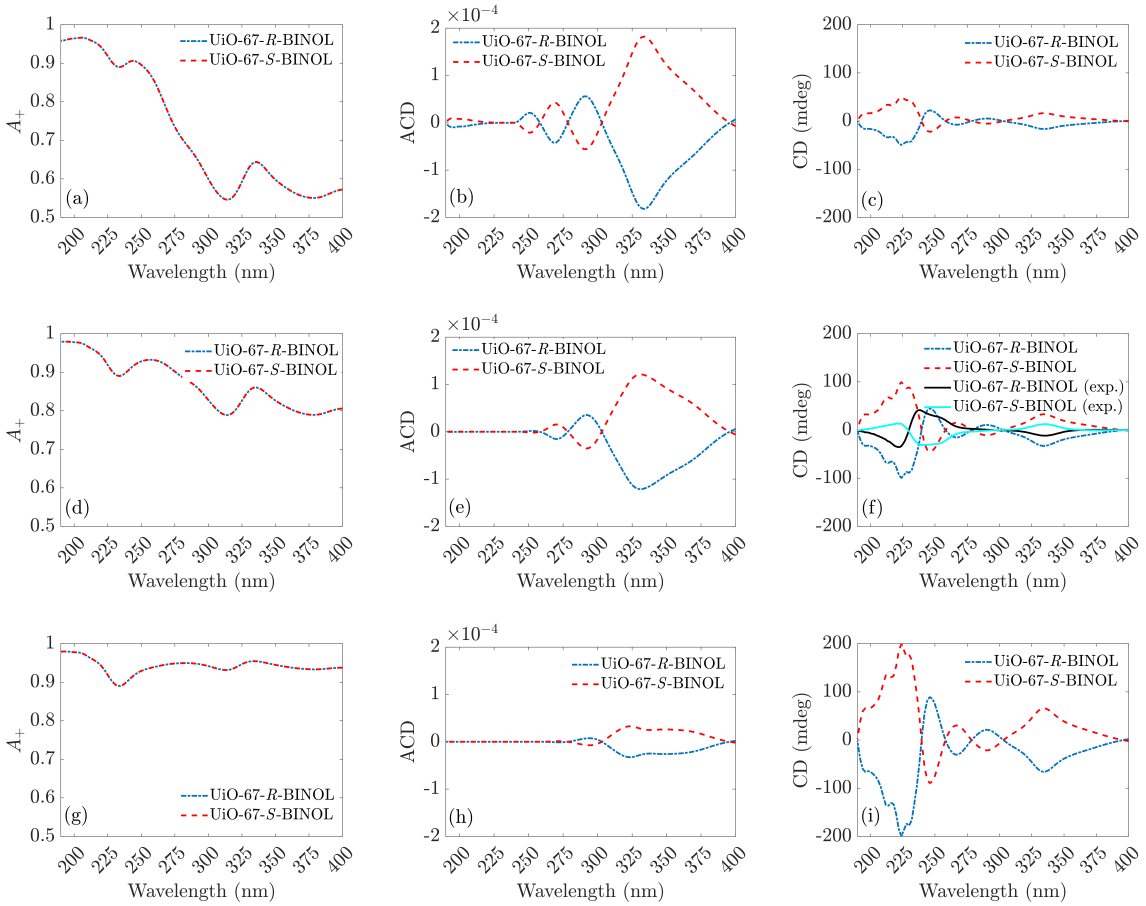

Figure 6.17.: Absorption **(a)**,**(d)**,**(g)**, ACD **(b)**,**(e)**,**(h)**, and CD spectra **(c)**,**(f)**,**(i)** for the chiral UiO-67-BINOL MOF film with a thickness of 250 nm **(a)-(c)**, 500 nm **(d)-(f)**, and 1000 nm **(g)-(i)**. For a thickness of 500 nm **(f)**, also the experimentally measured values of the CD are shown. The agreement of the resonances is very good. The intensity of the peaks agrees well. Adapted with permission from [P3]. Copyright © 2023 John Wiley and Sons.

signal. The ACD signal is at the cavity modes, however, larger than in the other parameter range since destructive interference leads to a cancellation of the signal.

In comparison to the Zn-SiPc-SURMOF-2, there is a main advantage providing a larger range of applications: The UiO-67-*R*-BINOL-MOF is chiral, providing an additional degree of freedom to the split energy states, as the absorption of the energy states depends on the polarization of the incident light.

6.3.3. TDBC J-Aggregates Embedded in a Polyvinyl Alcohol Polymer

As a third instance, we consider a film of randomly oriented 5,6-dichloro-2-[[5,6-dichloro-1-ethyl-3-(4-sulphobutyl)benzimidazol-2-ylidene]propenyl]-1-ethyl-3-(4-sulphobutyl) benzimidazolium hydroxide (TDBC) J-aggregates, embedded in a polyvinyl alcohol (PVA) polymer. For the molecular film inside a metallic cavity, time-resolved spectroscopic measurements have been performed [183], showing a clear experimental evidence for Rabi splitting and

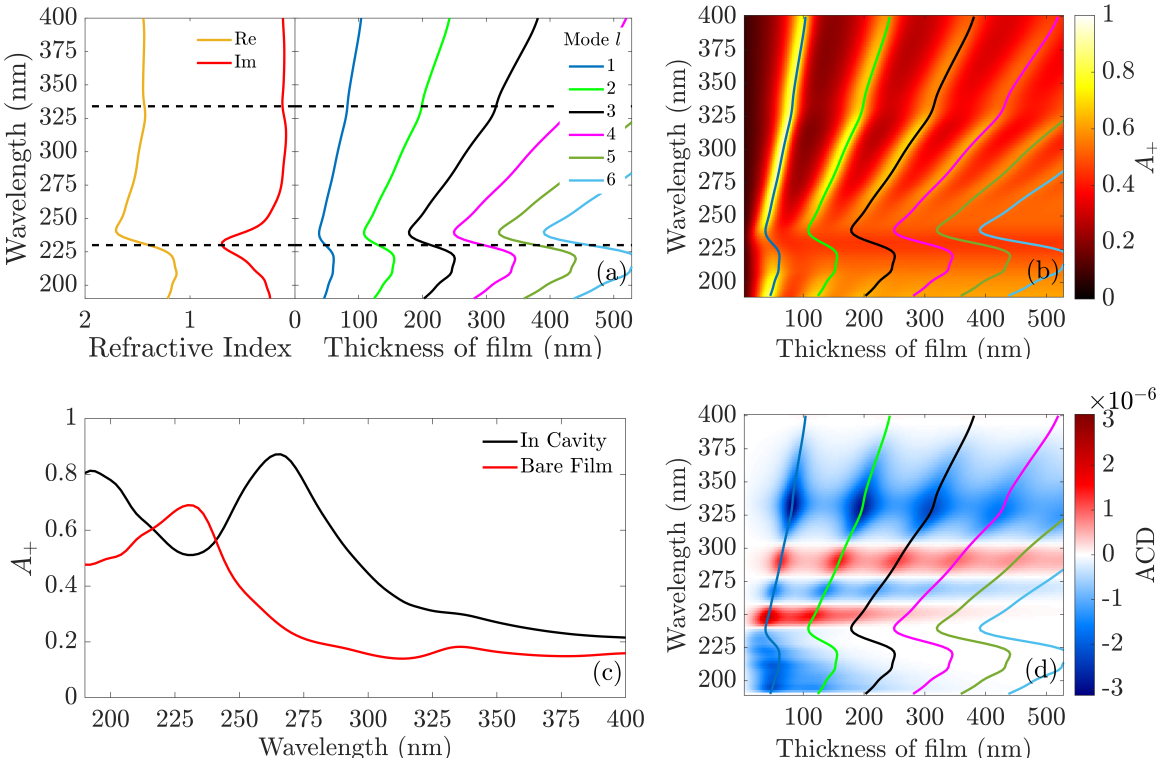

Figure 6.18.: Analysis of the coupling between the cavity and the UiO-67-*R*-BINOL-MOF thin film. Panel **(a)** shows the refractive index of UiO-67-*R*-BINOL-MOF and the mode analysis of the filled cavity. In panel **(b)**, the absorption of the cavity is depicted, filled with the UiO-67-*R*-BINOL-MOF. We observe for small values of the thickness that the respective two branches of high absorption belong to the same split cavity mode. Panel **(c)** shows the absorption of the filled cavity for a thickness of 47 nm. The absorption peak of the bare film in a vacuum is split into two peaks within the cavity. In panel **(d)**, the ACD spectrum of the filled cavity is depicted. We observe that the ACD is influenced by the cavity modes. In the entire parameter range, the values of the ACD are smaller in comparison to the film without cavity. Panels **(b)**, **(c)**, and **(d)** are adapted with permission from [P3]. Copyright © 2023 John Wiley and Sons.

strong coupling. In [183], an absorption peak of the thin film of TDBC J-aggregates on a substrate is observed at 2.14 eV. In comparison to the two systems above, the film of randomly oriented TDBC J-aggregates is not crystalline. With this instance, we demonstrate that the presented multi-scale approach is not limited to periodic structures.

The optical response of the thin film inside a cavity is analyzed in [P4]. Marjan Krstić and Christof Holzer have prepared and performed the DFT computations for this analysis. Ivan Fernandez-Corbaton has developed the mode analysis of the filled cavity. The optical simulations have been performed by the author with *mpGMM* [51].

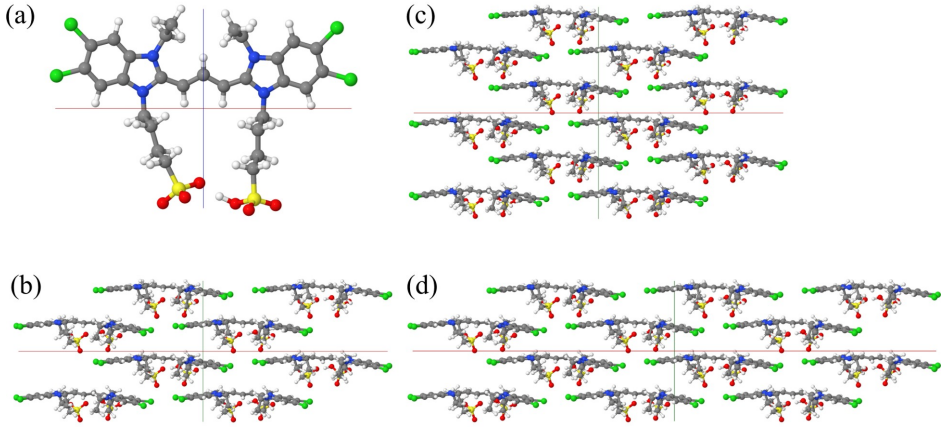

Figure 6.19.: Monomer **(a)**, "2×4" **(b)**, "2×6" **(c)**, and "3×4" **(d)** model of the cluster of the TDBC J-aggregates, used for the TD-DFT simulations. Originally created by Marjan Krstić. Adapted with permission from [P4]. Copyright © 2022 John Wiley and Sons.

(TD)-DFT Simulations

As the system is not crystalline, periodic DFT simulations are not used to optimize the system but a neutral cis-TDBC molecule is optimized with a polarizable continuum implicit solvation model. For the solvation model, a mixture of 95/5 wt% of PVA/H_2O with a refractive index of $n_\mathrm{h} = 1.4727$ is assumed. The cis-TDBC monomer is shown in Figure 6.19**(a)**. For the optimization, the Gaussian 16 code [191] with the hybrid PBE0 functional [166, 167] and the def2-TZVP basis set [99, 192] are used. Three different models are constructed from the optimized monomer. They are in one plane and are denoted by "2×4", "2×6", and "3×4", shown in Figure 6.19**(b)**-**(d)**. They correspond to different numbers and arrangements of the monomer.

To compute the polarizability tensors of the molecular models inside the host medium, the TDBC J-aggregates are considered in a conductor-like screening model (COSMO) PVA/H_2O implicit surrounding [193]. Here, the PBE functional is used [187, 188]. In Figure 6.20, the rotationally averaged absorption spectra of the models are shown computed from TD-DFT calculations. Comparing to the experimental measurement of the absorption of the thin film in [183], one can deduce that the agreement improves if the simulated model increases in size, both in x- and y-direction. For the model "3×4", the absorption peak is at approximately 2.3 eV, which agrees well with the experimentally measured value of 2.14 eV.

Optical Response of the Film of J-Aggregates Inside a Cavity

We continue with the multi-scale simulations of a thin film of TDBC J-aggregates. Here, we focus on the "3×4" model. In Appendix B, we also analyze the "2×4" and "2×6" models, which show a very good agreement to the results for the "3×4" model. The agreement of the spectra demonstrates that the chosen model is suitable for the multi-scale analysis. Based on the estimated concentration of the J-aggregates in the film from [183], the concentration for the "3×4" model is set to $\frac{1}{12} 10^{20}\,\mathrm{cm}^{-3}$. The polarizability tensors are rotationally averaged to obtain a scalar value for each of the four tensors. Then, with the Lorentz-Lorenz formulas

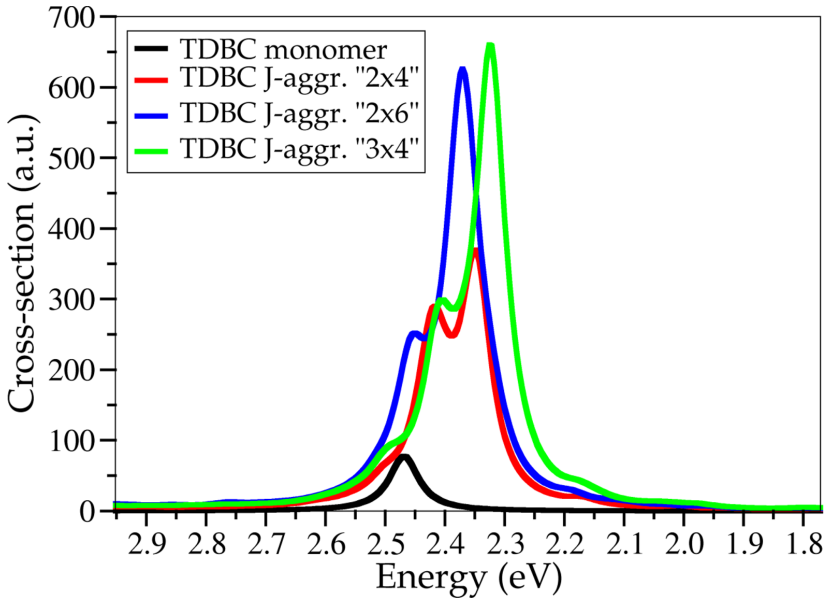

Figure 6.20.: Orientationally averaged absorption cross sections of the different molecular models from Figure 6.19, computed with TD-DFT. Originally created by Marjan Krstić. Adapted with permission from [P4]. Copyright © 2022 John Wiley and Sons.

from [113], the effective permittivity and permeability of the material are computed. Here, Lorentz-Lorenz formulas are used since the material consists of randomly oriented molecular clusters in a solution, that do not form a periodic lattice. The thin film is considered within a cavity of two planar silver mirrors. Both have a thickness of 30 nm, equivalently to the experimental setup in [183]. Figure 6.21**(a)** shows the refractive index, obtained from the effective material parameters, and the mode analysis. In **(b)** the absorption spectrum of the filled cavity is depicted. For a thickness of 145 nm used in the experiment [183], we observe two absorption lines, which correspond to the same split cavity mode. Figures 6.22**(a)** and **(b)** show the absorption spectra of the thin film in a vacuum and the filled cavity for a film thickness of 145 nm and 120 nm, respectively. We observe in both spectra that the single absorption peak of the film in vacuum is split into two absorption peaks, when placed into the cavity. For a thickness of 120 nm, the peaks are symmetrically arranged on both sides of the resonance of the thin film in a vacuum. Here, we clearly observe the behavior, demonstrated experimentally in [183]. The Rabi splitting energy of 250 meV is smaller than the experimentally observed value of 350 meV [183]. The differences of the chosen thickness and the Rabi splitting energy in comparison to the experimental measurements can be related to inaccuracies of the DFT simulations and the estimation of the concentration of the TDBC J-aggregates in the solution.

In contrast to the first instance of the Zn-SiPc-SURMOF-2, the refractive index of the material of TDBC J-aggregates is far less dispersive, as we see in Figure 6.21**(a)**. This is similar to the case of the UiO-67-*R*-BINOL MOF. Increasing the concentration artificially by a factor of five, a refractive index, cavity modes, and an absorption spectrum are obtained, which are shown in Figure 6.23. In Figure 6.23, we also observe in some regions for a specific thickness that two different split cavity modes occur, similar to the case of the Zn-SiPc-SURMOF-2. The dispersion of the refractive index is in this case also comparable to the dispersion of the

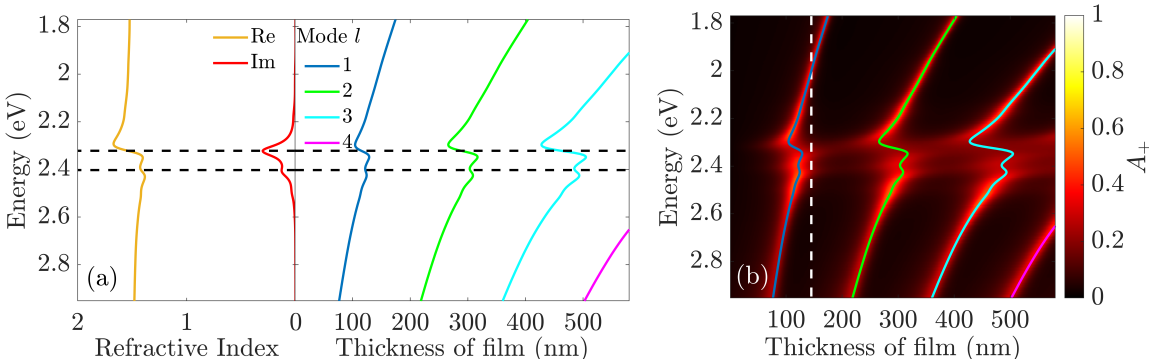

Figure 6.21.: Mode analysis of a cavity filled with TDBC J-aggregates in a PVA polymer. Panel **(a)** depicts the effective refractive index and the mode analysis. Panel **(b)** shows the absorption spectrum. The model "3 × 4" is used. All cavity modes are separated from each other in the sense that for each specific value of the thickness only one cavity mode is observed. The cavity modes show the coupling between the cavity and the molecular material resonances between 2.3 eV and 2.4 eV. Adapted with permission from [P4]. Copyright © 2022 John Wiley and Sons.

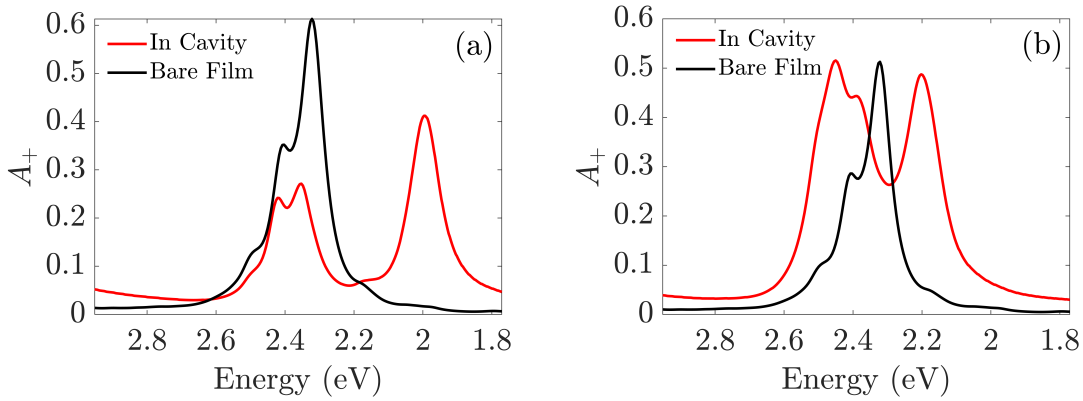

Figure 6.22.: Absorption spectra of the thin film of TDBC J-aggregates in the PVA polymer and of the cavity. Panels **(a)** and **(b)** depict the absorption spectra for a thickness of the film of 145 nm and 120 nm, respectively. For a thickness of 120 nm, the absorption peak of the thin film in vacuum is split into two peaks which are symmetrically positioned around the peak of the thin film in a vacuum. Adapted with permission from [P4]. Copyright © 2022 John Wiley and Sons.

refractive index of the Zn-SiPc-SURMOF-2. From all three examples we conclude, therefore, that increasing the concentration of the filling medium is not necessarily beneficial to increase the Rabi splitting, if one is considering a specific energy range. A concentration which is too large causes large dispersion of the refractive index, and consequently that two different split cavity modes are observed for a set value of the thickness. If one is able, however, to detect the absorption signal of the cavity filled with the Zn-SiPc-SURMOF-2 for energies

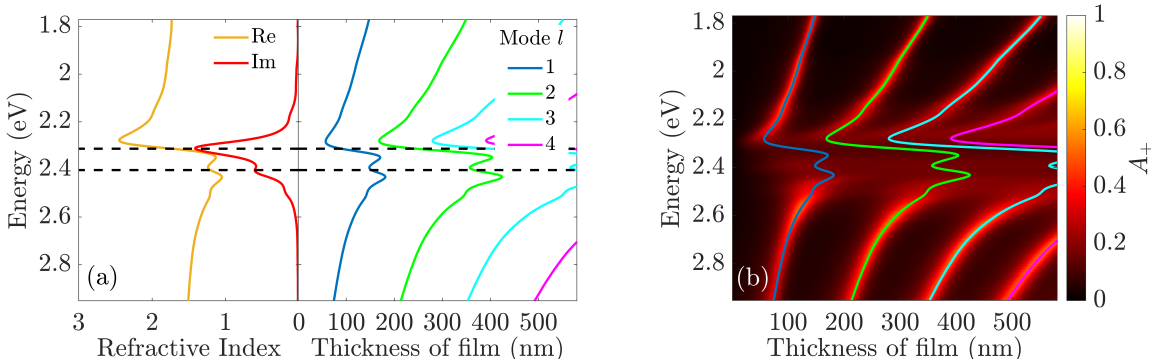

Figure 6.23.: Optical properties of a cavity filled with the TDBC J-aggregates in the PVA polymer. Panel **(a)** shows the effective refractive index and the mode analysis. Panel **(b)** depicts the absorption spectrum with the modes of the filled cavity. The model "3×4" is used, but the concentration of the J-aggregates is artificially increased by a factor of five. In this case, for larger values of the thickness, two different cavity modes are observed for the same value of the thickness, similar to the Zn-SiPc-SURMOF-2. This is due to the large dispersion of the refractive index of the molecular material. Adapted with permission from [P4]. Copyright © 2022 John Wiley and Sons.

beyond 2 eV and for small thicknesses in the range of 100 nm, one might be able to observe a splitting of the same cavity mode.

6.4. Metasurface of a Structured Molecular Film

In this section, we demonstrate that the multi-scale approach can be used to design photonic devices of higher complexity than planar, layered structures. We consider a metasurface consisting of a structured molecular film, analyzed in [P3]. It is a metasurface of cylinders, made of the chiral UiO-67-*R*-BINOL MOF, discussed in Section 6.3. Figure 6.24 displays a single cylinder and a metasurface of cylinders. The goal of the design is to enhance the ACD and CD signals of the MOF material. The calculation of the optical response of the metasurface is performed with the finite-element method in COMSOL Multiphysics [194].

The circular dichroism signal of molecules is an essential spectroscopic quantity to distinguish two enantiomers, which have a different effect in the human body, for instance. It is usually very small, and, therefore, difficult to detect. There are multiple approaches to increase the circular dichroism signal. A large group of them are based on strong near-fields of plasmonic structures or dielectric structures made of materials with a high refractive index such as silicon, for instance [195–204]. To quantify the enhancement of the circular dichroism signal by near-fields, a very common measure is the optical chirality density at the position $\boldsymbol{r}$ of the molecule [205]. In our notation it reads as [74, Eq. (4)], [199, Eq. (4)]

$$C(\boldsymbol{r};\omega) = -\frac{\varepsilon_{\mathrm{h}}\omega}{2}\mathrm{Im}\{\boldsymbol{E}^{\dagger}(\boldsymbol{r};\omega)\boldsymbol{B}(\boldsymbol{r};\omega)\}\,, \tag{6.7}$$

where $\boldsymbol{E}(\boldsymbol{r};\omega)$ and $\boldsymbol{B}(\boldsymbol{r};\omega)$ are the fields at the position of the molecule. From Eq. (7) in [199], one can deduce that the enhancement of the optical chirality density by an achiral

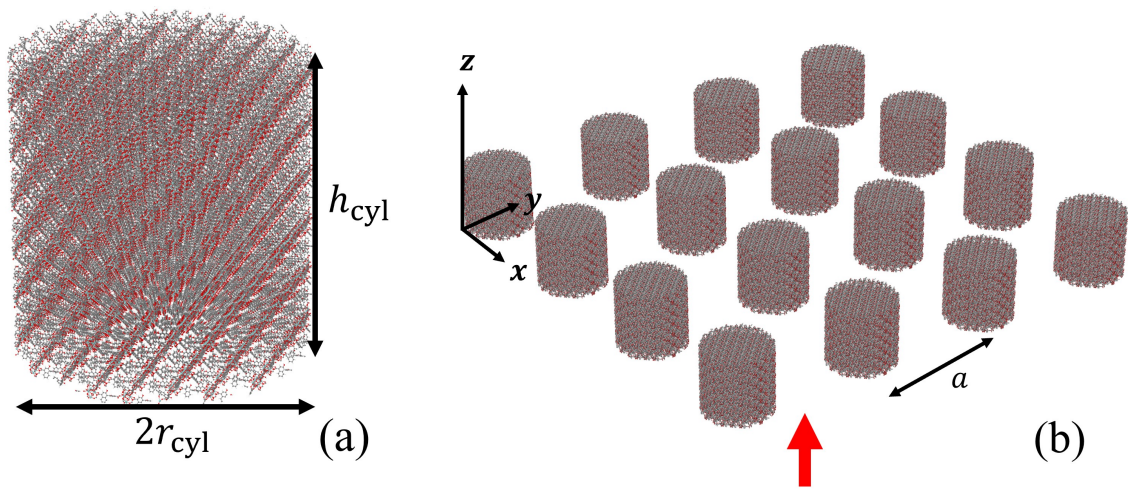

Figure 6.24.: Single cylinder with radius r_{cyl} and height h_{cyl} **(a)** and a metasurface of cylinders **(b)**. The cylinders consist of the UiO-67-*R*-BINOL MOF. The metasurface is illuminated from below with normal incident plane waves, which are circularly polarized. Created in cooperation with Marjan Krstić. Adapted with permission from [P3]. Copyright © 2023 John Wiley and Sons.

nano-scatterer is proportional to the enhancement of the circular dichroism signal. The enhancement of the optical chirality density is computed by comparing the optical chirality density to the case, for which the achiral nano-scatterer is not present. The optical chirality density is averaged over the volume of the molecules.

If the electric and magnetic dipole resonances of a nanostructure overlap, the optical chirality density is considerably increased [199, 200, 202]. This is due to two aspects. First, the left- and right-handed circularly polarized plane waves do not change their polarization upon interaction with the structure. Second, in such a situation, the field strength is considerably enhanced [199]. For metasurfaces, not only the single scatterer but also the design of the lattice dimensions is very important, as lattice resonances can modify and couple multipole moments [201, 203, 204].

In comparison to more traditional setups of a nanostructure enhancing the circular dichroism response of the surrounding molecules, the cylinders consisting of the MOF are designed to increase their own signal inside the metasurface. They simultaneously represent both the nanostructure enhancing the circular dichroism response and the molecules whose circular dichroism signal is enhanced. Additionally, the MOF material is of far more complexity, compared to silicon or other commonly used materials.

6.4.1. Design of the Metasurface

The design approach for the metasurface to enhance the circular dichroism signal is structured as follows. First, the effective material parameters of the UiO-67-*R*-BINOL-MOF material are computed with the homogenization approach from Chapter 5. Here, the effective permittivity and chirality are of major interest. They are both depicted in Figure 6.25. In the second step, a specific wavelength is chosen, for which we aim on enhancing the circular dichroism response. The design wavelength is set to 334 nm. Close to this wavelength, the ACD and CD spectra of the thin film in Figure 6.17 show maxima. Next, a metasurface of cylinders is

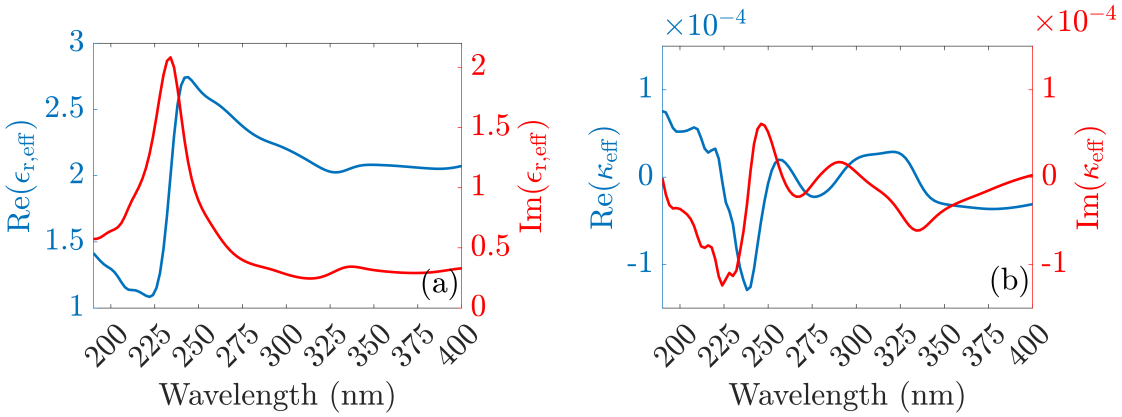

Figure 6.25.: Effective permittivity **(a)** and chirality **(b)** of the UiO-67-*R*-BINOL-MOF. Adapted with permission from [P3]. Copyright © 2023 John Wiley and Sons.

designed to maximize the optical chirality density enhancement, averaged over the volume of the cylinders. In this context, the radius r_{cyl} and the aspect ratio $r_{\mathrm{cyl}}/h_{\mathrm{cyl}}$ of the cylinders inside the lattice are varied. h_{cyl} is the height of the cylinders. Analogously to the study of achiral structures surrounded by chiral molecules, see [199, 200, 202], we neglect the chirality of the molecular material in this step. In this case, for nanostructures surrounded by chiral molecules, the enhancement of the optical chirality density is directly proportional to the enhancement of the circular dichroism. The lattice constant is set to $a = 325.65\,\mathrm{nm}$, which is very close to the design wavelength. This enables the occurrence of lattice resonances. The lattice resonances can be studied in detail with the methods presented in [78, 206].

Figure 6.26**(a)** shows the enhancement of the optical chirality density averaged over the volume of the cylinders for different radii and aspect ratios. We observe the largest enhancement of 2.7 for an aspect ratio of 0.475, which is chosen for the further studies. We continue by incorporating the chirality $\kappa(\omega)$ to the FEM simulations, and compute the ACD for different radii. It is depicted in Figure 6.26**(b)**. We observe a peak at 78.91 nm, which is close to the maximum enhancement of the optical chirality density. The inset in Figure 6.26**(b)** shows that the enhancement of both quantities is related to large near-fields. For the following studies, the radius is set to $r_{\mathrm{cyl}} = 78.91\,\mathrm{nm}$.

6.4.2. Circular Dichroism Signal of the Metasurface for Varying Wavelengths

Based on these obtained design parameters, the ACD and CD spectra are computed for different wavelengths. Here, also the dispersion of the effective material parameters of the MOF is incorporated. Figures 6.26**(c)** and **(d)** display the ACD and CD spectra. Additionally, we show their enhancement with respect to a slab of the same volume. All quantities show a peak at the design wavelength of 334 nm. The ACD has a value of $6.94 \cdot 10^{-5}$ and is enhanced by -1.24 at 334 nm. The CD has a value of 4.45 mdeg, and is enhanced by -2.22.

To explain the nature of the enhancement, we compute the renormalized T-matrix of the two-dimensional lattice of cylinders for normal incidence, analogously to Eq. (5.1) for the three-dimensional case. For this purpose, the T-matrix of a cylinder is computed with JCMsuite [207]. Figure 6.27**(a)** compares the electric and magnetic dipolar components of the T-matrix of the single cylinder and of the renormalized T-matrix. We only consider the components which are in the polarization plane of the incident electric field. Figure 6.27**(b)**

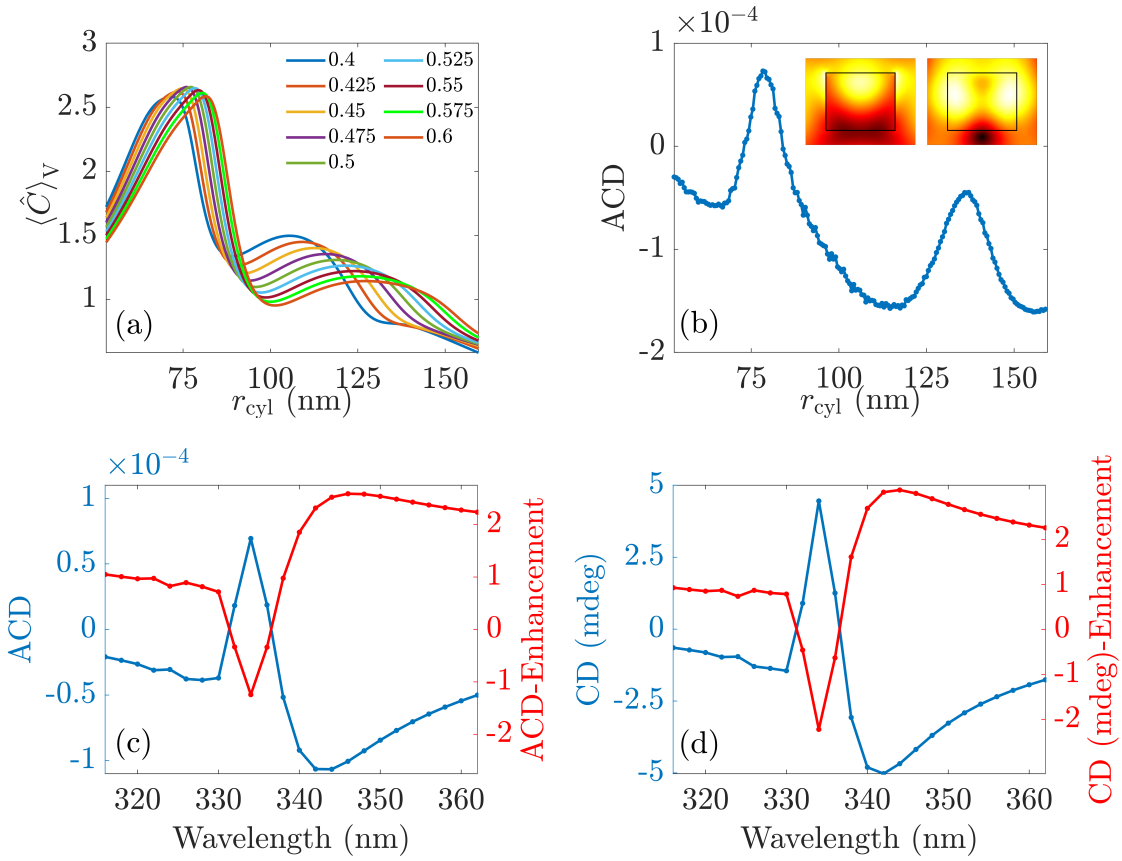

Figure 6.26.: Optical response of metasurface of cylinders. The cylinders consist of the chiral UiO-67-*R*-BINOL MOF. Panel **(a)** shows the enhancement of the optical chirality density averaged over the volume of the cylinder at the design wavelength of 334 nm. In panel **(b)**, the ACD spectrum is displayed for an aspect ratio of $r_{cyl}/h_{cyl} = 0.475$. Panels **(c)** and **(d)** depict the ACD and CD spectra for $r_{cyl}/h_{cyl} = 0.475$ and $r_{cyl} = 78.91$ nm. For the chosen aspect ratio, for which the enhancement of the optical chirality density shows its largest values in **(a)**, the ACD shows a maximum at the radius $r_{cyl} = 78.91$ nm in **(b)**. This is related to large near-fields shown in the inset. Choosing this radius, the ACD and CD exhibit large values close to the design wavelength in the shape of a Fano resonance in **(c)** and **(d)**. Adapted with permission from [P3]. Copyright © 2023 John Wiley and Sons.

depicts the negative real part of the electromagnetic coupling term of the respective T-matrices. This term is proportional to the imaginary part of the chirality, see [P5, Eq. (17)], which is mainly determining the circular dichroism signal. We observe that all entries of the renormalized T-matrix show spectrally narrow resonances close to the design wavelength of 334 nm. This is in contrast to the dipolar coefficients of the T-matrix of the single cylinder. The observation indicates that not only the shape of the cylinder but also the arrangement in the two-dimensional lattice is essential for enhancing the near-fields, the ACD, and the CD spectra.

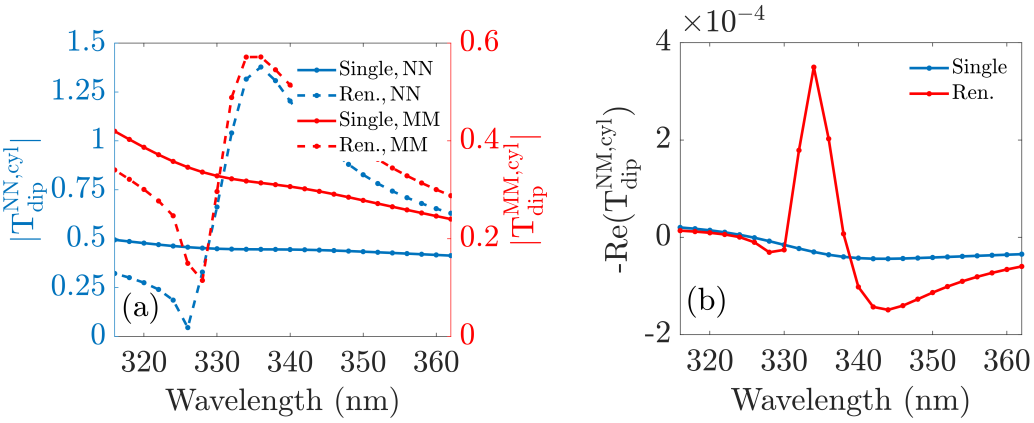

Figure 6.27.: Electric and magnetic dipolar entries **(a)** and negative real part of the electromagnetic coupling dipolar entries of the T-matrix of the single cylinder and of the renormalized T-matrix of the two-dimensional lattice **(b)**. All renormalized entries show a resonance close to the design wavelength of 334 nm. This indicates that the circular dichroism and the near-fields are enhanced due to lattice effects. Adapted with permission from [P3]. Copyright © 2023 John Wiley and Sons.

The ACD and CD spectra have the shape of an asymmetric Fano resonance. This can be related to the interference of different competing response tracks, which are influenced by the chiral response of the MOF material, the dipole moments of the single MOF cylinder, and the coupling of the cylinders. They determine whether the lattice resonance is left- or right-handed polarized [203]. Due to the influence of all these effects, the ACD and CD spectra are reversed at the design wavelength in comparison to a single cylinder and the material. We therefore relate the sign reversal of the circular dichroism signal to the collective multipolar lattice coupling.

For longer wavelengths around 344 nm, the enhancement of the ACD and CD spectra are, with values of 2.6 and 3.1, larger than at the design wavelength. The design wavelength of 334 nm has been chosen, as the circular dichroism of both the MOF material and the slab show a maximum at this wavelength, so that the quantities are easier to detect in a measurement than at the wavelength around 344 nm. We observe in Figure 6.27**(b)**, however, that the electric-magnetic coupling term of the T-matrix of the single cylinder is larger around 344 nm. At this wavelength, the near-fields and optical chirality density are also strong. Due to the dispersion of the MOF material and effects dependent on the geometry of the cylinder, we observe a larger enhancement around the wavelength 344 nm than around the design wavelength. Nevertheless, the designed structure enhances the circular dichroism signal considerably also at the design wavelength.

In this chapter, we presented a multi-scale approach to compute the linear optical response of molecules. It combines quantum-chemical and optical scattering methods. The approach can be used to design photonic devices for enhancing specific linear optical effects of the molecules. We demonstrated the workflow with several instances: First, we analyzed the polarization-dependent optical response of finite molecular islands and monolayers deposited on dielectric substrates. Then, we considered the coupling of different kinds of molecular films to photonic cavities. In the last section, a metasurface of cylinders was designed, consisting

of chiral molecules, which enhance their own circular dichroism signal. This demonstrates the wide area of applications of our multi-scale approach. In all studies, we made use of the fact that our multi-scale approach enables the analysis of single molecules, of finite-size molecular models, and of entire photonic devices. It is covering, therefore, the entire design space.

In the next chapter, we extend the multi-scale approach to include nonlinear optical effects.

7 | Nonlinear Optical Response of Molecules in Photonic Devices

In this chapter, we discuss how to simulate the nonlinear optical response of molecules and of photonic devices incorporating them. For this purpose, we introduce a multi-scale approach that transfers the nonlinear optical response of a finite-size molecular model to the response of a photonic device. This is in complete analogy to the multi-scale approach for linear optical effects presented in Chapter 6. Due to the ongoing research efforts in laser technology and the connected increase of achievable laser power, nonlinear optical effects have become essential for many photonic technologies. Some important instances are direct-write 3D laser lithography [208], high-speed data transmission [209–211], opto-electronic-signal processing in wireless THz networks [212], high-precision frequency metrology [213, 214], electro-optic modulators [215], and quantum optics information processing and second-harmonic efficiency enhancement using nanostructured nonlinear optical materials [216–218].

Molecular materials are very important for linear and nonlinear optical effects [219]. This is based on their large chemical design space. Instances for applications of molecular materials for nonlinear optical effects are multiphoton absorption [220], two-photon absorption of metal-assisted chromophores [221], second-harmonic generation (SHG) by SURMOFs [222], and the modification of the refractive index of organic chromophore-containing polymers [223]. Usually, qualitative and quantitiative knowledge about the nonlinear optical properties of these molecular materials is essential [P6]. Qualitatively, it is very important to know which entries of the tensor are non-zero describing the anisotropic nonlinear optical properties. In this regard, the polarization and the incidence angle of the fundamental waves can be adapted. Quantitatively, the size of these entries is important to predict the nonlinear optical response of a molecule. Both the qualitative and quantitative knowledge, however, is rather sparse.

It is very common to describe photonic devices showing nonlinear optical effects with Maxwell's equations and the nonlinear polarization introduced in Section 2.1.2. For this purpose, the materials involved in the devices are macroscopically described by a nonlinear optical susceptibility tensor [224], see also Eq. (2.13). The nonlinear optical susceptibility tensor is either computed based on phenomenological grounds, as we see below, or obtained experimentally [225–227]. These techniques, however, suffer from several limitations. For molecular materials, for instance, an experimental analysis of the large chemical design space cannot be performed efficiently. There is, therefore, a need for a multi-scale approach to accurately compute the nonlinear optical properties of the molecular materials. These properties can be used to compare different molecules to choose the most suitable candidate and to design photonic devices providing specific nonlinear optical effects.

In Section 4.2, we showed that the first-order hyperpolarizability tensor of a finite-size molecular model can be computed with *ab initio* quantum-chemical methods such as TD-DFT. Based on this microscopic quantity [228], the second-order nonlinear optical susceptibility of crystalline molecular materials has been computed in [100, 229–238], for instance. Urea is, in general, a very important example in such SHG studies, see also [239, 240], for instance. Computing the second-order nonlinear optical susceptibility tensor is, however,

often connected to approximations for the interaction between the molecules and to the assumption that the molecular material is infinitely extended in all three dimensions, as we see below. Surface nonlinear optical effects, which are originating mainly from a thin region close to the surface of the material, cannot be sufficiently described by such an approach.

In Section 7.1, we present a multi-scale approach that does not suffer from this limitation, transferring the nonlinear optical response of a single molecule to the response of a two-dimensional layer, and finally to a stack of layers forming a thin film. For this purpose, we introduce the Hyper-T-matrix. Similar to the dipolar T-matrix, which can be computed from the dipolar polarizability tensor, the Hyper-T-matrix is computed from the first-order hyperpolarizability tensor. We concentrate in this chapter on the SHG response of molecular materials. The approach, however, is general and can be adapted to other second-order and higher-order nonlinear optical effects. With the example of the SHG response of an urea thin film on a substrate and inside a metallic cavity, we demonstrate the multi-scale approach and its applicability.

In Section 7.2, we analyze the surface SHG response of a molecular film with the multi-scale approach. This is an application of the approach, which cannot be suitably performed by an effective medium theory, as each layer's response is different.

The multi-scale approach to compute the second-harmonic generated response of molecular bulk material, discussed in Section 7.1, has been introduced in [P6]. The source code to calculate the SHG response of molecular materials has been developed in cooperation with Dominik Beutel and is an extension of *mpGMM* [51]. Marjan Krstić and Christof Holzer have prepared and performed the DFT computations for the studies in Section 7.1 and [P6]. The surface SHG response of molecular films, discussed in Section 7.2, has been analyzed in [P7]. Marjan Krstić, Alejandro Luna Díaz, and Christof Holzer have developed and used the concept to compute the surface SHG of finite molecular materials with DFT. The concept of the Hyper-T-matrix has been developed and the optical simulations have been performed by the author.

7.1. Multi-Scale Approach to Compute the Nonlinear Optical Response of Molecules

In this section, we introduce a multi-scale approach to compute the nonlinear optical response of molecular materials and devices thereof. We concentrate in this regard on their SHG response. The essential requirement for the multi-scale approach is that it translates the SHG response of a finite-size molecular model to an entire photonic device, covering all intermediate length scales. We introduce the Hyper-T-matrix of a finite-size molecular model and use it to obtain the SHG response of a molecular material. Similar to the T-matrix, which is the bridge between the microscopic and macroscopic description of linear effects, the Hyper-T-matrix is the bridge between the microscopic and macroscopic description of nonlinear effects. First, we use the multi-scale approach to analyze the SHG response of a crystalline urea thin film in a vacuum. In this context, we compare the computed SHG field amplitudes to results obtained with COMSOL Multiphysics [241]. The latter are based on effective medium theory. Finally, we design a metallic cavity to enhance the SHG response of the urea thin film.

7.1.1. The Hyper-T-Matrix and its Role for the Multi-Scale Approach

The standard T-matrix for linear scattering phenomena describes the relationship between multipolar incident and multipolar scattered field coefficients of an object. In [242, 243] the T-matrix formalism is extended to obtain the SHG signal of finite clusters of objects, describing them with second-order susceptibilities. Here, we present an approach to obtain the nonlinear optical response of molecular systems based on their *ab initio* computed quantum-chemical properties. We use the Hyper-T-matrix from [P6] to compute the SHG response in a similar way as the T-matrix for linear effects. In analogy to the T-matrix, the Hyper-T-matrix relates the multipolar field coefficients of two incident fields at the fundamental frequency to the multipolar field coefficients of the scattered field at the SHG frequency. As we showed in Eq. (3.17), the dipolar T-matrix of a finite-size molecular model can be computed from its dipolar polarizability tensor. In the following, we derive how the Hyper-T-matrix can be computed from the first hyperpolarizability tensor of a finite-size molecular model. Note that in present implementations of DFT software packages such as TURBOMOLE [P9, 165], for instance, only the purely electric dipolar components of the first hyperpolarizability tensor are available. We, therefore, restrict the considerations to this case. Our procedure, however, can be extended to the case that a magnetic response is involved.

We start the derivation by expressing the dipole moment of a finite-size molecular model at the SHG frequency by the first hyperpolarizabiliy tensor. Then we relate this dipole moment to the multipolar field coefficients of a scattered SHG field. The multipolar field coefficients are expressed by the Hyper-T-matrix. This results in an equation relating the Hyper-T-matrix to the first hyperpolarizability tensor. In analogy to [59], we consider a finite-size molecular model located at the origin, $\boldsymbol{r} = (0,0,0)^{\mathrm{T}}$. We, therefore, omit in the following the spatial dependence as argument. We consider two monochromatic incident electric fields at the fundamental frequency ω with the complex field amplitudes $\boldsymbol{E}_1(\omega)$ and $\boldsymbol{E}_2(\omega)$. The nonlinear optical response of the finite-size model is represented by the first hyperpolarizability $\boldsymbol{\beta}(-\Omega,\omega,\omega)$. Due to the SHG interaction of the fields with the molecular model, a polarization and an electric field are generated at the frequency $\Omega = 2\omega$. In the Cartesian basis, one can express a component of the induced electric dipole moment of a single finite-size molecular model at the SHG frequency as [100, Eq.(1)]

$$p_{\mathrm{NL,e},i}(\Omega) = \frac{1}{2}\sum_{j,k} \beta_{ijk}(-\Omega,\omega,\omega)E_{1j}(\omega)E_{2k}(\omega)\,. \tag{7.1}$$

Equation (S11) from [59] gives a relationship between the electric dipolar expansion coefficients $\boldsymbol{c}^{\omega}$ of the scattered field and the electric dipole moment at the fundamental frequency,

$$\begin{pmatrix} c^{\omega}_{1,-1,\mathrm{N}} \\ c^{\omega}_{1,0,\mathrm{N}} \\ c^{\omega}_{1,1,\mathrm{N}} \end{pmatrix} = \frac{c_{\mathrm{h}}(\omega)Z_{\mathrm{h}}(\omega)(k_{\mathrm{h}}(\omega))^3}{\sqrt{6\pi}}\boldsymbol{p}_{\mathrm{e}}(\omega)\,. \tag{7.2}$$

Analogously, we find the relationship at the SHG frequency [P6, Eq. (3)]

$$\begin{pmatrix} c^{\Omega}_{1,-1,\mathrm{N}} \\ c^{\Omega}_{1,0,\mathrm{N}} \\ c^{\Omega}_{1,1,\mathrm{N}} \end{pmatrix} = \frac{c_{\mathrm{h}}(\Omega)Z_{\mathrm{h}}(\Omega)(k_{\mathrm{h}}(\Omega))^3}{\sqrt{6\pi}}\boldsymbol{p}_{\mathrm{NL,e}}(\Omega)\,. \tag{7.3}$$

We define the Hyper-T-matrix $\mathbf{T}^{\mathrm{Hyper}}(-\Omega,\omega,\omega)$ in the spherical vector basis as third-rank tensor, connecting the two incident field coefficients $a^{\omega}_{1;1,r,\mathrm{N}}$ and $a^{\omega}_{2;1,s,\mathrm{N}}$ at the fundamental

frequency to the scattered field coefficients at the SHG frequency [P6, Eq. (4)],

$$c^{\Omega}_{1,m,\mathrm{N}} = \sum_{r,s} \mathrm{T}^{\mathrm{Hyper}}_{mrs}(-\Omega,\omega,\omega) a^{\omega}_{1;1,r,\mathrm{N}} a^{\omega}_{2;1,s,\mathrm{N}} \,. \tag{7.4}$$

The multipolar expansion coefficients of the incident fundamental fields can be computed from [59, Eq. (S9)],

$$\boldsymbol{E}_{1,2}(\omega) = \mathrm{i}\sqrt{\frac{2}{12\pi}} \sum_{r=-1}^{1} a^{\omega}_{1,2;1,r,\mathrm{N}} \hat{\boldsymbol{e}}_r \,, \tag{7.5}$$

so that [P6, Eq. (6)]

$$a^{\omega}_{1,2;1,r,\mathrm{N}} = -\mathrm{i}\sqrt{\frac{12\pi}{2}} \hat{\boldsymbol{e}}^{\dagger}_r \cdot \boldsymbol{E}_{1,2}(\omega) \,. \tag{7.6}$$

Here, $\hat{\boldsymbol{e}}_r$ is a spherical basis vector, and r, s correspond to angular momentum indices. Furthermore, † denotes complex conjugation and transposition. With Eq. (7.6), we replace $a^{\omega}_{1;1,r,\mathrm{N}}$ and $a^{\omega}_{2;1,s,\mathrm{N}}$ in Eq. (7.4) by $\boldsymbol{E}_1(\omega)$ and $\boldsymbol{E}_2(\omega)$. From this, we compute $c^{\Omega}_{1,m,\mathrm{N}}$, which is inserted into Eq. (7.3). The dipole moment $\boldsymbol{p}_{\mathrm{e}}(\Omega)$ on the right-hand side of Eq. (7.3) is replaced by Eq. (7.1). Finally, we derive [P6, Eq. (7)]

$$\begin{aligned} -6\pi \mathbf{C}^{-1} \sum_{m,r,s} \hat{\boldsymbol{e}}_m \mathrm{T}^{\mathrm{Hyper}}_{mrs}(-\Omega,\omega,\omega) \hat{\boldsymbol{e}}^{\dagger}_r \cdot \boldsymbol{E}_1(\omega) \hat{\boldsymbol{e}}^{\dagger}_s \cdot \boldsymbol{E}_2(\omega) \\ = \frac{c_{\mathrm{h}}(\Omega) Z_{\mathrm{h}}(\Omega) (k_{\mathrm{h}}(\Omega))^3}{2\sqrt{6\pi}} \sum_{i,j,k} \hat{\boldsymbol{e}}_i \beta_{ijk}(-\Omega,\omega,\omega) E_{1j}(\omega) E_{2k}(\omega) \,, \end{aligned} \tag{7.7}$$

with the unit vector $\hat{\boldsymbol{e}}_i$ in the Cartesian basis. $\mathbf{C}^{-1}$ transforms a vector from the spherical to the Cartesian basis [59], see Eq. (3.18). In the process of solving Eq. (7.7), one computes the Hyper-T-matrix from the known first hyperpolarizability tensor. In this procedure, the incident electric fields cancel out.

Now we consider the procedure to compute the SHG response of a molecular lattice and a film. Note that we assume the undepleted pump approximation in the sense that the fundamental waves are not influenced by the SHG wave. The program suite *mpGMM* [51] can be used to obtain the linear response of a stack of two-dimensional molecular lattices. To extend *mpGMM* to obtain also the SHG signal of such a stack, one has to compute the SHG response of each lattice. The linear interactions between the lattices, occurring at the fundamental and at the SHG frequency, are still described with the Q-matrices from Chapter 3.

To compute the nonlinear optical response of a stack of molecular layers, we use the following approach. First, one solves the linear optical multi-scattering problem for the incident electric fields at the fundamental frequency with the methods presented in Chapter 3. For each two-dimensional lattice of finite-size molecular models, we compute the electric fields incident on a model in the origin of this lattice. Here, the multi-scattering at the fundamental frequency is incorporated. Second, we use these fields to compute the nonlinear optical response $\boldsymbol{c}^{\Omega}$ of a finite-size molecular model with Eq. (7.4). We transform the SHG field expansion coefficients $\boldsymbol{c}^{\Omega}$ into the basis of well-defined helicity according to Eq. (3.12), obtaining the expansion coefficients $\boldsymbol{d}^{\Omega}$. Then, we use Eq. (3.22) from Chapter 3 to compute

the multipolar expansion coefficients of the scattered electric field at the SHG frequency, incorporating the lattice interactions at the SHG frequency:

$$\boldsymbol{d}^{\Omega}_{0,\mathrm{tot}} = \left(\mathbb{1} - \mathbf{T}^{\mathrm{SHG}}_{\mathrm{Hel}} \sum_{\boldsymbol{R}\neq 0} \mathbf{C}^{(3)}(-\boldsymbol{R}) \mathrm{e}^{\mathrm{i}\boldsymbol{k}_{\parallel}(\Omega)\cdot\boldsymbol{R}} \right)^{-1} \boldsymbol{d}^{\Omega} \,. \tag{7.8}$$

Here, $\boldsymbol{k}_{\parallel}(\Omega)$ is the parallel component of the zeroth diffraction order of the SHG wave with respect to the two-dimensional lattice. $\mathbf{T}^{\mathrm{SHG}}_{\mathrm{Hel}}$ is the T-matrix for linear scattering at the SHG frequency. Analogously to Chapter 3, we insert $\boldsymbol{d}^{\Omega}_{0,\mathrm{tot}}$ into Eqs. (3.23) and (3.24) to obtain the SHG scattered electric field of the two-dimensional lattice expanded in diffracted plane waves. Furthermore, Q-matrices are used to describe the linear interaction at the SHG frequency, enabling the same possibilities for the simulations of SHG processes of photonic devices, which are offered for linear processes. These Q-matrices have the same shape as for the fundamental frequency and are defined in Section 3.2.

7.1.2. SHG Signal of a Crystalline Urea Thin Film in a Vacuum

We discuss in this subsection the instance of a crystalline urea molecular film in a vacuum. As we stated above, urea crystalline films are a very common example in SHG studies, so we use this instance for a proof of principle. The SHG response of the film computed with the presented multi-scale approach is compared to results obtained with COMSOL Multiphysics [241]. For the latter simulations, we describe the molecular film with effective medium tensors that are also obtained based on TD-DFT. The effective medium tensors for the linear response are computed with the homogenization approach from Chapter 5. Here, only the effective permittivity is important.

For the SHG response, we compute the effective second-order susceptibility tensor with

$$\chi^{(2)}_{ijk}(-\Omega,\omega,\omega) = \frac{1}{\varepsilon_0 V} f_i(\Omega) f_j(\omega) f_k(\omega) \beta_{ijk}(-\Omega,\omega,\omega) \,, \tag{7.9}$$

see [244, Eq. (1.1)] and [100, Eq. (5)]. In this equation, we assume that the finite-size molecular model's axes correspond to the axes of the crystal. V is the unit cell's volume. With [100, Eq. (6)], we have the local field factors

$$f_i(\omega) = \frac{(n_{ii}(\omega))^2 + 2}{3} \,. \tag{7.10}$$

Here, $n_{ii}(\omega)$ is the refractive index corresponding to the axis i of the molecular crystal. Similar to [100], we neglect the imaginary part of $n_{ii}(\omega)$ to compute $\boldsymbol{\chi}^{(2)}(-\Omega,\omega,\omega)$, because in this frequency range, the absorption of urea is very small. Equation (7.9) for $\boldsymbol{\chi}^{(2)}(-\Omega,\omega,\omega)$ is neglecting the nonlinear interaction between the finite-size molecular models building up the molecular crystal. In the presented multi-scale approach, the optical interactions between the finite-size molecular models are entirely incorporated, while the finite-size molecular model should be chosen large enough so that the chemical interactions are sufficiently represented. Similar to the case of the linear response, one aims at a perfect combination of both procedures to obtain accurate results for the nonlinear optical response. Note that in the pioneering work of [237], the intermolecular chemical interactions are analyzed and incorporated for urea.

With [100, Eq. (4)], we compute the nonlinear SHG polarization

$$P_{\mathrm{NL,e},i}(\Omega) = \frac{1}{2}\varepsilon_0 \sum_{j,k} \chi^{(2)}_{ijk}(-\Omega,\omega,\omega) E_{1j}(\omega) E_{2k}(\omega)\,, \tag{7.11}$$

which is used within COMSOL Multiphysics to obtain the SHG response of a thin film.

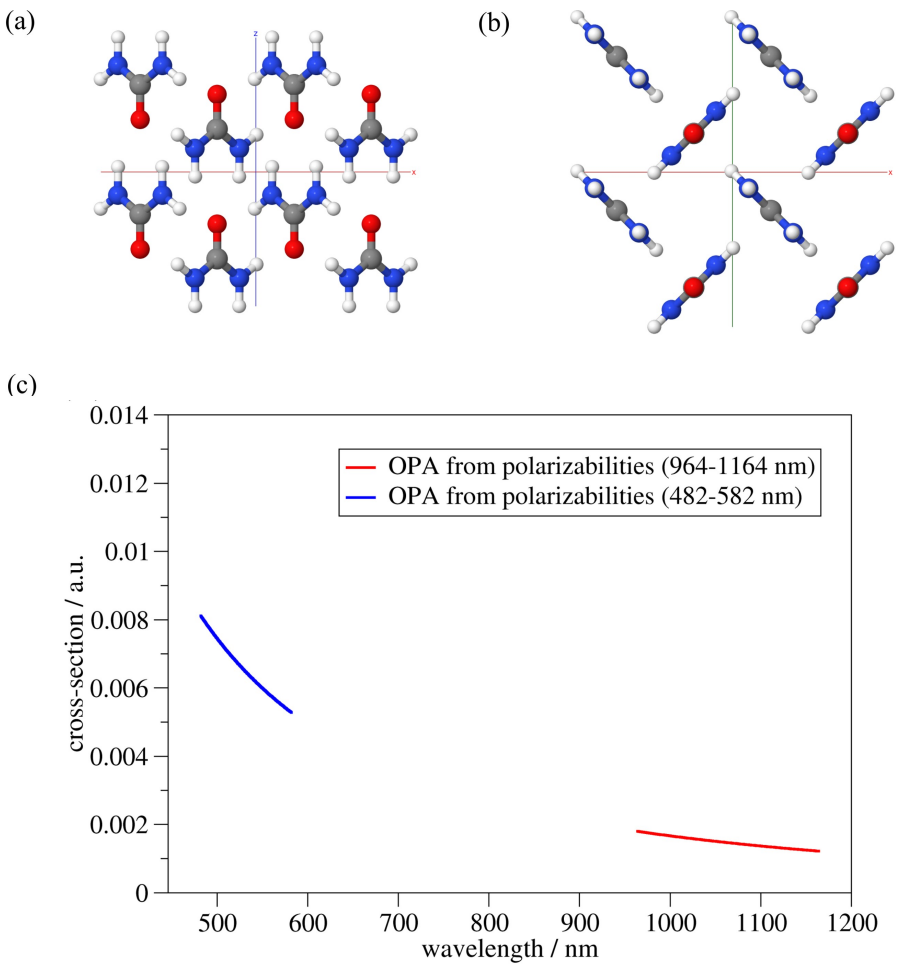

Figure 7.1.: Different views **(a)** and **(b)**, and one-photon absorption cross section **(c)** of the finite-size molecular model of urea. The one-photon absorption cross section is computed from the polarizability tensor. There are no resonances present. Originally created by Marjan Krstić. Adapted with permission from [P6]. Copyright © 2024 John Wiley and Sons.

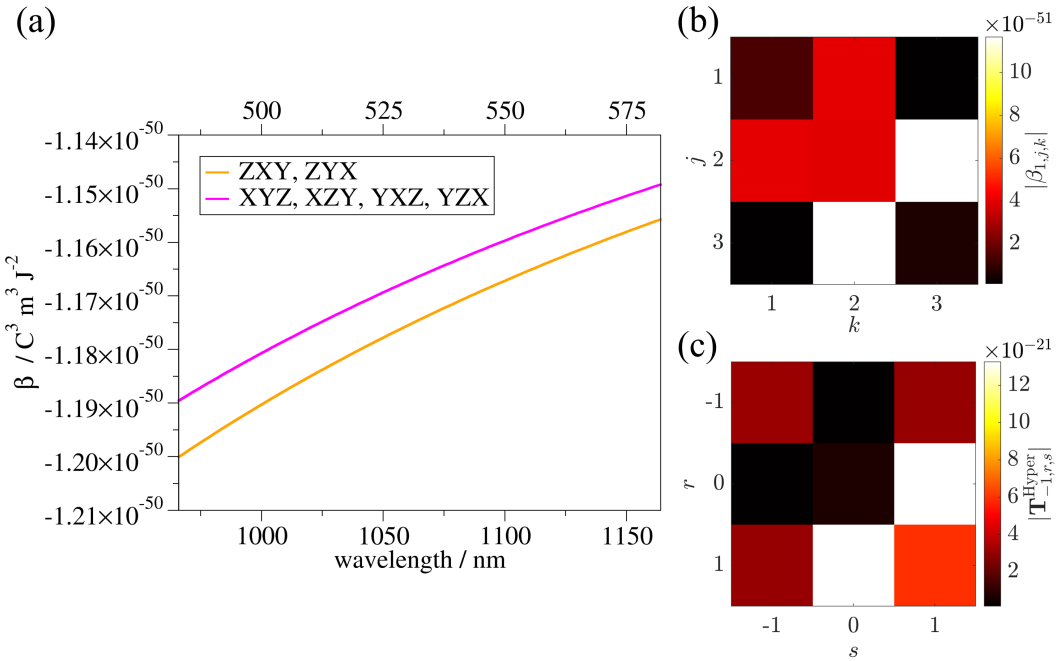

Figure 7.2.: Dominating components of the first hyperpolarizability tensor **(a)**, and scheme of the hyperpolarizability **(b)** and Hyper-T-matrix of urea at the fundamental wavelength of 1064 nm **(c)**. The tensors are contracted to their first respective entry. Created in cooperation with Marjan Krstić. Adapted with permission from [P6]. Copyright © 2024 John Wiley and Sons.

(TD)-DFT Simulations

To compute the SHG response of the urea thin film, the polarizability tensors at the fundamental frequency, the polarizability tensors at the SHG frequency, and the first hyperpolarizability tensors have to be obtained via TD-DFT with the methods presented in Chapter 4.2. Similar to Chapter 6, a finite-size model of the urea crystal is chosen first. It consists of $2 \times 2 \times 2$ unit cells depicted in Figures 7.1**(a)** and **(b)**. It is extracted from [245]. In Appendix C, a study on the influence of the size of the molecular model on the hyperpolarizability tensor is presented. There, models with two, 16, 54, and 128 molecules are compared. It is observed that the model corresponding to $2 \times 2 \times 2$ unit cells shows sufficient convergence, and it is computationally considerably less demanding than the larger models. Note that in comparison to the (linear) polarizabilities, the computation of hyperpolarizabilities is much more expensive.

The chosen functional is the hybrid B3LYP exchange-correlation functional [246, 247]. Additionally, the def2-TZVP basis set is chosen [99, 192]. In Figure 7.1**(c)**, the one-photon absorption cross section is depicted. It is computed from the polarizability tensor. Here, the wavelength range of ±100 nm around 1064 nm is covered for the fundamental wavelength. This is a typical wavelength of a laser used for SHG studies in experiments, see [100], for instance. The corresponding SHG wavelength range is 482 nm to 582 nm.

The one-photon absorption cross section shows the long-range tail of electronic transitions below 300 nm, both for the fundamental wavelengths (red) and the SHG wavelengths (blue).

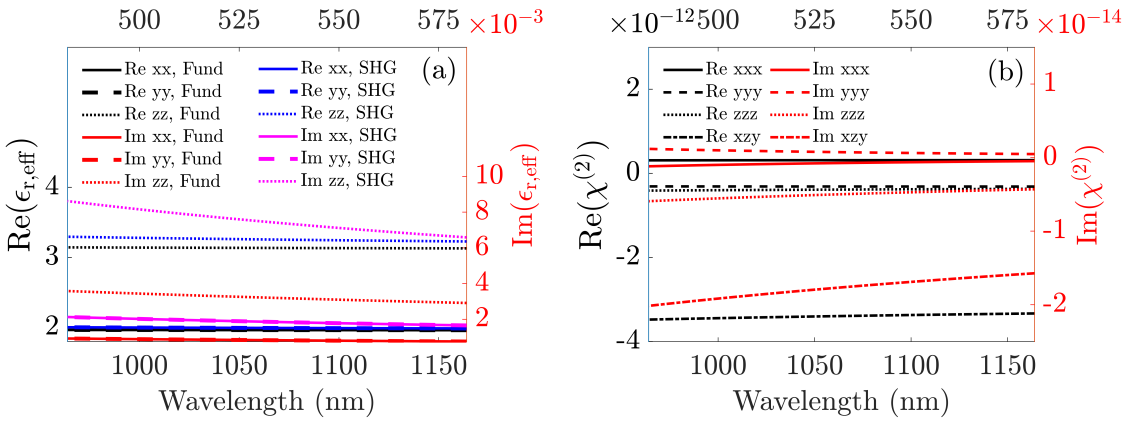

Figure 7.3.: **(a)** Diagonal entries of the permittivity tensor, and **(b)** selected entries of the second-order susceptibility tensor. The upper x-axis refers to the wavelength of the SHG wave and the lower x-axis refers to the wavelength of the incident fundamental waves. Adapted with permission from [P6]. Copyright © 2024 John Wiley and Sons.

They exhibit a Lorentzian line shape. In the spectral windows of the fundamental and the SHG wavelength range, resonances do not occur. Figure 7.2**(a)** displays the dominating components of the purely electric first hyperpolarizability tensor. We observe that the dispersion is very low. Figures 7.2**(b)** and **(c)** display the absolute values of the hyperpolarizability tensor and of the Hyper-T-matrix at the fundamental wavelength of 1064 nm in their respective basis and contracted to the first entry. Both matrices are anisotropic, showing that it is very important to include all their entries in the computation of the SHG response of the molecular material.

SHG Response of the Thin Film

We consider the SHG response of an urea thin film with a thickness of 94 nm, corresponding to 100 two-dimensional lattices. The finite-size molecular model of urea is periodically arranged in these lattices. For the COMSOL simulations, we use the effective medium model described above. Figure 7.3**(a)** shows the diagonal entries of the permittivity tensor, and **(b)** displays selected entries of the second-order susceptibility tensor. As expected from the DFT simulations, the dispersion of all quantities is low, because no resonances occur in this rather narrow wavelength range. The entries of the effective second-order susceptibility tensor can be compared to experimentally measured values from [100, 240, 248]. At the fundamental wavelength of 1064 nm, the relative difference in $|d_{14}^{\mathrm{Exp}}| = 1/2|\chi_{xzy}^{(2),\mathrm{Exp}}| = 1.2 - 1.4\,\mathrm{pm\,V^{-1}}$ is 21-41 %, in comparison to the value obtained with the effective medium theory. The relative difference can be related to possible inaccuracies in the DFT simulations, in the refractive index, and in Eq. (7.9) used to compute the second-order susceptibility. The refractive index is obtained from the presented homogenization approach, assuming a perfect periodic arrangement of the finite-size molecular models, which might not be the case in a experimental measurement. The homogenization approach incorporates also possible lattice interactions. The refractive index is used to compute the second-order susceptibility tensor in Eq. (7.9). This equation, however, neglects the nonlinear interaction between the molecules.

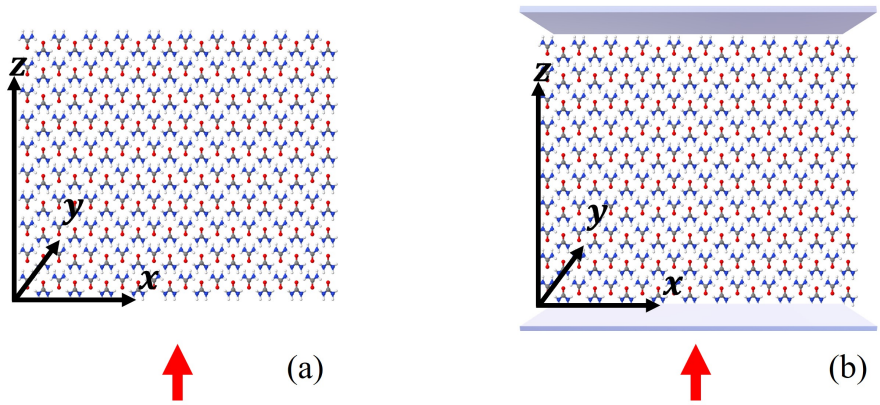

Figure 7.4.: **(a)** Thin film of the urea molecular crystal in a vacuum, and **(b)** in a cavity of silver mirrors. Both setups are illuminated from below with fundamental plane waves propagating in positive z-direction. For the cavity, the upper mirror has a thickness of 30 nm, and the lower mirror has a thickness of 10 nm. The molecular model was created by Marjan Krstić. Adapted with permission from [P6]. Copyright © 2024 John Wiley and Sons.

Figure 7.4**(a)** displays the thin film of the urea crystal in a vacuum. It is illuminated by plane waves at the fundamental frequency from below, which propagate in positive z-direction. Throughout the remaining chapter, the two electric field amplitudes of the illuminating plane waves are set to 1 V/m. In Figures 7.5**(a)**-**(c)**, we show the electric field amplitudes of the SHG plane wave which propagate in positive z-direction ("Co") and in negative z-direction ("Counter"). For Figure 7.5**(a)**, the fundamental plane waves are normal incident and TM-polarized. For **(b)**, both plane waves are normal incident, but one is TM- and one is TE-polarized. For **(c)**, the TM-polarized plane wave has an angle of incidence of 60°, and the TE-polarized plane wave has an angle of incidence of −25° in the yz-plane.

For all cases, we compare the results obtained with the presented multi-scale workflow (solid lines) to the results obtained with COMSOL Multiphysics (dashed lines). The maximum relative difference is 16.86 %, which can be related to two restrictions of both used methods [P6]. First, the effective medium theory used for the COMSOL simulations neglects the nonlinear interaction of the molecular unit cells. Second, both methods suffer from the fact that the Rayleigh spheres of neighboring unit cells overlap in all three dimensions. We mentioned the problem of overlapping Rayleigh spheres in Section 6.1. The overlap in z-direction is worse than in x- and y-direction. For the homogenization approach, the overlap in all dimensions is a restriction to the accuracy, as it is a three-dimensional approach, for which the interaction of the molecules is evaluated with vector spherical waves. For the multi-scale approach, the interaction in z-direction is described by plane waves for which the restrictions connected to the Rayleigh sphere overlap do not apply. Here, only the overlap in x- and y-directions is a restriction to the accuracy.

To satisfy all assumptions of the approaches, we artificially double the lattice constants in all three dimensions. Both the Rayleigh sphere overlap and the interaction of the molecules

are decreased by this measure. In Figure 7.5**(d)**, the spectra are depicted for this case. We observe an excellent agreement.

In this subsection, we showed the principles of the multi-scale approach by introducing the Hyper-T-matrix and explaining the computation of the nonlinear optical response of a finite-size molecular model, a two-dimensional lattice, and a molecular film. The approach is demonstrated and compared to a more traditional effective medium model for a crystalline urea thin film. We emphasize that different polarizations and angles of incidence of the fundamental plane waves can be considered to make use of the anisotropy of the nonlinear optical materials. Additionally, large wavelength ranges can be analyzed which might be accessible by future light sources.

7.1.3. Coupling of a Urea Thin Film to a Photonic Cavity

In the following, we show an application of the multi-scale approach. In [P6], an optical cavity is designed to enhance the SHG response of the urea thin film at a fundamental wavelength of 1064 nm. The cavity depicted in Figure 7.4**(b)** consists of two mirrors. The top mirror has a thickness of 30 nm, and the bottom mirror, which is illuminated from below, has a thickness of 10 nm. For the fundamental illumination, we choose a normal incident TM-polarized plane wave. The mirrors are separated by the urea thin film, and we aim on increasing its SHG signal. The enhancement of the usually small SHG signal by cavity modes has been analyzed in many theoretical and experimental studies [249–255].

First, we analyze the linear optical interaction inside the cavity. For this purpose, we consider the transmission of an incident plane wave, both at the fundamental and the SHG wavelengths. Figures 7.6**(a)** and **(c)** show the transmittance spectra for varying values of the thickness and varying values of the fundamental and SHG wavelengths, respectively. We additionally consider the mode analysis described in Chapter 6, where we use the refractive index related to the x-axis. The anisotropy of the film is neglected for the mode analysis.

It can be seen that for the SHG wavelengths, twice the number of cavity modes occur, as the SHG wavelengths are half as long compared to the fundamental wavelengths. Every second cavity mode at the SHG wavelengths coincides with a cavity mode at the fundamental wavelengths. This is due to the low dispersion of the refractive index. For the analysis of the field amplitude of the generated co- and counter-propagating SHG plane waves, we choose two values of the thickness. First, we select a thickness of 478 nm, for which a cavity mode only occurs at the SHG wavelength of 532 nm, which corresponds to the design wavelength. The second thickness is 665 nm, for which additionally a cavity mode occurs for the fundamental wavelength at 1064 nm. The cavity is, in this case, double resonant. Figures 7.6**(b)** and **(d)** display the field amplitudes of the SHG plane waves and their respective enhancement with respect to a thin film in a vacuum for both thicknesses. In contrast to the single resonant cavity, the double resonant cavity shows maxima of the enhancement close to the design wavelength of 1064 nm. For the field of the co-propagating wave, we observe an enhancement by a factor of 3.11, and for the counter-propagating wave, an enhancement of 12.75. For the single resonant cavity, destructive interference occurs for the illuminating plane waves at the fundamental wavelength, leading to a decreased field strength. For the double resonant cavity, also the fields at the fundamental wavelength show constructive interference, leading to an increased field strength.

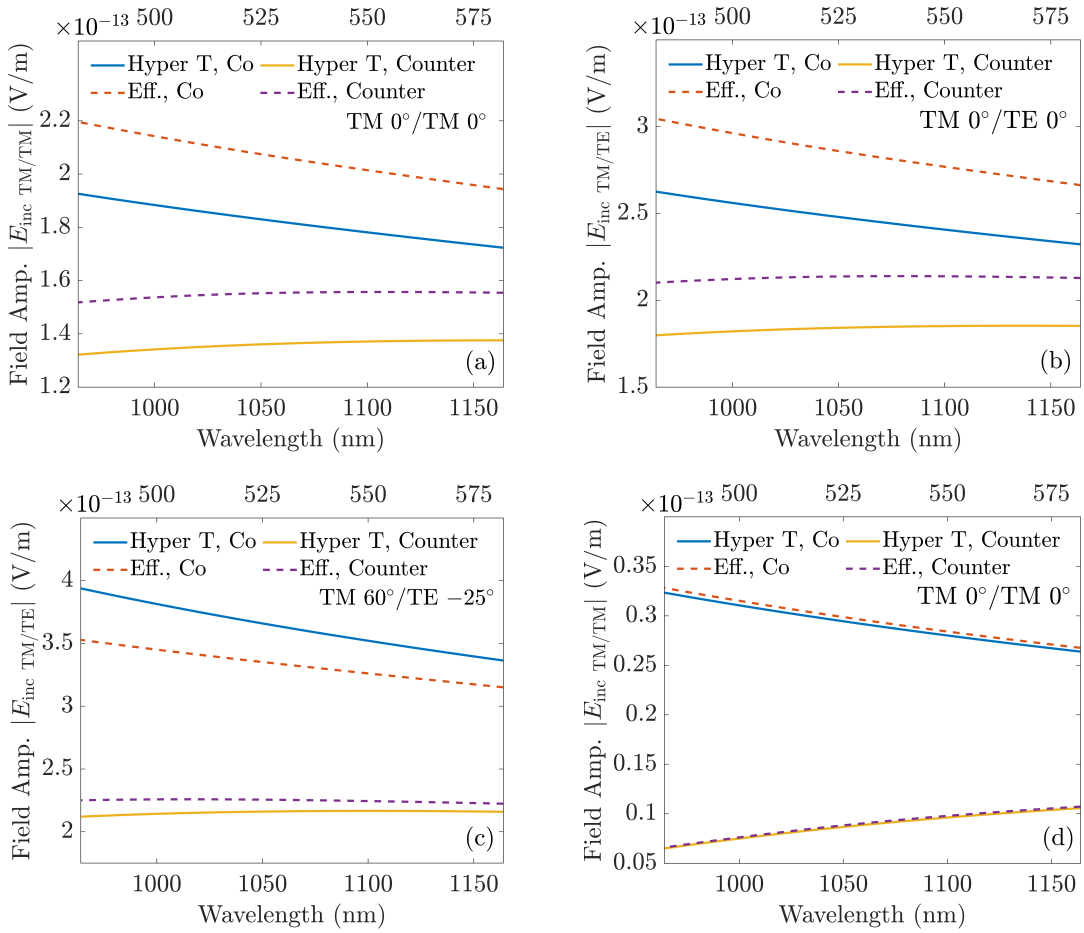

Figure 7.5.: Field amplitudes of the SHG plane waves leaving the molecular film in positive ("Co") and negative ("Counter") z-direction. The illumination are normal incident TM-polarized plane waves **(a)**, one normal incident TM- and one normal incident TE-polarized plane wave **(b)**, one TM-polarized plane wave with an angle of incidence of 60° and one TE-polarized plane wave with an angle of incidence of −25°, and for two normal incident TM-polarized plane waves **(d)** for an artificially diluted crystal. In the latter case, the lattice constants of the urea crystal are doubled. We recall that for normal incidence, TM-polarization corresponds to a polarization along the x-axis and TE-polarization corresponds to a polarization along the y-axis. In all subfigures, spectra are compared that are obtained with the presented multi-scale approach ("Hyper T") and with COMSOL Multiphysics based on effective material parameters ("Eff."). Due to inaccuracies concerning the evaluation of the interaction of the molecular unit cells inside the crystal in both methods, there are discrepancies in spectra **(a)**-**(c)**. In the case of the diluted crystal **(d)**, the agreement is very good, as these inaccuracies are considerably decreased. Adapted with permission from [P6]. Copyright © 2024 John Wiley and Sons.

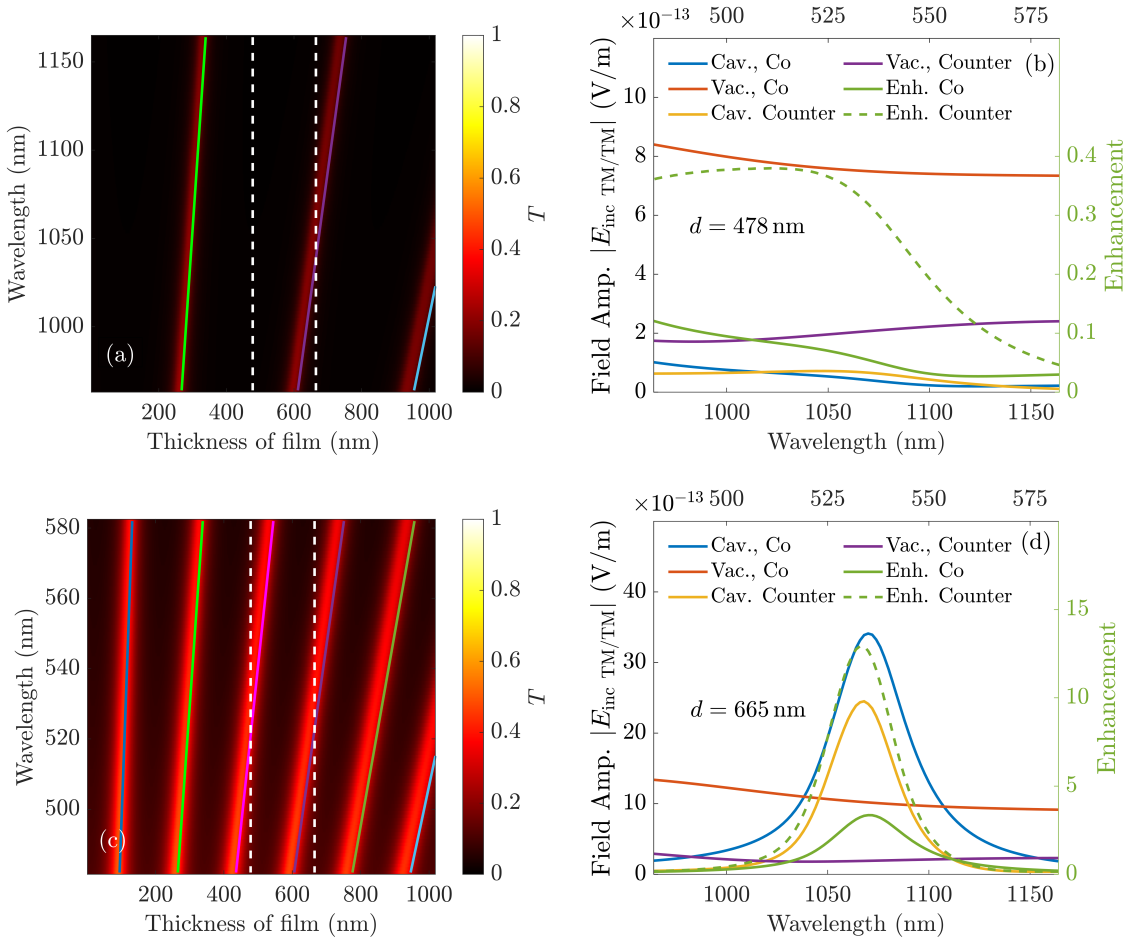

Figure 7.6.: Linear transmittance of the cavity filled with the urea molecular crystal for an incident plane wave at the fundamental **(a)** and at the SHG wavelength **(c)**. The white dashed lines indicate two values of the thickness of 478 nm and 665 nm, respectively. For 478 nm, a cavity mode occurs only at the SHG wavelength. For 665 nm, cavity modes occur both at the fundamental and at the SHG wavelengths. Panels **(b)** and **(d)** show the SHG field amplitudes and their enhancement for a thickness of 478 nm and a thickness of 665 nm, respectively. We observe that only for the double-resonant case, the SHG field amplitudes are increased. For all spectra, the fundamental plane wave is normal incident and TM-polarized. Adapted with permission from [P6]. Copyright © 2024 John Wiley and Sons.

7.2. Surface SHG Signal of Centrosymmetric Molecular Crystalline Materials

In this section, we discuss the surface SHG signal of films consisting of centrosymmetric molecular crystalline materials. Bloembergen and Pershan state in [256], that a SHG signal originating from electric dipoles cannot be produced by centrosymmetric materials, due to their inversion symmetry. For a centrosymmetric calcite crystal, however, a SHG signal has been observed [257]. Later, Bloembergen *et al.* theoretically prove that the SHG signal

originates from the surface [258]. Phenomenologically, one can state that at the surface of the material, the inversion symmetry of the bulk is broken. To quantify the phenomenon to some extent, one can describe the emergence of this surface SHG signal by a surface tensor at the material interface [259], which can be retrieved from experiments.

In [P7], the surface SHG signal of centrosymmetric molecular crystalline films is studied based on an *ab initio* analysis. As mentioned above, Zyss and Berthier analyzed and incorporated intermolecular chemical interactions for urea [237]. In this regard, they placed Coulombian point-charge potentials around the molecules inside the crystal and thereby changing the nonlinear optical response. In [P7], the surrounding of a unit cell is analogously considered via partial charges. Such an approach results in the computation of layer-dependent first hyperpolarizabilities, as the surrounding of each unit cell is different. The procedure enables qualitative and quantitative explanations on a molecular and on a macroscopic level. The hyperpolarizabilities are subsequently used to compute the Hyper-T-matrix of a finite-size molecular model of each layer and finally to obtain the optical response of a stack of layers. This is possible since the multi-scale approach treats each layer individually in contrast to homogenization approaches. It also enables us to distinguish contributions originating from the bulk and the surface. First, we explain the DFT approach for the instance of the centrosymmetric 7,9- Dibromobenzo[h]quinolin-1 molecular crystal. Based on this, we consider the SHG response of the film and the enhancement thereof by a Kretschmann-like setup. We note that quadrupoles can also cause a SHG signal in the case of centrosymmetric materials, see [260–262]. These contributions are not taken into account here. For thin layers, however, we expect that the surface SHG dominates. Furthermore, it is of high interest how many layers at the surface have to be taken into account to compute the surface SHG signal accurately.

7.2.1. (TD)-DFT Simulations

In this subsection, we explain the DFT approach from [P7] to compute the SHG response of a centrosymmetric molecular crystal. For this purpose, the centrosymmetric 7,9- Dibromobenzo[h]quinolin-1 molecular crystal [263] is analyzed. A finite number of stacked layers is considered. For each layer, the first hyperpolarizability of a finite-size molecular model is computed individually. Partial charges are used to describe the presence of the molecules in the other layers. At the top surface, only the lower region is occupied by partial charges. At the bottom surface, the upper region is occupied by partial charges. In the bulk, the molecular model is symmetrically surrounded by partial charges in +z- and −z-direction. The difference between bulk and surface is expected to lead to a SHG signal, which can be quantified and connected to the spatial domain from which it originates [P7].

Figures 7.7**(a)**-**(d)** shows the finite-size molecular model of the crystal. The model consists of 384 atoms. In the following, we refer to the considered finite-size molecular model of a specific layer as quantum region. The stack, which is analyzed, consists of 31 layers. The considered quantum region is embedded into the partial charge field from all other molecules above and below the corresponding layer in z-direction. For this purpose, the atoms of the molecules are replaced by partial charges, except of the considered quantum region.

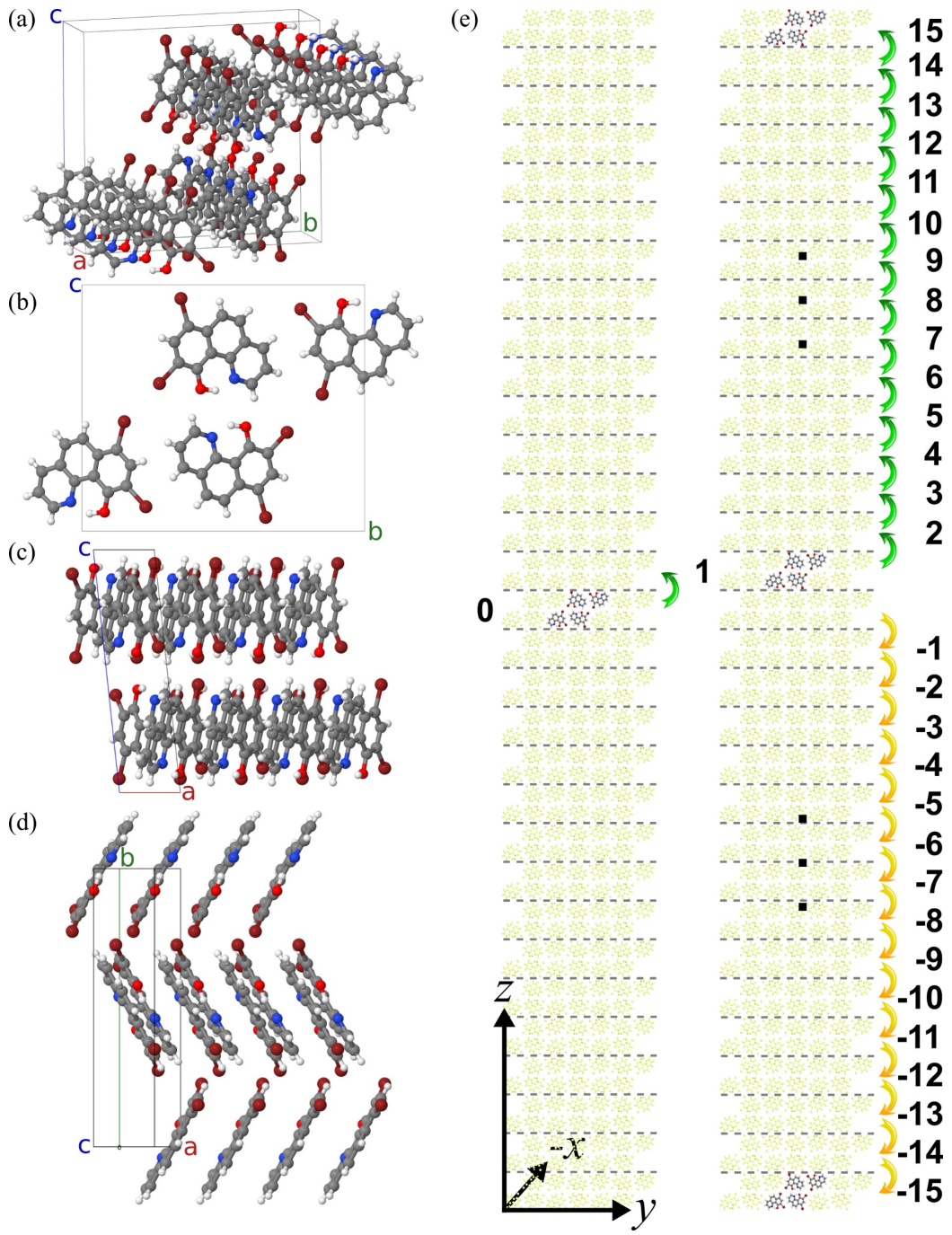

Figure 7.7.: Four unit cells of 7,9-Dibromobenzo[h]quinolin-10-ol crystal as seen from different directions **(a)**-**(d)**. This corresponds to the quantum region. Panel **(e)** displays a scheme of the stack of 31 molecular layers. To compute the polarizability and hyperpolarizability of a respective layer, the quantum region is moved to this respective layer and embedded into the partial charge field from all other molecules. These are stacked in positive and negative z-direction. The only layer which is surrounded by a symmetric partial charge field is the bulk layer "0". Created by Marjan Krstić. Reprinted with permission from [P7]. Copyright © 2024 John Wiley and Sons.

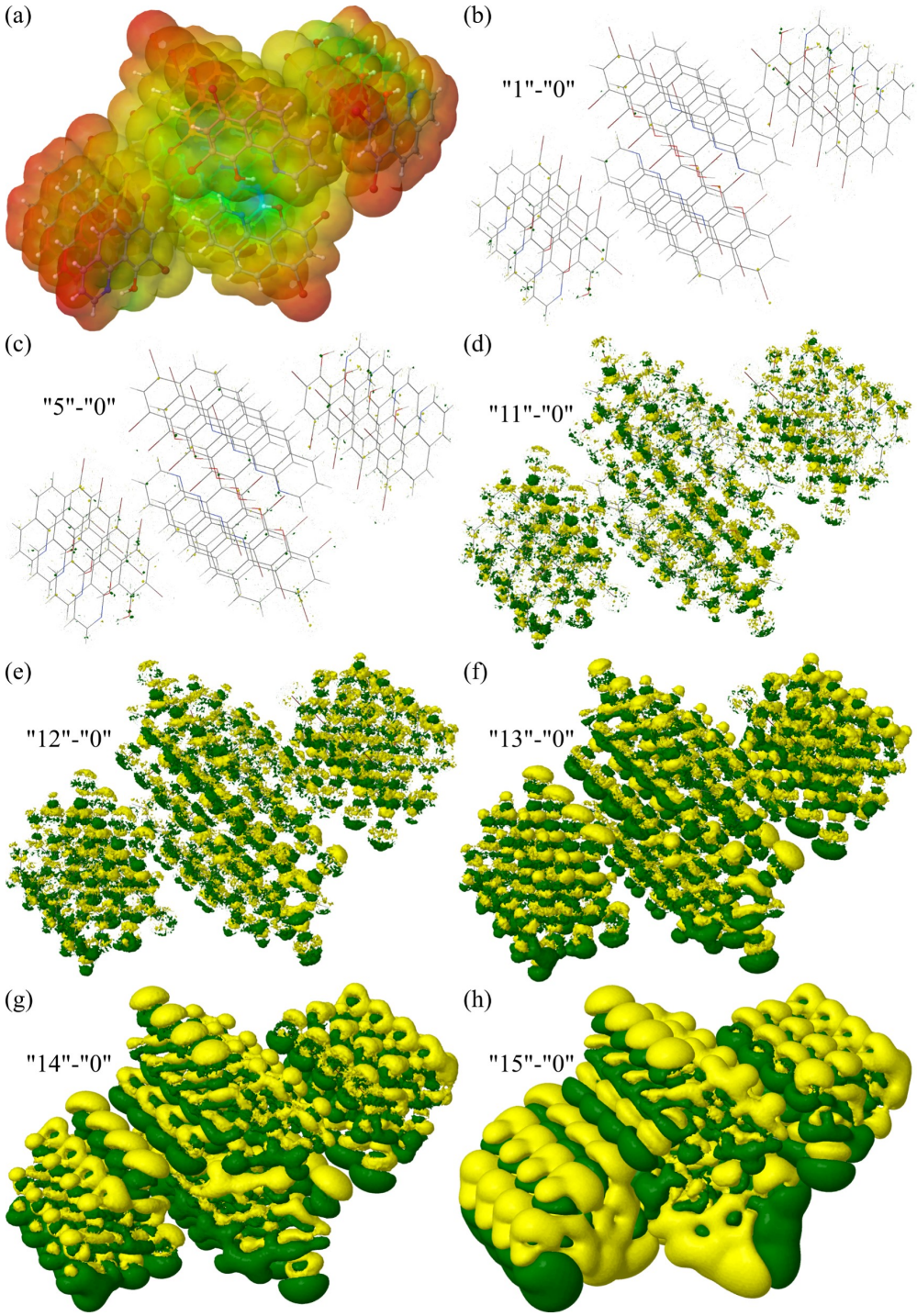

Figure 7.8.: Panel **(a)** depicts the electrostatic potential of the finite-size molecular model of the crystal. Panels **(b)**-**(h)** display the total electron density difference between different models with respect to the bulk model "0". Yellow indicates a negative difference and green indicates a positive difference. Created by Marjan Krstić. Reprinted with permission from [P7]. Copyright © 2024 John Wiley and Sons.

The situation is depicted in Figure 7.7**(e)**. Model "0" corresponds to the bulk layer. The layers are counted from "-15" (bottom layer) to "15" (top layer). Note that each quantum region is also surrounded by two partial charge unit cells in x- and y-direction. Therefore, the partial charge field has a total size of $3 \times 3 \times 31$ quantum regions. The hybrid PBE0 functional [166, 167] and the def2-TZVP basis set [99, 192] are used to compute the individual first hyperpolarizabilities.

Table 7.1 shows the dominating component of the hyperpolarizability tensor of the different layers at a fundamental wavelength of 1064 nm. We observe that the surface layers exhibit the largest values of the hyperpolarizability. Already after five layers approaching the bulk, the contribution of the remaining layers is smaller than 1 %. This shows that the main contribution to the SHG signal originates from the five top and bottom layers. Considering the partial charges, the centrosymmetry is broken the most at the surface.

On the quantum level, the origin of the SHG signal can be explained with the total electron density difference between the respective layer and the bulk layer "0". In Figures 7.8**(b)**-**(h)**, we observe that the difference between layers "5" and "1" with respect to "0" is rather small, since they are very close to the bulk. Approaching the top surface, however, the difference from layers "11" to "15" with respect to "0" increases considerably. From this observation, one can deduce that in the case of the layers close to the top surface, the total electron density of the molecules is additionally polarized by the lower layers, leading to the surface SHG signal. For the bottom layer, it is the other way round, in the sense that the sign of the total electron density is reversed.

One observes, therefore, the largest absolute values of the hyperpolarizabilities for the surface layers and values close to zero for the layers in the bulk. The sign of the hyperpolarizabilities of the surface layers is reversed with respect to each other, similar to the change of the total electron density.

7.2.2. Surface SHG Signal of a Finite Film of the Molecular Crystal in a Vacuum and on a Substrate

To analyze the surface SHG signal originating from a film of the 7,9- Dibromobenzo[h]quinolin-1 molecular crystal, infinitely extended into the x- and y-direction and finite in the z-direction, we use the multi-scale approach from Section 7.1. For each layer, the Hyper-T-matrix is computed from the first hyperpolarizability tensor. In comparison to the DFT analysis, we additionally vary the number of the bulk layers "0".

The thin film is illuminated from below under normal incidence with a TE-polarized plane wave propagating in the positive z-direction. The considered fundamental wavelength is 1064 nm. First, we set the number of bulk layers to one. This corresponds to the situation analyzed with DFT. The absolute values of the electric field amplitudes of the SHG plane waves are displayed in Figure 7.9**(a)**, with respect to the layer from which they originate. We distinguish plane waves co-propagating with respect to the illumination, corresponding to plane waves which leave the film in positive z-direction, from counter-propagating plane waves, leaving the film in negative z-direction.

We observe, especially on the logarithmic scale, that the contribution of the surface layers is several orders of magnitude larger than the contribution originating from the bulk layer. Considering the layers between the surfaces and the bulk, one deduces that the change of the SHG response occurs rather rapidly agreeing very well with the DFT analysis. Figure 7.9**(b)** displays the electric field amplitudes of the SHG waves for different numbers of the bulk layer, resulting in different values of the thickness of the entire film. Additionally, the linear

absorption of the incident field at the fundamental wavelength and of a field at the SHG wavelength are shown. One observes for all quantities Fabry-Perot resonances, as all present waves are reflected off the interfaces between vacuum and the crystalline molecular film.

In an experimental measurement, the molecular film is not placed in a vacuum but usually deposited on top of a substrate. In [P7], it is analyzed how the rather small surface SHG

Table 7.1.: Dominating component of the first hyperpolarizability tensors of the finite-size molecular models of the different layers of 7,9-Dibromobenzo[*h*]quinolin-10-ol. The values are given in atomic units. The values in brackets indicate in percentage how large the hyperpolarizability of the respective layer is in comparison to the surface layers. Adapted with permission from [P7]. Copyright © 2024 John Wiley and Sons.

Model	Re(β_{yyy})	Im(β_{yyy})
15	-2389.0(100.0)	-160.3(100.0)
14	-273.5(11.4)	-12.2(7.6)
13	-115.7(4.8)	-5.1(3.2)
12	-58.1(2.4)	-2.5(1.6)
11	-32.0(1.3)	-1.4(0.9)
10	-19.8(0.8)	-0.9(0.5)
9	-12.1(0.5)	-0.5(0.3)
8	-7.1(0.3)	-0.3(0.2)
7	-5.8(0.2)	-0.3(0.2)
6	-3.5(0.1)	-0.1(0.1)
5	-2.4(0.1)	-0.1(0.1)
4	-0.6(0.0)	0.0(0.0)
3	-1.4(0.1)	-0.1(0.0)
2	-0.2(0.0)	0.0(0.0)
1	0.2(0.0)	0.0(0.0)
0	0.0(0.0)	0.0(0.0)
-1	-0.2(0.0)	0.0(0.0)
-2	0.2(0.0)	0.0(0.0)
-3	1.4(0.1)	0.1(0.0)
-4	0.6(0.0)	0.0(0.0)
-5	2.4(0.1)	0.1(0.1)
-6	3.5(0.1)	0.1(0.1)
-7	5.8(0.2)	0.3(0.2)
-8	7.1(0.3)	0.3(0.2)
-9	12.1(0.5)	0.5(0.3)
-10	19.8(0.8)	0.9(0.5)
-11	32.0(1.3)	1.4(0.9)
-12	58.1(2.4)	2.5(1.6)
-13	115.7(4.8)	5.1(3.2)
-14	273.5(11.4)	12.2(7.6)
-15	2389.0(100.0)	160.3(100.0)

signal of the molecular film on top of a dielectric substrate can be enhanced by choosing a specific angle of incidence and making use of Fabry-Perot modes. Figure 7.10**(a)** shows this situation. The dielectric substrate is ceria, for which a relative permittivity of $\varepsilon_{\mathrm{r,subs}} = 5.57$ is assumed for the entire wavelength range, corresponding to a refractive index of $n_{\mathrm{subs}} = 2.36$ [264]. The angle of incidence is varied in the xz-plane. Again, a TE-polarized plane wave at the fundamental wavelength of 1064 nm is chosen for the illumination.

There are two angles of incidence which are of higher importance. The first angle is the angle of incidence, for which total internal reflection occurs at the interface between the molecular film and vacuum. This corresponds to $\theta_{\mathrm{c},1} = \arcsin(1/n_{\mathrm{subs}}) = 25°$. The second set of angles of incidence are $\theta_{\mathrm{c,2,fund}} = \arcsin(n_{\mathrm{film,yy,fund}}/n_{\mathrm{subs}})$ and $\theta_{\mathrm{c,2,SHG}} = \arcsin(n_{\mathrm{film,yy,SHG}}/n_{\mathrm{subs}})$ for which total reflection occurs at the interface between the substrate and the molecular film at the fundamental and the SHG wavelength, respectively. Neglecting off-diagonal entries of the permittivity tensor, we compute the refractive index of the crystalline molecular film with the homogenization approach from Chapter 5 to $n_{\mathrm{film,yy,fund}} = 1.79$ and $n_{\mathrm{film,yy,SHG}} = 1.88$. We have, therefore, $\theta_{\mathrm{c,2,fund}} = 49°$ and $\theta_{\mathrm{c,2,SHG}} = 53°$.

In the next step, we consider the linear reflection of a TE-polarized plane wave, which is incident under varying angles at the fundamental and at the SHG wavelength, respectively. Besides the angle of incidence, we also vary the thickness of the film. Figures 7.10**(b)** and **(c)** display the corresponding spectra. Close to the regions in which total reflection occurs,

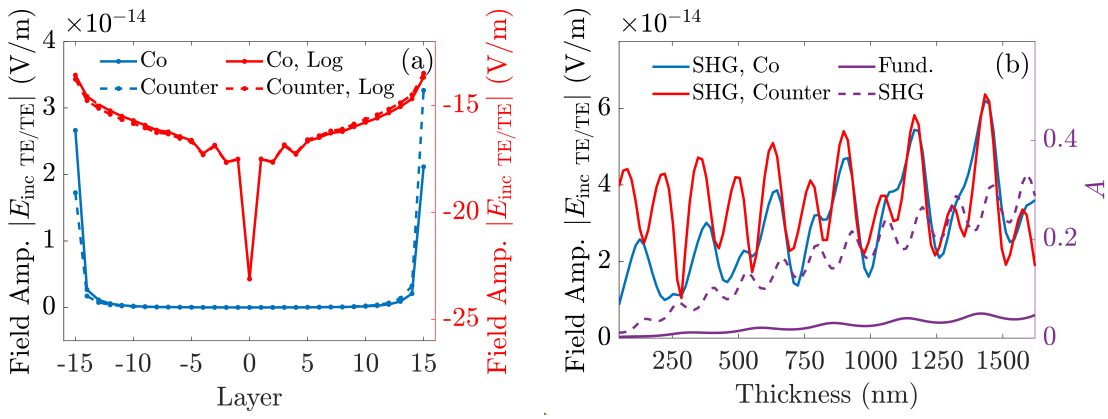

Figure 7.9.: SHG field amplitudes of the plane waves originating from the different layers of the crystalline molecular film of 7,9-Dibromobenzo[*h*]quinolin-10-ol **(a)**. They are co- and counter-propagating with respect to the normal incident fundamental TE-polarized plane wave, which illuminates the crystalline molecular film. The film consists of the model shown in Figure 7.7**(e)**, which is periodically repeated in the xy-plane. We observe that the contribution from the surface layers ("15" and "−15") is significantly larger than from the other layers. Panel **(b)** depicts the SHG field amplitudes originating from the film and the linear absorption at the fundamental and the SHG wavelength with respect to different values of the film thickness. The thickness is varied by changing the number of bulk layers "0". We observe Fabry-Perot resonances for all quantities, due to the reflection off the interfaces. Adapted with permission from [P7]. Copyright © 2024 John Wiley and Sons.

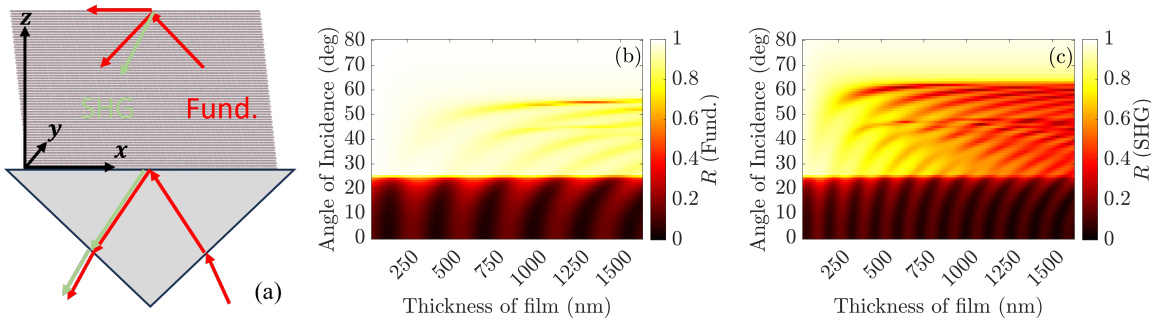

Figure 7.10.: Schematic setup of the molecular crystalline film on top of a ceria substrate **(a)**. The film is illuminated from below by a fundamental TE-polarized plane wave under oblique incidence in the yz-plane. Due to the nonlinear optical interaction between the fundamental wave and the molecular film, a SHG signal is produced. Panels **(b)** and **(c)** show the linear reflectance of the film at the fundamental wavelength 1064 nm and at the SHG wavelength 532 nm, respectively, for different angles of incidence and different values of the film thickness. Due to two different angles of incidence, for which total reflection occurs at the interfaces between film and vacuum and film and substrate, respectively, there are two regimes in which the reflectance changes considerably. Fabry-Perot modes are observable between those areas. The molecular model was created by Marjan Krstić. Adapted with permission from [P7]. Copyright © 2024 John Wiley and Sons.

the reflection rapidly changes. For the regions at angles of incidence corresponding to the total reflection off the interface between the substrate and the film, there is a deviation with respect to the predicted values, as we have neglected the anisotropy of the film in calculating these values. We observe in the spectra Fabry-Perot modes between $\theta_{c,1}$ and $\theta_{c,2,\mathrm{fund}}/\theta_{c,2,\mathrm{SHG}}$. In this regime, the light is reflected off both interfaces, but the reflection off the interface between molecular film and vacuum is total.

In the following, the most suitable angle of incidence is determined to enhance the SHG signal with respect to the case of a thin film with a specific thickness in a vacuum for normal incidence of the illuminating wave. The thickness of the film is set to 631 nm. For this thickness, the field amplitudes of the co- and counter-propagating SHG waves show a maximum in Figure 7.9**(b)** for normal incident illumination. Figure 7.11**(a)** displays the SHG field amplitudes and the linear reflection both at the fundamental and the SHG wavelength for different angles of incidence. For an angle of incidence of 31°, the counter-(downward) propagating SHG field shows a maximal amplitude. This is the field which shall be detected, as in this regime the co-propagating SHG wave leaving the film in upward direction is evanescent.

The field amplitude of the counter-propagating SHG wave is enhanced in this regime, as the Fabry-Perot modes occurring in the linear regime increase the light-matter interaction. As total internal reflection occurs at the top surface, the finesse of the modes is considerably increased and constructive interference of the SHG fields is possible. The resulting enhancement is in agreement with our observation from above that Fabry-Perot modes of a cavity can enhance the SHG signal. We relate shifts between the maxima of the SHG waves and the linear reflectance spectra to effects such as the phase relation between the incident and the SHG wave vectors, which also depend on the angle of incidence.

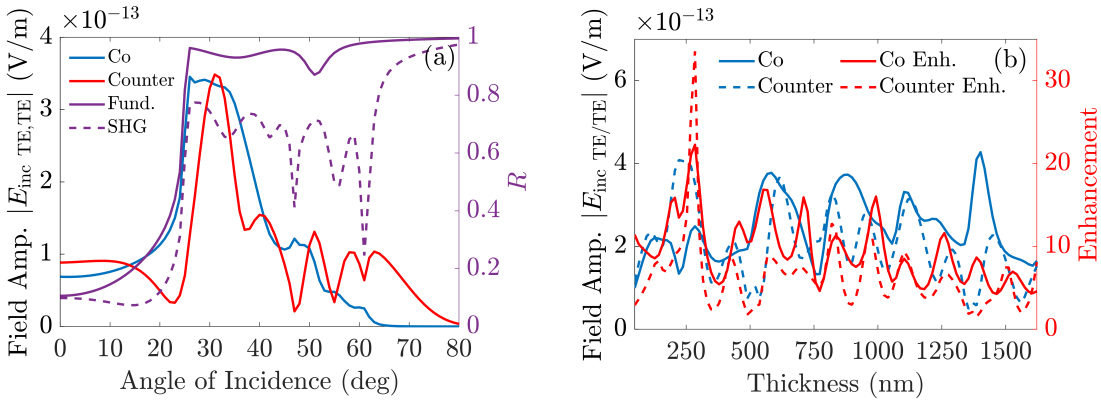

Figure 7.11.: SHG field amplitudes and linear reflectance spectra of the molecular crystalline film for different angles of incidence of the fundamental TE-polarized plane wave **(a)**. The thickness of the film is set to 631 nm. For an angle of incidence of 31°, a maximum of the amplitude of the counter-propagating SHG wave can be observed. Panel **(b)** displays the SHG field amplitudes for an angle of incidence of 31°. The film thickness is varied. For the counter-propagating SHG wave, a maximum field enhancement of 33 is achieved. The enhancement of the corresponding intensity is 1089. Adapted with permission from [P7]. Copyright © 2024 John Wiley and Sons.

In the last step, the angle of incidence is set to 31°, and the thickness is varied again. We note that the Fabry-Perot mode condition changes with the thickness and the angle of incidence. Therefore, one would have to optimize the angle of incidence for each thickness. However, the angle of incidence of 31° supports several Fabry-Perot modes and for all thicknesses it is suitable for total internal reflection. In Figure 7.11**(b)**, we show the SHG amplitudes and their respective enhancement compared to a thin film with the same thickness under normal incident illumination. For the counter-propagating SHG wave, we observe a maximum enhancement of 33 for a thickness of 285 nm. This corresponds to an increase of the intensity by $33^2 = 1089$. Such a significant enhancement demonstrates that with our multi-scale approach not only surface SHG signals can be detected and attributed to the layers from which they originate. Also, simple Kretschmann-like setups can be designed to considerably enhance these signals.

To sum up, we introduced in this chapter the concept of the Hyper-T-matrix and presented a multi-scale approach, which can be used to compute the nonlinear optical response of photonic devices. For these photonic devices, the Hyper-T-matrix is used to describe the nonlinear properties of a finite-size model of the molecules that serve as functional entities. We demonstrated the applicability of the workflow with the design of a cavity and a Kretschmann-like setup to enhance the SHG signal of molecular films. For the latter instance, the surface SHG of the molecular film and its physical origin were studied.

8 | Conclusions and Outlook

In this thesis, we present a multi-scale approach to analyze different molecules in photonic devices. The multi-scale approach connects *ab initio* quantum-chemical methods, such as TD-DFT, to classical Maxwell scattering simulations. In this regard, it is possible to compute the optical response of molecules based on their *ab initio* obtained quantum-chemical properties. This enables the consideration of single molecules, finite-size molecular models, a two-dimensional lattice of molecules, molecular films, and, finally, entire photonic devices. Therefore, the entire spatial scale from Ångströms to millimeters is covered, and size effects on the optical response can be analyzed. The multi-scale approach supports fast advancing fabrication techniques, as complicated experimental setups can be accurately simulated.

Conclusions

In Chapters 2, 3, and 4, we introduce the theoretical framework of classical electromagnetics for linear and nonlinear optics, the transition (T-) matrix formalism for linear optics, and the basics of (time-dependent) density functional theory (TD)-DFT to simulate the optical response of finite-size molecular models. We note that the T-matrix is the bridge between the microscopic description of the optical response of molecules, based on TD-DFT, and the macroscopic description, based on Maxwell scattering simulations. These three chapters provide the basis for the main part of the thesis.

To analyze the optical properties of molecular materials and to simulate the signal of macroscopic devices which are more complicated than planar films, effective parameters of the molecular materials are required. In Chapter 5, a homogenization approach is presented to obtain effective properties of materials based on their effective T-matrix. We introduce the effective T-matrix of a three-dimensional lattice of scatterers as an object, which does not depend on the propagation direction of the illumination. Based on this quantity, it is possible to obtain propagation-independent effective material parameters.

We demonstrate the workflow of the homogenization approach for the instances of a Zn-L-camphoric acid-dabco surface-mounted metal-organic framework (SURMOF), a three-dimensional lattice of gold spheres, and a three-dimensional lattice of cut-plate pairs. In this regard, we deduce that lattice interactions can significantly modify the optical response of the material. In contrast to traditional homogenization approaches, they are incorporated in the effective T-matrix. We also inspect band diagrams to decide whether a material is homogenizable at all. Such an analysis can always be performed before the material is homogenized. The material parameters obtained with the presented homogenization approach are used in Chapters 6 and 7 to inspect the optical modes of filled cavities and to design a metasurface of a structured molecular film. The design of the metasurface relies on the fact that the derived effective material parameters do not depend on the illumination direction.

In Chapter 6, we introduce a multi-scale approach to analyze linear optical phenomena of photonic devices incorporating molecular materials. We use the T-matrix of the finite-size molecular models, obtained with TD-DFT, to compute the optical response of the devices. First, we consider monolayers of CO and CO_2 molecules deposited on dielectric substrates. In

this regard, we compare the polarization dependence of the optical response of the monolayers to experimental spectra. The good agreement supports the predictive power of our approach.

In the second step, we analyze two-dimensional islands of one, four, and up to 441 molecules. The latter corresponds to an island size of 10 nm×10 nm. The multi-scale approach enables in this regard the transition from the optical response of a single molecule to the monolayer. For the considered systems, we conclude that finite-size effects are not important for structures with more than 441 molecules. This is an essential finding for the experimental investigation of structures smaller than molecular monolayers. A perspective application is the monitoring of chemical processes with infrared reflection-absorption spectroscopy.

Next, we perform the transition from the response of a monolayer to the optical response of molecular films. In this regard, we consider a Zn-SiPc-SURMOF-2, a chiral UiO-67-BINOL MOF, and randomly oriented TDBC J-aggregates embedded in a polyvinyl alcohol polymer. We compare the response of the film in a vacuum or on a substrate, and inside a photonic cavity. In this context, the splitting of the cavity modes, occurring due to their coupling to the molecular material, is observed, analyzed, and compared to measurements. In the analysis of the coupling between the cavity and the materials, we present how the properties of the molecular material, such as their concentration, influence the optical response. We show that high concentrations, leading to a large dispersion of the refractive index, can cause two different splitted cavity modes at the same thickness of the filling medium. The occurrence of two different splitted cavity modes at the same thickness might not be preferable for the experimental design and can be predicted beforehand with the multi-scale approach. In this context, it is also possible to explore different kinds of molecules to find a suitable candidate for applications.

For the case of the chiral UiO-67-BINOL MOF, the investigation is additionally focused on the circular dichroism spectra of thin films. The circular dichroism spectra show a very good agreement to experimental findings. We finalize Chapter 6 by designing a metasurface of cylinders consisting of the chiral MOF material to enhance the circular dichroism signal of the material. In this regard, we obtain suitable geometry parameters for the metasurface, which can be used for a future experimental investigation.

In Chapter 7, we introduce a multi-scale approach to simulate nonlinear optical phenomena of molecular materials inside photonic devices. Here, we concentrate on second-harmonic generation (SHG), but the approach can be extended to consider other nonlinear optical effects. Equivalently to linear optical phenomena, the nonlinear optical response of molecules is obtained based on properties computed with TD-DFT. An object is introduced, which is termed Hyper-T-matrix and serves as pendant to the T-matrix. We apply the multi-scale approach to compute the SHG response of an urea thin film and design a cavity to considerably enhance the signal. This is very important for an experimental investigation, since the SHG signal is usually low. We conclude Chapter 7 by studying the SHG response of the surface of a centrosymmetric molecular material. Here the multi-scale approach enables us to differentiate the contributions of different layers, observing that the surface layers cause a contribution that is several orders of magnitude larger than the contribution from the bulk. We also design a Kretschmann-like setup to enhance the surface SHG response.

Outlook

Future investigations can focus on several aspects of the thesis. The applications of the presented homogenization approach go far beyond the scope of this thesis. While we focus

on molecular materials which are in general always homogenizable, due to their small size, the approach can be used for various different kinds of metamaterials. As the band diagrams of such materials can be computed before the homogenization, it is not only possible to clarify whether a material is homogenizable, but also to design the material so that it satisfies the necessary requirement that its band diagram is not close to the edge of the first Brillouin zone.

The insights into the coupling of optical cavities and molecular films, obtained with the presented multi-scale approach, can be used to study the influence of cavities on chemical reactions. In this regard, we see the potential of inserting the optical information of the filled cavity into the TD-DFT computations.

While we demonstrate a considerable enhancement of the circular dichroism signal in the ultraviolet wavelength range caused by cylinders consisting of a chiral MOF, the infrared wavelength range can potentially be of more interest. As the geometry parameters of the structures are smaller than the considered design wavelengths, the fabrication of devices to enhance the signal in the ultraviolet wavelength range is very demanding. Devices, which enhance the circular dichroism signal in the infrared wavelength range, have considerably larger structures size and are, therefore, easier to produce.

The multi-scale approach for the computation of the SHG signal of molecules can be extended to other second-order nonlinear optical effects, such as sum-frequency generation, and also to higher-order effects, such as third-harmonic generation. In this context, it is also possible to study the change of the optical response by structuring a molecular film into a metasurface. The simulation can be enabled by a homogenization approach for nonlinear optics or by extending a feature of *treams* [52, 53], which currently allows to compute the linear optical response of a superlattice of islands consisting themselves of a finite number of molecules, see Section 6.2. Such an extension of the multi-scale approach can potentially lead to a broad range of applications in the field of metasurfaces and metamaterials.

Bibliography

[1] Y. Fu and N. S. Finney, "Small-molecule fluorescent probes and their design," *RSC Advances* **8**, 29051–29061 (2018).

[2] A. Condon, "Designed DNA molecules: principles and applications of molecular nanotechnology," *Nature Reviews Genetics* **7**, 565–575 (2006).

[3] Q. Shao and B. Xing, "Photoactive molecules for applications in molecular imaging and cell biology," *Chemical Society Reviews* **39**, 2835–2846 (2010).

[4] N. Kerru, L. Gummidi, S. Maddila, K. K. Gangu, and S. B. Jonnalagadda, "A review on recent advances in nitrogen-containing molecules and their biological applications," *Molecules* **25** (2020).

[5] C. Dugave and L. Demange, "Cis−trans isomerization of organic molecules and biomolecules: Implications and applications," *Chemical Reviews* **103**, 2475–2532 (2003).

[6] Z.-j. Xu, Y. Jin, X.-l. Zhang, P.-h. Xia, X.-m. Wen, J.-c. Ma, J. Lin, and J. Qian, "Pan-cancer analysis identifies CD300 molecules as potential immune regulators and promising therapeutic targets in acute myeloid leukemia," *Cancer Medicine* **12**, 789–807 (2023).

[7] D. Kotani, E. Oki, Y. Nakamura, H. Yukami, S. Mishima, H. Bando, H. Shirasu, K. Yamazaki, J. Watanabe, M. Kotaka, K. Hirata, N. Akazawa, K. Kataoka, S. Sharma, V. N. Aushev, A. Aleshin, T. Misumi, H. Taniguchi, I. Takemasa, T. Kato, M. Mori, and T. Yoshino, "Molecular residual disease and efficacy of adjuvant chemotherapy in patients with colorectal cancer," *Nature Medicine* **29**, 127–134 (2023).

[8] R. C. Thompson, N. W. Simons, L. Wilkins, E. Cheng, D. M. D. Valle, G. E. Hoffman, C. Cervia, B. Fennessy, K. Mouskas, N. J. Francoeur, J. S. Johnson, L. Lepow, J. L. Berichel, C. Chang, A. G. Beckmann, Y.-c. Wang, K. Nie, N. Zaki, K. Tuballes, V. Barcessat, M. A. Cedillo, D. Yuan, L. Huckins, P. Roussos, T. U. Marron, The Mount Sinai COVID-19 Biobank Team, B. S. Glicksberg, G. Nadkarni, J. R. Heath, E. Gonzalez-Kozlova, O. Boyman, S. Kim-Schulze, R. Sebra, M. Merad, S. Gnjatic, E. E. Schadt, A. W. Charney, and N. D. Beckmann, "Molecular states during acute covid-19 reveal distinct etiologies of long-term sequelae," *Nature Medicine* **29**, 236–246 (2023).

[9] X. Hu, Z. Zeng, J. Zhang, D. Wu, H. Li, and F. Geng, "Molecular dynamics simulation of the interaction of food proteins with small molecules," *Food Chemistry* **405**, 134824 (2023).

[10] N. Echegaray, N. Guzel, M. Kumar, M. Guzel, A. Hassoun, and J. M. Lorenzo, "Recent advancements in natural colorants and their application as coloring in food and in intelligent food packaging," *Food Chemistry* **404**, 134453 (2023).

[11] M. Dharini, S. Jaspin, and R. Mahendran, "Cold plasma reactive species: Generation, properties, and interaction with food biomolecules," *Food Chemistry* **405**, 134746 (2023).

[12] M. Bragaglia, L. Paleari, J. A. Berrocal, F. R. Lamastra, and F. Nanni, "Towards sustainable rubber compounds: the use of waste raw materials," *Journal of Applied Polymer Science* **140**, e53750 (2023).

[13] W. Fang, Z. Mu, Y. He, K. Kong, K. Jiang, R. Tang, and Z. Liu, "Organic–inorganic covalent–ionic molecules for elastic ceramic plastic," *Nature* **619**, 293–299 (2023).

[14] K. Zheng, Y. Wu, Z. Hu, S. Wang, X. Jiao, J. Zhu, Y. Sun, and Y. Xie, "Progress and perspective for conversion of plastic wastes into valuable chemicals," *Chemical Society Reviews* **52**, 8–29 (2023).

[15] D. Wang, S. Shi, Y. Mao, L. Lei, S. Fu, and J. Hu, "Biodegradable dual-network cellulosic composite bioplastic metafilm for plastic substitute," *Angewandte Chemie International Edition* **62**, e202310995 (2023).

[16] J. Wei, J. Liu, W. Zeng, Z. Dong, J. Song, S. Liu, and G. Liu, "Catalytic hydroconversion processes for upcycling plastic waste to fuels and chemicals," *Catalysis Science & Technology* **13**, 1258–1280 (2023).

[17] S. Kim, D. Kong, X. Zheng, and J. H. Park, "Upcycling plastic wastes into value-added products via electrocatalysis and photoelectrocatalysis," *Journal of Energy Chemistry* **91**, 522–541 (2024).

[18] T. Quintes, M. Mayländer, and S. Richert, "Properties and applications of photoexcited chromophore–radical systems," *Nature Reviews Chemistry* **7**, 75–90 (2023).

[19] A. A. Fursina and A. Sinitskii, "Toward molecular spin qubit devices: Integration of magnetic molecules into solid-state devices," *ACS Applied Electronic Materials* **5**, 3531–3545 (2023).

[20] A. Chiesa, S. Roca, S. Chicco, M. de Ory, A. Gómez-León, A. Gomez, D. Zueco, F. Luis, and S. Carretta, "Blueprint for a molecular-spin quantum processor," *Physical Review Applied* **19**, 064060 (2023).

[21] X. Yang, X. Lin, Y. S. Zhao, and D. Yan, "Recent advances in micro-/nanostructured metal–organic frameworks towards photonic and electronic applications," *Chemistry – A European Journal* **24**, 6484–6493 (2018).

[22] L. Heinke, M. Cakici, M. Dommaschk, S. Grosjean, R. Herges, S. Bräse, and C. Wöll, "Photoswitching in two-component surface-mounted metal–organic frameworks: Optically triggered release from a molecular container," *ACS Nano* **8**, 1463–1467 (2014).

[23] D. Wöhrle and D. Meissner, "Organic solar cells," *Advanced Materials* **3**, 129–138 (1991).

[24] Y. Wei, Z. Chen, G. Lu, N. Yu, C. Li, J. Gao, X. Gu, X. Hao, G. Lu, Z. Tang, J. Zhang, Z. Wei, X. Zhang, and H. Huang, "Binary organic solar cells breaking 19% via manipulating the vertical component distribution," *Advanced Materials* **34**, 2204718 (2022).

[25] H. Chen, R. Zhang, X. Chen, G. Zeng, L. Kobera, S. Abbrent, B. Zhang, W. Chen, G. Xu, J. Oh, S.-H. Kang, S. Chen, C. Yang, J. Brus, J. Hou, F. Gao, Y. Li, and Y. Li, "A guest-assisted molecular-organization approach for > 17% efficiency organic solar cells using environmentally friendly solvents," *Nature Energy* **6**, 1045–1053 (2021).

[26] J. S. Park, G.-U. Kim, S. Lee, J.-W. Lee, S. Li, J.-Y. Lee, and B. J. Kim, "Material design and device fabrication strategies for stretchable organic solar cells," *Advanced Materials* **34**, 2201623 (2022).

[27] Z. You, Y. Song, W. Liu, W. Wang, C. Zhu, Y. Duan, and Y. Liu, "Diazabicyclic electroactive ionenes for efficient and stable organic solar cells," *Angewandte Chemie International Edition* **62**, e202302538 (2023).

[28] L. Duan and A. Uddin, "Progress in stability of organic solar cells," *Advanced Science* **7**, 1903259 (2020).

[29] J. Song, H. Lee, E. G. Jeong, K. C. Choi, and S. Yoo, "Organic light-emitting diodes: Pushing toward the limits and beyond," *Advanced Materials* **32**, 1907539 (2020).

[30] S. Nam, J. W. Kim, H. J. Bae, Y. M. Maruyama, D. Jeong, J. Kim, J. S. Kim, W.-J. Son, H. Jeong, J. Lee, S.-G. Ihn, and H. Choi, "Improved efficiency and lifetime of deep-blue hyperfluorescent organic light-emitting diode using Pt(II) complex as phosphorescent sensitizer," *Advanced Science* **8**, 2100586 (2021).

[31] H. Zhao, C. E. Arneson, D. Fan, and S. R. Forrest, "Stable blue phosphorescent organic leds that use polariton-enhanced purcell effects," *Nature* **626**, 300–305 (2024).

[32] P. Sun, D. Liu, F. Zhu, and D. Yan, "An efficient solid-solution crystalline organic light-emitting diode with deep-blue emission," *Nature Photonics* **17**, 264–272 (2023).

[33] Y.-Z. Shi, K. Wang, S.-L. Zhang, X.-C. Fan, Y. Tsuchiya, Y.-T. Lee, G.-L. Dai, J.-X. Chen, C.-J. Zheng, S.-Y. Xiong, X.-M. Ou, J. Yu, J.-S. Jie, C.-S. Lee, C. Adachi, and X.-H. Zhang, "Characterizing the conformational distribution in an amorphous film of an organic emitter and its application in a "self-doping" organic light-emitting diode," *Angewandte Chemie International Edition* **60**, 25878–25883 (2021).

[34] S. Zhang, "Fabrication of novel biomaterials through molecular self-assembly," *Nature Biotechnology* **21**, 1171–1178 (2003).

[35] J. Cao, X. Jing, J. Yan, C. Hu, R. Chen, J. Yin, J. Li, and N. Zheng, "Identifying the molecular structures of intermediates for optimizing the fabrication of high-quality perovskite films," *Journal of the American Chemical Society* **138**, 9919–9926 (2016).

[36] B.-K. An, S. H. Gihm, J. W. Chung, C. R. Park, S.-K. Kwon, and S. Y. Park, "Color-tuned highly fluorescent organic nanowires/nanofabrics: Easy massive fabrication and molecular structural origin," *Journal of the American Chemical Society* **131**, 3950–3957 (2009).

[37] G. S. McCarty, "Molecular lithography for wafer-scale fabrication of molecular junctions," *Nano Letters* **4**, 1391–1394 (2004).

[38] R. L. McCreery and A. J. Bergren, "Progress with molecular electronic junctions: Meeting experimental challenges in design and fabrication," *Advanced Materials* **21**, 4303–4322 (2009).

[39] D.-H. Chen, H. Gliemann, and C. Wöll, "Layer-by-layer assembly of metal-organic framework thin films: Fabrication and advanced applications," *Chemical Physics Reviews* **4**, 011305 (2023).

[40] D. Yan, Z. Wang, and Z. Zhang, "Stimuli-responsive crystalline smart materials: From rational design and fabrication to applications," *Accounts of Chemical Research* **55**, 1047–1058 (2022).

[41] B. Yang, L. Wang, M. Zhang, J. Luo, Z. Lu, and X. Ding, "Fabrication, applications, and prospects of aramid nanofiber," *Advanced Functional Materials* **30**, 2000186 (2020).

[42] C. Yang, W. Wang, A. Nefedov, Y. Wang, T. G. Mayerhöfer, and C. Wöll, "Polarization-dependent vibrational shifts on dielectric substrates," *Physical Chemistry Chemical Physics* **22**, 17129–17133 (2020).

[43] C. Yang, Y. Cao, P. N. Plessow, J. Wang, A. Nefedov, S. Heissler, F. Studt, Y. Wang, H. Idriss, T. G. Mayerhöfer, and C. Wöll, "N_2O adsorption and photochemistry on ceria surfaces," *The Journal of Physical Chemistry C* **126**, 2253–2263 (2022).

[44] S. F. Elena and F. García-Arenal, "*Plant Virus Adaptation to New Hosts: A Multi-scale Approach*," in *Viral Fitness and Evolution: Population Dynamics and Adaptive Mechanisms*, edited by E. Domingo, P. Schuster, S. F. Elena, and C. Perales (Springer International Publishing, Cham, 2023), pp. 167–196.

[45] J. M. Reisner, A. J. Josephson, K. J. Gorkowski, E. Koo, D. K. Thompson, D. Schroeder, and M. K. Dubey, "Informed multi-scale approach applied to the British Columbia fires of late summer 2017," *Journal of Geophysical Research: Atmospheres* **128**, e2022JD037238 (2023).

[46] A. Adamu and A. M. Yola, "Assessing the vitality of Gombe dialect of Fulfulde: A multi-scale approach," *International Journal of the Sociology of Language* **279**, 193–231 (2023).

[47] K. Skianis, G. Nikolentzos, B. Gallix, R. Thiebaut, and G. Exarchakis, "Predicting COVID-19 positivity and hospitalization with multi-scale graph neural networks," *Scientific Reports* **13**, 5235 (2023).

[48] R. H. Tichauer, J. Feist, and G. Groenhof, "Multi-scale dynamics simulations of molecular polaritons: The effect of multiple cavity modes on polariton relaxation," *The Journal of Chemical Physics* **154**, 104112 (2021).

[49] I. Sokolovskii, R. H. Tichauer, D. Morozov, J. Feist, and G. Groenhof, "Multi-scale molecular dynamics simulations of enhanced energy transfer in organic molecules under strong coupling," *Nature Communications* **14**, 6613 (2023).

[50] P. C. Waterman, "Matrix formulation of electromagnetic scattering," *Proceedings of the IEEE* **53**, 805–812 (1965).

[51] D. Beutel, A. Groner, C. Rockstuhl, and I. Fernandez-Corbaton, "Efficient simulation of bi-periodic, layered structures based on the T-matrix method," *Journal of the Optical Society of America B* **38**, 1782–1791 (2021).

[52] D. Beutel, I. Fernandez-Corbaton, and C. Rockstuhl, "Treams – A T-matrix-based scattering code for nanophotonics," *Computer Physics Communications*, 109076 (2024).

[53] Dominik Beutel, *Treams*, `https://github.com/tfp-photonics/treams.git`, (accessed: 2023-06-22), 2023.

[54] A. Egel, L. Pattelli, G. Mazzamuto, D. S. Wiersma, and U. Lemmer, "CELES: CUDA-accelerated simulation of electromagnetic scattering by large ensembles of spheres," *Journal of Quantitative Spectroscopy and Radiative Transfer* **199**, 103–110 (2017).

[55] Amos Egel and Lorenzo Pattelli and Giacomo Mazzamuto and Diederik S. Wiersma and Uli Lemmer, *CELES*, `https://github.com/disordered-photonics/celes`, (accessed: 2024-03-07), 2017.

[56] A. Egel, K. M. Czajkowski, D. Theobald, K. Ladutenko, A. S. Kuznetsov, and L. Pattelli, "SMUTHI: a python package for the simulation of light scattering by multiple particles near or between planar interfaces," *Journal of Quantitative Spectroscopy and Radiative Transfer* **273**, 107846 (2021).

[57] Amos Egel and Krzysztof M. Czajkowski and Dominik Theobald and Konstantin Ladutenko and Alexey S. Kuznetsov and Lorenzo Pattelli, *SMUTHI*, `https://gitlab.com/AmosEgel/smuthi`, (accessed: 2024-03-07), 2017.

[58] N. Stefanou, V. Yannopapas, and A. Modinos, "Multem 2: A new version of the program for transmission and band-structure calculations of photonic crystals," *Computer Physics Communications* **132**, 189–196 (2000).

[59] I. Fernandez-Corbaton, D. Beutel, C. Rockstuhl, A. Pausch, and W. Klopper, "Computation of electromagnetic properties of molecular ensembles," *ChemPhysChem* **21**, 878–887 (2020).

[60] F. Crimin, N. Mackinnon, J. B. Götte, and S. M. Barnett, "Optical helicity and chirality: Conservation and sources," *Applied Sciences* **9**, 828 (2019).

[61] J. D. Jackson, *Classical Electrodynamics* (John Wiley & Sons, New York, Weinheim [i.a.], 1999).

[62] P. A. Franken, A. E. Hill, C. W. Peters, and G. Weinreich, "Generation of optical harmonics," *Physical Review Letters* **7**, 118–119 (1961).

[63] R. W. Boyd, *Nonlinear Optics* (Elsevier, Academic Press, Amsterdam, Heidelberg [i.a.], 2008).

[64] B. E. A. Saleh and M. C. Teich, *Fundamentals of Photonics* (John Wiley & Sons, Wiley-Interscience, Hoboken, New Jersey, 2007).

[65] G. Kristensson, *Scattering of Electromagnetic Waves by Obstacles* (SciTech Publishing, Danvers, Massachusetts, 2016).

[66] A. H. Sihvola and I. V. Lindell, "Bi-isotropic constitutive relations," *Microwave and Optical Technology Letters* **4**, 295–297 (1991).

[67] R. Venkitakrishnan, T. Höß, T. Repän, F. Z. Goffi, M. Plum, and C. Rockstuhl, "Lower limits for the homogenization of periodic metamaterials made from electric dipolar scatterers," *Physical Review B* **103**, 195425 (2021).

[68] D. J. Griffiths, *Introduction to Electrodynamics* (Pearson, Harlow, Essex, 2014).

[69] C. F. Bohren and D. R. Huffman, *Absorption and Scattering of Light by Small Particles* (WILEY-VCH Verlag GmbH & Co. KGaA, Weinheim, 2004).

[70] I. Bialynicki-Birula, "V photon wave function," in *Progress in Optics*, Vol. 36, edited by E. Wolf (Elsevier, Amsterdam, 1996), pp. 245–294.

[71] I. Bialynicki-Birula and Z. Bialynicka-Birula, "The role of the riemann–silberstein vector in classical and quantum theories of electromagnetism," *Journal of Physics A: Mathematical and Theoretical* **46**, 053001 (2013).

[72] I. Fernandez-Corbaton, "Helicity and duality symmetry in light matter interactions: Theory and applications," *(PhD Thesis, Department of Physics and Astronomy, Macquarie University) arXiv:1407.4432* (2014).

[73] I. Fernandez-Corbaton, X. Zambrana-Puyalto, N. Tischler, X. Vidal, M. L. Juan, and G. Molina-Terriza, "Electromagnetic duality symmetry and helicity conservation for the macroscopic maxwell's equations," *Physical Review Letters* **111**, 060401 (2013).

[74] I. Fernandez-Corbaton, M. Fruhnert, and C. Rockstuhl, "Objects of maximum electromagnetic chirality," *Physical Review X* **6**, 031013 (2016).

[75] Z.-G. Gu, J. Bürck, A. Bihlmeier, J. Liu, O. Shekhah, P. G. Weidler, C. Azucena, Z. Wang, S. Heissler, H. Gliemann, W. Klopper, A. S. Ulrich, and C. Wöll, "Oriented circular dichroism analysis of chiral surface-anchored metal–organic frameworks grown by liquid-phase epitaxy and upon loading with chiral guest compounds," *Chemistry – A European Journal* **20**, 9879–9882 (2014).

[76] P. Scott, X. Garcia-Santiago, D. Beutel, C. Rockstuhl, M. Wegener, and I. Fernandez-Corbaton, "On enhanced sensing of chiral molecules in optical cavities," *Applied Physics Reviews* **7**, 041413 (2020).

[77] D. Beutel, P. Scott, M. Wegener, C. Rockstuhl, and I. Fernandez-Corbaton, "Enhancing the optical rotation of chiral molecules using helicity preserving all-dielectric metasurfaces," *Applied Physics Letters* **118**, 221108 (2021).

[78] A. Rahimzadegan, T. D. Karamanos, R. Alaee, A. G. Lamprianidis, D. Beutel, R. W. Boyd, and C. Rockstuhl, "A comprehensive multipolar theory for periodic metasurfaces," *Advanced Optical Materials* **10**, 2102059 (2022).

[79] Y.-L. Xu, "Scattering of electromagnetic radiation by three-dimensional periodic arrays of identical particles," *Journal of the Optical Society of America A* **31**, 322–331 (2014).

[80] M. I. Mishchenko, L. D. Travis, and D. W. Mackowski, "T-matrix computations of light scattering by nonspherical particles: A review," *Journal of Quantitative Spectroscopy and Radiative Transfer* **55**, 535–575 (1996).

[81] Q.-C. Shang, Z.-S. Wu, T. Qu, Z.-J. Li, and L. Bai, "Scattering from a multilayered chiral sphere using an iterative method," *Journal of Quantitative Spectroscopy and Radiative Transfer* **173**, 72–82 (2016).

[82] M. Fruhnert, I. Fernandez-Corbaton, V. Yannopapas, and C. Rockstuhl, "Computing the T-matrix of a scattering object with multiple plane wave illuminations," *Beilstein Journal of Nanotechnology* **8**, 614–626 (2017).

[83] X. G. Santiago, M. Hammerschmidt, S. Burger, C. Rockstuhl, I. Fernandez-Corbaton, and L. Zschiedrich, "Decomposition of scattered electromagnetic fields into vector spherical wave functions on surfaces with general shapes," *Physical Review B* **99**, 045406 (2019).

[84] G. Demésy, J.-C. Auger, and B. Stout, "Scattering matrix of arbitrarily shaped objects: combining finite elements and vector partial waves," *Journal of the Optical Society of America A* **35**, 1401–1409 (2018).

[85] *MATLAB® ver. R2018b, https://www.mathworks.com*, The MathWorks Inc. (Natick, Massachusetts, 2018).

[86] N. Stefanou, V. Yannopapas, and A. Modinos, "Heterostructures of photonic crystals: Frequency bands and transmission coefficients," *Computer Physics Communications* **113**, 49–77 (1998).

[87] G. Gantzounis and N. Stefanou, "Layer-multiple-scattering method for photonic crystals of nonspherical particles," *Physical Review B* **73**, 035115 (2006).

[88] O. R. Cruzan, "Translational addition theorems for spherical vector wave functions," *Quarterly of Applied Mathematics* **20**, 33–40 (1962).

[89] S. Stein, "Addition theorems for spherical wave functions," *Quarterly of Applied Mathematics* **19**, 15–24 (1961).

[90] L. Tsang, J. A. Kong, and R. T. Shin, *Theory of Microwave Remote Sensing (Wiley Series in Remote Sensing and Image Processing)* (John Wiley & Sons, Wiley-Interscience, New York [i.a.], 1985).

[91] K. Kambe, "Theory of low-energy electron diffraction: I. application of the cellular method to monatomic layers," *Zeitschrift für Naturforschung A* **22**, 322–330 (1967).

[92] P. P. Ewald, "Die berechnung optischer und elektrostatischer gitterpotentiale," *Annalen der Physik* **369**, 253–287 (1921).

[93] D. Beutel, I. Fernandez-Corbaton, and C. Rockstuhl, "Unified lattice sums accommodating multiple sublattices for solutions of the helmholtz equation in two and three dimensions," *Physical Review A* **107**, 013508 (2023).

[94] R. C. Wittmann, "Spherical wave operators and the translation formulas," *IEEE Transactions on Antennas and Propagation* **36**, 1078–1087 (1988).

[95] E. Cancès and G. Friesecke (eds.), *Density Functional Theory - Modeling, Mathematical Analysis, Computational Methods, and Applications* (Springer, Cham, 2023).

[96] F. Jensen, *Introduction to Computational Chemistry* (John Wiley & Sons, Chichester, West Sussex; Hoboken, New Jersey, 2017).

[97] G. Czycholl, *Solid State Theory, Volume 1 - Basics: Phonons and Electrons in Crystals* (Springer, Berlin, 2023).

[98] W. Kohn and L. J. Sham, "Self-consistent equations including exchange and correlation effects," *Physical Review* **140**, A1133–A1138 (1965).

[99] F. Weigend and R. Ahlrichs, "Balanced basis sets of split valence, triple zeta valence and quadruple zeta valence quality for h to rn: Design and assessment of accuracy," *Physical Chemistry Chemical Physics* **7**, 3297 (2005).

[100] A. Miniewicz, S. Bartkiewicz, E. Wojaczynska, T. Galica, R. Zalesny, and R. Jakubas, "Second harmonic generation in nonlinear optical crystals formed from propellane-type molecules," *Journal of Materials Chemistry C* **7**, 1255–1262 (2019).

[101] F. Furche, "On the density matrix based approach to time-dependent density functional response theory," *The Journal of Chemical Physics* **114**, 5982–5992 (2001).

[102] R. Bauernschmitt and R. Ahlrichs, "Treatment of electronic excitations within the adiabatic approximation of time dependent density functional theory," *Chemical Physics Letters* **256**, 454–464 (1996).

[103] M. Kehry, Y. J. Franzke, C. Holzer, and W. Klopper, "Quasirelativistic two-component core excitations and polarisabilities from a damped-response formulation of the bethe–salpeter equation," *Molecular Physics* **118**, e1755064 (2020).

[104] R. Bauernschmitt and R. Ahlrichs, "Stability analysis for solutions of the closed shell Kohn–Sham equation," *The Journal of Chemical Physics* **104**, 9047–9052 (1996).

[105] S. M. Parker, D. Rappoport, and F. Furche, "Quadratic response properties from TDDFT: Trials and tribulations," *Journal of Chemical Theory and Computation* **14**, 807–819 (2018).

[106] M. Nyman, X. Garcia-Santiago, M. Krstić, L. Materne, I. Fernandez-Corbaton, C. Holzer, P. Scott, M. Wegener, W. Klopper, and C. Rockstuhl, "A digital twin for a chiral sensing platform," *Laser & Photonics Reviews*, 2300967 (2024).

[107] A. Sihvola, "*Electromagnetic emergence in metamaterials*," in *Advances in electromagnetics of complex media and metamaterials*, edited by S. Zouhdi, A. Sihvola, and M. Arsalane (Springer Netherlands, Dordrecht, 2002), pp. 3–17.

[108] V. M. Agranovich and V. Ginzburg, *Crystal optics with spatial dispersion, and excitons*, Vol. 42 (Springer, Berlin, Heidelberg, 2013).

[109] D. R. Smith and J. B. Pendry, "Homogenization of metamaterials by field averaging," *Journal of the Optical Society of America B* **23**, 391–403 (2006).

[110] M. G. Silveirinha, "Nonlocal homogenization model for a periodic array of ϵ-negative rods," *Physical Review E* **73**, 046612 (2006).

[111] A. S. Hossain, I. Tsukerman, and V. A. Markel, "Homogenization of periodic structures: One layer is "bulk"," *Europhysics Letters* **138**, 35001 (2022).

[112] A. Alù, "First-principles homogenization theory for periodic metamaterials," *Physical Review B* **84**, 075153 (2011).

[113] A. H. Sihvola and I. V. Lindell, "Analysis on chiral mixtures," *Journal of Electromagnetic Waves and Applications* **6**, 553–572 (1992).

[114] M. G. Silveirinha, "Metamaterial homogenization approach with application to the characterization of microstructured composites with negative parameters," *Physical Review B* **75**, 115104 (2007).

[115] A. Monti, F. Bilotti, and A. Toscano, "Optical cloaking of cylindrical objects by using covers made of core-shell nanoparticles," *Optics Letters* **36**, 4479–4481 (2011).

[116] C. Rockstuhl and T. Scharf, *Amorphous nanophotonics* (Springer, Berlin, Heidelberg, 2013).

[117] N. Mortensen, S. Xiao, and D. Felbacq, "Mesoscopic magnetism in dielectric photonic crystal meta materials: topology and inhomogeneous broadening," *Journal of the European Optical Society: Rapid Publications* **1**, 06019 (2006).

[118] M. G. Silveirinha and P. A. Belov, "Spatial dispersion in lattices of split ring resonators with permeability near zero," *Physical Review B* **77**, 233104 (2008).

[119] A. Monti, A. Alù, A. Toscano, and F. Bilotti, "Optical scattering cancellation through arrays of plasmonic nanoparticles: A review," *Photonics* **2**, 540–552 (2015).

[120] M. Yan and N. A. Mortensen, "Hollow-core infrared fiber incorporating metal-wire metamaterial," *Optics Express* **17**, 14851–14864 (2009).

[121] A. Ishimaru, S.-W. Lee, Y. Kuga, and V. Jandhyala, "Generalized constitutive relations for metamaterials based on the quasi-static lorentz theory," *IEEE Transactions on Antennas and Propagation* **51**, 2550–2557 (2003).

[122] G. T. Papadakis, P. Yeh, and H. A. Atwater, "Retrieval of material parameters for uniaxial metamaterials," *Physical Review B* **91**, 155406 (2015).

[123] G. Papadakis, D. Fleischman, A. Davoyan, P. Yeh, and H. A. Atwater, "Optical magnetism in planar metamaterial heterostructures," *Nature Communications* **9**, 296 (2018).

[124] S. I. Maslovski, S. A. Tretyakov, and P. A. Belov, "Wire media with negative effective permittivity: A quasi-static model," *Microwave and Optical Technology Letters* **35**, 47–51 (2002).

[125] K. Mnasri, F. Z. Goffi, M. Plum, and C. Rockstuhl, "Homogenization of wire media with a general purpose nonlocal constitutive relation," *Journal of the Optical Society of America B* **36**, F99–F108 (2019).

[126] S. A. Tretyakov, "A personal view on the origins and developments of the metamaterial concept," *Journal of Optics* **19**, 013002 (2016).

[127] M. G. Silveirinha, A. Alù, and N. Engheta, "Parallel-plate metamaterials for cloaking structures," *Physical Review E* **75**, 036603 (2007).

[128] A. V. Chebykin, M. A. Gorlach, and P. A. Belov, "Spatial-dispersion-induced birefringence in metamaterials with cubic symmetry," *Physical Review B* **92**, 045127 (2015).

[129] K. W. Whites, "Permittivity of a multiphase and isotropic lattice of spheres at low frequency," *Journal of Applied Physics* **88**, 1962–1970 (2000).

[130] P. A. Belov and C. R. Simovski, "Homogenization of electromagnetic crystals formed by uniaxial resonant scatterers," *Physical Review E* **72**, 026615 (2005).

[131] M. G. Silveirinha, "Generalized Lorentz-Lorenz formulas for microstructured materials," *Physical Review B* **76**, 245117 (2007).

[132] X.-X. Liu and A. Alù, "Limitations and potentials of metamaterial lenses," *Journal of Nanophotonics* **5**, 053509 (2011).

[133] A. Ciattoni and C. Rizza, "Nonlocal homogenization theory in metamaterials: Effective electromagnetic spatial dispersion and artificial chirality," *Physical Review B* **91**, 184207 (2015).

[134] M. G. Silveirinha, "Metamaterial homogenization approach with application to the characterization of microstructured composites with negative parameters," *Physical Review B* **75**, 115104 (2007).

[135] T. Repän, R. Venkitakrishnan, and C. Rockstuhl, "Artificial neural networks used to retrieve effective properties of metamaterials," *Optics Express* **29**, 36072–36085 (2021).

[136] D. A. G. Bruggeman, "Berechnung verschiedener physikalischer Konstanten von heterogenen Substanzen. I. Dielektrizitätskonstanten und Leitfähigkeiten der Mischkörper aus isotropen Substanzen," *Annalen der Physik* **416**, 636–664 (1935).

[137] Semechko, A., *Suite of functions to perform uniform sampling of a sphere*, MATLAB Central File Exchange, `https://www.mathworks.com/matlabcentral/fileexchange/37004-suite-of-functions-to-perform-uniform-sampling-of-a-sphere`, (accessed: 2022-03-24), 2021.

[138] R. Giannini, C. V. Hafner, and J. F. Löffler, "Scaling behavior of individual nanoparticle plasmon resonances," *The Journal of Physical Chemistry C* **119**, 6138–6147 (2015).

[139] A. Aharoni, "Demagnetizing factors for rectangular ferromagnetic prisms," *Journal of Applied Physics* **83**, 3432–3434 (1998).

[140] M. V. Rybin, D. S. Filonov, K. B. Samusev, P. A. Belov, Y. S. Kivshar, and M. F. Limonov, "Phase diagram for the transition from photonic crystals to dielectric metamaterials," *Nature Communications* **6**, 10102 (2015).

[141] *COMSOL Multiphysics® ver. 5.6, https://www.comsol.com/comsol-multiphysics*, COMSOL AB (Stockholm, 2020).

[142] *JCMsuite® ver. 4.6.3, http://www.jcmwave.com*, JCMwave GmbH (Berlin, 2021).

[143] S. L. James, "Metal-organic frameworks," *Chemical Society Reviews* **32**, 276–288 (2003).

[144] J.-L. Zhuang, A. Terfort, and C. Wöll, "Formation of oriented and patterned films of metal–organic frameworks by liquid phase epitaxy: A review," *Coordination Chemistry Reviews* **307**, 391–424 (2016).

[145] Z. Wang and C. Wöll, "Fabrication of metal–organic framework thin films using programmed layer-by-layer assembly techniques," *Advanced Materials Technologies* **4**, 1800413 (2019).

[146] S. Begum, Z. Hassan, S. Bräse, C. Wöll, and M. Tsotsalas, "Metal–organic framework-templated biomaterials: Recent progress in synthesis, functionalization, and applications," *Accounts of Chemical Research* **52**, 1598–1610 (2019).

[147] L. Heinke and C. Wöll, "Surface-mounted metal–organic frameworks: Crystalline and porous molecular assemblies for fundamental insights and advanced applications," *Advanced Materials* **31**, 1806324 (2019).

[148] *TURBOMOLE® ver. 7.6, https://www.turbomole.org*, TURBOMOLE GmbH (Karlsruhe, 2021).

[149] T. Yanai, D. P. Tew, and N. C. Handy, "A new hybrid exchange–correlation functional using the coulomb-attenuating method (cam-b3lyp)," *Chemical Physics Letters* **393**, 51–57 (2004).

[150] C. Rockstuhl and T. Scharf, "A metamaterial based on coupled metallic nanoparticles and its band-gap property," *Journal of Microscopy* **229**, 281–286 (2008).

[151] P. B. Johnson and R. W. Christy, "Optical constants of the noble metals," *Physical Review B* **6**, 4370–4379 (1972).

[152] W. Park, "Optical interactions in plasmonic nanostructures," *Nano Convergence* **1**, 2 (2014).

[153] C. Menzel, E. Hebestreit, R. Alaee, M. Albooyeh, S. Mühlig, S. Burger, C. Rockstuhl, C. Simovski, S. Tretyakov, F. Lederer, and T. Pertsch, "Extreme coupling: A route towards local magnetic metamaterials," *Physical Review B* **89**, 155125 (2014).

[154] S. Babar and J. H. Weaver, "Optical constants of Cu, Ag, and Au revisited," *Applied Optics* **54**, 477–481 (2015).

[155] N. Liu, H. Guo, L. Fu, S. Kaiser, H. Schweizer, and H. Giessen, "Plasmon hybridization in stacked cut-wire metamaterials," *Advanced Materials* **19**, 3628–3632 (2007).

[156] T. D. Kühne, M. Iannuzzi, M. Del Ben, V. V. Rybkin, P. Seewald, F. Stein, T. Laino, R. Z. Khaliullin, O. Schütt, F. Schiffmann, D. Golze, J. Wilhelm, S. Chulkov, M. H. Bani-Hashemian, V. Weber, U. Borštnik, M. Taillefumier, A. S. Jakobovits, A. Lazzaro, H. Pabst, T. Müller, R. Schade, M. Guidon, S. Andermatt, N. Holmberg, G. K. Schenter, A. Hehn, A. Bussy, F. Belleflamme, G. Tabacchi, A. Glöß, M. Lass, I. Bethune, C. J. Mundy, C. Plessl, M. Watkins, J. VandeVondele, M. Krack, and J. Hutter, "CP2K: An electronic structure and molecular dynamics software package - quickstep: Efficient and accurate electronic structure calculations," *Journal of Chemical Physics* **152**, 194103 (2020).

[157] A. G. Lamprianidis, C. Rockstuhl, and I. Fernandez-Corbaton, "Transcending the rayleigh hypothesis with multipolar sources distributed across the topological skeleton of a scatterer," *Journal of Quantitative Spectroscopy and Radiative Transfer* **296**, 108455 (2023).

[158] B. Peterson and S. Ström, "T Matrix for electromagnetic scattering from an arbitrary number of scatterers and representations of e(3)," *Physical Review D* **8**, 3661–3678 (1973).

[159] D. Schebarchov, E. C. L. Ru, J. Grand, and B. Auguié, "Mind the gap: Testing the rayleigh hypothesis in T-matrix calculations with adjacent spheroids," *Optics Express* **27**, 35750–35760 (2019).

[160] W. Golden, D. S. Dunn, and J. Overend, "A method for measuring infrared reflection—absorption spectra of molecules adsorbed on low-area surfaces at monolayer and submonolayer concentrations," *Journal of Catalysis* **71**, 395–404 (1981).

[161] R. G. Greenler, "Infrared Study of Adsorbed Molecules on Metal Surfaces by Reflection Techniques," *The Journal of Chemical Physics* **44**, 310–315 (1966).

[162] F. M. Hoffmann, "Infrared reflection-absorption spectroscopy of adsorbed molecules," *Surface Science Reports* **3**, 107–192 (1983).

[163] K. Molt, "Die Infrarot-Spektroskopie als Methode zur chemischen Charakterisierung von dünnen Schichten auf Metallen," *Fresenius' Zeitschrift für analytische Chemie* **319**, 743–750 (1984).

[164] Y. J. Chabal and K. Raghavachari, "New ordered structure for the H-saturated Si(100) surface: The (3×1) phase," *Physical Review Letters* **54**, 1055–1058 (1985).

[165] *TURBOMOLE® ver. 7.7, https://www.turbomole.org*, TURBOMOLE GmbH (Karlsruhe, 2022).

[166] C. Adamo and V. Barone, "Toward reliable density functional methods without adjustable parameters: The PBE0 model," *The Journal of Chemical Physics* **110**, 6158–6170 (1999).

[167] M. Ernzerhof and G. E. Scuseria, "Assessment of the Perdew–Burke–Ernzerhof exchange-correlation functional," *The Journal of Chemical Physics* **110**, 5029–5036 (1999).

[168] M. I. Mishchenko, L. D. Travis, and A. A. Lacis, *Scattering, Absorption, and Emission of Light by Small Particles* (Cambridge University Press, Cambridge, 2002).

[169] M. Schubert, T. E. Tiwald, and C. M. Herzinger, "Infrared dielectric anisotropy and phonon modes of sapphire," *Physical Review B* **61**, 8187–8201 (2000).

[170] Y. Wang and C. Wöll, "Ir spectroscopic investigations of chemical and photochemical reactions on metal oxides: bridging the materials gap," *Chemical Society Reviews* **46**, 1875–1932 (2017).

[171] C. Yang and C. Wöll, "IR spectroscopy applied to metal oxide surfaces: adsorbate vibrations and beyond," *Advances in Physics: X* **2**, 373–408 (2017).

[172] R. Haldar, Z. Fu, R. Joseph, D. Herrero, L. Martín-Gomis, B. S. Richards, I. A. Howard, A. Sastre-Santos, and C. Wöll, "Guest-responsive polaritons in a porous framework: Chromophoric sponges in optical QED cavities," *Chemical Science* **11**, 7972–7978 (2020).

[173] M. Rödel, P. Lisinetskaya, M. Rudloff, T. Stark, J. Manara, R. Mitric, and J. Pflaum, "The role of molecular arrangement on the strongly coupled exciton–plasmon polariton dispersion in metal–organic hybrid structures," *The Journal of Physical Chemistry C* **126**, 4163–4171 (2022).

[174] J. Fregoni, F. J. Garcia-Vidal, and J. Feist, "Theoretical challenges in polaritonic chemistry," *ACS Photonics* **9**, 1096–1107 (2022).

[175] M. Malerba, M. Jeannin, P. Goulain, A. Bousseksou, R. Colombelli, and J.-M. Manceau, "Multiple vibro-polaritons formation from a thin polyethylene film embedded in a resonant mid-infrared cavity," *(Preprint) arXiv:2108.02433* (2021).

[176] A. Thomas, J. George, A. Shalabney, M. Dryzhakov, S. J. Varma, J. Moran, T. Chervy, X. Zhong, E. Devaux, C. Genet, J. A. Hutchison, and T. W. Ebbesen, "Ground-state chemical reactivity under vibrational coupling to the vacuum electromagnetic field," *Angewandte Chemie International Edition* **55**, 11462–11466 (2016).

[177] F. J. Garcia-Vidal, C. Ciuti, and T. W. Ebbesen, "Manipulating matter by strong coupling to vacuum fields," *Science* **373**, eabd0336 (2021).

[178] D. S. Wang and S. F. Yelin, "A roadmap toward the theory of vibrational polariton chemistry," *ACS Photonics* **8**, 2818–2826 (2021).

[179] D. G. Baranov, M. Wersäll, J. Cuadra, T. J. Antosiewicz, and T. Shegai, "Novel nanostructures and materials for strong light–matter interactions," *ACS Photonics* **5**, 24–42 (2018).

[180] D. S. Dovzhenko, S. V. Ryabchuk, Y. P. Rakovich, and I. R. Nabiev, "Light–matter interaction in the strong coupling regime: Configurations, conditions, and applications," *Nanoscale* **10**, 3589–3605 (2018).

[181] Z. Jiang, A. Ren, Y. Yan, J. Yao, and Y. S. Zhao, "Exciton-polaritons and their bose–einstein condensates in organic semiconductor microcavities," *Advanced Materials* **34**, 2106095 (2022).

[182] J. Liu, B. Lukose, O. Shekhah, H. K. Arslan, P. Weidler, H. Gliemann, S. Bräse, S. Grosjean, A. Godt, X. Feng, K. Müllen, I.-B. Magdau, T. Heine, and C. Wöll, "A novel series of isoreticular metal organic frameworks: Realizing metastable structures by liquid phase epitaxy," *Scientific Reports* **2**, 921 (2012).

[183] T. Schwartz, J. A. Hutchison, J. Léonard, C. Genet, S. Haacke, and T. W. Ebbesen, "Polariton dynamics under strong light–molecule coupling," *ChemPhysChem* **14**, 125–131 (2013).

[184] J.-D. Chai and M. Head-Gordon, "Long-range corrected hybrid density functionals with damped atom–atom dispersion corrections," *Physical Chemistry Chemical Physics* **10**, 6615–6620 (2008).

[185] Frederic Moisy, *UIMAGE-UIMAGESC*, MATLAB Central File Exchange, `https://www.mathworks.com/matlabcentral/fileexchange/11368-uimage-uimagesc`, (accessed: 2021-03-30), 2021.

[186] E. Virmani, J. M. Rotter, A. Mähringer, T. von Zons, A. Godt, T. Bein, S. Wuttke, and D. D. Medina, "On-surface synthesis of highly oriented thin metal–organic framework films through vapor-assisted conversion," *Journal of the American Chemical Society* **140**, 4812–4819 (2018).

[187] J. P. Perdew, K. Burke, and M. Ernzerhof, "Generalized gradient approximation made simple," *Physical Review Letters* **77**, 3865–3868 (1996).

[188] J. P. Perdew, K. Burke, and M. Ernzerhof, "Generalized gradient approximation made simple [Physical Review Lett. 77, 3865 (1996)]," *Physical Review Letters* **78**, 1396–1396 (1997).

[189] K. M. McPeak, S. V. Jayanti, S. J. P. Kress, S. Meyer, S. Iotti, A. Rossinelli, and D. J. Norris, "Plasmonic films can easily be better: Rules and recipes," *ACS Photonics* **2**, 326–333 (2015).

[190] J. Feis, D. Beutel, J. Köpfler, X. Garcia-Santiago, C. Rockstuhl, M. Wegener, and I. Fernandez-Corbaton, "Helicity-preserving optical cavity modes for enhanced sensing of chiral molecules," *Physical Review Letters* **124**, 033201 (2020).

[191] M. J. Frisch, G. W. Trucks, H. B. Schlegel, G. E. Scuseria, M. A. Robb, J. R. Cheeseman, G. Scalmani, V. Barone, G. A. Petersson, H. Nakatsuji, X. Li, M. Caricato, A. V. Marenich, J. Bloino, B. G. Janesko, R. Gomperts, B. Mennucci, H. P. Hratchian, J. V. Ortiz, A. F. Izmaylov, J. L. Sonnenberg, D. Williams-Young, F. Ding, F. Lipparini, F. Egidi, J. Goings, B. Peng, A. Petrone, T. Henderson, D. Ranasinghe, V. G. Zakrzewski, J. Gao, N. Rega, G. Zheng, W. Liang, M. Hada, M. Ehara, K. Toyota, R. Fukuda, J. Hasegawa, M. Ishida, T. Nakajima, Y. Honda, O. Kitao, H. Nakai, T. Vreven, K. Throssell, J. A. Montgomery Jr., J. E. Peralta, F. Ogliaro, M. J. Bearpark, J. J. Heyd, E. N. Brothers, K. N. Kudin, V. N. Staroverov, T. A. Keith, R. Kobayashi, J. Normand, K. Raghavachari, A. P. Rendell, J. C. Burant, S. S. Iyengar, J. Tomasi, M. Cossi, J. M. Millam, M. Klene, C. Adamo, R. Cammi, J. W. Ochterski, R. L. Martin, K. Morokuma, O. Farkas, J. B. Foresman, and D. J. Fox, *Gaussian˜16 Revision C.01*, Gaussian Inc. Wallingford CT, 2016.

[192] F. Weigend, "Accurate Coulomb-fitting basis sets for H to Rn," *Physical Chemistry Chemical Physics* **8**, 1057–1065 (2006).

[193] A. Klamt and G. Schüürmann, "COSMO: a new approach to dielectric screening in solvents with explicit expressions for the screening energy and its gradient," *Journal of the Chemical Society, Perkin Transactions 2*, 799–805 (1993).

[194] *COMSOL Multiphysics® ver. 5.4, https://www.comsol.com/comsol-multiphysics*, COMSOL AB (Stockholm, 2018).

[195] Y. Hou, M. Qiu, Z. Cao, J. Zhou, H. C. Ong, W. Jin, J. Du, and D. Lei, "High-q circular dichroism resonances in plasmonic lattices with chiral unit cells," *Advanced Functional Materials* **32**, 2204095 (2022).

[196] E. Hendry, R. V. Mikhaylovskiy, L. D. Barron, M. Kadodwala, and T. J. Davis, "Chiral electromagnetic fields generated by arrays of nanoslits," *Nano Letters* **12**, 3640–3644 (2012).

[197] M. Schäferling, D. Dregely, M. Hentschel, and H. Giessen, "Tailoring enhanced optical chirality: Design principles for chiral plasmonic nanostructures," *Physical Review X* **2**, 031010 (2012).

[198] C. Kelly, L. Khosravi Khorashad, N. Gadegaard, L. D. Barron, A. O. Govorov, A. S. Karimullah, and M. Kadodwala, "Controlling metamaterial transparency with superchiral fields," *ACS Photonics* **5**, 535–543 (2018).

[199] F. Graf, J. Feis, X. Garcia-Santiago, M. Wegener, C. Rockstuhl, and I. Fernandez-Corbaton, "Achiral, helicity preserving, and resonant structures for enhanced sensing of chiral molecules," *ACS Photonics* **6**, 482–491 (2019).

[200] M. L. Solomon, J. Hu, M. Lawrence, A. García-Etxarri, and J. A. Dionne, "Enantiospecific optical enhancement of chiral sensing and separation with dielectric metasurfaces," *ACS Photonics* **6**, 43–49 (2019).

[201] J. Lasa-Alonso, D. R. Abujetas, Á. Nodar, J. A. Dionne, J. J. Sáenz, G. Molina-Terriza, J. Aizpurua, and A. García-Etxarri, "Surface-enhanced circular dichroism spectroscopy on periodic dual nanostructures," *ACS Photonics* **7**, 2978–2986 (2020).

[202] J. Hu, M. Lawrence, and J. A. Dionne, "High quality factor dielectric metasurfaces for ultraviolet circular dichroism spectroscopy," *ACS Photonics* **7**, 36–42 (2020).

[203] S. Qiao, Q. Liang, X. Zhang, X. Liu, S. Feng, C.-Y. Ji, H. Guo, and J. Li, "Flexible engineering of circular dichroism enabled by chiral surface lattice resonances," *APL Photonics* **7**, 116104 (2022).

[204] S. Zong, D. Zeng, G. Liu, Y. Wang, Z. Liu, and J. Chen, "Multiple resonant modes coupling enabled strong cd response in a chiral metasurface," *Optics Express* **30**, 40470–40481 (2022).

[205] Y. Tang and A. E. Cohen, "Optical chirality and its interaction with matter," *Physical Review Letters* **104**, 163901 (2010).

[206] V. E. Babicheva and A. B. Evlyukhin, "Multipole lattice effects in high refractive index metasurfaces," *Journal of Applied Physics* **129**, 040902 (2021).

[207] *JCMsuite® ver. 5.2.4, http://www.jcmwave.com*, JCMwave GmbH (Berlin, 2022).

[208] A.-I. Bunea, N. del Castillo Iniesta, A. Droumpali, A. E. Wetzel, E. Engay, and R. Taboryski, "Micro 3D printing by two-photon polymerization: Configurations and parameters for the nanoscribe system," *Micro* **1**, 164–180 (2021).

[209] M. Nakazawa, E. Yamada, H. Kubota, and K. Suzuki, "10 Gbit/s soliton data transmission over one million kilometres," *Electronics Letters* **27**, 1270–1272 (1991).

[210] T. Herr, V. Brasch, J. D. Jost, C. Y. Wang, N. M. Kondratiev, M. L. Gorodetsky, and T. J. Kippenberg, "Temporal solitons in optical microresonators," *Nature Photonics* **8**, 145–152 (2014).

[211] P. Marin-Palomo, J. N. Kemal, M. Karpov, A. Kordts, J. Pfeifle, M. H. P. Pfeiffer, P. Trocha, S. Wolf, V. Brasch, M. H. Anderson, R. Rosenberger, K. Vijayan, W. Freude, T. J. Kippenberg, and C. Koos, "Microresonator-based solitons for massively parallel coherent optical communications," *Nature* **546**, 274–279 (2017).

[212] T. Harter, S. Ummethala, M. Blaicher, S. Muehlbrandt, S. Wolf, M. Weber, M. M. H. Adib, J. N. Kemal, M. Merboldt, F. Boes, S. Nellen, A. Tessmann, M. Walther, B. Globisch, T. Zwick, W. Freude, S. Randel, and C. Koos, "Wireless THz link with optoelectronic transmitter and receiver," *Optica* **6**, 1063–1070 (2019).

[213] T. Udem, R. Holzwarth, and T. W. Hänsch, "Optical frequency metrology," *Nature* **416**, 233–237 (2002).

[214] S. A. Diddams, K. Vahala, and T. Udem, "Optical frequency combs: Coherently uniting the electromagnetic spectrum," *Science* **369** (2020).

[215] E. L. Wooten, K. M. Kissa, A. Yi-Yan, E. J. Murphy, D. A. Lafaw, P. F. Hallemeier, D. Maack, D. V. Attanasio, D. J. Fritz, G. J. McBrien, and D. E. Bossi, "A review of lithium niobate modulators for fiber-optic communications systems," *IEEE Journal of Selected Topics in Quantum Electronics* **6**, 69–82 (2000).

[216] S. Liu, P. P. Vabishchevich, A. Vaskin, J. L. Reno, G. A. Keeler, M. B. Sinclair, I. Staude, and I. Brener, "An all-dielectric metasurface as a broadband optical frequency mixer," *Nature Communications* **9**, 2507 (2018).

[217] A. Fedotova, L. Carletti, A. Zilli, F. Setzpfandt, I. Staude, A. Toma, M. Finazzi, C. De Angelis, T. Pertsch, D. N. Neshev, and M. Celebrano, "Lithium niobate meta-optics," *ACS Photonics* **9**, 3745–3763 (2022).

[218] P. P. Vabishchevich, S. Liu, M. B. Sinclair, G. A. Keeler, G. M. Peake, and I. Brener, "Enhanced second-harmonic generation using broken symmetry iii–v semiconductor fano metasurfaces," *ACS Photonics* **5**, 1685–1690 (2018).

[219] B. Gu, C. Zhao, A. Baev, K.-T. Yong, S. Wen, and P. N. Prasad, "Molecular nonlinear optics: Recent advances and applications," *Advances in Optics and Photonics* **8**, 328–369 (2016).

[220] G. S. He, L.-S. Tan, Q. Zheng, and P. N. Prasad, "Multiphoton absorbing materials: Molecular designs, characterizations, and applications," *Chemical Reviews* **108**, 1245–1330 (2008).

[221] X. Li, Z. Rinkevicius, and H. Ågren, "Two-photon absorption of metal-assisted chromophores," *Journal of Chemical Theory and Computation* **10**, 5630–5639 (2014).

[222] A. Nefedov, R. Haldar, Z. Xu, H. Kühner, D. Hofmann, D. Goll, B. Sapotta, S. Hecht, M. Krstić, C. Rockstuhl, W. Wenzel, S. Bräse, P. Tegeder, E. Zojer, and C. Wöll, "Avoiding the center-symmetry trap: Programmed assembly of dipolar precursors into porous, crystalline molecular thin films," *Advanced Materials* **33**, 2103287 (2021).

[223] S. R. Marder, B. Kippelen, A. K.-Y. Jen, and N. Peyghambarian, "Design and synthesis of chromophores and polymers for electro-optic and photorefractive applications," *Nature* **388**, 845–851 (1997).

[224] S. S. Kruk, R. Camacho-Morales, L. Xu, M. Rahmani, D. A. Smirnova, L. Wang, H. H. Tan, C. Jagadish, D. N. Neshev, and Y. S. Kivshar, "Nonlinear optical magnetism revealed by second-harmonic generation in nanoantennas," *Nano Letters* **17**, 3914–3918 (2017).

[225] G. Boudebs, M. Chis, and X. N. Phu, "Third-order susceptibility measurement by a new Mach-Zehnder interferometry technique," *Journal of the Optical Society of America B* **18**, 623–627 (2001).

[226] S. Wolf, H. Zwickel, W. Hartmann, M. Lauermann, Y. Kutuvantavida, C. Kieninger, L. Altenhain, R. Schmid, J. Luo, A. K.-Y. Jen, S. Randel, W. Freude, and C. Koos, "Silicon-organic hybrid (SOH) Mach-Zehnder modulators for 100 Gbit/s on-off keying," *Scientific Reports* **8**, 2598 (2018).

[227] R. W. Boyd, Z. Shi, and I. De Leon, "The third-order nonlinear optical susceptibility of gold," *Optics Communications* **326**, 74–79 (2014).

[228] R. W. Munn, "Electric dipole interactions in molecular crystals," *Molecular Physics* **64**, 1–20 (1988).

[229] H. Reis, M. G. Papadopoulos, and R. W. Munn, "Calculation of macroscopic first-, second-, and third-order optical susceptibilities for the urea crystal," *The Journal of Chemical Physics* **109**, 6828–6838 (1998).

[230] H. Reis, M. G. Papadopoulos, C. Hättig, J. G. Ángyán, and R. W. Munn, "Distributed first and second order hyperpolarizabilities: An improved calculation of nonlinear optical susceptibilities of molecular crystals," *The Journal of Chemical Physics* **112**, 6161–6172 (2000).

[231] Z. Lin, Z. Wang, C. Chen, and M.-H. Lee, "Mechanism of linear and nonlinear optical effects of KDP and urea crystals," *The Journal of Chemical Physics* **118**, 2349–2356 (2003).

[232] M. Olejniczak, M. Pecul, B. Champagne, and E. Botek, "Theoretical investigation on the linear and nonlinear susceptibilities of urea crystal," *The Journal of Chemical Physics* **128**, 244713 (2008).

[233] S. J. Luo, J. T. Yang, W. F. Du, and A. Laref, "Mechanism of linear and nonlinear optical properties of the urea crystal family," *The Journal of Physical Chemistry A* **115**, 5192–5200 (2011).

[234] M. Rérat, L. Maschio, B. Kirtman, B. Civalleri, and R. Dovesi, "Computation of second harmonic generation for crystalline urea and KDP. An ab initio approach through the coupled perturbed Hartree–Fock/Kohn–Sham scheme," *Journal of Chemical Theory and Computation* **12**, 107–113 (2016).

[235] F. Mairesse, L. Maschio, and B. Champagne, "First-principles evaluation of the second harmonic generation response of reference organic and inorganic crystals," *The Journal of Chemical Physics* **158**, 064707 (2023).

[236] J. A. Morrell, A. C. Albrecht, K. H. Levin, and C. L. Tang, "The electro-optic coefficients of urea," *The Journal of Chemical Physics* **71**, 5063–5068 (1979).

[237] J. Zyss and G. Berthier, "Nonlinear optical properties of organic crystals with hydrogen-bonded molecular units: The case of urea," *The Journal of Chemical Physics* **77**, 3635–3653 (1982).

[238] I. Ledoux and J. Zyss, "*Influence of the molecular environment in solution measurements of the Second-order optical susceptibility for urea and derivatives*," Chemical Physics **73**, 203–213 (1982).

[239] C. Cassidy, J. M. Halbout, W. Donaldson, and C. L. Tang, "Nonlinear optical properties of urea," *Optics Communications* **29**, 243–246 (1979).

[240] J.-M. Halbout, S. Blit, W. Donaldson, and C. Tang, "Efficient phase-matched second-harmonic generation and sum-frequency mixing in urea," *IEEE Journal of Quantum Electronics* **15**, 1176–1180 (1979).

[241] *COMSOL Multiphysics® ver. 6.1, https://www.comsol.com/comsol-multiphysics*, COMSOL AB (Stockholm, 2022).

[242] I. Sekulic, J. W. You, and N. C. Panoiu, "T-matrix method for calculation of second-harmonic generation in clusters of spherical particles," *Journal of Quantitative Spectroscopy and Radiative Transfer* **268**, 107643 (2021).

[243] I. Sekulic, J. W. You, and N. C. Panoiu, "T-matrix method for computation of second-harmonic generation upon optical wave scattering from clusters of arbitrary particles," *(Preprint) arXiv:2208.13977v1* (2022).

[244] J. Zyss and J. L. Oudar, "Relations between microscopic and macroscopic lowest-order optical nonlinearities of molecular crystals with one- or two-dimensional units," *Physical Review A* **26**, 2028–2048 (1982).

[245] H. Guth, G. Heger, S. Klein, W. Treutmann, and C. Scheringer, "Strukturverfeinerung von Harnstoff mit Neutronenbeugungsdaten bei 60, 123 und 293 K und X-N- und X-X(1s2)-Synthesen bei etwa 100 K," *Zeitschrift für Kristallographie - Crystalline Materials* **153**, 237–254 (1980).

[246] A. D. Becke, "Density-functional thermochemistry. III. The role of exact exchange," *The Journal of Chemical Physics* **98**, 5648–5652 (1993).

[247] C. Lee, W. Yang, and R. G. Parr, "Development of the Colle-Salvetti correlation-energy formula into a functional of the electron density," *Physical Review B* **37**, 785–789 (1988).

[248] Z. H. Levine and D. C. Allan, "Large local-field effects in the second-harmonic susceptibility of crystalline urea," *Physical Review B* **48**, 7783–7789 (1993).

[249] J. Shi, X. He, W. Chen, Y. Li, M. Kang, Y. Cai, and H. Xu, "Remote dual-cavity enhanced second harmonic generation in a hybrid plasmonic waveguide," *Nano Letters* **22**, 688–694 (2022).

[250] J. Shi, X. Wu, K. Wu, S. Zhang, X. Sui, W. Du, S. Yue, Y. Liang, C. Jiang, Z. Wang, W. Wang, L. Liu, B. Wu, Q. Zhang, Y. Huang, C.-W. Qiu, and X. Liu, "Giant enhancement and directional second harmonic emission from monolayer WS_2 on silicon substrate via Fabry-Pérot micro-cavity," *ACS Nano* **16**, 13933–13941 (2022).

[251] Y. Qiao, F. Ye, Y. Zheng, and X. Chen, "Cavity-enhanced second-harmonic generation in strongly scattering nonlinear media," *Physical Review A* **99**, 043844 (2019).

[252] P. Parra-Rivas, C. M. Arabí, and F. Leo, "Dark quadratic localized states and collapsed snaking in doubly resonant dispersive cavity-enhanced second-harmonic generation," *Physical Review A* **104**, 063502 (2021).

[253] S. Yuan, Y. Wu, Z. Dang, C. Zeng, X. Qi, G. Guo, X. Ren, and J. Xia, "Strongly enhanced second harmonic generation in a thin film lithium niobate heterostructure cavity," *Physical Review Letters* **127**, 153901 (2021).

[254] P. E. Barclay, K. Srinivasan, and O. Painter, "Nonlinear response of silicon photonic crystal microresonators excited via an integrated waveguide and fiber taper," *Optics Express* **13**, 801–820 (2005).

[255] B. McLaughlin, D. P. Lake, M. Mitchell, and P. E. Barclay, "Nonlinear optics in gallium phosphide cavities: Simultaneous second and third harmonic generation," *Journal of the Optical Society of America B* **39**, 1853–1860 (2022).

[256] N. Bloembergen and P. S. Pershan, "Light waves at the boundary of nonlinear media," *Physical Review* **128**, 606–622 (1962).

[257] R. W. Terhune, P. D. Maker, and C. M. Savage, "Optical harmonic generation in calcite," *Physical Review Lett.* **8**, 404–406 (1962).

[258] N. Bloembergen, R. K. Chang, S. S. Jha, and C. H. Lee, "Optical second-harmonic generation in reflection from media with inversion symmetry," *Physical Review* **174**, 813–822 (1968).

[259] J. I. Dadap, J. Shan, K. B. Eisenthal, and T. F. Heinz, "Second-harmonic Rayleigh scattering from a sphere of centrosymmetric material," *Physical Review Letters* **83**, 4045–4048 (1999).

[260] J. E. Sipe, D. J. Moss, and H. M. van Driel, "Phenomenological theory of optical second- and third-harmonic generation from cubic centrosymmetric crystals," *Physical Review B* **35**, 1129–1141 (1987).

[261] P. Guyot-Sionnest, W. Chen, and Y. R. Shen, "General considerations on optical second-harmonic generation from surfaces and interfaces," *Physical Review B* **33**, 8254–8263 (1986).

[262] O. A. Aktsipetrov, A. A. Fedyanin, E. D. Mishina, A. N. Rubtsov, C. W. van Hasselt, M. A. C. Devillers, and T. Rasing, "Dc-electric-field-induced second-harmonic generation in Si(111)-SiO_2-Cr metal-oxide-semiconductor structures," *Physical Review B* **54**, 1825–1832 (1996).

[263] H.-Y. Tsai, Y. J. Chang, J.-W. Hu, and K.-Y. Chen, "Synthesis, crystal structure, spectroscopic properties, and DFT studies of 7,9-Dibromobenzo[h]quinolin-10-ol," *Crystals* **7**, 60 (2017).

[264] S. Kanakaraju, S. Mohan, and A. Sood, "Optical and structural properties of reactive ion beam sputter deposited CeO_2 films," *Thin Solid Films* **305**, 191–195 (1997).

A | Results for Three-Linker Model of Zn-SiPc-SURMOF-2

In the following, we discuss a second finite-size model of the Zn-SiPc-SURMOF-2. In comparison to the first model, analyzed in Section 6.3, it is approximately half as large because it consists only of three linkers. In the context of the TD-DFT simulations, the unit cell is optimized with CP2K first [156]. Then the functional CAM-B3LYP [149] and the def2-TZVP basis set [99] are used to obtain the polarizability tensors. Figure A.1 displays the orientationally averaged absorption cross sections, computed directly with TD-DFT and obtained from the polarizabilities of the finite-size molecular model. The absorption cross sections show two instead of three peaks, which are observed for the first model in Figure 6.9. This can be related to the fact that the second model is considerably smaller so that the TD-DFT results are not perfectly converged. In the next step, the optical response is computed of the thin film in a vacuum and inside the cavity from Figure 6.8. To construct a unit cell for the scattering simulations with *mpGMM* [51], the T-matrix from the three-linker model in Figure A.1 is combined with the T-matrix from a $\frac{\pi}{2}$-rotated version of the model. With [52, Eq.(22)], the global T-matrix of the unit cell is obtained, which is periodically arranged in two dimensions and stacked in z-direction to build a film as described in Section 3.2. Figure A.2 shows the absorption spectra of the thin film in a vacuum and inside the cavity for a normal incident left-handed circularly polarized plane wave. We observe that although a

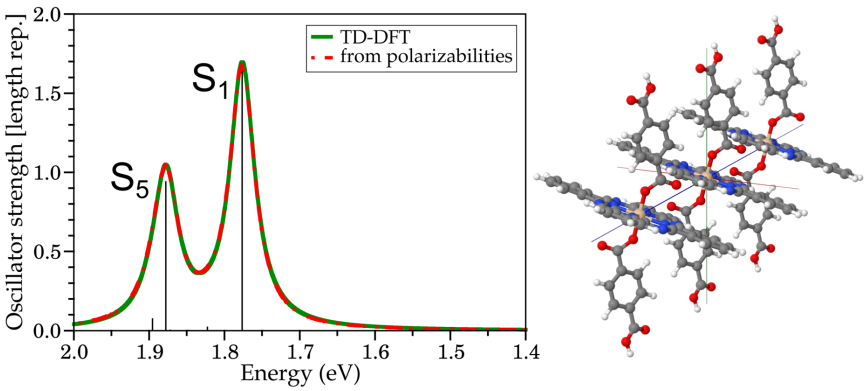

Figure A.1.: Orientationally averaged absorption cross sections (left) computed directly with TD-DFT and obtained from the polarizability tensor of the finite-size model of the Zn-SiPc-SURMOF-2 (right). The finite-size molecular model is half as large as compared to the finite-size model in Figure 6.8**(b)**. Originally created by Marjan Krstić. Adapted with permission from [P4]. Copyright © 2022 John Wiley and Sons.

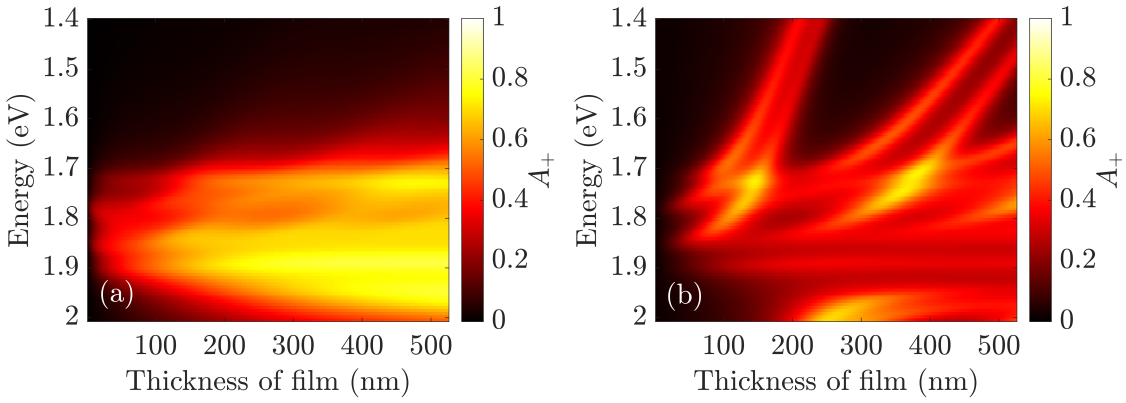

Figure A.2.: Absorption spectra of the Zn-SiPc-SURMOF-2 for the second finite-size model in Figure A.1. **(a)** Spectrum of the SURMOF in a vacuum. **(b)** Spectrum of the filled cavity. The agreement to the spectra for the first model in Figure 6.10 and Figure 6.11 is good. Adapted with permission from [P4]. Copyright © 2022 John Wiley and Sons.

peak is missing in the absorption cross sections obtained with TD-DFT, the spectra are very similar to the spectra computed for the first model, see Figures 6.10**(a)** and 6.11**(a)**.

B | Results for Different Molecular Models of TDBC-J-Aggregates in a PVA Polymer

In Section 6.3, we consider the coupling of a cavity and a molecular film of TDBC-J-aggregates in a PVA polymer. We show in Figures 6.19 and 6.20 different molecular models of the material and their corresponding orientationally averaged absorption cross sections. For the simulation of the optical response of the molecular film within the cavity in Section 6.3, we concentrate on the "3×4" model. In the following, we also analyze the "2×4" and "2×6" models. We obtain the effective material parameters with the Lorentz-Lorenz formulas from [113] based on the TD-DFT obtained polarizabilities, setting the concentrations to $\frac{1}{8} \cdot 10^{20}\,\mathrm{cm}^{-3}$ and $\frac{1}{12} \cdot 10^{20}\,\mathrm{cm}^{-3}$, respectively. Figures B.1 and B.2 display the refractive indices, the mode analysis, and the absorption spectra of the filled cavities. We observe a very good agreement to the results for the "3×4" model shown in Figure 6.21.

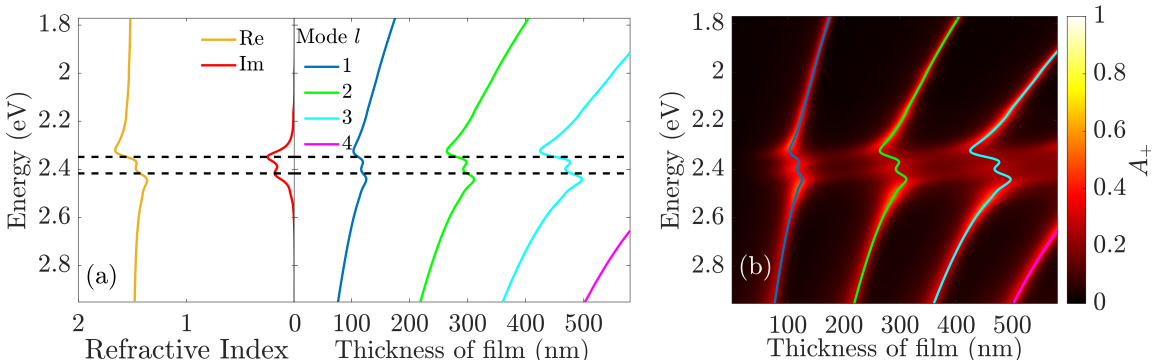

Figure B.1.: Mode analysis of a cavity filled with TDBC J-aggregates in a PVA polymer, using the "2×4" model. In panel **(a)**, the effective refractive index and the model analysis are shown. Panel **(b)** depicts the absorption spectrum of the filled cavity. The spectrum agrees well with Figure 6.21**(b)**, showing the absorption spectrum for the "3×4" model. Adapted with permission from [P4]. Copyright © 2022 John Wiley and Sons.

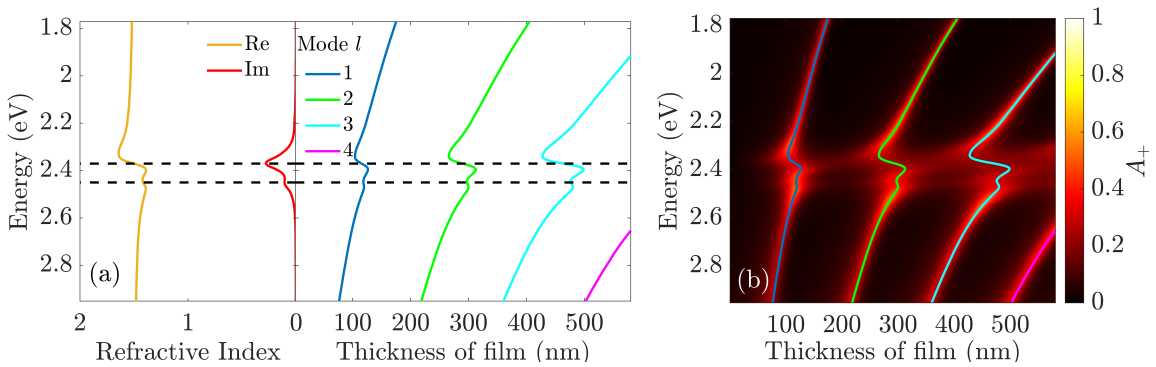

Figure B.2.: Mode analysis of a cavity filled with TDBC J-aggregates in a PVA polymer, using the "2×6" model. Panel **(a)** shows the effective refractive index and the model analysis. In Panel **(b)** the absorption spectrum of the filled cavity is displayed which agrees well with the spectrum for the "3×4" model in Figure 6.21**(b)**. Adapted with permission from [P4]. Copyright © 2022 John Wiley and Sons.

C | Study of Different Finite-Size Molecular Models of the Urea Crystal

In Section 7.1, we consider a finite-size molecular model of the urea crystal consisting of 16 molecules (128 atoms). Figure C.1 displays the xyz-component of the first hyperpolarizability per molecule for different models, obtained with TD-DFT. The xyz-component is one of the most dominating components of the first hyperpolarizability. The models consist of two, 16, 54, and 128 molecules. We observe that the value for 16 molecules, used in the multi-scale simulations, is sufficiently close to the values for the larger models considering also that the computational time is 17 times faster than for the next larger model and 155 times faster than for the largest model [P6].

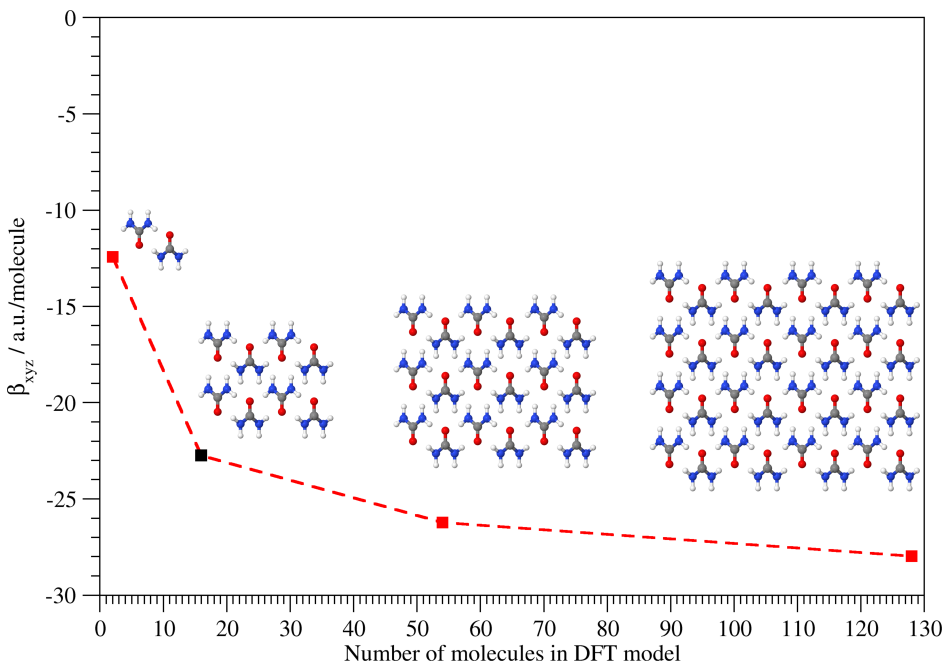

Figure C.1.: Component of the first hyperpolarizability of differently sized molecular models of the urea crystal. The model considered in Section 7.1 consists of 16 molecules. The convergence is sufficiently good. Created by Marjan Krstić. Reprinted with permission from [P6]. Copyright © 2024 John Wiley and Sons.

Acknowledgements

A doctoral thesis is accompanied by many challenges. Overcoming these challenges, I enjoyed the support from many people. In the following, I would like to sincerely thank these persons.

First of all, I would like to express my deep gratitude to my supervisor Carsten Rockstuhl. I benefited a lot from his enormous knowledge in all topics related to Optics and Photonics. He showed me routes to continue with a project and also provided me freedom to pursuit my own ideas. The members of his group are outstanding friendly and support each other. I am sure that this behavior is also tightly connected to the character of his leadership.

I want to thank Igor Tsukerman very much for reviewing my thesis as second referee.

Almost during my entire PhD time, I shared an office with three postdocs who worked on the same research area like me: Marjan Krstić, Christof Holzer, and Markus Nyman. I want to thank them very much as I benefited all the time from their support and different perspective having already finished their PhD some years ago. Furthermore, I enjoyed very much our collaborations. Marjan and Christof helped me with their deep knowledge in density-functional theory, and Markus supported me concerning optical aspects. Our collaborations were always great teamwork, and we also had a lot of fun all the time. I want to especially thank Christof Holzer for reading the DFT chapter of this thesis.

In the context of collaborations, I also want to express my gratitude to Dominik Beutel and Ivan Fernandez-Corbaton. While Dominik helped me a lot concerning Computational Photonics, Ivan supported me with his knowledge about scattering theory. I am thankful to Ramakrishna Venkitakrishnan for sharing his insights into effective medium theory with me.

I also want to thank my experimental collaborators who provided me with their perspective concerning the realization of projects in a laboratory. I would like to express my gratitude explicitly to Christof Wöll, Lars Heinke, Ana Fingolo, and Benedikt Sapotta. I additionally want to thank all my other collaborators who supported me during several projects with their intriguing ideas.

I am very thankful to all previous members of the group who were sharing the office with me: Taavi Repän, Marvin Müller, Lukas Materne, Patrick Golz, Martin Mäck, Daniel Sitter, and Joshua McCauley.

I would like to deeply thank all current and former members of the group for all the great time we spent together on working, discussing, and having fun together. As special highlight I want to point out our great group retreats.

Finally, I want to express my deep gratitude to my parents and to my brother Konstantin for all their support during my entire life.

Selbstständigkeitserklärung

Eidesstattliche Versicherung gemäß § 13 Absatz 2 Ziffer 3 der Promotionsordnung des Karlsruher Instituts für Technologie (KIT) für die KIT-Fakultät für Physik:

1. Bei der eingereichten Dissertation zu dem Thema
   „Photonic Devices Made from Molecular Materials: A Multi-Scale Modeling Approach"
   handelt es sich um meine eigenständig erbrachte Leistung.

2. Ich habe nur die angegebenen Quellen und Hilfsmittel benutzt und mich keiner unzulässigen Hilfe Dritter bedient. Insbesondere habe ich wörtlich oder sinngemäß aus anderen Werken übernommene Inhalte als solche kenntlich gemacht.

3. Die Arbeit oder Teile davon habe ich wie folgt/ bislang nicht[1] an einer Hochschule des In- oder Auslands als Bestandteil einer Prüfungs- oder Qualifikationsleistung vorgelegt.

   Titel der Arbeit: Photonic Devices Made from Molecular Materials: A Multi-Scale Modeling Approach

   Hochschule und Jahr: KIT-Fakultät für Physik, 2024

   Art der Prüfungs- oder Qualifikationsleistung: Dissertation

4. Die Richtigkeit der vorstehenden Erklärungen bestätige ich.

5. Die Bedeutung der eidesstattlichen Versicherung und die strafrechtlichen Folgen einer unrichtigen oder unvollständigen eidesstattlichen Versicherung sind mir bekannt.

Ich versichere an Eides statt, dass ich nach bestem Wissen die reine Wahrheit erklärt und nichts verschwiegen habe.

Ort und Datum Unterschrift

[1] Nicht Zutreffendes streichen. Bei Bejahung sind anzugeben: der Titel der andernorts vorgelegten Arbeit, die Hochschule, das Jahr der Vorlage und die Art der Prüfungs- oder Qualifikationsleistung.